Alma Mater Studiorum – Università di Bologna

DOTTORATO DI RICERCA IN
NANOSCIENZE PER LA MEDICINA E L'AMBIENTE

Ciclo XXXIV

Settore concorsuale: 03/A1
Settore Scientifico Disciplinare: CHIM/01

POLYANILINE–BASED MATERIALS AND NANOCOMPOSITES: FROM ENERGY STORAGE TO SENSING APPLICATIONS

Presentata da: Ilaria Ragazzini

Coordinatore Dottorato: Prof. Dario Braga

Supervisore: Prof. Barbara Ballarin

Co-Supervisore: Prof. Stefano Stagni

Anno 2022

Abstract

The research work described in this thesis concerns materials for both energy storage and sensoristics applications. Firstly, the synthesis and characterization of magnetite (Fe_3O_4) functionalyzed with [3-(2-propynylcarbamate)propyl]triethoxysilane (PPTEOS) capable to reduce the gold precursor chloroauric acid ($HAuCl_4$) without the need of additional reducing or stabilising agents is described. These nanoparticles were tested to improve performances of symmetric capacitors based on polyaniline and graphite foil.

Energy storage applications were investigated also during six months stay at EPFL University of Lausanne where an investigation about different tailored catalysts for Oxygen Evolution Reaction in a particular Redox Flow Battery was carried out.

For what concerns sensing applications, new materials based on cellulose modified with polyaniline and poly(2-acrylamido-2-methyl-1-propanesulfonic acid) (PAAMPSA) were synthesized, characterized and applied to monitor pressure, humidity, heart rate and lastly, bread fermentation in collaboration with the University of Fribourg and Zurich.

The characterizations of all the materials investigated compriseed numerous techniques such as infrared attenuated total reflectance spectroscopy (IR-ATR), thermogravimetric analysis (TGA), scanning and transmission electron microscopy (SEM and TEM), alongside linear and cyclic voltammetry (LSV and CV), electrochemical impedance spectroscopy (EIS) and chronoamperometric analyses.

The thesis organisation and the content of each chapter can be summarized as follows:

Chapter 1. General introduction on the topic of nanotechnologies, followed by an overview on their applications in energy storage devices, with a particular focus on pseudocapacitors and redox flow batteries. In this perspective, a brief discussion on polyaniline as electroactive material is reported. Lastly, the same conductive polymer for sensing applications as paper-based material was investigated.

Chapter 2. Synthesis of magnetic Fe_3O_4 (magnetite) nanoparticles in different alkaline environments (NH_3 or NaOH) and successive functionalization with PPTEOS to promote the nucleation and stabilisation of gold nanoparticles to obtain Au/Fe_3O_4@Yne composites. The characterization was carried out using different and complementary techniques and a comparison among the materials obtained was performed.

Chapter 3. Magnetite nanoparticles described in the previous chapter were used to prepare pseudocapacitors based on polyaniline electrodepositated on graphite foils. The obtained electrodes were firstly characterized from the chemico-physical and electroanalytical point of view in order to choose the best one that was, successively employed to assemble a prototype of symmetric gel state supercapacitor. Lastly, the performances of the supercapacitor were investigated.

Chapter 4. An industrial paper process to prepare sheets of cellulose covered with polyaniline was presented. The material was fully characterized and its properties were demonstrated assembling a capacitive touch sensor. Different geometries were tested and the best one was chosen in terms of response time and pressure-stimuli behaviour. A description of the material as sensor to detect the state of fermentation of bread is also carried out.

Chapter 5. The synthesis and characterization of a new material based on cellulose modified with polyaniline and poly(2-acrylamido-2-methyl-1-propanesulfonic acid)

(PAAMPSA) is presented. After the characterization, the material was studied as humidity sensor to be applied in museums with a relative humidity range between 30% and 50 % and compared with a cheap and commercial sensor. A comparison between the new material and the already presented PANI-modified cellulose was carried out. In addition, a brief discussion about the PANI-PAAMPSA-modified cellulose as electrode for ECG monitoring is conducted.

Chapter 6. The possibility to synthesize catalysts for OER with a new technique called photonic curing was investigated. Firstly, a study of the reaction condition and the machine paramenters to produce IrO_x was carried out in comparison with a well-known pathway. Moreover, the synthesis of Mn-doped RuO_2 and Zn-doped RuO_2 was carried out with the same technique and their performances were evaluated electrochemically. Once the best synthesized catalyst was chosen, it was applied in a dual circuit Redox Flow Battery where the electrolyte was used as electrons mediator together with the catalyst to produce oxygen *via* water splitting reaction.

Table of contents

1 General introduction

1.1 Nanotechnologies and nanomaterials

Nanotechnology is the science that deals with the development and application of materials with at least one size at the nanometric scale (1 – 100 nm). *Nanomaterials* display a high surface to volume ratio which allows applications in several different fields, such as chemistry, engineering, medicine, biotechnology, environmental science, etc [1-3].

Contrary to what one might believe, nanotechnologies are not new, since the first examples of the production of nanostructured materials can be dated back to ancient history, when for example gold, silver and copper nanoparticles were used as coloured pigments in stained glass and ceramics [4]. The natural world also presents many examples of nanoscale structures, from milk (a nanoscale colloid) to more sophisticated nanostructured proteins [2].

However, the ideas and concepts at the base of nowadays nanotechnologies were first discussed in 1959 by the physicist Richard Feynman during the famous talk entitled "*There's plenty of room at the bottom*", in which the possibility to manipulate and control individual atoms and molecules was described, though the term "nanotechnology" was coined by Prof. Norio Taniguchi only several years later.

One of the most important developments that gave a boost to the studies in this field was the invention of the scanning tunnelling microscope by Gerd Binnig and Heinrich Rohrer in 1981, which allowed scientists to "see" individual atoms for the first time.

Looking fast forward to last two years in which I competed my PhD studies, it is impossible not to think about the social disaster represented by Coronavirus infection that changed all our lives. Improvement in nanotechnologies, made possible thanks to researches, plays an important role also in combat against this disease[3-5]. For example, graphene oxide nanosheets, thanks to their two-dimensional shape, are able to play an antiviral impact on the virus disturbing their plasma layer or creating reactive oxygen species to activate oxidative reactions[6]. Moreover, the colorimetric detection of Covid-19 is possible due to the capacity of AuNPs to absorb particular filaments of nucleic acids on their surface[7]. Lastly, SARS vaccine nano-delivery system is disclosed in the Korean patent where a SARS-CoV2 DNA vaccine encoding the spike protein was complexed with a polymer polyethyleneimine (PEI) for effective delivery into cells. That intranasal immunization with nanoparticles stimulates antigen specified humeral and cellular immune responses[8].

Nanomaterials in general are synthesized by two main approaches, depending on the end-user demand. The first one is **top-down**, in which the size of larger molecules makes smaller to nanoscale and the other is a **bottom-up** approach, in which small molecules or atoms are combined to produce nanomaterials. These approaches involve several synthesis methods and four major categories like chemical, physical, mechanical, and biological. Generally, the top-down approach involves methods like high-energy ball milling, etching, mechanical alloying, lithography, reactive milling, and micromachining methods. Whereas bottom-up includes molecular self-assembly, sol-gel, electron (or ion) beams, metal-organic chemical vapor deposition, vacuum arc deposition, inert gas condensation, electrodeposition, and ultrasonic dispersion [9].

1.2 Nanotechnologies and renewable energy

An increase in global economy implies a growth in energy demand. Unfortunately, the world energy supply relies mainly on non-renewable sources, such as petroleum, coal and natural gases that are non-environmentally friendly[10-11]. A representation is shown in Scheme 1.

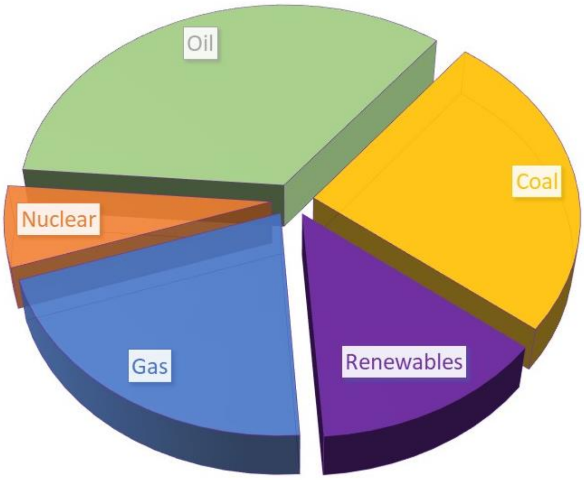

Scheme 1: pie chart of main world energy supplies

In addition, the production and transmission of energy coming from fossil fuels are causes of global conflicts and also lead environmental degradation. In fact, combustion of them generates air pollutants such as sulphur oxides and heavy metals, but also CO_2, the greenhouse gas responsible of global climate change[12].

Hence, the transition to the alternative and renewable sources (nuclear power, solar energy, wind power, geothermal energy, biofuels, hydropower, etc.) represent a possible solution coupled with the increasing the efficiency in production, transmission and utilization of the remaining non-renewable sources[13-15].

Energy storage technologies can help to meet the demand for supply at the point of consumption, allowing the production of energy at a different location[16]. Different types of energy storage devices are currently in use, depending on the specific energy and power requested from the end-user. Among them, capacitors, batteries, flywheels, superconducting magnetic energy storage (SMES) systems and solid oxide fuel cells (SOCF) are present and shown in Fig. 1[17].

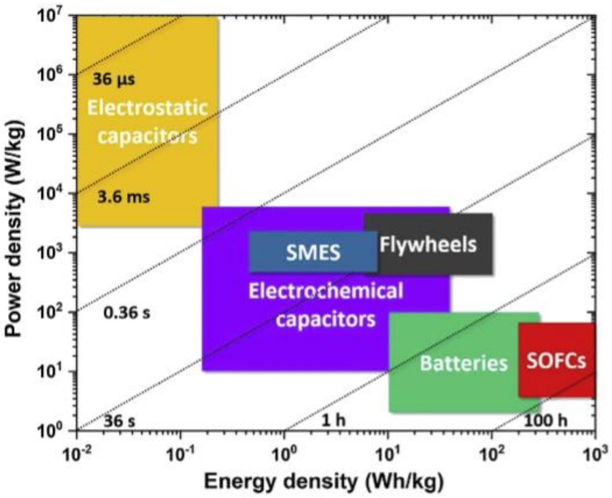

Fig. 1: specific power against specific energy of different electrical devices[17].

Development on nanotechnologies of the last two decades has demonstrated that these materials with superior properties could give a huge inprovement in the energy sector, starting from the elaboration of primary energy sources to the end-user devices. Some examples of utilization of nanotechnologies for energy applications is given in Fig. 2.

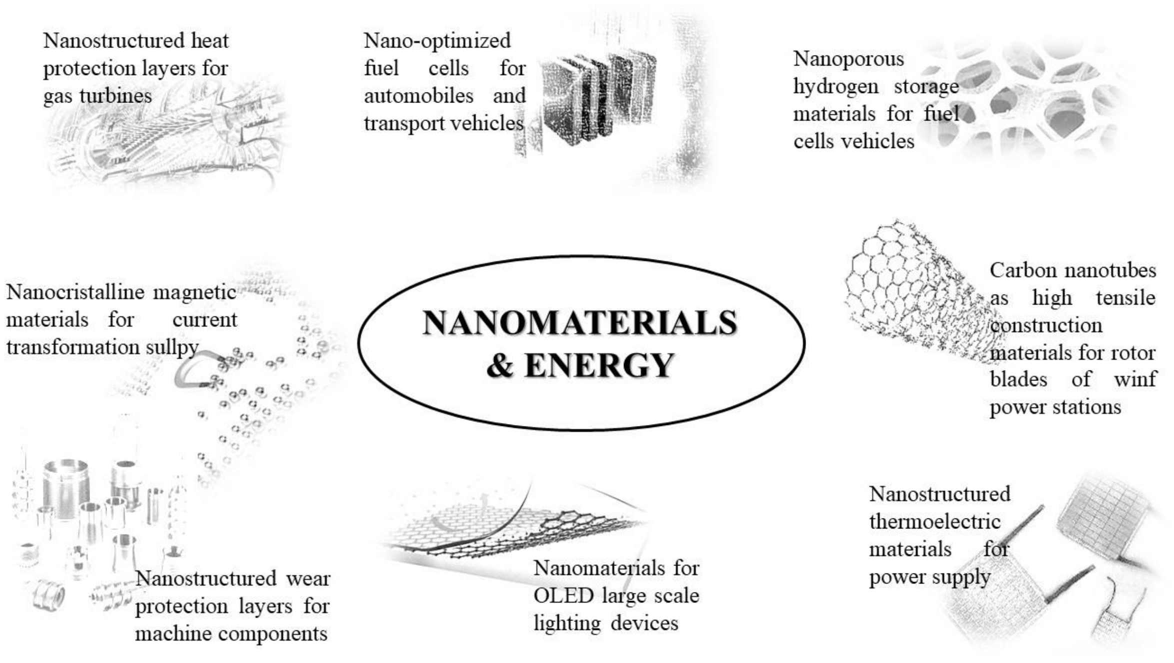

Fig. 2: examples of nanomaterials for energy applications

1.3 Nanomaterials and Redox Flow Batteries (RFB)

Electrochemical energy storage techniques which can balance the intermittent production and smooth consumption are effective routes to fulfil the highly penetration of renewable energy sources. Among them, redox flow batteries (RFBs) are one of the most promising large-scale energy storage technologies ascribed to the decoupled energy capacity and power output, long lifetime, full charge and discharge capability, high safety and environmental-friendly[19-21].

As depicted in Fig. 3, RFBs comprise three main components: electrolyte, electrode, and ion exchange membrane.

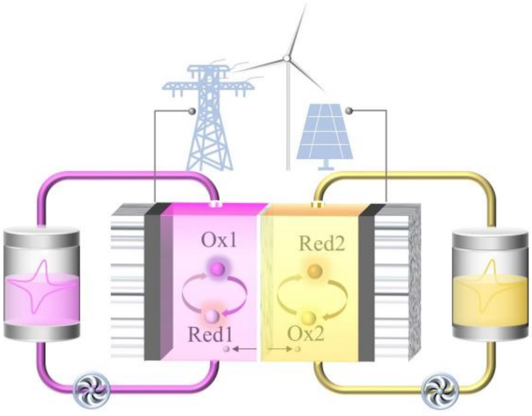

Fig. 3: typical schematic of a redox flow battery[20]

Electrolyte is the energy storage media in which electroactive materials are dissolved. *Electrode* is the component that fulfill electron transfer between external circuit and electrolytes. The material constituting the electrode also provides sites for redox reactions of electroactive species and a key role in accelerating electrochemical reactions rates and reducing charge transfer overpotentials ensuring the reversibility of redox reactions. A desirable electrode exhibits high chemical stability and electrocatalytic activity, large specific surface area and low cost[22].

Carbon materials with large three-dimensional porous structures such as carbon felt (CF), carbon paper (CP) and graphite felt (GF) have been widely used as electrodes. These carbon materials are commonly made of smooth carbon fibers which interlace with one another. To balance the electrochemical activity, hydrophilicity and porous structures of carbon materials still remains a big challenge which significantly affects the polarization and overall cell performance (e.g., voltage efficiency, energy efficiency, and output power)[23-25].

Nanomaterials with abundant oxygen-containing groups can increase the electrode/electrolyte contact area and numbers of adsorption sites for redox reactions, offer shortcuts for mass transfer and optimize electrocatalysis activities. Thus, the application of nanomaterials in the preparation of advanced electrodes for RFBs can not only promote the reversibility of redox couples, but also accelerate redox reactions, mass transfer and proton transport process[26].

Ion exchange membrane is employed to separate the catholyte and anolyte of RFBs to prevent short circuit caused by the crossover of active species. Meanwhile, balance ions can transfer through the membrane to complete the circuit and maintain electroneutrality of the cell. Hence, an ideal ion exchange membrane should possess good chemical stability, high ion selectivity (eg., high ionic conductivity, low permeability of active species), and low cost. The widely used commercial ion exchange membrane in aqueous RFBs is a kind of perfluorosulfonic acid membrane, known as Nafion membrane with merits of high chemical stability and conductivity. The ion transport channels of Nafion membrane are constructed by the hydrophilic groups which are branches of the hydrophobic backbones. And the ion transportation process can be efficiently fulfilled through Grotthuss and vehicular mechanisms[27]. Both nonfluorinated polymer membranes and porous membranes which contain the hydrophilic/hydrophobic phases have also been applied in RFBs. The three-dimensional nanochannels of membrane can be modified by the contents and size of hydrophilic or hydrophobic groups. Recently, intensive attention has been attracted on the modification of membrane structures to decrease the ionic permeability and cost. Application of nanomaterials as nanofillers into different polymer matrix can reshape the structure of composite membrane, alter the interaction between nanofillers and polymer chains, and tune ions transport channels via introducing functional groups[28-30]. A summary of nanomaterials currently used in RFBs is reported in Table 1.

Table 1: some nanomaterials currently used in RFBs.

Compmonent application	**Materials**	**Energy efficiency (%)**	**Cycle numbers**	**Current density (mA cm^{-2})**
Electrodes	Cu nanoparticles[31]	84	50	50
	Bi nanoparticles[32]	87	50	200
	MnO_2 [33]	75	50	50
	MWCNTs[34]	82	50	50
Membrane	ZrNT/Nafion composite[35]	78,5	100	40
	TiO_2 nanotubes[36]	84,4	1400	120
	nanoporous PES[37]	78,4	200	80
	nanoporous PBI[38]	88,7	200	80

1.4 Nanomaterials and capacitors

A capacitor is a device that can store electric charge when a voltage is applied in the circuit and release on demand. As shown in Fig. 4, a capacitor consists of two usually planar electrodes and a dielectric between them. When a voltage is applied, the plates produce positive and negative charges and the dielectric material doesn't allow them passing through, resulting in storage polarization[39].

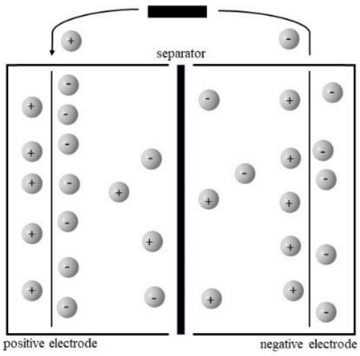

Fig. 4: schematic representation of a typical capacitor

Electrochemical capacitors (ECs) can be fully charged or discharged in few seconds; as a consequence, compared to batteries, their energy density is lower (about 5 Wh kg^{-1}), but a high power uptake (10 kW kg^{-1}) can be reached for shorter times. That is the reason why batteries and capacitors can be considered as complementary[40].

Depending on the charge storage mechanism or on the materials used, ECs could be divided into different categories:

- Electrical double layer capacitors (EDLCs), the charge is stored only electrostatically, no faradaic reactions occur;
- Pseudo-capacitors or redox capacitors, characteristics for their fast and reversible surface or near-surface reactions for charge storage;
- Hybrid capacitors, devices that combine a pseudocapacitive electrode with a battery electrode.

The major shortcoming of ECs is the low energy density compared to batteries, wich results in less than a minute discharge time, strongly limiting their application[41]. Research efforts about the use of nanomaterials to overcome that problem has been made principally in the past few years[42].

Graphitic carbon represents the best candidate because of its high conductivity, electrochemical stability and open porosity[43]. Activated, templated and carbide-derived carbons, carbon fabrics, fibres, nanotubes, onions and nanohorns have been tested in ECs,[44-47]. Because of ECs store charge in the first few nanometres of surface, decreasing the particle size can help to improve the performances of the active material. Transition metal oxides nanoparticles represent valid alternatives for carbon-based materials, such as RuO_2 or Fe_3O_4 that combine an high surface exchange area typical of nanoparticles and faradaic behaviour of metals in the case of pseudocapacitors[48].

Among the pseudocapacitive materials, also conducting polymers have been studied and have shown high pseudo-capacitance in various non-aqueous electrolytes. When used as bulk materials, conducting polymers suffer from a limited stability during cycling that reduces the initial performance. Research efforts with conducting polymers for supercapacitor applications are nowadays directed towards hybrid systems combining them with metal oxides nanoparticles or graphitic materials[49-52].

1.5 Conductive polymers and polyaniline

Conductive polymers (CPs) are a class of organic molecules with particular electrical properties that find a wide range of applications in batteries, supercapacitors, electrochromic devices, solar cells, sensors, and biomedical applications[53-55].

The first study of CPs was reported by Letherby in 1862 with the electrochemical preparation and characterization of polyaniline formed by the oxidation of aniline on a platinum electrode in diluted sulfuric acid. CPs did not recieve much interest until the end of 1970, when Shirakawa, together with MacDiarmid and Heeger discovered that the polyacetylene (structure shown in Scheme 2) can be made conductive after exposing it to the oxidizing agents like chlorine, bromine or iodine which made polyacetylene 10^9 times more conductive than the pristine polyacetylene for which they were awarded Nobel Prize in 2000[56]. This breakthrough gave the rise to the development of new kind of materials with combine the properties of plastic and electrical conductivity.

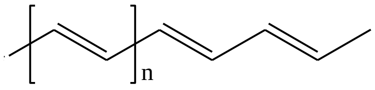

Scheme 2: chemical structure of polyacetilene

Unlike plastic, conducting polymers have alternating single and double bond with sp2 hybridized structure in conjugated sequence along the chain backbone of the polymer, which acquires delocalization of π-electron and consequently leads electrical conduction.

Various CPs were studied, such as polypyrrole (PPy), polyazulene, polyfluorene, polythiophene, polyterthiophene, and polyaminonaphthalenes[57].

The CP investigated in this thesis is **Polyaniline**, which have the chemical structure presented in Scheme 3, where $0 \leq y \leq 1$.

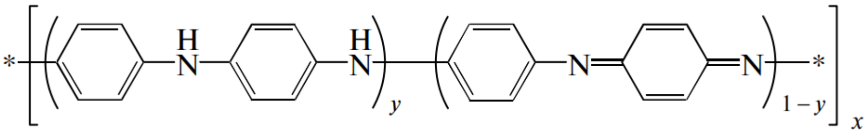

Scheme 3: chemical structure of polyaniline

Depending on the value of y, polyaniline could have different states of oxidation: if $y = 0$, polyaniline is in the fully-oxidized state and called pernigraniline base, if $y = 1$ polyaniline is in the fully-reduced state called leucoemeraldine and half oxidized state is gained when

y = 0,5 and called emeraldine base. Doping the pernigraniline and emeraldine bases, respective salts can be obtained[58-60]. A schematic representation is given in Scheme 4.

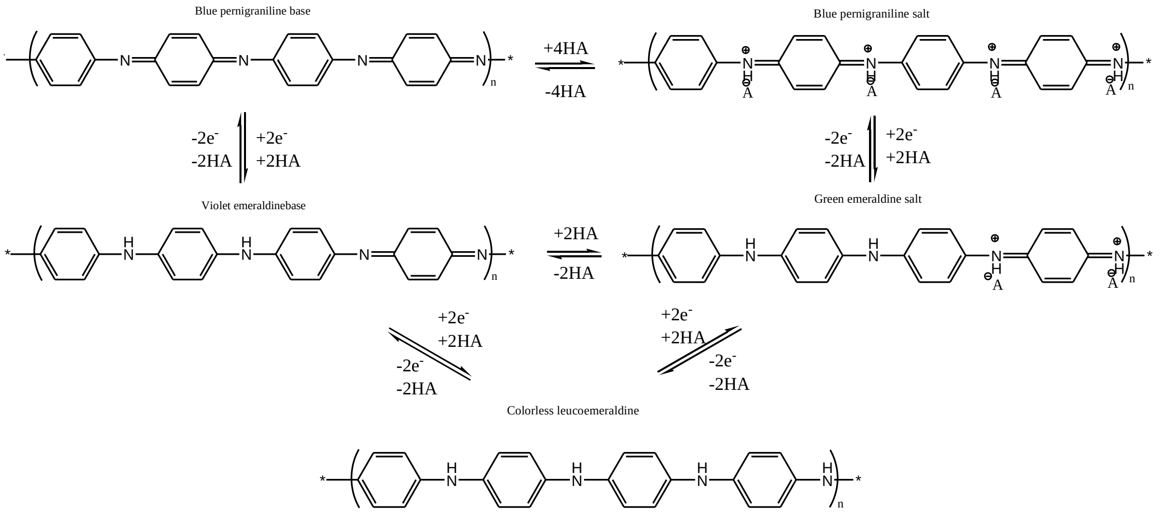

Scheme 4: different states of oxidation of polyaniline

Leucoemeraldine is a colorless form of polyaniline. It is not conductive, but can slowly oxidize at air. *Pernigraniline* form is composed of aminobenzene and quinonediimine fragments that rapidly decompose in water and air due to the presence of nucleophiles.

Emeraldine salt is the most interesting form of PANI because shows electrical conductivity. It is formed by protonation of the emeraldine base with organic and inorganic acids. This process is conventionally called *doping* and results in the formation of polycations due to the interaction between protons and imine atoms of nitrogen. Accordingly electrons undergo redistributions over a certain conjugation lenght providing the electrical conductivity of the polymer [61].

Cation radicals in PANI could be delocalized also by an intramolecular mechanism. The so called π stacking is based on the Van der Waals interactions between benzene and quinoid rings of different chains of PANI oriented in one direction. The electron conductivity of such a structured polyaniline is reported to be about 10^3 S cm^{-1} [62].

Structure, morphology and oxidation state of polyaniline can be tailored varying the synthesis conditions in an electrochemical or chemical route.

The *electrochemical polymerization* of aniline is conducted on the surface of a conductive working electrode usually in aqueous solution containing acids. Different methods can be used: potentiostatic with a fixed potential around 0,7 – 1,2 V *vs* SCE, potentiodinamic varying the potential from -0,2 to 1,2 V *vs* SCE or galvanostatic, with a fixed current density of about 10 mA cm^{-2}. This type of polymerization leads to the formation of PANI with controlled morphology and high purity[63,64]. A schematic representation of the electrochemical polymerization mechanism is given in Scheme 5.

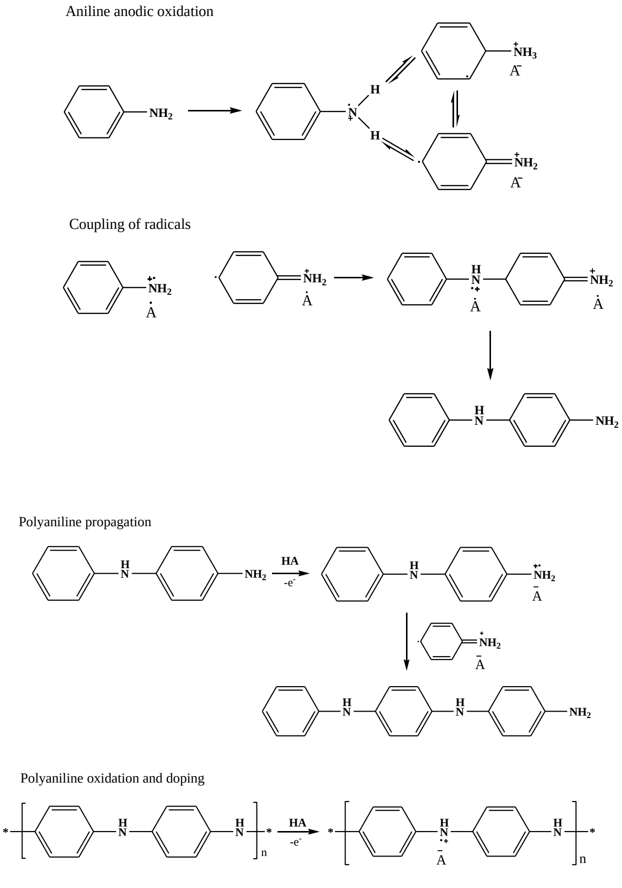

Scheme 5: electrochemical polymerization mechanism of aniline

The *chemical polymerization* of aniline is possible due to the presence of an oxidant, commonly ammonium persulfate (Scheme 6). Polymerization is conducted in acidic solution at $1 < pH < 3$ to have the emeraldine salt form. Using that method, PANI result in the highest yield (more than 90%) and a conductivity of about 1.2 S cm^{-1}. The main advantage of this method is that a conductive substrate is not needed[65,66].

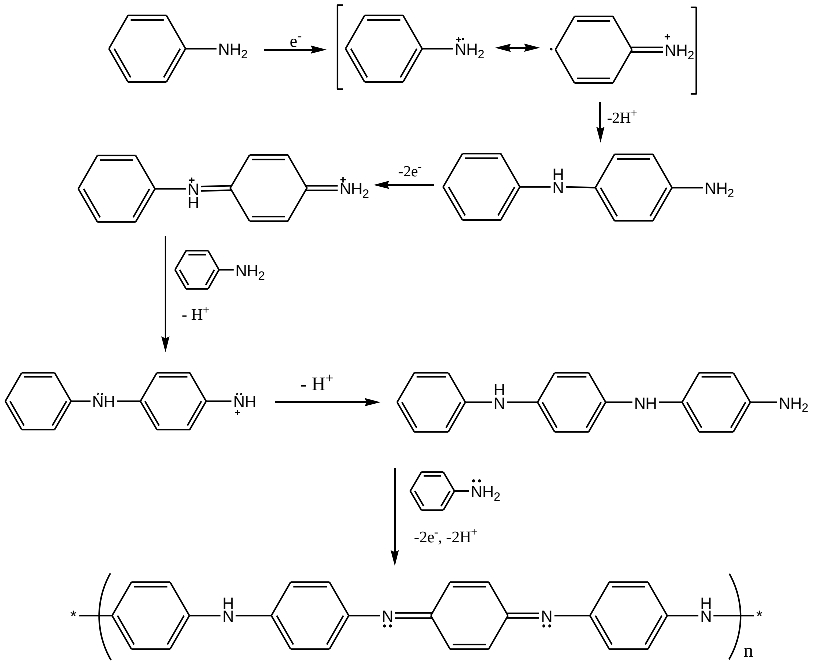

Scheme 6: mechanism of chemical polymerization of aniline

Among the conducting polymers, PANI is known for having probably the best combination of stability, conductivity and low cost[60]. Despite having versatile use in large scale industrial applications, many of the potential use of PANI yet need to be explored. One of the major drawbacks of PANI is the lack of its processability, its conductivity unstable at neutral pH and its insolubility in water. The most promising approach to overcome this problem of PANI is the formation of composite with using nonconducting polymers as matrix. Adding water-soluble polymers for example, hydrogen bonds could be formed improving not only water dispersibility, but also thermal stability[67]. Polymerization with these template materials is performed for example in the presence of strong polyacids, such as poly(4-styrenesulfonic acid) and poly(2-acrylamido-2-methyl-1-propanesulfonic acid), as well as weak polyacids, such as poly(vinylphosphonic acid) and poly(acrylic acid)[68].

In addition, the creation of composite CPs with metal/metal oxides nanoparticles such as Au, Pt, Pd, Ni, Cu, TiO_2, MnO_2, ZnO, and Fe_3O_4 have been intensively studied. CPs and metal NPs can prevent agglomeration and restacking of metal NPs by steric hindrance and electrostatic interactions. Moreover, in electrochemical devices, these composites can increase the electron transport rates between the electrolyte and current collectors or electrode materials[69-71].

A particular emphasis on the application in the sensoristic field, where polyaniline represent an interesting material due to its easiness to be synthesized and tailored, its light weight and its low cost, is given in this thesis.

1.6 Polyaniline as electrochemical sensor

An electrochemical sensor is a material that is able to convert chemical reactions that a target species makes on its surface, into an electrical signal that exibit changes in current, potential and conductivity. Thus, depending on the type of response, sensors can be divided into voltammetric/amperometric, potentiometric or impedimetric categories[72].

Voltammetric/amperometric sensors, in a typical three electrode cell, measure the current while a potential is applied between the working and the counter electrode. The response is the result of electrochemical reactions that occur on the surface of the electrode and the interface between electrode and electrolyte. The mass transport of active species on the surface is the rate determining step in this case[73]. Voltammetric methods include linear sweep voltammetry, cyclic voltammetry, hydrodynamic voltammetry, differential pulse voltammetry, square-wave voltammetry, polarography, and stripping voltammetry[74]. The only difference between voltammetric and amperometric sensors is that the second one lacks a potential sweep, instead using a potential step. The resulting current at a given potential is proportional to the concentration of the electroactive species in the sample, and the current is given by Cottrell's equation[75]:

$$i = \frac{nFAc_j^o\sqrt{D_j}}{\sqrt{t\pi}}$$

Where *i* is the current (A), *n* is the number of electrons to reduce or oxidize one molecule of analyte *j*, *F* is the Faraday constant (96485 C/mol), *A* is the electrode's area in cm^2, c_j^o is the initial concentration of analyte in mol cm^{-3}, *t* is the time in s and D_j is the diffusion coefficient for the analyte *j* in cm^2 s^{-1}. Amperometric sensors have more sensitive and selectivity because the oxidation or reduction potential used for detection is characteristic of the analyte species[76].

Potentiometric sensors measure the potential difference between the working electrode and the reference electrode when no significant current is flowing. The potential difference is given by the Nerst equation:

$$E_{cell} = E_{cell}^0 - \frac{RT}{zF}\ln Q_r$$

Where E_{cell} is the observed cell potential at zero current, E_{cell}^0 is the standard potential of the cell, *R* is the universal gas constant (8,314 J K^{-1} mol^{-1}), *T* is the temperature in K, *z* is the number of electrons transferred in the cell reaction, F is the Faraday constant and Q_r is the reaction quotient of the cell in terms of activities of the oxidized and reduced species.

The lowest detection limits of potentiometric devices are currently often realized with ion-selective electrodes (ISE)[74].

Impedimetric sensors are based on surface changes caused by adsorption and desorption of target species that cause a modification of the conductivity of the material. The experimental approach is to perturb the cell with a small-magnitude alternating potential and to observe the way in which the system reacts to the perturbation in the steady state[75].

In any case, electrochemical methods allow very low detection limits, high selectivity and a small active area and consequently a very small volume of analytes. In this framework polyaniline is widely studied as material for electrochemical sensors because of its high sensitivity and selectivity to a large numbers of target molecules thanks to its easiness to be tailored. For example, a glucose-sensor made of PANI and $NiCo_2O_4$ is reported[80]. The catalytic active sites in $NiCo_2O_4$ with conductive PANI played a synergetic role in the oxidation of glucose and exhibited good sensitivity and a lower detection limit. Moreover, a surface with PANI deposited upon is used for the sensitive detection of nucleic acids., gene sensing is a very powerful tool for the diagnosis of a wide variety of diseases, from common viral infections to cardiovascular diseases and cancer. For the purpose a new method was developed for the sensitive detection of nucleic acids using it. In this case, the polymer was deposited by enzyme-catalyzed formation and template-guided deposition in which a reporter enzyme catalyzed the deposition of PANI onto the analyzed nucleic acid molecules by forming an intramolecular complex[76,77].

1.7 Paper-based sensors

Cellulosic materials are valuable owing to their chemical uniqueness, shape flexibility, ease of processing, mechanical strength, and biodegradability[78]. it is found in many plants and is also bio-synthesized by some certain microorganisms like the *Acetobacter xylinum*. In addition, via a simple carbonization process, cellulosic materials can be transformed into electronically conductive carbon materials with high specific surface areas and rich pore structures. These characteristics make cellulosic materials suitable for use as flexible/transparent substrates, separators, electronic–ionic conductors, electrolytes, and electrochemical electrode materials in flexible circuits or sensors, conductive transistors, organic light-emitting diodes (OLEDs), organic thin-film transistors (OTFTs), supercapacitors, batteries, triboelectric nanogenerators (TENGs), tissue bioelectronics, and other flexible electronics. At present, different substrate are used for sensors, such as polyimide (PI), polydimethylsiloxane (PDMS), polyester (PE), and polyethylene terephthalate (PET). Despite their excellent flexibility and stability, they are difficult to degrade, resulting in electronic pollutants and that is why paper as substrate represents a valid alternative[79].

The evolution and development of cellulosic materials, as shown as Fig. 5, demonstrates their potential for use in emerging sustainable, flexible, and portable intelligent electronics.

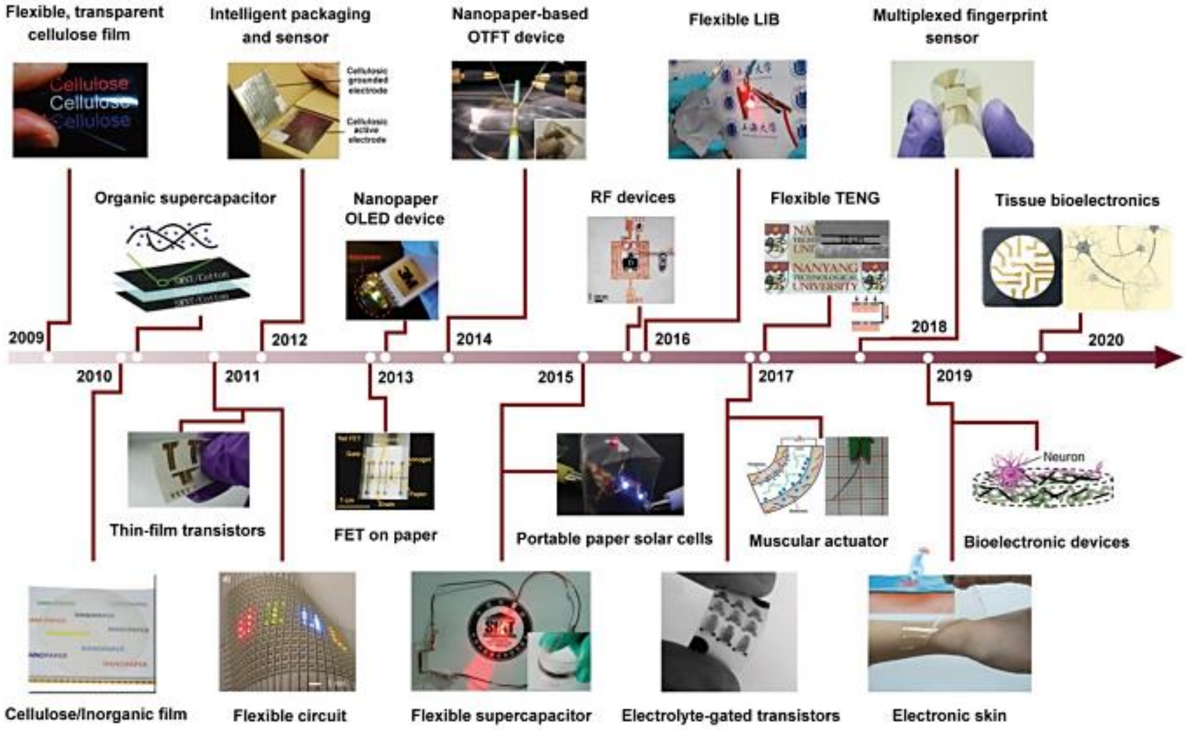

Fig. 5: timeline of cellulosic materials[79]

Cellulose consists of linear β-1,4-linked D-glucose units, and has abundant hydroxyl (–OH) active groups that can form inter and intramolecular bonds between polymeric chains, resulting in strong hydrogen-bond networks (Fig. 6).

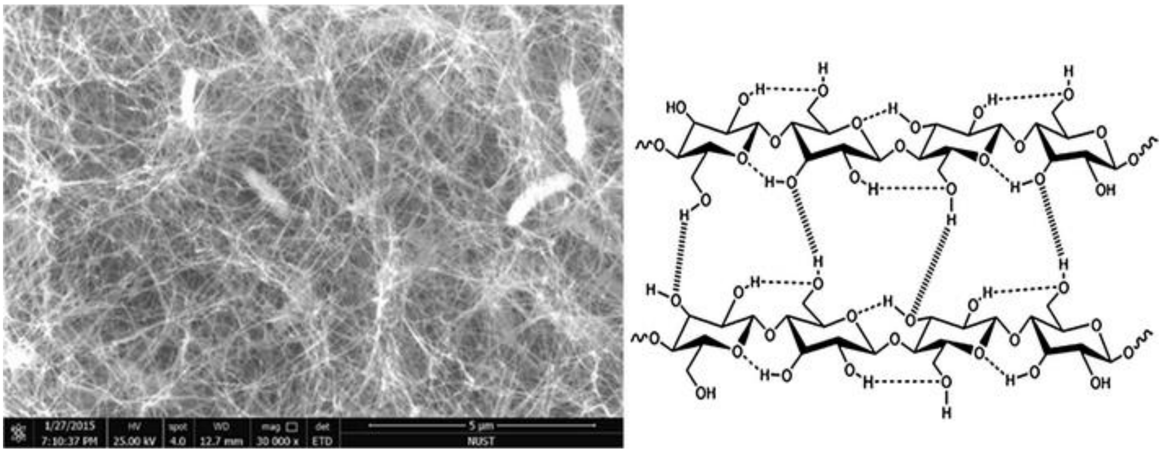

Fig. 6: SEM image and scheme of cellulosic network[82]

Purified cellulose can be obtained by removing lignin and hemicellulose from plants *via* chemical pretreatments[80,81]. Within these cellulose fibers, there are regions where the macromolecular chains are arranged in a highly ordered (crystalline) structure, and regions where the chains are messy and disordered (Fig. 7). The structure and distribution of these crystalline and disordered domains depend on the raw materials and pretreatment methods.

Cellulose can be processed to obtain various morphologies. Cellulose nanofibers (CNFs) for example, have a web entangled morphologies and an high specific moduli; they are obtained by mechanical nanofibrillation methods such as high-pressure homogenization, high-intensity ultrasonication, high-speed stirring or ultrafine grinding [34]. In contrast, cellulose nanocrystals (CNCs) are obtained by acid hydrolysis of disordered and polycristalline regions of cellulose[82, 83].

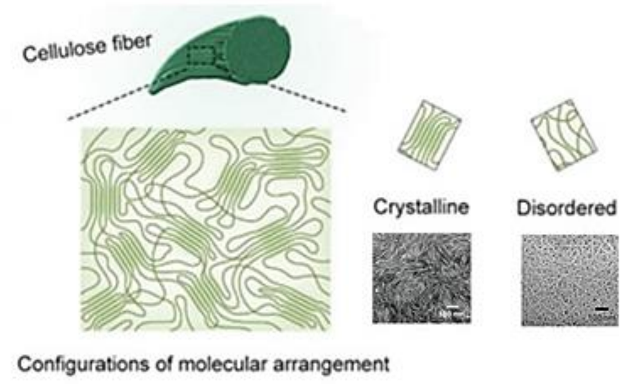

Fig. 7: crystalline and disordered macromolecular structure of cellulose[83]

Flexible sensing devices have received tremendous attention because of their valuable applications in human health monitoring, human–machine interaction, and wearable devices. Unlike synthetic polymers, cellulose materials are biocompatible and renewable, which increases the recyclability of wearable sensors[84]. Functional inorganic and organic materials such as metal oxides, carbon materials, and conductive polymers can be incorporated into cellulosic materials to develop conductive electrodes and dielectric layers for the fabrication of flexible sensors[85,86].

For example, regenerated cellulose was combined with poly(3,4-ethylene dioxythiophene)–poly(styrene-sulfonate) (PEDOT:PSS) to protect silver nanowires (AgNWs) from oxidizing and falling. Subsequently, a flexible and conductivity-stable hybrid film was fabricated. The synergy of coordination complexation and hydrogen bonding of cellulose and PEDOT:PSS significantly improved the robustness of the interfaces and the structural stability of the hybrid film. The hybrid film had a stable conductivity, even when subjected to severe conditions (90% relative ambient humidity and 65 °C for 60 days) and repeated bending and peeling tests. This hybrid film was used to construct a strain-to-electricity sensor that showed excellent flexibility and biocompatibility. The sensor had a high sensitivity of 23.35 kPa^{-1} and could detect different mechanical strains including pressing, touching, bending, and even breathing airflow[86].

For the fabrication of complicated “bottom-up” nanostructures, CNFs possess distinct advantages, making them ideal electrode components for piezoresistive sensors. Guo’s group assembled a conductive CNF/AgNWs-coated polyurethane (CA@PU) sponge using a dip-coating process. The application of CNFs helped to disperse the AgNWs and provided strong adhesion between the layers. The CA@PU sponge-based sensor exhibited a high piezoresistive effect and could record slight sounds and detect when an object was placed onto its surface[87].

Cellulose-based carbon materials have also been explored for constructing strain sensors. CNF/Ti_3C_2 MXene hybrid aerogels and their corresponding sintered carbon aerogels exhibited high structural stability and could undergo a high strain of 99% for more than 100 cycles. As sensors, these carbon aerogels showed high sensitivity and very low detection limits for small pressures and strains. Due to the scalable piezoelectric responses of cellulose, self-standing CNF films can be used as functional sensing layers in piezoelectric sensors, with a high piezoelectric sensitivity of up to 6.4 pC N^{-1} in ambient conditions. This is comparable to that of commercial poly(vinylidene fluoride) (PVDF) piezoelectric polymer sensors. The capacitive sensing of metallized cellulose materials provides a low-cost solution for integrating electronic interfaces into “smart” packaging[88]. For example, Whitesides’ group developed a paper-based intelligent packaging device that integrated sensing and alarm functions to ensure seal integrity and prevent theft from containers[89].

Finally, a PANI nanorod-based gas sensor via in situ co-doped with 5-sulfosalicylic acid (SSA) on a 3D interconnected cellulose network substrate was presented as ammonia sensor with a high response (21.3 for 50 ppm ammonia) and quick response/recovery time (4.1 s/16 s). Furthermore, the sensor also demonstrates excellent ammonia selectivity among different interfering agents, with a lower detection limit (LOD) of 10 ppb at room temperature, and the limit sensing temperature even below -10 °C[90].

References

1. T.A. Saleh, *Environ. Technol. Innov.*, **2020**, 20, 101067.
2. The Royal Society & The Royal Academy of Engineering, *Nanoscience and nanotechnologies. Opportunities and uncertainties*, Royal Society, London, **2004**.
3. R. Lozano, M. Naghavi, K. Foreman, S. Lim, *Lancet*, **2012**, 380, 2095–2128.
4. K. Watkins, *Curr. Emerg. Hosp. Med. Rep.*, **2018**, 6, 86–93.
5. K. Kostarelos, *Nat. Nanotechnol.*, **2020**, 15, 343–344.
6. Stat Nano, *An Overview of Nanotechnology Patents Focusing on Coronaviruses*, STAT NANO, **2020**.
7. H. Li, L. Rothberg, *Proc. Natl. Acad. Sci. Unit. StatesAm.*, **2004**, 101, 14036–14039.
8. G. Chandra, *Sens. Int.*, **2020**, 1, 100019.
9. D. M. Kahan, D. Braman, P. Slovic, J. Gastil, G. Cohen, *Nat. Nanotechnol.*, **2009**, 4, 87–90.
10. M.Y. Ho, P.S. Khiew, D. Isa, T.K. Tan, W.S. Chiu, C.H. Chia, *Nano*, **2014** 1-25.
11. L. Yang, *Prog. Mater. Sci.*, 2018, 102, 72-108.
12. G. M. Whitesides, *Sci Am.*, **2001**, 285, 78-83.
13. M. Zäch, C. Hägglund, D. Chakarov, B. Kasemo, *Solid State Mater Sci.*, **2006**, 10, 132-143.
14. M. F. Ashby, P. J. Ferreira, D. L. Schodek, *Nanomaterials, nanotechnologies and design*, BH, **2009**.

15. R. N. Kostoff, R. G. Koytcheff, C. G. Y. Lau, *Technol Forecast Soc Change*, **2007**, 9, 1733-1747.

16. M.Y. Ho, P.S. Khiew, D. Isa, T.K. Tan, W.S. Chiu, C.H. Chia, *Nano*, 2014, 9, 1-25.

17. L. Yang, X. Kong, F. Li, H. Hao, Z. Cheng, H. Liu, J. F. Li, F. Zhang, *Prog. Mater. Sci.*, **2019**, 102, 72-108.

18. B. E. Conway, *Electrochemical Supercapacitors: Scientific Fundamentals and Technological Applications*, Kluwer, **1999**.

19. F. Cheng, J. Liang, Z. Tao, J. Chen, *Adv. Mater.*, **2011**, 23, 1695–1715.

20. Y. Zhang, J. Xu, Y. Long, L. Tao, M. Ding, C. Jia, *Chem Nano Mat*, **2020**, 6, 1589–1600.

21. Y. Zhang, L. Tao, C. Xie, D. Wang, Y. Zou, R. Chen, Y. Wang, C. Jia, S. Wang, *Adv. Mater.*, **2020**, 32, 1905923.

22. J. Ye, Y. Cheng, L. Sun, M. Ding, C. Wu, D. Yuan, X. Zhao, C. Xiang, C. Jia, *J. Membr. Sci.*, **2019**, 572, 110–118.

23. A. Abbas, S. Abbas, A. Bhattarai, N. M. Latiff, N. Wai, A. N. Phan, T. M. Lim, *J. Power Sources*, **2021**, 488, 229411.

24. L. Liu, Y. Yao, Z. Wang, Y.-C. Lu, *Nano Energy*, **2021**, 84, 105897.

25. M. Mousavi, H. Dou, H. Fathiannasab, C. J. Silva, A. Yu, Z. Chen, *Chem. Eng. J.* **2021**, 412, 128499.

26. K. Amini, J. Gostick, M. D. Pritzker, *Adv. Funct. Mater.*, **2020**, 30, 1910564.

27. L. Hu, L. Gao, M. Di, X. Jiang, X. Wu, X. Yan, X. Li, G. He, *Energy Storage Mater.*, **2021**, 34, 648–668.

28. C. A. Machado, G. O. Brown, R. Yang, T. E. Hopkins, J. G. Pribyl, T. H. Epps, *ACS Energy Lett.*, **2021**, 6, 158–176.

29. B. Sun, M. Skyllas-Kazakos, *Electrochim. Acta*, **1991**, 36, 513–517.

30. W. H. Wang, X. D. Wang, *Electrochim. Acta*, **2007**, 52, 6755–6762.

31. L. Wei, T. S. Zhao, L. Zeng, X. L. Zhou, Y. K. Zeng, *Appl. Energy*, **2016**, 180, 386–391.

32. B. Li, M. Gu, Z. Nie, Y. Shao, Q. Luo, X. Wei, X. Li, J. Xiao, C. Wang, V. Sprenkle, W. Wang, *Nano Lett.*, **2013**, 13, 1330–1335.

33. Y. Jiang, X. Feng, G. Cheng, Y. Li, C. Li, Z. He, J. Zhu, W. Meng, H. Zhou, L. Dai, L. Wang, *Electrochim. Acta*, **2019**, 322, 134754.

34. G. Wei, C. Jia, J. Liu, C. Yan, J. *Power Sources*, **2012**, 220, 185–192.

35. A. Aziz, S. Shanmugam, *J. Power Sources*, **2017**, 337, 36–44.

36. J. Ye, X. Zhao, Y. Ma, J. Su, C. Xiang, K. Zhao, M. Ding, C. Jia, L. Sun, *Adv. Energy Mater.*, **2020**, 10, 1904041.

37. W. Xu, X. Li, J. Cao, Z. Yuan, H. Zhang, *RSC Adv.*, **2014**, 4, 40400–40406.

38. Z. Yuan, Y. Duan, H. Zhang, X. Li, H. Zhang, I. Vankelecom, *Energy Environ. Sci*. **2016**, 9, 441–447.

39. B. E. Conway, *Electrochemical Supercapacitors: Scientific Fundamentals and Technological Applications*, Kluwer, **1999**.

40. J. R. Miller, P. Simon, *Science*, **2008**, 321, 651–652.

41. R. Kötz, M. Carlen, *Electrochim. Acta*, **2000**, 45, 2483–2498.

42. A. S. Arico, P. Bruce, B. Scrosati, J. M. Tarascon, W. V. Schalkwijk, *Nature Mater.*, **2005**, 4, 366–377.

43. Y. Gogotsi, *Carbon Nanomaterials*, CRC, **2006**.

44. T. Kyotani, J. Chmiola, Y. Gogotsi, *Carbon Materials for Electrochemical Energy Storage Systems*, Taylor and Francis, **2020**.

45. D. N. Futaba,K. Hata, T. Yamada, T. Hiraoka, Y. Hayamizu, Y. Kakudate, O. Tanaike, H. Hatori, M. Yumura, S. Iijima. *Nature Mater.*, **2006**, 5, 987–994.

46. C. Portet, J. Chmiola, Y. Gogotsi, S. Park, K. Lian, *Electrochim. Acta*, **2008**, 53, 7675–7680.

47. C. M. Yang, *J. Am. Chem. Soc.*, **2007**, 129, 20–21.

48. K. Machida, K. Furuuchi, M. Min, K. Naoi, *Electrochemistry*, **2004**, 72, 402–404.

49. A. Rudge, I. Raistrick, S. Gottesfeld, J. P. Ferraris, *J. Power Sources*, **1994**, 47, 89–107.

50. J.P. Zheng, T.R. Jow, *J. Power Sources*, **1996**, 62, 155–159 (1996).

51. A. Laforgue, P. Simon, J.F. Fauvarque, *Synth. Met.*, **2001**, 123, 311–319.

52. K. Naoi, S. Suematsu, A. Manago, *J. Electrochem. Soc.*, 2000147, 420–426.

53. J. Mort, *Science*, **1980**, 208, 819–825.

54. T.A. Skotheim, R. Lelsenbaumer, J.R. Reynolds, *Handbook of Conducting Polymers, Conjugated Polymers: Processing and Applications*, CRS Press, **2006**.

55. M.J. Sailor, F.L. Klavetter, R.H. Grubbs, N.S. Lewis, *Nature*, **1990**, 346, 155–157.

56. H. Shirakawa, E.J. Louis, A.G. MacDiarmid, C.K. Chiang, A.J. Heeger, *J. Chem. Soc. Chem. Commun. London*, **1977**, 20, 578-580.

57. A. G. MacDiarmid, *Angew. Chem. Int. Ed*, **2001**, 40, 2581-2590.

58. J. G. Masters, Y. Sun, A. G. MacDiarmid, and A. J. Epstein, *Synth. Met.*, **1991**, 41, 715.

59. A. G. MacDiarmid and A. J. Epstein, *Faraday Discuss. Chem. Soc.*, **1989**, 88, 317.

60. J. C. Chiang and A. G. MacDiarmid, *Synth. Met.*, **1986**, 13, 193.

61. W. W. Focke, G. E. Wnek, and Y. J. Wei, *Phys. Chem.*,**1987**, 91, 5813.

62. K. Lee, S. Cho, S. H. Park, A. J. Heeger, C.W. Lee, and S.H. Lee, *Nature (London)*, **2006**, 441, 65.

63. T. Lindfors and L. Harju, *Synth. Met.*, **2008**, 158, 233.

64. S. K. Mondal, K. R. Prasad, and N. Munichandraiah, *Synth. Met.*, **2005**, 148, 275.

65. O. L. Gribkova, A. A. Nekrasov, A. A. Isakova, V. F. Ivanov, A. V. Vannikov, *Elektrokhimiya,* **2006**, 42, 1208.

66. T. Kobayashi, H. Yoneyama, and H. Tamura, *J. Elec troanal. Chem.*, **1984**, 177, 293.

67. S. Polowinski, *Prog. Polym. Sci.,* **2002**, 27, 537.

68. M. Gonzalez, B. G. Soares, M. Magioli, J. A. Marins, and J. Rieumont, *J. SolGel Sci. Technol.*, **2012**, 63, 373.

69. T.A. Saleh, *Environ. Technol. Innov.* **2020**, 20, 101067.

70. The Royal Society & The Royal Academy of Engineering, *Nanoscience and nanotechnologies. Opportunities and uncertainties*, Royal Society, London, **2004**.

71. R. Lozano, M. Naghavi, K. Foreman, S. Lim, *Lancet*, **2012**, 380, 2095–2128.

72. T. Ahuja, I.A. Mir, D. Kumar, Rajesh, *Biomaterials*, **2007**, 28, 791–805.

73. H. Yao, S.H. Jenkins, A.J. Pesce, H.B. Halsall, W.R. Heineman, *Clin. Chem.*, **1993**, 39, 1432.

74. P.T. Kissinger, W.R. Heineman, *Laboratory Techniques in Electroanalytical Chemistry*, Marcel Dekker Inc, New York, NY, USA, **1996**.

75. B.R. Eggins, *Chemical Sensors and Biosensors*, John Wiley & Sons, West Sussex, England, **2002**.

76. J. Wang, M. Musameh, Y. Lin, *J. Am. Chem. Soc.,* **2003**, 125, 2408–2409.

77. J. Bobacka, A. Ivaska, A. Lewenstam, *Chem. Rev.,* **2008**, 108, 329–351.

78. C. Chen, L. Hu, *Acc. Chem. Res*., **2018**, 51, 3154.

79. H. Yuk, B. Lu, X. Zhao, *Chem. Soc. Rev*. **2019**, 48, 1642.

80. S. Ling, W. Chen, Y. Fan, K. Zheng, K. Jin, H. Yu, M. J. Buehler, D. L. Kaplan, *Prog. Polym. Sci.* **2018**, 85, 1.

81. J. Qi, Y. Xie, H. Liang, Y. Wang, T. Ge, Y. Song, M. Wang, Q. Li, H. Yu, Z. Fan, S. Liu, Q. Wang, Y. Liu, J. Li, P. Lu, W. Chen, *ACS Sustainable Chem. Eng.*, **2019**, 7, 9202.

82. L. Chen, J. Y. Zhu, C. Baez, P. Kitin, T. Elder, *Green Chem*. **2016**, 18, 3835;

83. W. Chen, Q. Li, Y. Wang, X. Yi, J. Zeng, H. Yu, Y. Liu, J. Li, *Chem Sus Chem* **2014**, 7, 154.

84. X. Jing, H. Li, H. Y. Mi, Y. J. Liu, P. Y. Feng, Y. M. Tan, L. S. Turng, *Sens. Actuator B Chem*. **2019**, 295, 159.

85. S. Chen, Y. Song, F. Xu, *ACS Appl. Mater. Interfaces*, **2018**, 10, 34646.

86. X. Wang, J. Zhou, Y. Zhu, W. Cheng, D. Zhao, G. Xu, H. Yu, *Chem. Eng. J.*, **2019** 10, 123644.

87. L. Zhu, X. Zhou, Y. Liu, Q. Fu, ACS *Appl. Mater. Interfaces*, **2019**, 11, 12968.

88. N. Sriplai, R. Mangayil, A. Pammo, V. Santala, S. Tuukkanen, S. Pinitsoontorn, *Carbohydr. Polym*. **2020**, 231, 115730.

89. S. Rajala, T. Siponkoski, E. Sarlin, M. Mettänen, M. Vuoriluoto, A. Pammo, J. Juuti, O. J. Rojas, S. Franssila, S. Tuukkanen, *ACS Appl. Mater. Interfaces* **2016**, 8, 15607.

90. L. Yang, X. Xu, M. Liu, C. Chen, J. Cui, X. Chen, K. Wu, D. Sun, *Sens. Actuators B Chem*. **2021**, 334, 129647.

2 Synthesis and characterisation of Au/Fe_3O_4 nanocomposites

2.1 Aim of the chapter

Magnetic Fe_3O_4 (magnetite) nanoparticles were synthesized via a chemical precipitation route in different alkaline environments (NH_3 or NaOH) and subsequently functionalised with PPTEOS, with the aim of promoting the nucleation and subsequent stabilisation of gold nanoparticles to obtain Au/Fe_3O_4@Yne composites. The morphology, structure, composition and AuNPs binding capacity of the modified Fe_3O_4 nanoparticles were investigated by means of complementary characterization techniques. Moreover, their magnetic properties were studied as a function of the adopted processing conditions. Part of the work reported in the present chapter was published by my research group in Ceramics International[1].

2.2 Introduction

2.2.1 Magnetism in materials

In materials, every atom possesses a magnetic dipole that is generated by two different phenomena:

1. The spin movement of the electrons around their axis;
2. The orbital movement of electrons around their nucleus.

Neighbouring atoms spins could be aligned in a parallel or antiparallel way due to a quantum exchange force; the magnetic moment oriented in a particular direction generated by a spin movement is neutralized by a moment oriented in the opposite way; only the unpaired electrons are responsible for the magnetism in the material as result[2,3].

When a material is inserted in an external magnetic field H, the magnetic response B (intrinsic magnetic field) can be expressed as:

$$B = \mu_0 \, (H + M)$$

where μ_0 is the magnetic permeability under vacuum, and M is the magnetisation of the material. Magnetisation can be described as the vectorial measure of the magnetic dipole moment by volume unit in all the considered volume, and is represented by:

$$M = m/V = n\mu B/V$$

where m is the total magnetic moment, which corresponds to the number of atoms (n) that have unpaired electrons multiplied by the elemental magnetic moment μB and divided by the volume V occupied by the material. The proportionality between magnetisation M and exciting field H is described by the magnetic susceptibility χ and is characteristic of each substance, at a given temperature[2].

Based on the magnetic behaviour, it is possible to make a distinction between materials that do not have permanent magnetisation and exhibit a linear response to a moderate applied field, and materials that have an intrinsic magnetisation and exhibit a non-linear response to the applied field (Fig. 1)[4].

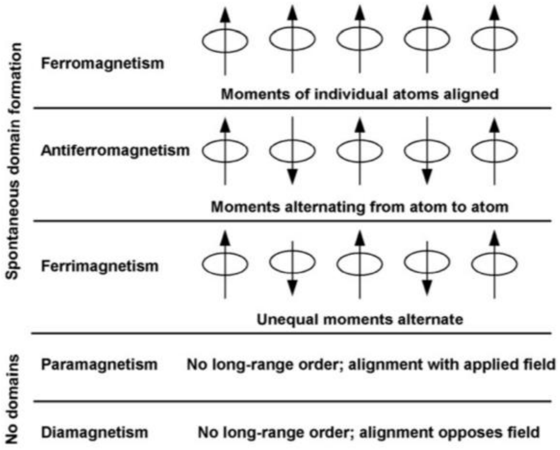

Fig. 1: different type of magnetic behaviour[4].

In general, all materials display a weak repulsion to an applied magnetic field, known as *diamagnetism*, due to the motion of electrons which generates atomic current loops to oppose the external field ($\chi < 0$). Typically, diamagnetic materials, such as quartz SiO_2 and calcite $CaCO_3$, are characterised by filled electronic subshells where the magnetic moments are paired and overall cancel each other. Since diamagnetism is very weak, any other form of magnetic behaviour that a material may possess usually overpowers the effects of these current loops.

Paramagnetism is associated to materials whose atomic magnetic moments are uncoupled, resulting in a small positive susceptibility in the presence of applied external fields ($\chi \sim 0$). In ferromagnetic materials (Fe, Ni, Co) the parallel alignment of atomic magnetic moments of equal magnitude causes a spontaneous permanent magnetisation, while in the case of *antiferromagnetism* the antiparallel coupling of these moments results in a zero net magnetisation. Finally, *ferrimagnetism* is a property exhibited by materials, such as Fe_3O_4, in which two types of atoms or ions with moments of different strengths are arranged in an antiparallel way, generating a net magnetisation[5].

Furthermore, the magnetic behaviour also depends on the size of the material, as indicated by the shape of the magnetic susceptibility curve. In the case of ferromagnetic and ferrimagnetic bulk materials, a hysteresis loop can be observed, due to the multidomain structure in which regions of uniform magnetisation are separated by domain walls. The application of a sufficiently large magnetic field causes the spins within the material to align with the field. The maximum value of the magnetisation achieved in this state is called the saturation magnetisation (Ms). As the magnitude of the magnetic field decreases, spins cease to be aligned with the field and the total magnetisation decreases, however a residual magnetic moment at zero field remains (remanent magnetisation, Mr). The coercive field Hc is the magnitude of the field that must be applied in the negative direction to bring the magnetization of the sample back to zero (Fig. 2).

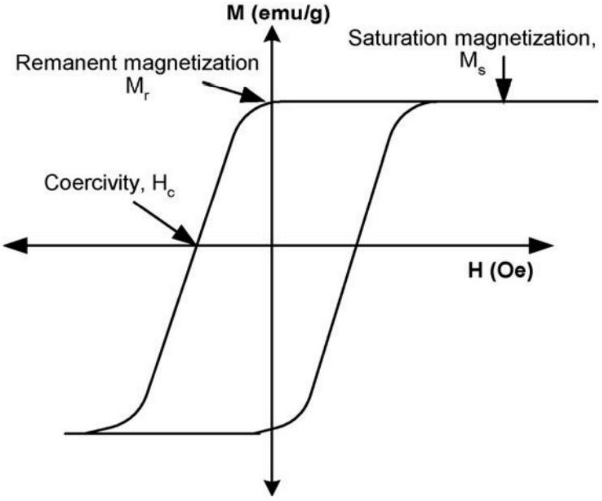

Fig. 2: Magnetisation M as a function of the applied magnetic field H [5].

On the contrary, when the sample size is reduced under a critical value at the nanometre scale, the formation of multi-domains is not favourable and the particles remain as a single domain so that their magnetic moments could be visualized as one large magnetic moment. In this case, the application of a magnetic field gives rise to the phenomenon of *superparamagnetism*, in which no hysteresis is observed since no energy is dispersed in the motion of domain walls (Mr ~ 0, Hc ~ 0). Superparamagnetic nanoparticles are strongly attracted to an applied magnetic field, due to the contribution of large magnetic moments within the individual particles, however they behave as non-magnetic materials in the absence of external fields. Indeed, repeated cycles of separation and dispersion are possible because of the absence of "magnetic memory"[2].

In the past two decades, the growing interest in the synthesis and application of magnetic nanoparticles has resulted in an advanced understanding of their properties and the demonstration of their great potential in a wide range of applications[6,7]. Nowadays, magnetic nanosystems find application in catalysis[8-10], biotechnology and biomedicine[11], magnetic resonance imaging[12], data storage[13] and environmental remediation[14].

2.2.2 Magnetite nanoparticles

Magnetite (Fe_3O_4) is a mixed iron oxide with an inverse spinel structure, in which Fe(III) ions occupy 1/4 of the octahedral coordination sites, while Fe(III) ions are equally distributed in 1/8 of the tetrahedral and 1/4 of the octahedral holes (Fig. 3).

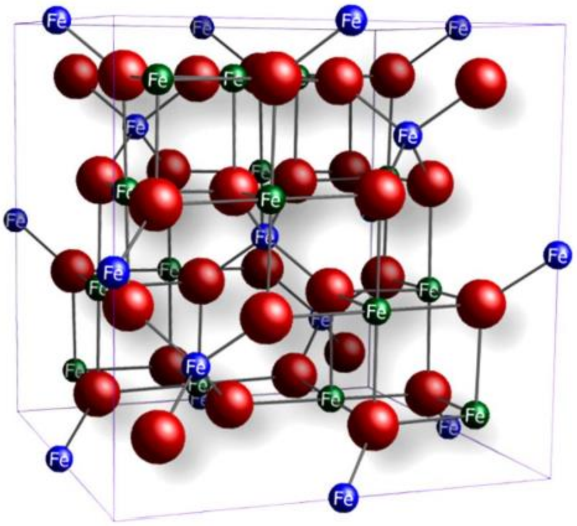

Fig. 3: Unit cell of magnetite [Fe(III)oct and Fe(II)oct: green, Fe(III)tetr: blue and O^{2-}: red][6].

The electron spins of Fe(III) ions in the tetrahedral sites are aligned antiparallel to those in the octahedral sites, so that no net magnetisation is observed form these ions. However, the parallel alignment of Fe(II) and Fe(III) spins in the octahedral holes generates a net magnetisation due to electron exchange, making bulk magnetite a ferromagnetic material[15]. On the contrary, Fe3O4 nanoparticles display a superparamagnetic behaviour when their size is approximately below 25 nm[16].

Since the properties of magnetic nanoparticles are strongly related to their dimension and shape, extensive efforts have been made to develop synthetic methods which allow to finely control these two parameters.

The *co-precipitation method* is an easy and convenient way to prepare iron oxides from Fe(II) and Fe(III) salt solutions, by addition of a base under inert atmosphere. The type of salts used (e.g. sulphates, nitrates, chlorides), the Fe(II)/Fe(III) ratio, the reaction temperature, the pH value and the ionic strength of the media are all factors which influence the size, shape and composition of the obtained magnetic nanoparticles[17]. In order to obtain monodispersed NPs, the synthesis is often carry out in the presence of organic additives, such as poly vinyl alcohol (PVA), as stabilising agents[18]. With this procedure, once the synthetic conditions are optimised, the quality of the magnetite nanoparticles is fully reproducible.

Another way to synthesize monodispersed magnetic NPs is by thermal decomposition of organometallic compounds, such as iron acetyl acetonates, in highboiling organic solvents containing stabilising surfactants (e.g. fatty acids, oleic acid, hexadecylamine)[19,20]. In this case the ratios of the starting reagents, i.e. organometallic precursor/surfactant/solvent, the reaction temperature, the reaction time and the aging period are the crucial parameters for the precise control of size and morphology.

In the *sol-gel* method, also known as chemical solution deposition, a sol of nanoparticles is obtained by hydroxylation and condensation of metal precursor solutions, with formation of a three dimensional metal oxide network. The crystalline state is then obtained upon heat treatment. The pH, the temperature, the nature and the concentration of the precursors and the nature of the solvent have been described to influence the synthetic process[21,22].

Finally, other known strategies for the preparation of Fe_3O_4 nanoparticles are gasphase deposition[23], hydrothermal method[24], electrochemical method[25] and sonochemical decomposition[26].

2.2.3 Functionalisation of magnetic nanoparticles

The functionalisation of the surface of magnetic nanoparticles is an important step in the design of supported magnetic materials, since it allows the immobilisation of a wide range of molecular catalysts, biocatalysts, organocatalysts and metal NPs[2,27]. The surface modification can be performed following three main approaches:

1. non-covalent absorption of bifunctional molecules, surfactant or polymers,
2. formation of core-shell structures by coating with other oxides, carbon, polymers or metallic layers,
3. grafting with organic or inorganic functional molecules, such as carboxylic acids, phosphonic acids or alkoxysilanes (Fig. 4).

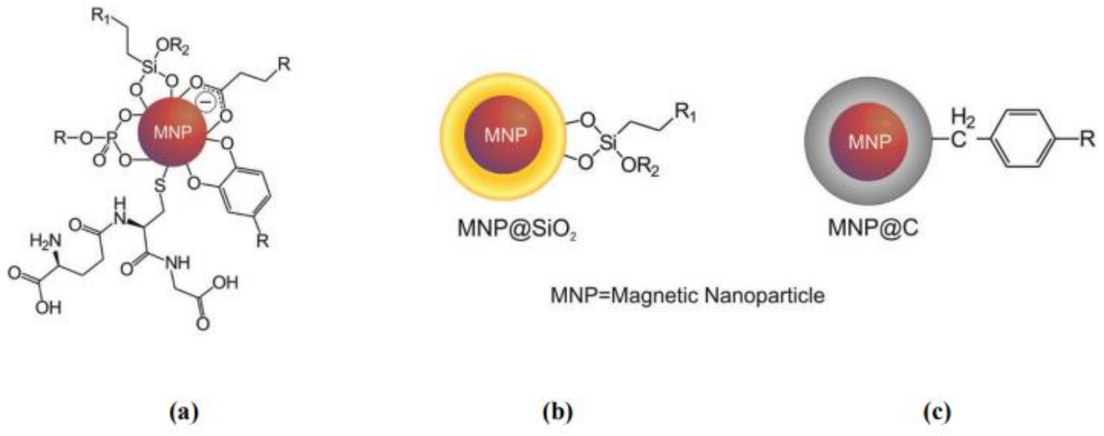

(a) (b) (c)

Fig. 4: different approaches for the functionalisation of magnetic nanoparticles (MNPs): a) grafting with inorganic/organic functional molecules, b) silica coating and c) carbon coating[2].

The binding of bifunctional carboxylate molecules to the metal oxide surface, by strong bidentate metal-carboxylate bonds, can easily afford surface functionalised Fe_3O_4 nanoparticles. In this regard, oleic acid is often attached to the iron oxide surface so that the hydrophobic tails can provide steric hindrance to stabilise NPs in solution[28]. Furthermore, it is possible to introduce –SH terminal groups by immobilisation of 3-mercaptopropionic acid[29], as well as functional acids containing multiple bonds, such as linolenic and linoleic acids, or pyridine moieties, such as 6-methylpyridine-2-carboxylic acid[30].

However, the most studied strategy for the functionalisation of magnetic nanomaterials consists in the condensation of the –OH groups of the oxide surface with the -OR terminal groups of alkoxyorganosilanes, which can be exploited both for bare magnetite nanoparticles and for silica-coated Fe_3O_4 NPs. For instance, Wang et al. reported the synthesis of magnetite NPs functionalised with 3-aminopropyl(triethoxysilane) for the further immobilisation of a Pd-based catalyst[31], while Yi et al. employed the same organosilane for the preparation of highly dispersed PdNPs on silica-coated Fe_3O_4 [32]. Furthermore, Rossi et al. described the synthesis of very small supported Pd NPs by an impregnation-reduction process using an amine and an ethylendiamine functionalised silica-coated magnetic support[33].

2.3 Results and discussion

2.3.1 Synthesis of Au/Fe_3O_4 @Yne and Au/Fe_3O_4 nanocomposites

The synthesis of magnetite nanoparticles was carried out *via* a co-precipitation method using two different basic media, i.e. NH_3 and NaOH ($Fe_3O_{4\text{-}NH_3}$ and $Fe_3O_{4\text{-}\mathbf{NaOH}}$). In particular, the amount of ammonia used was twice the equimolar amount given by the stoichiometry of the reaction (Scheme 1a), in order to achieve a basic pH. On the contrary, when the synthesis was performed in the presence of NaOH, the addition of the stoichiometric 8 equivalents of base led to a final pH value of 13.4 (Scheme 1b).

$$\textbf{a)}\ \mathbf{FeSO_4 + Fe_2(SO_4)_3 + 8NH_3 + 4H_2O \longrightarrow Fe_3O_4 + 4(NH_4)_2SO_4}$$

$$\textbf{b)}\ \mathbf{FeSO_4 + Fe_2(SO_4)_3 + 8NaOH \longrightarrow Fe_3O_4 + 4Na_2SO_4 + 4H_2O}$$

Scheme 1: Synthesis of magnetite in the presence of a) ammonia and b) sodium hydroxide.

Afterwards, the obtained Fe_3O_4 nanoparticles were functionalised with PPTEOS and decorated with AuNPs[35]. Briefly, the first step consisted in the coupling of the silane PPTEOS to the magnetite surface hydroxyl groups to yield Fe_3O_4@Yne. Successively in the second step, the addition of aqueous $HAuCl_4$ led to the in-situ formation of Au/Fe_3O_4@Yne (Scheme 2a). The amount of Au(III) precursor was chosen in order to have a nominal total gold amount in the range 4.5 - 5.0 wt %. The formation of metallic gold nanoparticles was obtained even on bare Fe_3O_4 (Au/ Fe_3O_4 composites, Scheme 2b). This finding is in line with the results reported by Alorro et al., according to which Au(III) chloride complexes are spontaneously reduced to metallic gold on Fe_3O_4 surfaces[36,37].

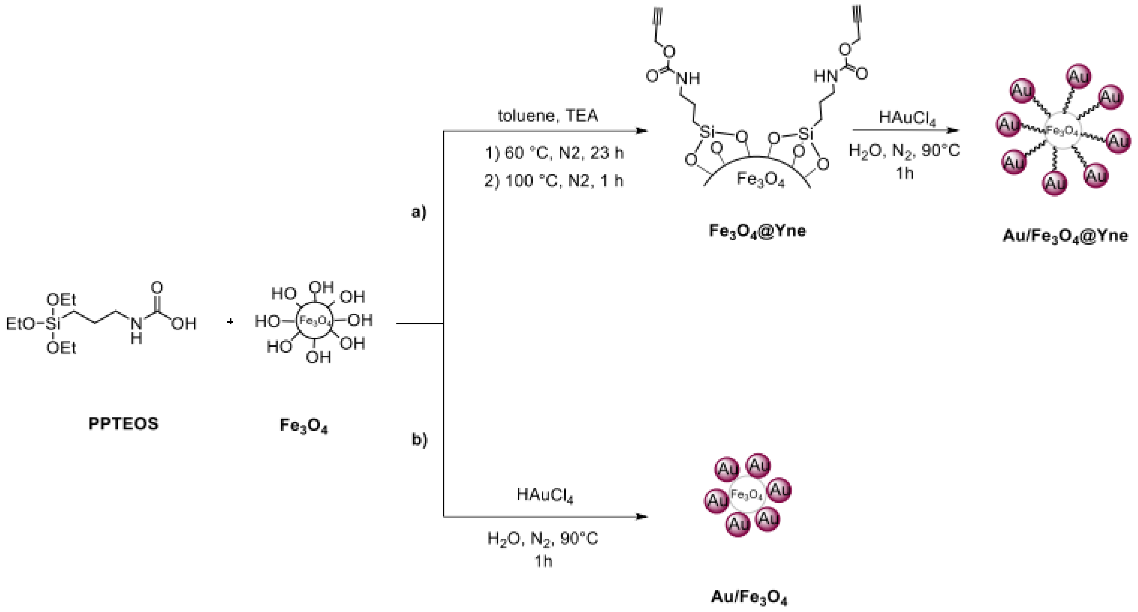

Scheme 2: Synthesis of a) Au/Fe_3O_4@Yne and b) Au/Fe_3O_4.

2.3.2 Characterisation of Fe_3O_4 and Fe_3O_4@Yne

Firstly, the morphology and nano-organisation of the synthesized magnetite nanoparticles was investigated by TEM analyses. In line with reported literature data, the material obtained in the presence of ammonia ($Fe_3O_{4\text{-}NH3}$) presented spherically shaped nanoparticles with an average size of 12 nm (Fig. 5a), whereas a different particle shape was observed for $Fe_3O_{4\text{-}\mathbf{NaOH}}$, alongside a larger mean particle diameter of 23 nm (Fig. 5b)$^{38\text{-}41}$.

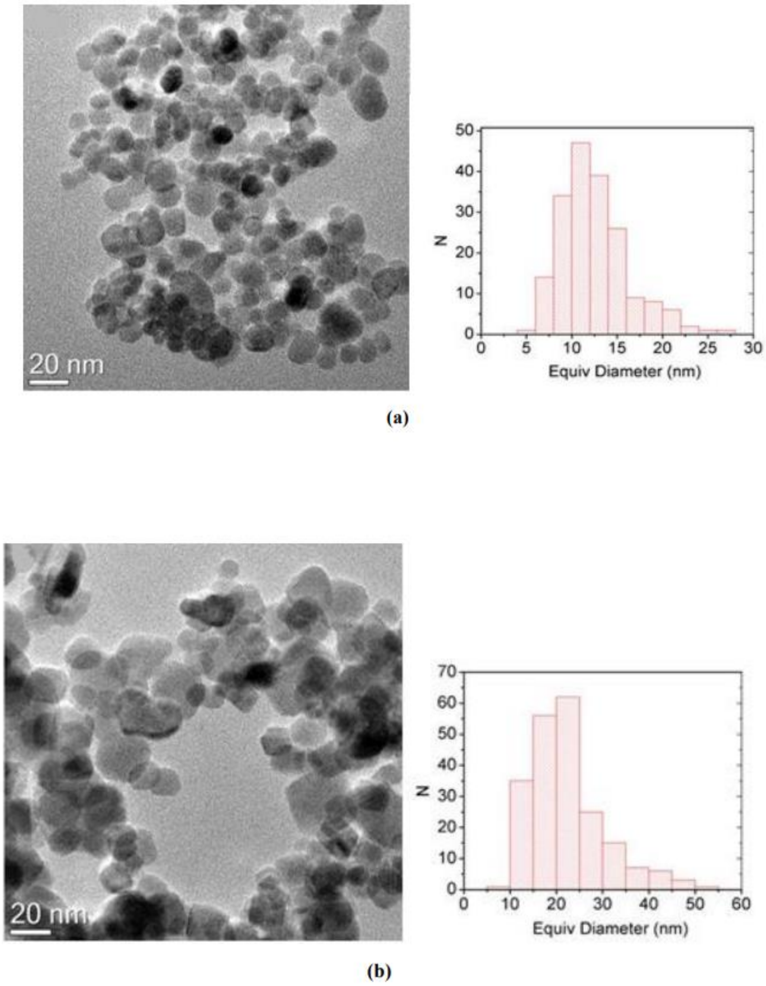

(a)

(b)

Fig. 5: Bright field (BF) image and particle size distribution of a) $Fe_3O_{4\text{-}NH_3}$ and b) $Fe_3O_{4\text{-}NaOH}$.

The Select Area Electron Diffraction (SAED) patterns of $Fe_3O_{4\text{-}NH_3}$ and $Fe_3O_{4\text{-}\mathbf{NaOH}}$ samples, recorded on a 200 nm^2 area, showed distinct diffraction rings indexed as magnetite (Fe_3O_4, cubic, space group F*d-3m*) (Fig. 6, Table 1).

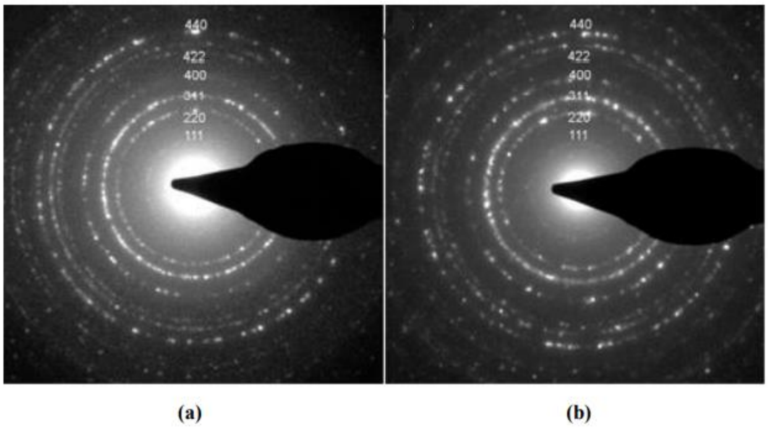

Fig. 6: Selected Area Electron Diffraction (SAED) recorded on 200 nm2 area of a) $Fe_3O_{4\text{-}NH3}$ and b) Fe_3O_{4NaOH}.

Table 1: SAED reflection indexes for $Fe_3O_{4\text{-}NH3}$

Reflection N°	hkl	d^{-1} (nm^{-1}) measured	d^{-1} (nm^{-1})[a]
1	111	2,1	2,066
2	220	3,4	3,374
3	311	4,0	3,956
4	222	4,1	4,131
5	400	4,8	4,770
6	331	-	5,199
7	422	5,9	5,843
8	511 – 333	6,2	6,198
9	440	6,8	6,745

a)JCPDS N°01-075-0033

The functionalisation of the magnetite support with the organic moieties was confirmed by the presence in the ATR-FTIR spectra of the two characteristic bands at 1700 and 1523 cm^{-1} associated to the C-O stretching and the N-H bending of the propynylcarbamate group.

Furthermore, the organic functionalisation had no significant influence on the size of the magnetite nanoparticles, nor on the crystalline structure of the materials, as evidence in the XRD spectra reported in Fig. 7. All samples patterns showed the presence of magnetite as the sole crystalline phase.

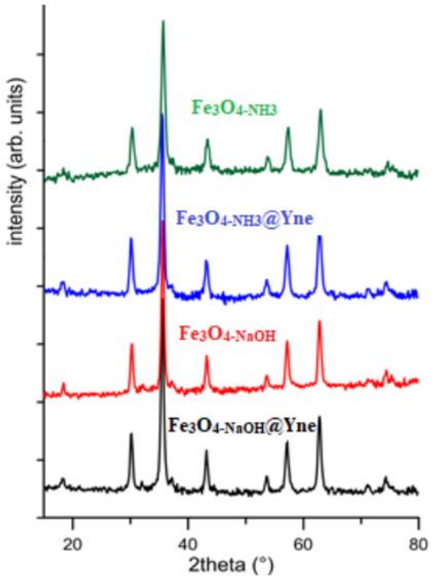

Fig. 7: XRD patterns of $Fe_3O_{4\text{-}NH3}$ and $Fe_3O_{4\text{-}NaOH}$ samples as-prepared, and after surface functionalisation.

On the contrary, the introduction of the organic capping resulted in a shift of the zeta potential of magnetite (Table 2)[42]. Indeed, the zeta potential (measured for a suspension in a 10.0 mM NaCl solution) of $Fe_3O_{4\text{-}NH3}$ was initially 28.0 mV (at spontaneous pH 5-6) and decreased down to 8.0 mV for $Fe_3O_{4\text{-}NH3}$@Yne, whereas the zeta potential of $Fe_3O_{4\text{-}NaOH}$ was decreased from 6.5 mV down to -0.4 mV ($Fe_3O_{4\text{-}NaOH}$@Yne).

Table 2: Zeta potentials of bare and functionalised magnetite.

Sample	Zeta potential (mV)	Spontaneous pH
$Fe_3O_{4\text{-}NH3}$	28.0 ± 1.0	5,14
$Fe_3O_{4\text{-}NH3}$@Yne	8.0 ± 0.6	5,24
$Fe_3O_{4\text{-}NaOH}$	6.5 ± 0.9	6,03
$Fe_3O_{4\text{-}NaOH}$@Yne	-0,4 ± 0,2	5,63

Moreover, the TGA analysis of Fe_3O_4@Yne showed three regions of mass loss, attributed respectively to the evaporation of adsorbed water and ethanol (30 -170 °C), organic material degradation (170 – 570 °C) and transformation of Fe_3O_4 into Fe_2O_3 (500 – 710 °C) (Fig. 8). Specifically, the weight loss associated to the organic functionalisation was found to be 5.0 wt % for both $Fe_3O_{4\text{-}NH3}$@Yne and $Fe_3O_{4\text{-}NaOH}$@Yne[43].

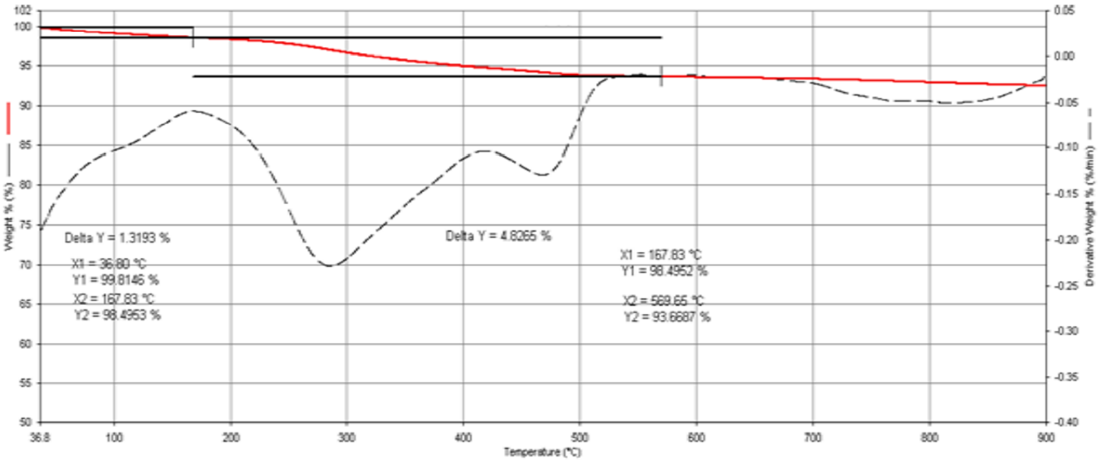

Fig. 8: TGA analysis of $Fe_3O_{4\text{-}NH3}$@Yne. The red line represents the weight loss percentage while the dotted line is the derivative of weight loss percentage

Characterisation of Au/Fe_3O_4 @Yne and Au/Fe_3O_4

The gold content determined by AAS spectroscopy was found to be around the 5.0 wt % for all the prepared samples, independently from the presence of the organic functionalisation (Table 3). Furthermore, the deposition of gold nanoparticles on magnetite did not influence the particle size and crystallinity of the support, as shown from comparison of the data reported in Table 3.

Table 3: TEM, XRD and AAS data for Fe3O4, Fe_3O_4@Yne, Au/Fe_3O_4@Yne and Au/Fe_3O_4

Sample	Fe_3O_4 d_{TEM}^a (nm)	Au d_{TEM}^a (nm)	Fe_3O_4 crystal size^b (nm)	Au crystal size^b (nm)	Au^c (wy%)
$Fe_3O_{4\text{-}NH3}$	12 ± 1	-	16 ±2	-	-
$Fe_3O_{4\text{-}NH3}$@Yne	12 ± 2	-	18 ± 2	-	-
$Au/Fe_3O_{4\text{-}NH3}$@Yne	12 ± 3	15 ± 3	18 ± 1	24 ± 3	4,4 ± 0,1
$Au/Fe_3O_{4\text{-}NH3}$	13 ± 3	74 ± 20	19 ± 2	38 ± 5	4,6 ± 0,1
$Fe_3O_{4\text{-}NaOH}$	23 ± 3	-	23 ± 1	.	-
$Fe_3O_{4\text{-}NaOH}$@Yne	22 ± 2	-	21 ± 1	.	-
$Au/Fe_3O_{4\text{-}NaOH}$@Yne	19 ± 5	30 ± 4	21 ± 1	32 ± 2	4,8 ± 0,1
$Au/Fe_3O_{4\text{-}NaOH}$	23 ± 2	42 ± 8	21 ± 1	36 ± 2	4,8 ± 0,1

a)Estimated on STEM images measurement using a confidence interval of 99%; b)calculated by scherrer equation; c)determined by AAS spectroscopy.

In particular, Bright Field (BF) and HAADF TEM images showed the presence of spherical shaped gold nanoparticles, whose mean diameter underwent a two-fold increase from $Au/Fe_3O_{4\text{-}NH3}$@Yne (15 ± 3 nm) to $Au/Fe_3O_{4\text{-}NaOH}$@Yne (30 ± 4 nm) (Fig. 9).

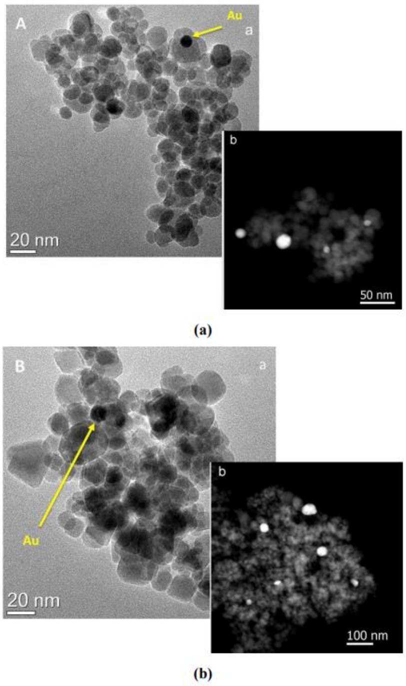

(a)

(b)

Fig. 9: Representative BF-TEM and HAADF-STEM micrographs of a) Au/$Fe_3O_{4\text{-}NH3}$@Yne and b) Au/$Fe_3O_{4\text{-}NaOH}$@Yne.

This difference in the AuNPs size could be tentatively explained by the presence of a higher concentration of adsorbed OH-groups on the $Fe_3O_{4\text{-}NaOH}$@Yne magnetite surface, responsible for the further aggregation of gold nanoparticles[44]. Furthermore, in the absence of the propynilcarbamate functionalisation, the average diameter of the anchored AuNPs turned out to be higher (74 ± 20 nm for Au/$Fe_3O_{4\text{-}NH3}$ and 42 ± 8 for Au/ $Fe_3O_{4\text{-}NaOH}$, Fig. 10).

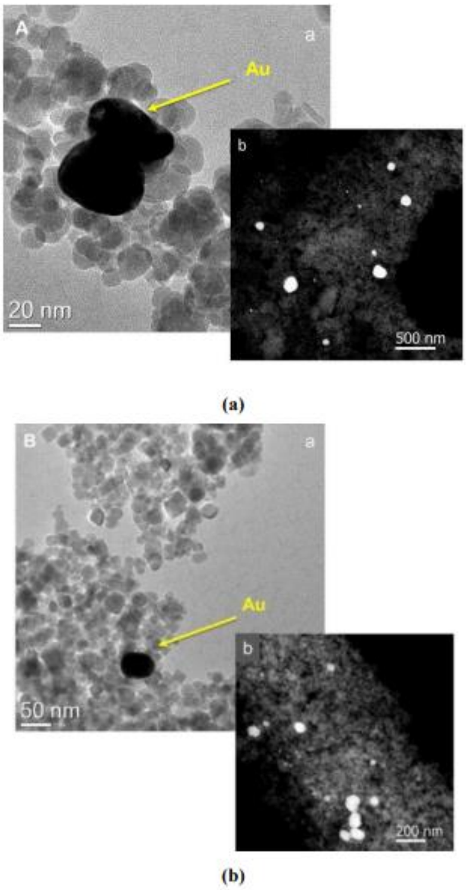

(a)

(b)

Fig. 10: Representative BF-TEM and HAADF-STEM micrographs of a) Au/$Fe_3O_{4\text{-}NH_3}$ and b) Au/Fe_3O_{4NaOH}.

These findings confirm the influence and importance of the pendant organic group in the reduction and successive stabilisation of the attached gold nanoparticles. Finally, the AuNPs particle diameter obtained from the TEM images of Au/$Fe_3O_{4\text{-}NH_3}$ and Au/$Fe_3O_{4\text{-}NaOH}$ was significantly larger than the crystalline domain size measure by XRD. This discrepancy can be explained with the agglomeration of crystalline domains to form larger nanoparticles but also with the presence of partially crystallized particles and defects.

The XRD patterns of Au/ Fe_3O_4 composites showed, beside Fe_3O_4 peaks, additional reflections located at 38.2 °, 44.4 °, 64.6 ° and 77.7 °, related to (111), (200), (220) and (311) crystallographic planes of cubic Au (Fig. 11).

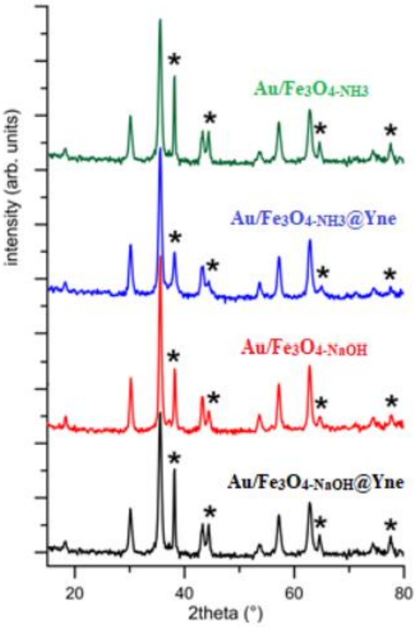

Fig. 11: XRD patterns of Au/ $Fe_3O_{4\text{-NH3}}$, Au/ $Fe_3O_{4\text{-NH3}}$@Yne, Au/ $Fe_3O_{4\text{-NaOH}}$ and Au/ $Fe_3O_{4\text{- NaOH}}$@Yne. Peaks indicated by (*) are referred to metallic gold. All the other peaks are due to Fe_3O_4.

Moreover, the surface chemical composition of the target systems was analysed by XPS. The wide-scan spectra of the NaOH-based samples are reported as a representative example in Fig. 12. The spectra displayed the presence of C, O and Fe photopeaks, along with N and Au, depending on the adopted processing conditions.

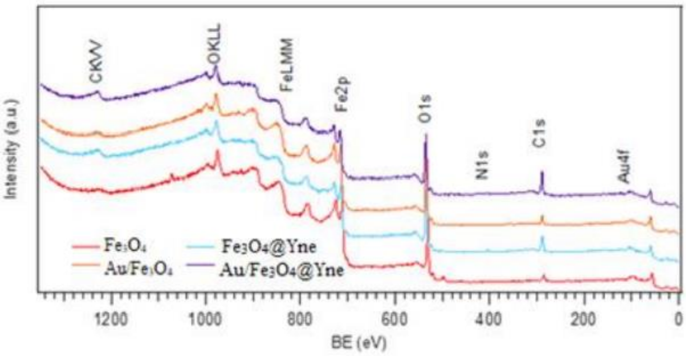

Fig. 12: Wide-scan X-ray photoelectron spectroscopy analyses of Fe_3O_4-NaOH, Fe_3O_4-NaOH@Yne, Au/Fe_3O_4-NaOH and Au/Fe_3O_4-NaOH@Yne

XPS analyses confirmed the formation of Fe_3O_4, as evidenced by the slight shift of the Fe2p component [BE(Fe2p3/2) = 710.9 eV] to lower BE values with respect to the ones reported for Fe_2O_3 (Figure 5.13a).44,45 The O1s signal (Fig. 13b) was located at BE = 530.3 eV, in line with the occurrence of lattice oxygen in Fe_3O_4. In addition, the tailing at higher BEs indicated also the presence of surface hydroxyl groups on the oxide surfaces. Due to the presence of the latter, the calculated ratio between O and Fe atomic percentages (O/Fe ≈ 1.45) was slightly higher than the value expected for stoichiometric Fe_3O_4 (O/Fe = 1.33). The N1s signal could be decomposed by means of two different contributing bands, a main component due to N in amino-groups (BE ≈ 399.5 eV) and an additional higher BE one (BE ≈ 401 eV) related to NH-CO(O)- moieties (Fig. 13c).

Regarding gold photopeaks, both Au containing samples showed similar spectral features [BE(Au4f7/2) = 84.0 eV] and no signals related to Au(I) and Au(III) species could be clearly identified, indicating the formation of pure metallic Au aggregates (Figure 5.13d)[46,47].

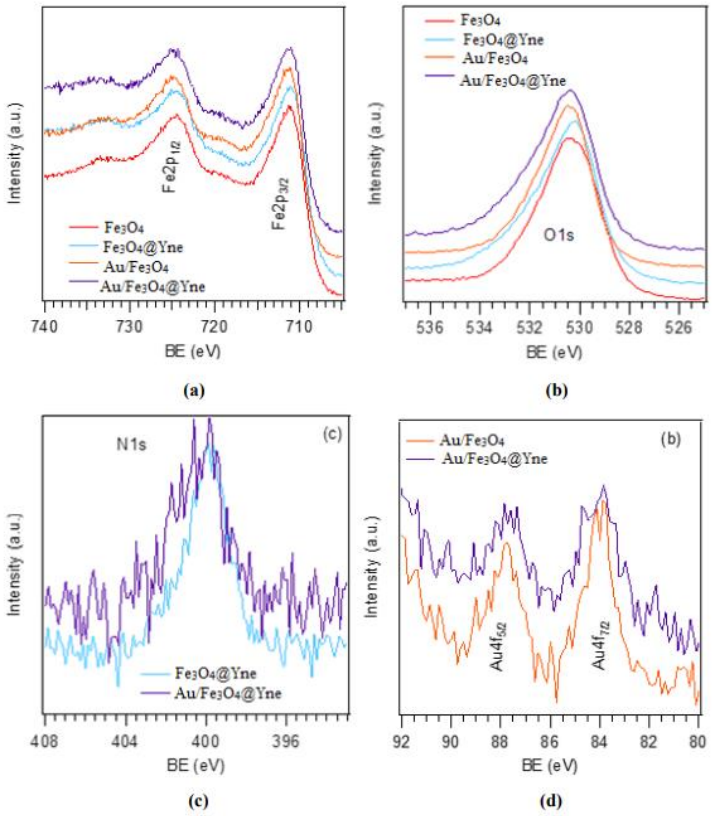

(a) (b)

(c) (d)

Fig. 13: Surface a) Fe2p b) O1s, c) N1s and d) Au4f XPS spectra of $Fe_3O_{4\text{-NaOH}}$, $Fe_3O_{4\text{-NaOH}}$@Yne, Au/$Fe_3O_{4\text{-NaOH}}$ and Au/$Fe_3O_{4\text{-NaOH}}$@Yne.

Independently from the preparative conditions, the gold surface concentration was close to 0.2 at.%. The samples functionalised with the propynilcarbamate pendant revealed also the presence of nitrogen with a mean content of 2.0 at.%.

2.3.3 Magnetic properties

The magnetic properties of the synthesized materials were also investigated. The specific moment σ as function of the applied magnetic field (Fig. 14) was used to calculate some characteristic quantities: the remanent specific moment *Mr*, which is the specific moment at 0 applied field, the coercive field *Hc* and the specific moment at an applied magnetic field of 1000 Oe ($\sigma_{1000\ \mathrm{Oe}}$).

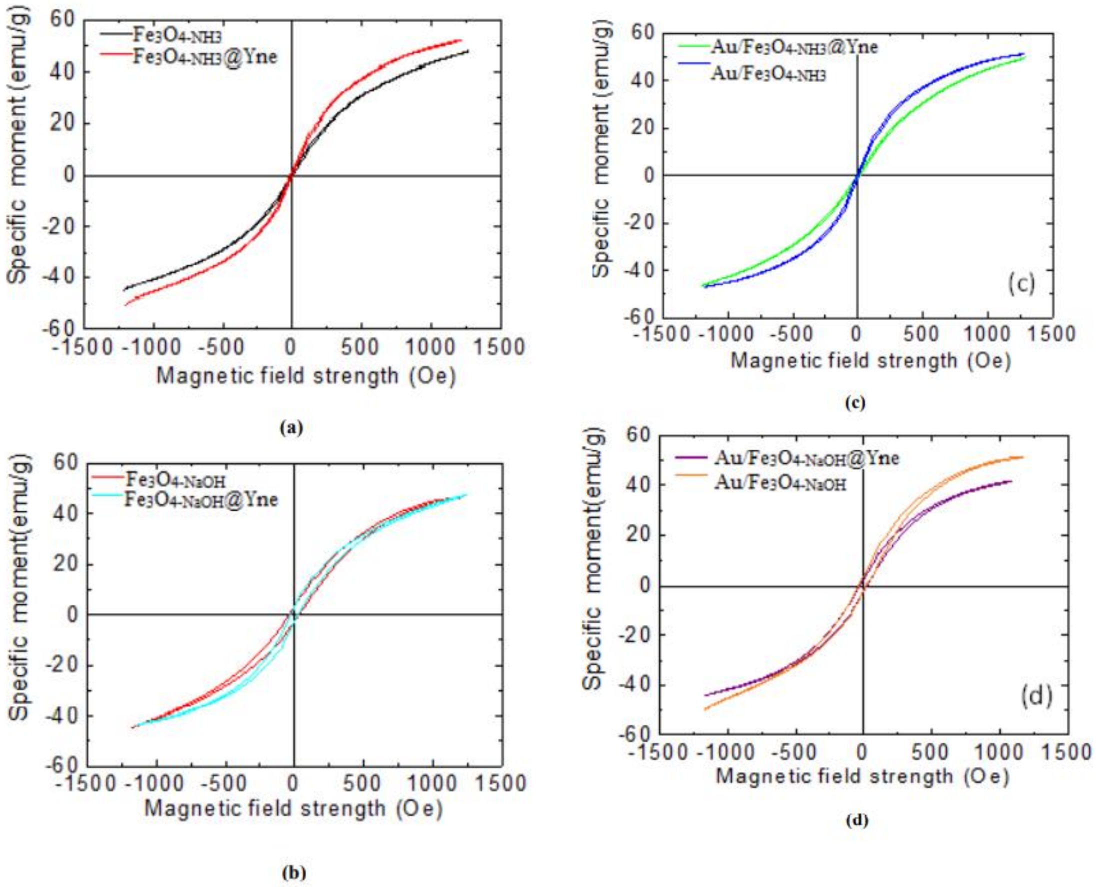

(a)

(c)

(d)

(b)

Fig. 14: Specific moment σ as a function of the applied magnetic field, measured at 300 K. In a) and b) curves refer to Fe_3O_4 and Fe_3O_4@Yne samples, respectively. In c) and d) curves refer to Au/Fe_3O_4 and Au/Fe_3O_4@Yne samples, respectively.

The magnetic properties of nanoparticles are influenced by the concurrence of various factors, which include the particle size and contributions from their shape and surface functionalisation[48,49]. In particular, Fe_3O_4 nanoparticles with an average size lower than 25 nm display a superparamagnetic behavior, with no magnetic hysteresis, at variance with bulk Fe_3O_4. To evaluate the superparamagnetism of the target materials, we considered $Mr/\sigma_{1000\ Oe}$ and *Hc,* whose values should be close to 0 for superparamagnetic nanoparticles[50,51].

The data reported in Table 5 indicate that the organic/inorganic modification did not affect magnetic properties although $Fe_3O_{4\text{-}NH3}$-based samples showed consistently smaller *Hc* and *Mr* values (av. values of 7.4 Oe and 0.8 emu/g) than those observed for $Fe_3O_{4\text{-}NaOH}$-based ones (av. values of 28 Oe and 2.8 emu/g). The specific moment at 1000 Oe ($\sigma_{1000\ Oe}$) was ca. 45 emu/g in both cases, in agreement with previous literature data[52,53].

Table 2: Magnetic properties of Fe_3O_4, Fe_3O_4@Yne, Au/Fe_3O_4 and Au/Fe_3O_4@Yne.

Sample	$\sigma_{1000\ Oe}$ (emu/g)	Hc (Oe)	Mr (emu/g)	$Mr/\sigma_{1000\ Oe}$ ($x\ 10^{-3}$)
$Fe_3O_{4\text{-}NH3}$	44 ± 2	6,0 ± 0,7	0,60 ± 0,07	14 ± 2
$Fe_3O_{4\text{-}NH3}$@Yne	49 ± 2	7,5 ± 0,9	0,9 ± 0,1	18 ± 2
Au/$Fe_3O_{4\text{-}NH3}$@Yne	45 ± 2	8 ± 1	0,60 ± 0,07	13 ± 2
Au/$Fe_3O_{4\text{-}NH3}$	48 ± 2	8 ± 1	1,0 ± 1,2	21 ± 3
$Fe_3O_{4\text{-}NaOH}$	45 ± 2	35 ± 4	3,0 ± 0,4	67 ± 9
$Fe_3O_{4\text{-}NaOH}$@Yne	44 ± 2	24 ± 3	2,8 ± 0,3	64 ± 8
Au/$Fe_3O_{4\text{-}NaOH}$@Yne	40 ± 2	27 ± 3	2,8 ± 0,3	70 ± 9
Au/$Fe_3O_{4\text{-}NaOH}$	50 ± 2	26 ± 3	2,8 ± 0,3	56 ± 7

The obtained values $Mr/\sigma_{1000\ Oe}$ ($<70 \cdot 10^{-3}$) and *Hc* (< 35 Oe) are compatible with a behavior dominated by superparamagnetism[54]. Furthermore, the difference in magnetic behavior between $Fe_3O_{4\text{-}NH3}$-based and $Fe_3O_{4\text{-}NaOH}$-based samples could be explained by the fact that the $Fe_3O_{4\text{-}NH3}$ nanoparticles are on average smaller than those in $Fe_3O_{4\text{-}\mathbf{NaOH}}$ samples. The broader size distribution and higher shape anisotropy observed for $Fe_3O_{4\text{-}NaOH}$ samples implies a greater number of nanoparticles that exceed the superparamagnetic limit of 25 nm and that have a non-zero coercive field. In addition, their shape anisotropy produces a magnetic anisotropy which, in turn, contributes to the obtainment of a higher coercive field[51].

2.4 Conclusions

Gold nanoparticles were successfully immobilised on alkynyl-carbamate functionalised Fe_3O_4 nanosystems by a straightforward procedure, without additional reducing and stabilising agents. Indeed, the organic functionalisation was found to promote the in situ formation of AuNPs without affecting neither the dimensions nor the magnetic properties of the initial superparamagnetic supports.

Furthermore, when Fe_3O_4 was prepared with ammonia ($Fe_3O_{4\text{-}NH3}$) instead of sodium hydroxide ($Fe_3O_{4\text{-}NaOH}$), the average size of the supported gold nanoparticles was found to be significantly different (15 ± 3 nm for Au/$Fe_3O_{4\text{-}NH3}$@Yne and 30 ± 4 nm for Au/$Fe_3O_{4\text{-}NaOH}$@Yne). In the latter case, the larger dimensions of AuNPs could be tentatively explained by the presence, even after the organic functionalisation, of a higher concentration of adsorbed OHgroups on the magnetite surface, responsible for the further aggregation of gold nanoparticles.

The addition of $HAuCl_4$ to bare magnetite resulted in the immobilisation of AuNPs, large aggregates were observed (av. AuNPs diameters: 74 ± 20 nm for Au/$Fe_3O_{4\text{-}NH3}$ and 42 ± 8 nm for Au/ $Fe_3O_{4\text{-}NaOH}$).

On the base of the obtained results, the most appealing perspectives for future development of the present research activities will concern the use of these nanocomposites with polyaniline, exploiting their magnetic nature for an easy and efficient separation from the reaction mixture.

2.5 Experimental section

2.5.1 Materials

Iron(II) heptahydrate sulphate ($Fe_2SO_4 \cdot 5H_2O$, 95%), sodium hydroxide (NaOH) and triethylamine (TEA, 99%) were purchased from Carlo Erba. Hydrocloric acid (HCl, 37 %), nitric acid (HNO_3, 65%), iron(III) pentahydrate sulphate ($Fe_2(SO_4)_3 \cdot 5H_2O$, 97%), ammonia (NH_3, 28-30 %, d = 0.9 g/cm^3) were purchased from Sigma-Aldrich. Toluene was dehydrated by distillation under nitrogen on Na/K amalgam and stored under nitrogen on 4 Å molecular sieves. PPTEOS already synthesized from my research group and chloroauric acid ($HAuCl_4 \cdot 3H_2O$) was prepared following a literature procedure[55]. Ultrapure water purified with the Milli-Q plus system (Millipore Co, resistivity over 18 MΩ cm) was used in all cases.

2.5.2 Synthesis of $Fe_3O_{4\text{-}NH3}$ and $Fe_3O_{4\text{-}NaOH}$

The synthesis of $Fe_3O_{4\text{-}NH3}$ was carried out following a previous protocol[56]. $FeSO_4 \cdot 7H_2O$ (2.788 g, 0.010 mol) and $Fe_2(SO_4)_3 \cdot 5H_2O$ (5.131 g, 0.010 mol) were dissolved in 100 mL of water and the yellow-orange solution was degassed with three vacuum/nitrogen purging cycles. Subsequently, an excess of ammonia (13.0 mL, 0.200 mol) was added dropwise, up to a final pH value of 10.4.56 The black suspension was then continuously stirred for 2 h at 60 °C and finally cooled down to room temperature. Magnetic nanoparticles were first separated from the supernatant solution using an external magnet and then thoroughly washed with water and ethanol, dried at 60 °C and then under vacuum for 12 h. The final material (2.220 g, yield = 96%) was stored under nitrogen. The synthesis of $Fe_3O_{4\text{-}NaOH}$ was carried out following the same procedure, by dropwise addition of a stoichiometric 1.0 M solution of NaOH (80 mL, 0.08 mol) to the water mixture of Fe(II) and Fe(III) sulphates, reaching a final pH of 13.4. The obtained material (2.199 g, yield = 95%) was stored under nitrogen.

2.5.3 Synthesis of Fe_3O_{4-NH3}@Yne and Fe_3O_{4-NaOH}@Yne

In a typical procedure, Fe_3O_4 (1.011 g), toluene (10 mL) and TEA (20 µL, 0.14 mmol) were mixed with PPTEOS (0.499 g, 1.65 mmol) dissolved in toluene (20 mL) under vigorous stirring. The reaction mixture was stirred for 23 h at 60 °C, and subsequently maintained at 100 °C for 1 h. The obtained Fe_3O_4@Yne was magnetically separated by the supernatant and then washed three times (3x20 mL) with toluene. The samples were first dried at 60 °C for 12 h and then kept under vacuum to remove the residual solvent, finally yielding 0.888 g of black powder.

2.5.4 Synthesis of Au/Fe_3O_{4-NH3}@Yne and Au/Fe_3O_{4-NaOH}@Yne Yne

In a 500 mL three-necked round bottom flask under nitrogen atmosphere, a suspension of 0.897 g of Fe_3O_4 @Yne in 50 mL H_2O was heated to 90 °C. Subsequently, a solution of $HAuCl_4 \cdot 3H_2O$ (0.088 g, 0.22 mmol) in 170 mL of water was rapidly added, in order to have a 1.00 mM final concentration of chloroauric acid. After stirring for 1 h, the obtained Au/Fe_3O_4@Yne was magnetically separated from the colorless supernatant solution, thoroughly washed three times with water, and dried at 60 °C for 12 h and finally under vacuum. The brownish-black powder (0.80 g) was stored under nitrogen. The synthesis of Au/Fe_3O_4 was performed following the same procedure but using bare magnetite.

2.5.5 Instruments and methods

TEM analyses were performed by a TECNAI F20 FEG apparatus operated both in transmission (TEM) and in scanning mode (STEM) at 200 keV. For the target analysis, samples were dispersed in isopropyl alcohol and sonicated for 15 min. A few drops of the solution were then deposited on a holey carbon film supported by a copper grid and dried at 80 °C. High Angle Annular Dark Field (HAADF, Z contrast) images were formed by collecting only Rutherford scattered electrons with an annular dark-field detector. The image intensity is proportional to the mean atomic number Z^2 and the thickness[58] t:

$$I(x, y) \propto Z^2$$

ATR-FTIR analysis were performed with a Perkin Elmer Spectrum Two spectrophotometer, equipped with an Universal ATR accessory, in the range 4000-400 cm^{-1}, with a resolution of 0.5 cm-1. Pristine and modified Fe_3O_4 powders were directly analyzed after being ground in a mortar performing 40 scans for each analysis.

XRD was performed by a Philips X'Pert Pro instrument equipped with a fast X'Celerator detector, working at 40 mA and 40 kV and using CuKα radiation. For phase identification, the 2θ angle range was from 10° to 80° (step size 0.1°; time/step 100 seconds). The peak broadening was used to evaluate the crystal size (τhkl), which was calculated from the widths at half maximum intensity (β1/2) using the Scherrer equation[58]:

$$\tau_{hkl} = k\,\lambda /\, \beta_{1/2}\, cos\theta$$

where λ is the wavelength, θ the diffraction angle and K a constant depending on crystal habit (chosen as 1). For crystal size calculation, the most intense reflections for each crystalline phase were taken into consideration. i.e. peak (310) for magnetite and (111) for Au.

Zeta potential was measured using Electrophoretic Light Scattering (ZetasizerNano; Malvern Instruments). In each analysis, 5 mg of powder sample were suspended in 50 mL of a 10 mM NaCl solution and sonicated for 4 minutes before measurement. Each analysis was performed in triplicate[42].

TGA characterization was carried out using a Perkin Elmer TGA-7 instrument. In each analysis, 5–10 mg of the target sample was heated in a platinum crucible from room temperature to 900 °C, at a rate of 10 °C/min.

The overall amount of gold present on the different samples was determined by means of flame atomic absorption spectroscopy (AAS, Thermo Scientific) in air-acetylene flame with a wavelength of 242.8 nm and a spectral band width of 0.5 nm. The analyses were conducted by comparison with six calibration standards (2.0, 4.0, 6.0, 8.0, 10.0 ppm) prepared by dilution to 50 mL of different amounts of a concentrated $HAuCl4\cdot3H_2O$ aqueous solution (100 ppm). The samples of Au/ Fe_3O_4@Yne and Au/ Fe_3O_4 were prepared by dissolving the solid (ca. 10 mg) in 2 mL of aqua regia under sonication. Subsequently, the solution was diluted with HCl 0.5 M up to a final volume of 50 mL.

X-ray photoelectron spectroscopy (XPS) analyses were conducted on a PerkinElmer Φ 5600ci spectrometer using a standard AlKα excitation source (hν = 1486.6 eV), at a working pressure lower than 10^{-8} mbar. The reported binding energies (BEs; uncertainty ± 0.1 eV) were corrected for charging effects by assigning a BE of 284.8 eV to the C1s line of adventitious carbon[60]. After a Shirley-type background subtraction[61], atomic percentages (at. %) were calculated by signal integration using Perkin-Elmer sensitivity factors (Φ V5.4A). Whenever necessary, peak fitting was performed adopting Gaussian−Lorentzian peak shapes by means of the XPS Peak software (version 4.1)[62].

A custom-built Faraday magnetometer was used to measure the sample specific moment σ (i.e. the magnetic moment per unit mass) as a function of the applied field at 300 K.The magnetometer is based on a Sartorius ME235S analytical balance and a NdFeB permanent magnet, with a maximum applied magnetic field of approximately 0.12 T. The experimental uncertainties were calculated based on the performance of the Faraday magnetometer. For the value of $\sigma_{1000\ \mathrm{Oe}}$, an uncertainty of 5 % of the measured value was considered, while for the $_{\mathrm{Mr}}$ and $_{\mathrm{Hc}}$ an uncertainty of 12 % of the measured values was used. For the uncertainty on the Mr/$\sigma_{1000\ \mathrm{Oe}}$ ratio, the rule of the composition of uncertainties was applied:

$$\Delta\left(\frac{M_r}{\sigma_{1000\ Oe}}\right) = \sqrt{(\frac{1}{\sigma_{1000\ Oe}}\Delta M_r)^2 + (\frac{M_r}{{\sigma_{1000\ Oe}}^2}\Delta\sigma_{1000\ Oe})^2}$$

where *Δ* $(\frac{M_r}{\sigma_{1000\ Oe}})$ is the uncertainty on the *Mr*/$\sigma_{1000\ \mathrm{Oe}}$, ΔMr is the uncertainty on *Mr* and $\Delta\sigma_{1000\ \mathrm{Oe}}$ is the uncertainty on the specific moment at 1000 O.

References

1. B. Ballarin, M. C. Cassani, D. Nanni, C. Parise, D. Barreca, G. Carraro, A. Riminucci, I. Bergenti, V. Morandi, A. Migliori, E. Boanini, *Ceram. Int.*, **2019**, 45, 449.
2. 1 L. M. Rossi, N. J. S. Costa, F. P. Silva, R. Wojcieszak, *Green Chem*., **2014**, 16, 2906.
3. S. Blundell, *Magnetism in Condensed Matter,* Oxford University Press, Oxford, **2001**.
4. D. Jiles, *Introduction to Magnetism and Magnetic Materials*, CRC Press, London, **1998**.
5. C.Ó. Dálaigh, S.A. Corr, Y. Gun'ko, S.J. Connon, *Angew. Chem. Int. Ed*, **2007**, 46, 4329–4332.
6. A.H. Lu, E.L. Salabas, F. Schüth, *Angew. Chem. Int. Ed.*, **2007**, 46, 1222–1244.
7. M.B. Gawande, P.S. Branco, R.S. Varma, *Chem. Soc. Rev.*, **2013**, 42, 3371.
8. L.M. Rossi, N.J.S. Costa, F.P. Silva, R. Wojcieszak, *Green Chem.*, **2014**, 16, 2906.
9. V. Polshettiwar, R. Luque, A. Fihri, H. Zhu, M. Bouhrara, J.M. Basset, *Chem. Rev.*, 2011, 111, 3036–3075.
10. S. Shylesh, V. Schünemann, W.R. Thiel, *Angew. Chem. Int. Ed.*, **2010**, 49, 3428–3459.
11. V. Polshettiwar, R.S. Varma, *Green Chem.*, **2010**, 12, 743.

12. B. Karimi, F. Mansouri, H.M. Mirzaei, *Chem. Cat. Chem.*, **2015**, 7, 1736–1789.

13. F. Gao, Y. Jiang, M. Hu, S. Li, Q. Zhai, *Mater. Des.*, **2016**, 111, 414–420.

14. R.L. Oliveira, P.K. Kiyohara, L.M. Rossi, *Green Chem.* **2010**, 12, 144–149.

15. M. Shokouhimehr, Y. Piao, J. Kim, Y. Jang, T. Hyeon, *Angew. Chem. Int. Ed.*, **2007**, 46, 7039–7043.

16. C.W. Lim, I.S. Lee, *Nano Today,* **2010**, 5, 412–434.

17. L.H. Reddy, J.L. Arias, J. Nicolas, P. Couvreur, *Chem. Rev*., **2012**, 112 5818–5878.

18. S. Laurent, D. Forge, M. Port, A. Roch, C. Robic, L.V. Elst, R.N. Muller, *Chem. Rev.*, **2008**, 108, 2064–2110.

19. Y.Q. Zhang, X.W. Wei, R. Yu, *Catal. Lett.*, 2010, 135, 256–262.

20. M. Stratakis, H. Garcia, *Chem. Rev*., **2012**, 112, 4469–4506.

21. T. Ishida, H. Koga, M. Okumura, M. Haruta, *Chem. Rec.*, 2016, 16, 2278–2293.

22. B. Ballarin, D. Barreca, E. Boanini, M.C. Cassani, P. Dambruoso, A. Massi, A. Mignani, D. Nanni, C. Parise, A. Zaghi, *ACS Sustain. Chem. Eng.*, **2017**, 5, 4746–4756.

23. J. Ni, W.-J. Yu, L. He, H. Sun, Y. Cao, H.-Y. He, K.-N. Fan, *Green Chem.,* **2009**, 11, 756.

24. X. Zhao, Y. Cai, T. Wang, Y. Shi, G. Jiang, *Anal. Chem.* **2008**, 80, 9091–9096.

25. P. Miao, Y. Tang, L. Wang, *ACS Appl. Mater. Interfaces*, **2017**, 9, 3940–3947.

26. Z. Xu, Y. Hou, S. Sun, *J. Am. Chem. Soc.*, 2017, 129, 8698–8699.

27. Y. Cui, Y. Wang, W. Hui, Z. Zhang, X. Xin, C. Chen, *Biomed. Microdev.*, **2005**, 7, 153–156.

28. B. Ballarin, M. C. Cassani, D. Nanni, C. Parise, D. Barreca, G. Carraro, A. Riminucci, I. Bergenti, V. Morandi, A. Migliori, E. Boanini, *Ceram. Int.*, **2019**, 45, 449.

29. S. Fazzini, M.C. Cassani, B. Ballarin, E. Boanini, J.S. Girardon, A.-S. Mamede, A. Mignani, D. Nanni, *J. Phys. Chem. C*, **2014**, 118, 24538–24547.

30. B. Ballarin, D. Barreca, E. Boanini, E. Bonansegna, M.C. Cassani, G. Carraro, S. Fazzini, A. Mignani, D. Nanni, D. Pinelli, *RSC Adv.*, **2016**, 6 25780–25788.

31. J.P. Jolivet, É. Tronc, C. Chanéac, *Comptes Rendus Chim.*, **2002**, 5, 659–664.

32. P. Berger, N.B. Adelman, K.J. Beckman, D.J. Campbell, A.B. Ellis, G.C. Lisensky, *J. Chem. Educ.*, **1999**, 76, 943–948.

33. R.B.N. Baig, R.S. Varma, *Chem. Commun.*, **2012**, 48, 6220.

34. X. Lu, F. Sun, J. Wang, J. Zhong, Q. Dong, *Macromol. Rapid Commun.*, **2009**, 30, 2116–2120.

35. G. Braurer, *Handbook of preparative inorganic chemistry*, New York, **1963**.

36. S.J. Pennycook, P.D. Nellist (Eds.), *Scanning Transmission Electron Microscopy*, Springer, New York, **2011**.

37. H.P. Klug, L.E. Alexander, *X-ray Diffraction Procedures for Polycrystalline and Amorphous materials*, 2nd ed., Wiley-Interscience, New York, **1974**.

38. D. Briggs, M.P. Seah, *Practical Surface Analysis*: vol. 1, Auger and X-ray Photoelectron Spectroscopy, Wiley, New York, **1990**.

39. L. Armelao, D. Barreca, G. Bottaro, A. Bovo, A. Gasparotto, E. Tondello, *Surf. Sci. Spectra*, **2003**, 10, 1.

40. http://xpspeak.software.informer.com/4.1.

41. A. Riminucci, M. Uhlarz, R. De Santis, T. Herrmannsdörfer, *J. Appl. Phys.*, **2017**, 121.

42. E. Aghaei, R.D. Alorro, A.N. Encila, K. Yoo, *Metals*, **2017**, 7, 1–32.

43. R.D. Alorro, N. Hiroyoshi, H. Kijitani, M. Ito, M. Tsunekawa, Miner. *Process. Extr. Metall. Rev.*, **2010**, 31, 201–213.

44. R.Y. Hong, J.H. Li, H.Z. Li, J. Ding, Y. Zheng, D.G. Wei, *J. Magn. Mater.*, **2008**, 320, 1605–1614.

45. X.-C. Yang, Y.-L. Shang, Y.-H. Li, J. Zhai, N.R. Foster, Y.-X. Li, D. Zou, Y. Pu, *J. Nanomater*. 2014, 1–5.

46. H. Iida, K. Takayanagi, T. Nakanishi, T. Osaka, *J. Colloid Interface Sci.*, **2007**, 314 274–280.

47. R.A. Bini, R.F.C. Marques, F.J. Santos, J.A. Chaker, M. Jafelicci, *J. Magn. Magn. Mater.*, **2012**, 324, 534–539.

48. M.E.A. Warwick, D. Barreca, E. Bontempi, G. Carraro, A. Gasparotto, C. Maccato, K. Kaunisto, T.-P. Ruoko, H. Lemmetyinen, C. Sada, Y. Gönüllü, S. Mathur, *Phys. Chem. Chem. Phys.*, **2015**, 17, 12899–12907.

49. https://srdata.nist.gov/xps.

50. J.F. Moulder, W.F. Stickle, P.E. Sobol, K.D. Bomben, *Handbook of X-ray Photoelectron Spectroscopy*, Perkin Elmer Corporation, Eden Prairie, MN., **1992**.

51. K.M. Krishnan, A.B. Pakhomov, Y. Bao, P. Blomqvist, Y. Chun, M. Gonzales, K. Griffin, X. Ji, B.K. Roberts, *J. Mater. Sci.*, **2006**, 41, 793–815.

52. F. Heider, D.J. Dunlop, N. Sugiura, *Science*, **1987**, 236, 1287–1290.

53. J.S. Lee, J.M. Cha, H.Y. Yoon, J.K. Lee, Y.K. Kim, *Sci. Rep.*, **2015**, 5, 1–7.

54. S. Sun, H. Zeng, D.B. Robinson, S. Raoux, P.M. Rice, S.X. Wang, G. Li, *J. Am. Chem. Soc.*, **2004**, 126, 273–279.

55. S.H. Gee, Y.K. Hong, D.W. Erickson, M.H. Park, J.C. Sur, *J. Appl. Phys.*, **2003**, 93.

56. G.F. Goya, T.S. Berquó, F.C. Fonseca, M.P. Morales, *J. Appl. Phys.*, **2003**, 94, 3520–3528.

57. J.L. Dormann, D. Fiorani (Eds.), *Magnetic properties of fine particles*, 1st ed., Elsevier, Amsterdam, **1992**.

58. D. Fiorani (Ed.), *Surface Effects in Magnetic Nanoparticles*, Springer, New York, **2005**.

59. S. Bedanta, W. Kleemann, Supermagnetism, *J. Phys. D. Appl. Phys.*, **2009**, 42.

60. G.C. Papaefthymiou, *Nano Today*, **2009**, 4, 438–447.

61. G. Muscas, G. Concas, C. Cannas, A. Musinu, A. Ardu, F. Orrù, D. Fiorani, S. Laureti, D. Rinaldi, G. Piccaluga, D. Peddis, *J. Phys. Chem. C*, **2013**, 117, 23378–23384.
62. A. Riminucci, M. Uhlarz, R. De Santis, T. Herrmannsdörfer, *J. Appl. Phys*., **2017**, 121, 94701.

3 Investigation on PANI/Au$_{NPs}$-supported Magnetite Nanoparticles as a Composite Material for high performance energy storage.

3.1 Aim of the chapter

A flexible graphite current collector suitably modified with polyanialine (PANI, a conductive polymer) and nanoparticles based on Fe_3O_4 functionalized with gold for their use in the preparation of pseudocapacitors is investigated in this chapter. The optimal conditions for the electrosynthesis of these nanocomposite films was studied.

The obtained films, called PANI, PANI/Fe_3O_4, PANI/Au/Fe_3O_4 and PANI/Au/Fe_3O_4@Yne, are characterized by CV, SEM, TGA and infrared spectroscopy (ATR IR). A galvanostatic charge-discharge test (C/D) and impedance test (EIS) are also performed to verify their efficiency.

The best performing electrodes PANI/Au/Fe_3O_4 and PANI/Au/Fe_3O_4@Yne are finally employed to assemble a prototype of gel-state symmetric supercapacitor, consisting of two electrodes made with the same active materials separated from a polymeric gel electrolyte. C/D, EIS tests and longtime resistance of the device are investigated.

Part of the work reported in the present chapter was published in Electrochimica Acta[1].

3.2 Introduction

Electrochemical energy storage (EES) systems, including batteries and electrochemical capacitors (ECs) or supercapacitors (SC), have attracted intense interests in these last years owing to the tremendous need for energy consumption at every step in our modern daily lives[2-5]. Among EES, ECs present a high energy storage capacity and power density, portability, high efficiency, fast charge–discharge capability and long lifecycle stability that make them very promising for applications ranging from portable electronics to large industrial scale power and energy managements. Based from the different charged mechanism two different types of ECs have been proposed: i) the electric double layer capacitors (EDLCs), mainly made of high surface-area materials, such as porous carbon or carbon aerogels in order to maximize the surface area of the double-layer in which only ion adsorption/desorption take place between the electrode/electrolyte interfaces; and ii) the pseudocapacitors based on Faradic process where the energy storage is achieved by electrons transfer that follows redox reaction in the same materials[2,6].

Metal oxides, such as RuO_2, NiO, MnO_2, Fe_3O_4 as well as conducting polymers (polypyrrole, PPy, and polyaniline, PANI) are classic examples of redox pseudocapacitive materials[7-18]. Compared to EDLCs, pseudocapacitors possess higher specific capacitance (Cs), higher energy density but lower cycle stability. Moreover, pseudocapactive reactions occur only on surface layers that are in contact with the electrolyte with the inner part inactive. Therefore, increasing the active sites exposed to the electrolyte is of great importance for increasing the utilization efficiency and the specific capacitance, particularly when PANI is used[18-21]. PANI has received special attentions among the conductive polymer because it has the highest specific capacitance due to multi-redox reactions, good electronic properties due to protonation, and low cost for its infinite abundance, better thermal stability and can be easily synthesized by chemical or electrochemical methods, resulting in powder or thin film[22-24].

Despite all these positive features, a major problem of using PANI-based materials is that they exhibit poor stabilities during the charge/discharge process. A great number of studies have been therefore devoted to improving the utilization efficiency and specific capacitance of PANI. One common strategy is to modify PANI with inorganic nanoadditives such as graphene or metal oxides nanoparticles that can drastically modify the electrical, optical, and dielectric properties of the resulting nanocomposite pseudocapacitors (CPs)[12,19-23].

The presence of inorganic nanoparticles into the prepared polymers nanocomposites confers high specific surface area and/or shorter diffusion path due to the higher porosity, allows faster transport of electrolyte ions and may enhance the adsorbtion/desorption of electroactive species, hence increasing the current and leading to improved performances for supercapacitor applications [7,19].

Among the metal oxides/hydroxides employed, Fe_3O_4 is one of the most attractive materials because of its natural abundance, low cost, and low toxicity[10,11,21,25,29]. Moreover, to enhance its capacitive performance, Fe_3O_4 can be coupled with metal nanoparticles or conductive carbon. Although several studies concerning the preparation of capacitors (CPs) via chemical synthesis have been reported[10,25-30], few are dedicated to their synthesis via in situ electropolymerization, a process that presents significant advantages, such as enhanced homogeneity and electrode stability[19-23].

We have recently reported the preparation of gold nanoparticles (AuNP) supported on Fe_3O_4 systems covalently functionalized by a propynylcarbamate group (hereafter labelled Au/Fe_3O_4@Yne, Yne = propynylcarbamate). This organic functionalization promotes the in situ nucleation, growth and stabilization of anchored AuNP having an av.

diameter of 15 nm, without affecting neither the dimensions nor the magnetic properties of the superparamagnetic core[31].

We herein employed the Au/Fe_3O_4@Yne system as component for PANI nanocomposite electrodes to be used for energy storage and compared its electrochemical behavior with that of Au/Fe_3O_4 in which the supported AuNP on bare magnetite have a larger diameter (74 nm). The PANI nanocomposite electrodes have been obtained by electrochemical synthesis in acid aqueous media of aniline on flexible graphite foil (GrF) current collector[19,22,24,32]. The resulting films termed PANI/Au/Fe_3O_4 and PANI/Au/ Fe_3O_4@Yne were characterized with Attenuated Total Reflectance Infrared spectroscopy (ATR-IR), Scanning Electron Microscopy (SEM), Molecular PlasmaeAtomic Emission Spectroscopy (MP-AES) and Cyclic Voltammetry (CV). For comparison, electrodes based on electropolymerized PANI and PANI/Fe_3O_4 were also studied. The charge storage properties of all the electrodes were investigated with galvanostatic Charge/Discharge curves (CD) and Electrochemical Impedance Spectroscopy (EIS) measurements in 0.5 M H_2SO_4 + 0.1 M $LiClO_4$ electrolyte solution. PANI/Au/Fe_3O_4 and PANI/Au/Fe_3O_4@Yne electrodes were then employed to assemble gel-state symmetric devices whose electrochemical behavior (CD and EIS) as well as the long-term stability has been even investigated.

3.3 Results and discussion

3.3.1 Electrochemical deposition of PANI and PANI-nanocomposites on graphite foil

The deposition of conductive films on graphite foil was conducted electrochemically using a cyclic voltammetry technique with potential range of − 0.20 to + 0.89 V (*vs* SCE) and a scan rate of 50 mV s^{-1} for 40 or 60 cycles[7,19]. A representation of a PANI-nanocomposite electrode obtained is reported in Scheme 1.

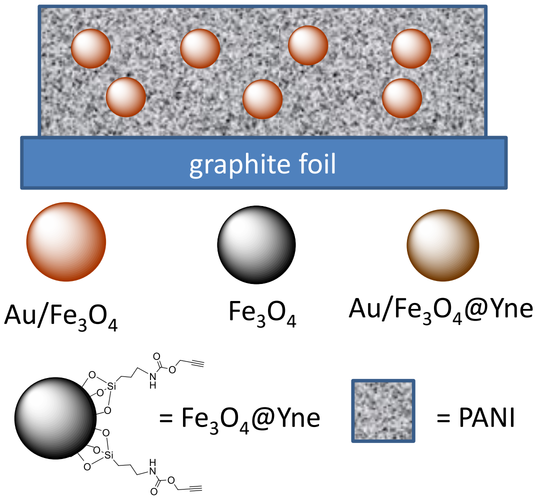

Scheme 1: representation of an example of a PANI-nanocomposite electrode and different materials used.

The growth of the electrodeposited film on graphite foil was followed by multi-sweep CVs, as shown in Fig.1**.** For all samples an increase in current was always observed during the cycling and a steadystate electrochemical signal was never reached neither after 60 scans. The typical PANI oxidation and reduction peaks were observed at ~0.2 V (I/I’ in Fig.1A) that refers to the transformation of the leucoemeraldine base to emeraldine salt, ~0.8 V (II/II’) characteristic of the formation of fully oxidized pernigraniline salt and ~0.4 V (III/III’) corresponding to the formation of degradation quinone-like soluble species and hydrolysis products[19,34,40].

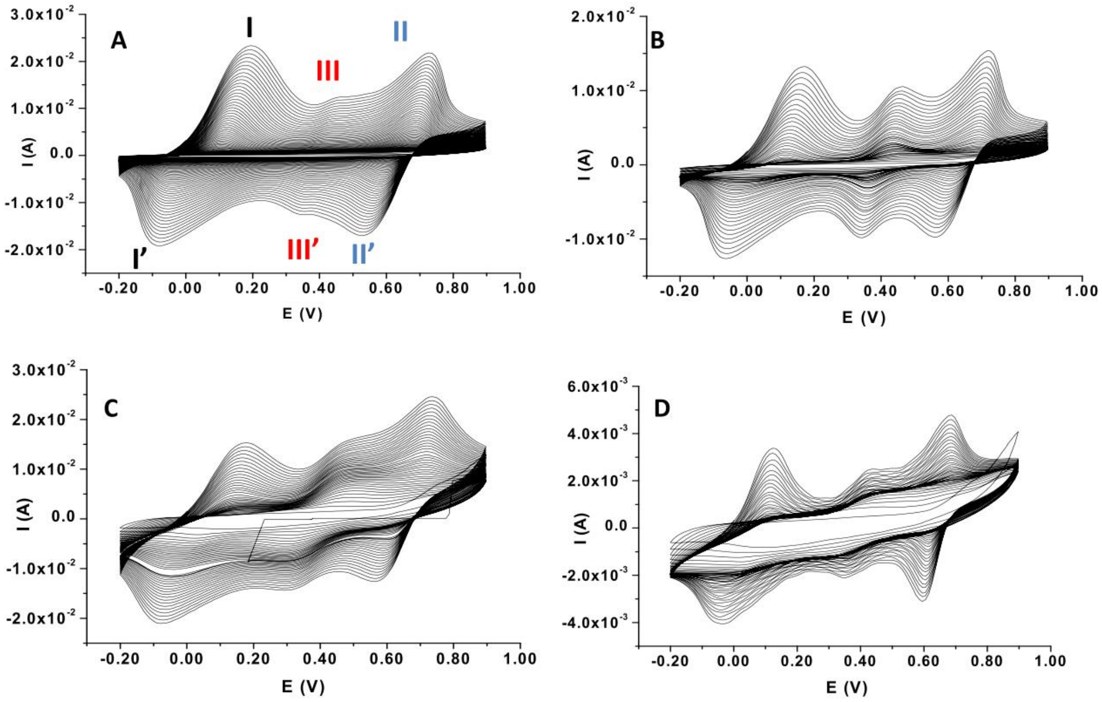

Fig. 1: cyclic voltammograms registered during the formation of PANI (A), PANI-Fe_3O_4 (B), PANI-Au/Fe_3O_4 (C) and PANI-Au/Fe_3O_4@Yne (D)

The effect of the presence of metal nanoparticles (Fe_3O_4, Au/Fe_3O_4 or Fe_3O_4@Yne) on the electropolymerization process of aniline can be observed in the initial CVs of the monomer (Fig.2): the first reverse scan indicates that trace crossing, that occurs at E_{SCE} = 0.772 V for aniline alone, was moved towards higher values.

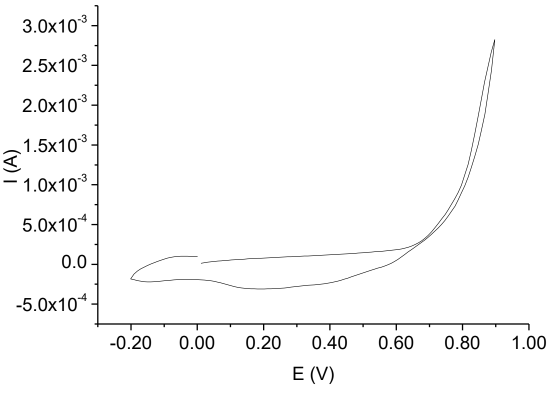

Fig. 2: first cycle of voltammograms registered during the formation of PANI at 50 mV s^{-1} potential sweep rate.

As the number of cycles was raised from 40 to 60, the current density also increased, indicating that the growth of the electrochemically active surface area is due to formation of electrically conducting PANI film. A dark green colored coating was formed on the surface of the working electrode during all the electrochemical syntheses. The complete CV data set is reported in Table 1 and all the following electrodes characterizations have been made on films growth up to 60 cycles. The increased current of the III redox couple, observed in the presence of Fe_3O_4, Fig.1 B, C and D, is originate from the redox between Fe^{2+} and Fe^{+3} during the in situ electropolymerization of PANI/Fe_3O_4. This observation was confirmed via cyclic voltammetry measurements of Fe_3O_4 dispersed in 0.5 M H_2SO_4 + 0.1 M $LiClO_4$ on bare GrF.

Table 1: CV data recorded for all the electrodes.

	PANI	**PANI/Fe_3O_4**	**PANI-Au/Fe_3O_4**	**PANI-Au/Fe_3O_4@Yne**
ΔE_I (mV)	191	191	241	242
E_{aI} (V)	0.141	0.131	0.161	0.161
E_{cI} (V)	-0.050	-0.060	-0.080	-0.081
ΔE_{III} (mV)	50	82	151	121
E_{aIII} (V)	0.413	0.434	0.463	0.453
E_{cIII} (V)	0.363	0.352	0.312	0.332
ΔE_{II} (mV)	105	101	151	151
E_{aII} (V)	0.695	0.705	0.735	0.725
E_{cII} (V)	0.584	0.604	0.584	0.574

Ea = anodic potential and Ec = cathodic potential *vs* SCE; 40th cycle.

3.3.2 Characterization of PANI and PANI nanocomposites electrodes

Firstly, the PANI and PANI nanocomposite electrodeposited samples (PANI/Fe_3O_4, PANI/Au/Fe_3O_4 and PANI/Au/Fe_3O_4@Yne) were characterized by TGA analyses. As can be observed in Fig.3, three regions of mass loss could be attributed respectively to the evaporation of adsorbed water and ethanol (up to about 170 °C), PANI degradation (about 170−550 °C), and transformation of Fe_3O_4 into Fe_2O_3 which is thermodynamically stable above 570 °C in phase diagram of the Fe–O system[41-43].

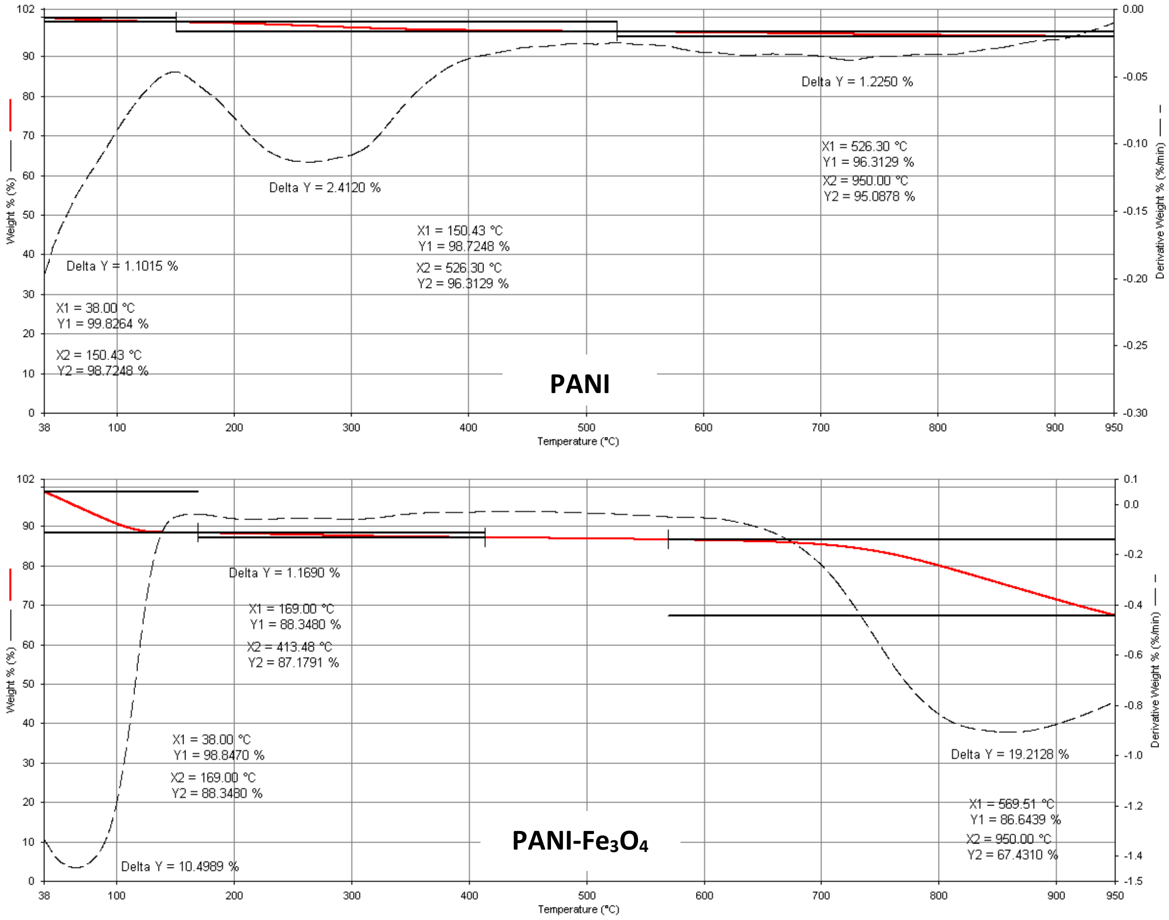

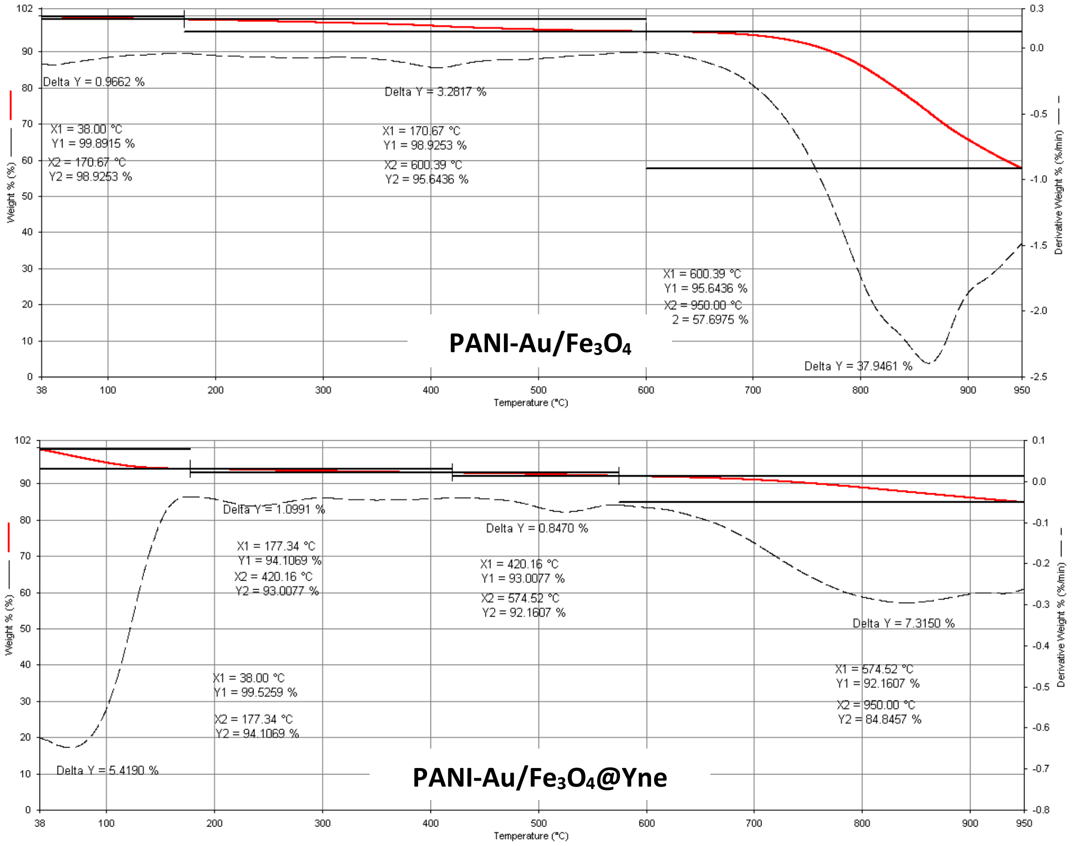

Fig. 3: TGA curves for PANI, PANI-Fe$_3$O$_4$, PANI-Au/Fe$_3$O$_4$ and PANI-Au/Fe$_3$O$_4$@Yne

The amount of Fe$_3$O$_4$, Au and PANI, defined as wt% with respect to 1.0 g of graphite and deposited material, is calculated by MP-AES and reported in Table 2.

Table 2: amount of PANI, Fe$_3$O$_4$ and Au in the electrodeposited films

Electrode	PANI^b (wt %)	Fe$_3$O$_4$^{c} (wt %)	Au^c (wt %)
PANI	2.4 ± 0.1	------	------
PANI-Fe$_3$O$_4$	1.0 ± 0.2	$3.4\ 10^{-2} \pm 0.2\ 10^{-2}$	------
PANI-Au/Fe$_3$O$_4$	3.3 ± 0.1	$17.0\ 10^{-2} \pm 0.1\ 10^{-2}$	$2.0\ 10^{-2} \pm 0.1\ 10^{-2}$
PANI-Au/Fe$_3$O$_4$@Yne	1.1 ± 0.2	$6.0\ 10^{-2} \pm 0.2\ 10^{-2}$	$0.6\ 10^{-2} \pm 0.2\ 10^{-2}$

b)Weight loss by TGA. c)Determined by MP-AES.

The ATR-FTIR spectra of the samples, reported in Fig.4 shows the presence of the characteristic peaks of PANI in its conjugated emeraldine form[44-46]. Due to the preparation of Fe_3O_4 and Au/Fe_3O_4 in aqueous environment, spectral bands at around 1630 cm^{-1} and 3400 cm^{-1}, corresponding to surface-sorbed water or hydroxyl groups are observed in PANI-Fe_3O_4 and PANI-Au/Fe_3O_4 films (Fig. 5b,c). PANI-Au/Fe_3O_4@Yne spectra, not reported, is similar to PANI-Au/Fe_3O_4 one.

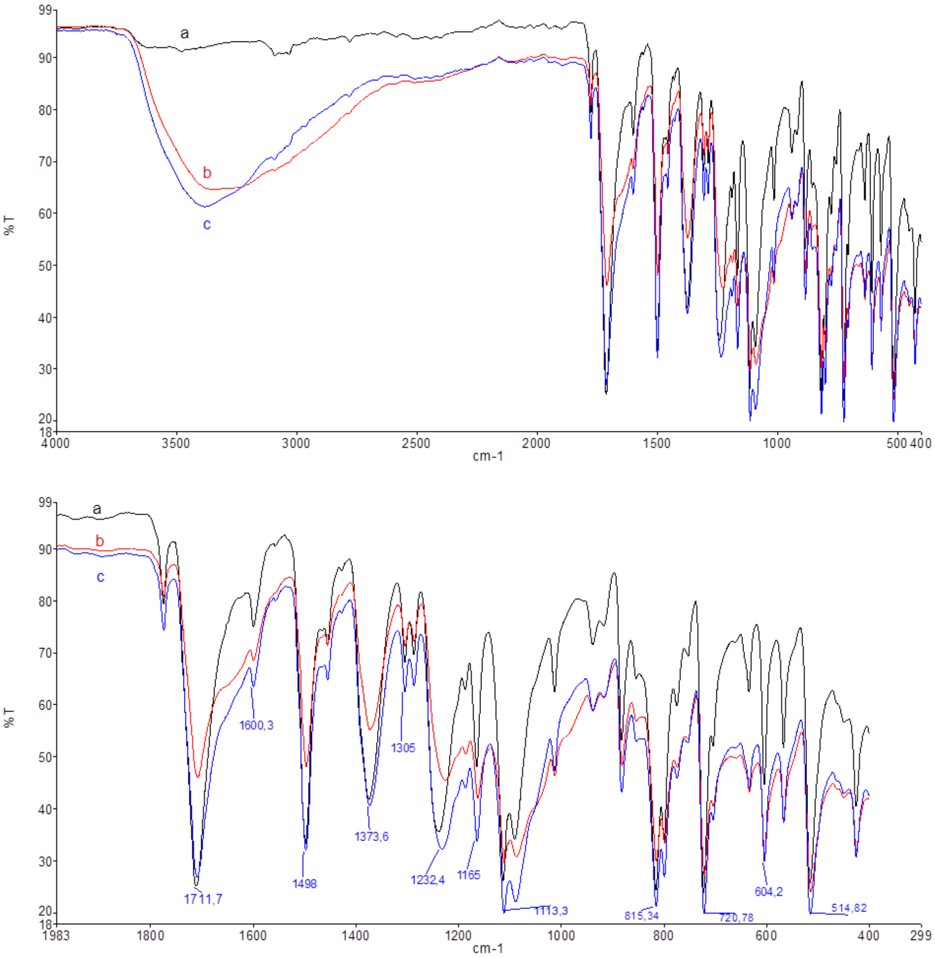

Fig. 4: ATR-FTIR spectra of PANI (a), PANI-Fe_3O_4 (b) and PANI-Au/Fe_3O_4 and an enlargement on the bottom.

The SEM images of PANI and PANI nanocomposite electrodes are shown in Fig. 5; in all samples the morphology is found to be porous in nature.

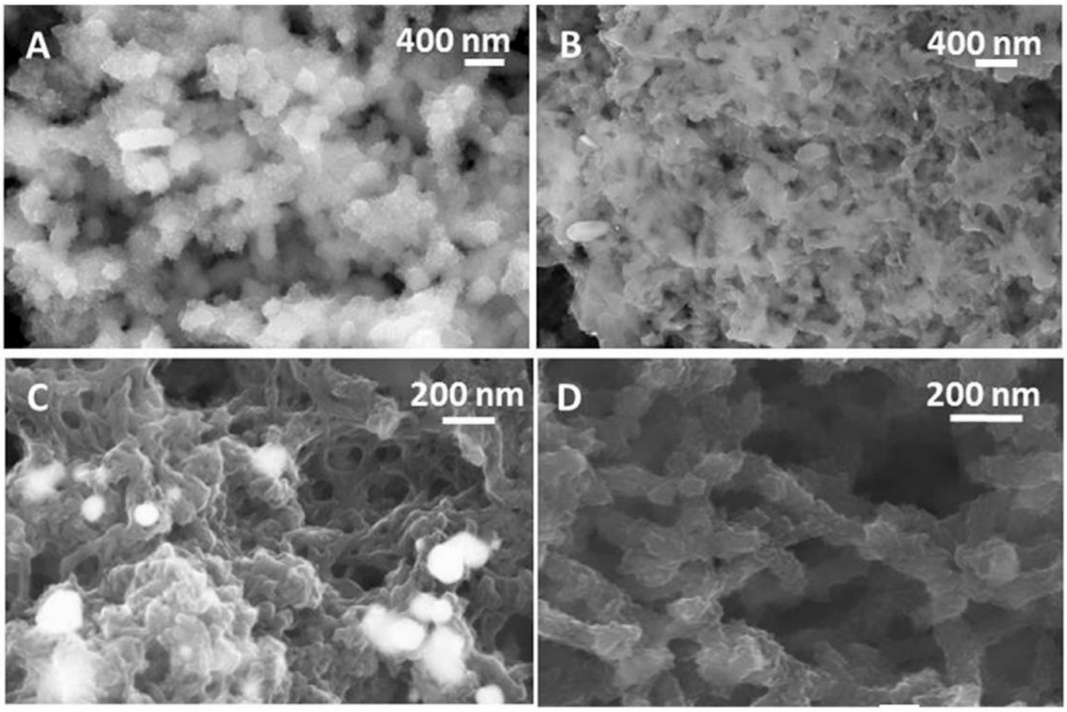

Fig. 5: SEM images of PANI (A), PANI-Fe_3O_4 SE (B), PANI-Au/Fe_3O_4 in-lens (C) and PANI-Au/Fe_3O_4@Yne SE (D)

Fig. 5A shows the surface structure of PANI collected in SE mode. EDX analysis (Fig. 6) of PANI detected the presence of S and Cl, deriving from the electrolyte used during the electrodeposition, while cross sectional observations allowed to estimate a total layer thickness of about 130 µm. The surface structure of PANI/Fe_3O_4 is shown in Fig. 5B (SE mode). Although the Fe_3O_4 nanoparticles are not visible, the EDX analysis taken on a large area of sample evidenced a low intensity Fe peak, confirming the presence of magnetite in the sample (Fig. 7); the thickness of the PANI-Fe_3O_4 layer measured in cross section SEM images is around 170 µm (Fig. 6). SEM image of PANI-Au/Fe_3O_4 were taken by the in-lens detector (in-lens) in order to highlight the compositional contrast (Fig. 5C). In this case, Au-Fe_3O_4 nanoparticles with overall size around 70 nm are clearly visible in bright contrast. EDX analysis evidenced the presence of Au (Fig. 8), while the Fe peak is always faint; the layer thickness is around 130 µm. Finally, Fig. 5D shows the SEM image of the

PANI-Au/Fe_3O_4@Yne sample. The widespread presence of nanoparticles with a whole average size of 20 nm is evident only in the low magnification SEM image in Fig. 9. The layer thickness is about 150 µm, while EDX analysis shows only a low intensity Au peak without any contribution from Fe.

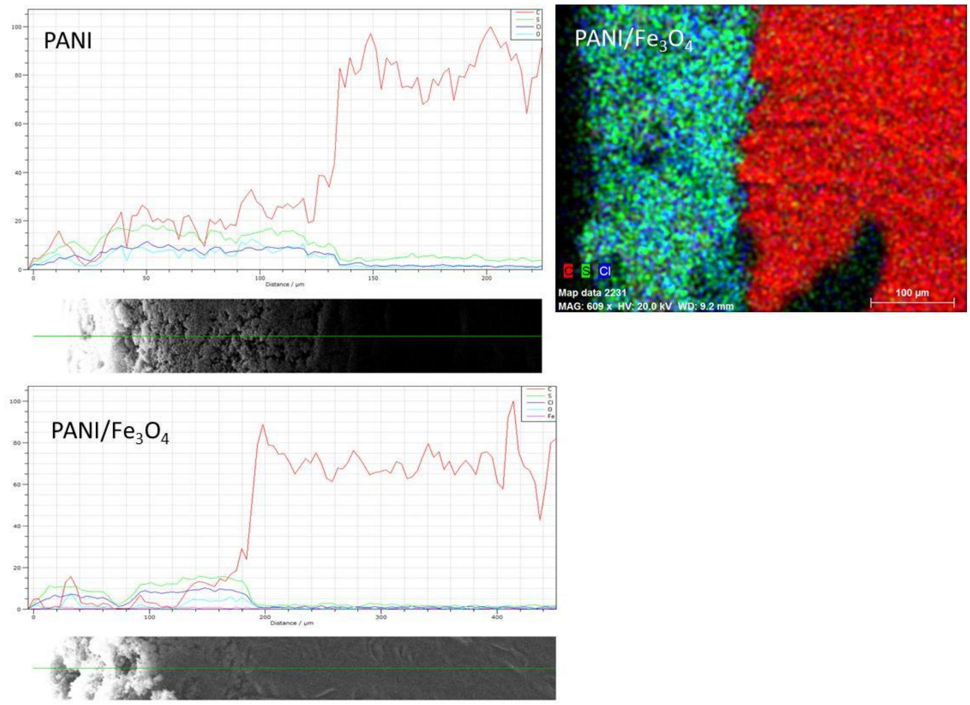

Fig. 6: SEM analyses of samples cross-sections: elements profile and element map of C, S, Cl; the deposited film is on the left edge.

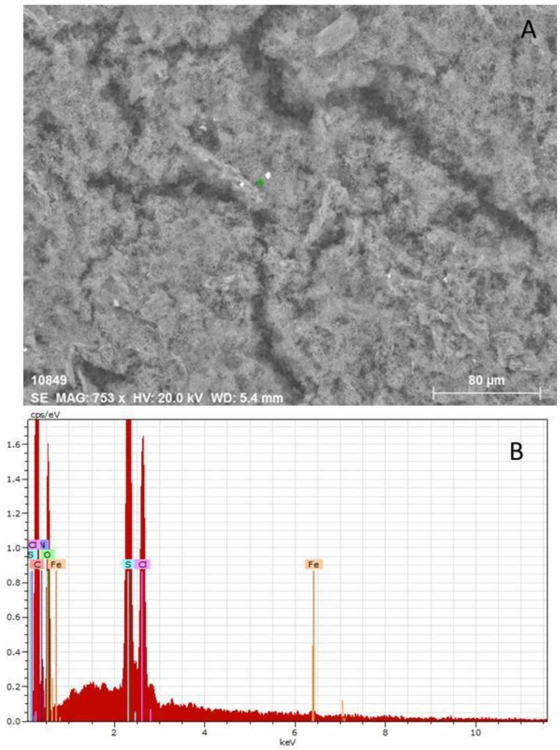

Fig. 7: surface image (A) and microanalysis on sample PANI/Fe_3O_4 (B). EDX (B) is performed on the green cross spot (A).

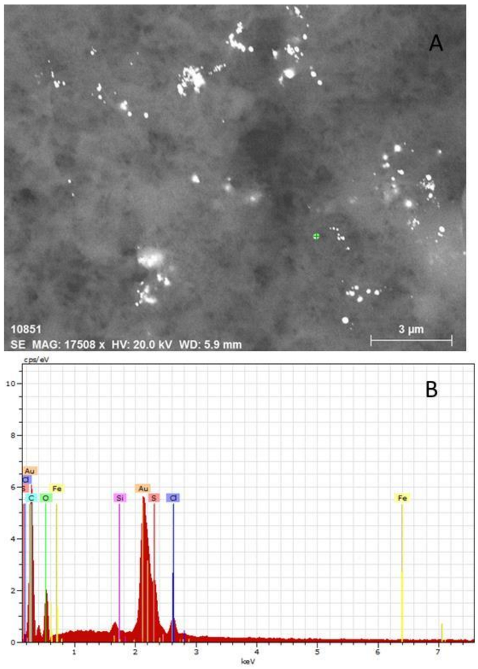

Fig. 8: surface image (A) and microanalysis on sample PANI/Au/Fe_3O_4 (B). EDX (B) is performed on the green cross spot (A) and confirms the presence of Au in the bright spot.

The nanoparticles distribution in the PANI-Au/Fe_3O_4@Yne sample is shown in the low magnification SEM image in Fig. 9 obtained by backscattered electrons to evidence compositional contrast; the nanoparticles are visible in bright contrast.

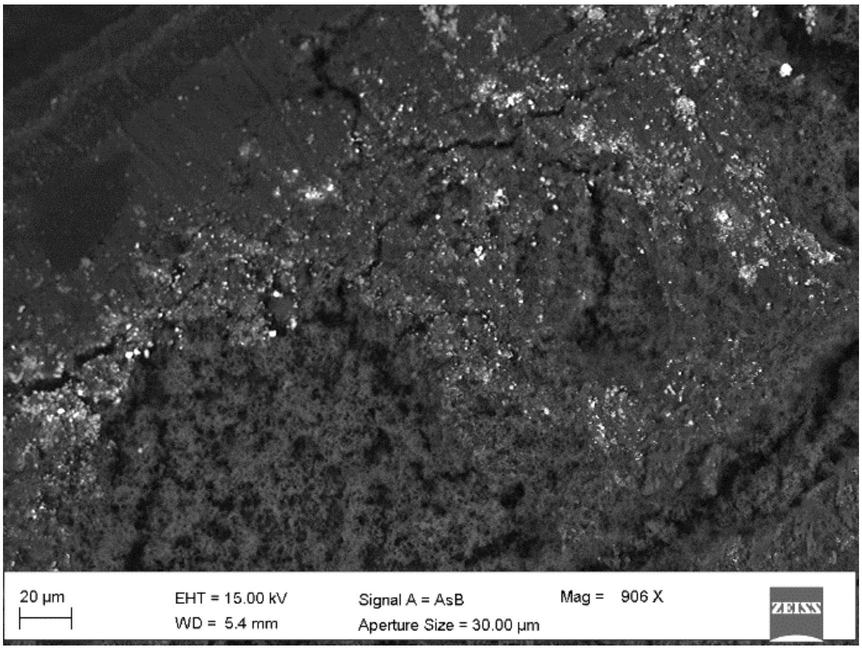

Fig. 9: Nanoparticles distribution over the surface of the PANI-Au/Fe_3O_4@Yne sample.

3.3.3 Electrochemical properties of single electrodes

CV curves of PANI, and PANI nanocomposite electrodes are shown in Fig. 10. In order to evaluate the scan rate-dependent performance of the samples, the CVs were performed in 0.5 M H_2SO_4 + 0.1 M $LiClO_4$ electrolyte solution at scan rates ranging from 5 mV s^{-1} to 50 mV s^{-1} at a fixed potential range from -0.2 to +0.89 V (*vs* SCE)[12,13]. The peak current rises along with scan rate increase hence demonstrating the high-power capability and reversibility of the material under examination. The redox peaks of PANI are due to the transformation during the Faradaic process of PANI from the half-doped emeraldine form to the fully-doped pernigraniline form[13].

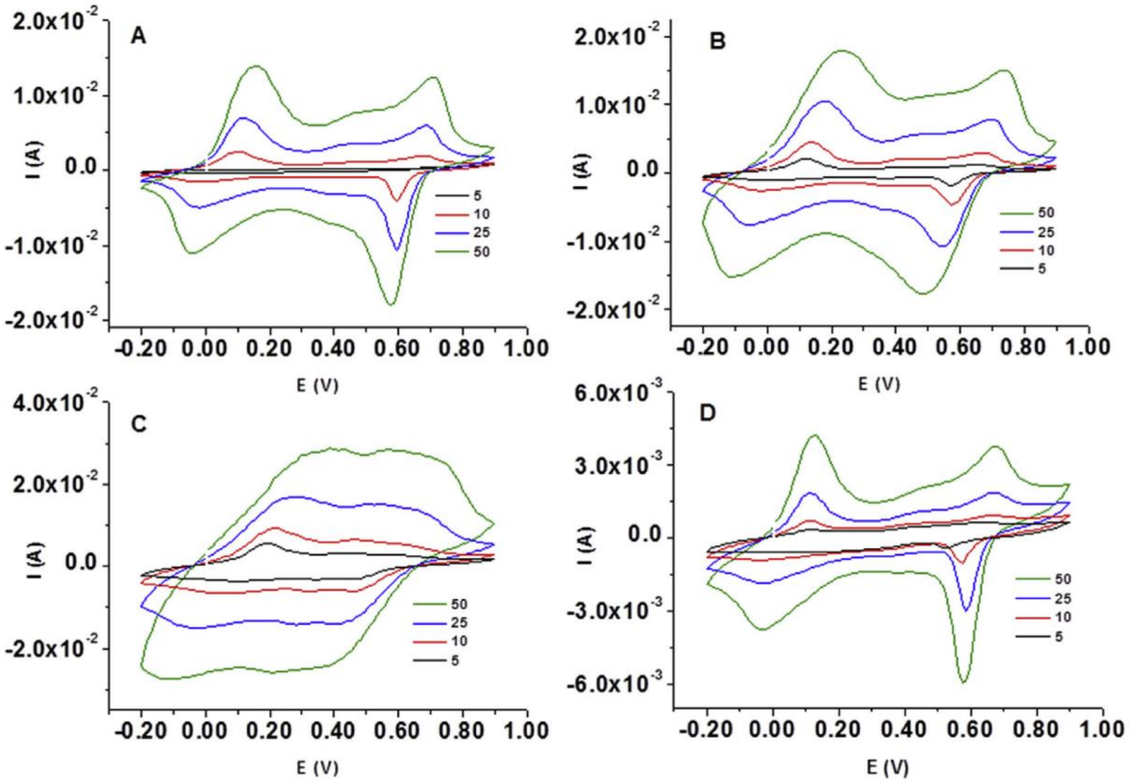

Fig. 10: CV curves at various scan rates of PANI (A), PANI/Fe_3O_4 (B), PANI-Au/Fe_3O_4 (C) and PANI-Au/Fe_3O_4 @Yne.

The higher current response observed for PANI-Fe_3O_4 (Fig. 10B) was exhaustively described by Prasankumar et al. and was explained with the coupling of two Faradaic reactions that occur at the electrode surface and enhance the electrode performance with respect of pristine PANI:

- the doping and de-doping that PANI experiences during the charge and discharge process and
- a preferential oxidation of Fe(II) to Fe(III) during the intake of electrolyte anions into the composite and their expulsion in the discharge step due to the reduction of Fe(III) back to Fe(II).

Overall, the lower resistance and better capacitance of the nanocomposite films depends on the strong interfacial interactions between PANI, magnetite and the support. About the gold-containing composites, the lower current response observed for PANI-Au/Fe_3O_4@Yne (Fig. 10D) compared to PANI-Au/Fe_3O_4 (Fig. 10C) can be explained with a lower Au/Fe_3O_4 ratio (shown in Table 3) and the presence of the organic functionalization; the enhanced capacitance performance shown by PANI-Au/Fe_3O_4 may be attributed to the synergistic effect of the three components. Indeed, the presence of AuNp increase the overall electrical conductivity of the composite electrodes[13].

Table 3: Amount of magnetite and gold.

Electrode	Fe_3O_4/PANI (wt%)	Au/PANI (wt%)	Au/Fe_3O_4 ratio
PANI	-	-	
PANI-Fe_3O_4	0.10	-	
PANI-Au/Fe_3O_4	0.16	0.020	0.125
PANI-Au/Fe_3O_4@Yne	0.26	0.026	0.100

The galvanostatic charge–discharge (CD) and electrochemical impedance spectroscopies (EIS) studies of PANI and PANI nanocomposites electrodes were performed in 0.5 M H_2SO_4 + 0.1 M $LiClO_4$ electrolyte. The specific capacitance of PANI and PANI nanocomposites were obtained by CD measurements performed at a constant current density of 0.5 mA cm^{-2} within the potential window 0.00 - 0.89 V *vs* SCE (Fig. 11).

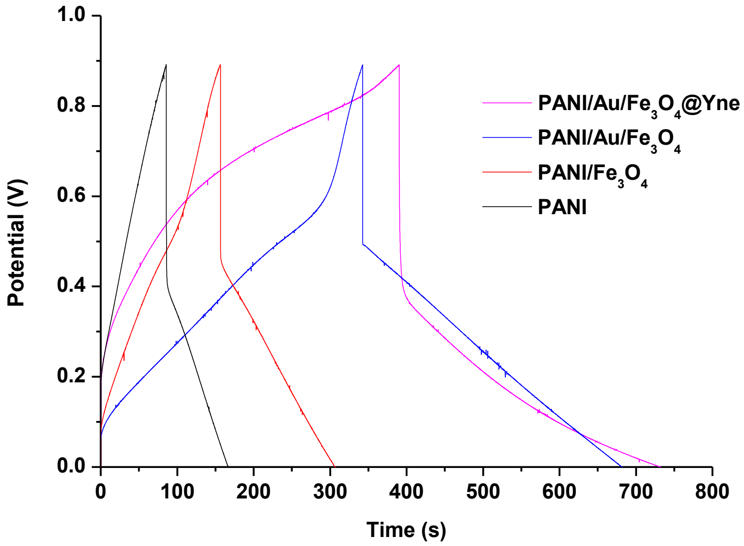

Fig. 11: CD curves of PANI and PANI nanocomposites in 0.5 M H_2SO_4 + 0.1 M $LiClO_4$

Nonlinear and asymmetrical charge-discharge curves resulting from redox reactions at the electrode/electrolyte interface are observed[13,27]. When the current reversed from charge to discharge an omhic drop (IR_{drop}) occurred due to internal resistance. As expected, the presence of AuNP reduce the internal resistance with regard to pristine PANI (IR_{drop} 0.395 V vs 0.439 V) but a higher value is obtained when Yne organic functionalization is present (IR_{drop} 0.500 V). In Table 4 are shown the energy efficiencies and areal capacities in terms of mC cm^{-2} or mAh cm^{-2} [34-36,40].

Table 4: areal capacity and energy efficiency (η)

Electrode	Areal capacity (mC cm^{-2})	Areal capacity (mAh cm^{-2})	η %
PANI	39.5	11.0	98
PANI-Fe_3O_4	73.5	20.4	98
PANI-Au/Fe_3O_4	164.0	45.6	97
PANI-Au/Fe_3O_4@Yne	167.5	46.5	98

In agreement with what observed in the CV studies, the areal capacity of the single electrode PANI increased after the addition of magnetite and these values become significantly higher in the presence of the magnetite modified with the high conductive AuNP[41,42].

EIS measurements were performed under open circuit potential (OCP) in the ac frequency range 1x10^5 and 1x10^{-2} Hz with an excitation signal of 10 mV [6,14,15,43].

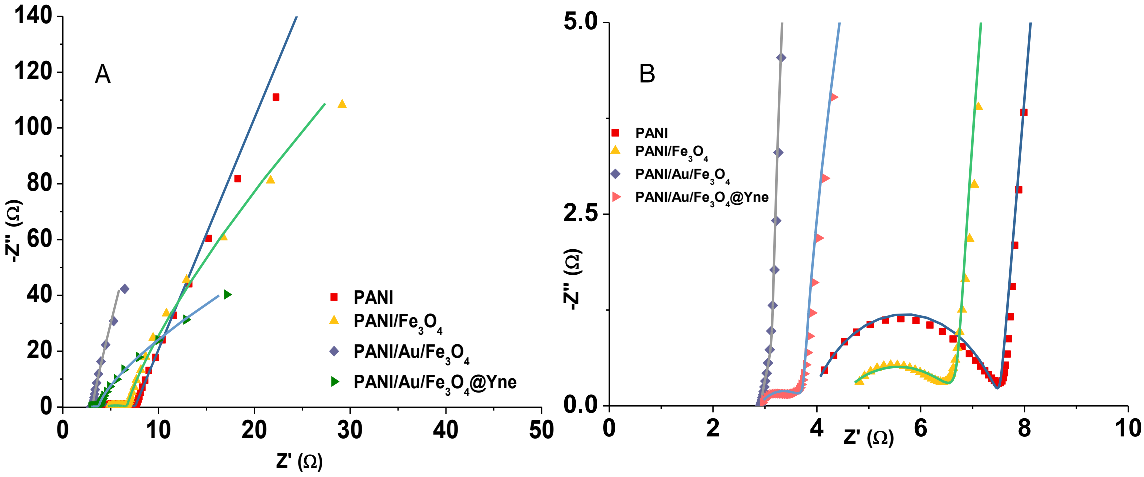

Fig. 12: Nyquist plots of PANI, PANI-Fe_3O_4, PANI-Au/ Fe_3O_4 and PANI-Au/ Fe_3O_4@Yne (A) and an enlargement (B).

The Nyquist plots reported in Fig. 12 display a depressed semi-circle at the high frequency region, whose diameter confirms the charge transfer resistance in the film, ending up to a quasi-vertical line in the low frequency region due to the pseudocapacitance impedance[12,13,19]. The smaller semicircles observed for all the PANI nanocomposites in the higher-frequency region compared to those found for PANI only, are due to the lower resistivity and higher diffusion of ions at the electrode-electrolyte interface during the electrochemical reaction (i.e. significantly lower interfacial charge-transfer resistance).

Moreover, for PANI-Au/Fe_3O_4 and PANI-Au/Fe_3O_4@Yne the slopes of the vertical lines in the low-frequency region Nyquist plot are ~70°, indicating the nearly ideal capacitive behavior of these nanocomposites[21].

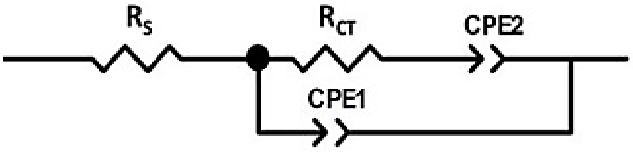

Scheme 2: equivalent circuit model obtained from EIS measurements

Scheme 2 shows the equivalent circuit model that simulates the capacitive and resistive elements of the electrodes. It consists of a solution resistance (R_S), a charge transfer resistance (R_{CT}) and two constant phase elements CPE1 and CPE2 employed considering the deviation from the ideal capacitor behavior (exponent n = 1)[5-11]. R_S is mainly arising from the electrolyte, the intrinsic resistance of the active material and the contact resistance at the active material current collector interface. R_{CT} represents the resistance at the electrode/electrolyte interface; CPE1 can be used to describe the double layer capacitance at the electrode/electrolyte interface (Cdl) and CPE2 the pseudocapacitance (Cp) in the film. The EIS results are reported in Table 5 and $\chi 2$ values of 1 10^{-4} obtained in all cases indicate good fitting procedures.

Table 5: EIS data

Electrode	R_S (Ω)	R_{CT} (Ω)	CPE1 (Ω^{-1} s^n)	CPE2 (Ω^{-1} s^n)
PANI	3.8	3.70	0.0002	0.085
PANI-Fe_3O_4	4.3	2.50	0.006	0.107
PANI-Au/Fe_3O_4	2.9	0.57	0.137	0.214
PANI-Au/Fe_3O_4*@Yne*	2.9	0.96	0.033	0.237

More specifically, R_S values are lower when AuNP are present; this behavior can be attributed to a decrease in the resistance of the materials, which is in good agreement with the CV and CD measurements. In PANI nanocomposite materials the lower R_{CT} values is due to a lower resistance and higher capacitive behavior[12]. The dramatic decrease of R_{CT} observed in the presence of AuNP can be explained with a more facile interfacial electron transfer process that improves their capacitive performance of the electrode[8,11]. In agreement with the results previously discussed, when the organic moiety Yne is present, the R_{CT} value slightly increases indicating the effect of this component on the electronic properties of the composite electrode. All the nanocomposite electrodes exhibit a CPE2 much higher than CPE1, suggesting a predominance of the pseudocapacitor contribution[5].

In consideration of the results discussed in the previous paragraphs, PANI-Au/Fe_3O_4 and PANI-Au/Fe_3O_4@Yne electrodes were chosen to prepare gel-state symmetric cells made of two identical electrodes separated from a polymeric gel electrolyte (based on 0.5 M H_2SO_4 + 0.1 M $LiClO_4$ and PMMA, Fig. 13)[1].

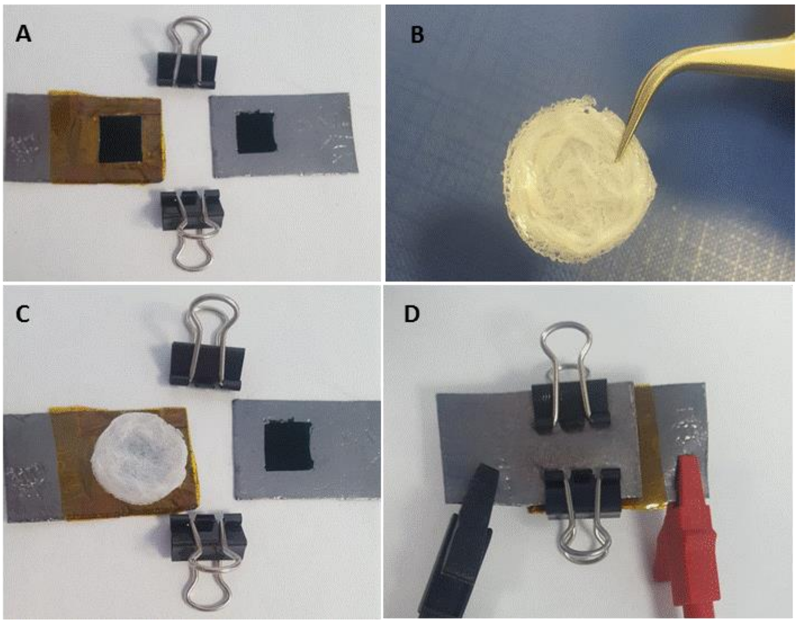

Fig. 13: Symmetrical solid state pseudocapacitor preparation: A) electrodes with active surface area of 1 cm^2 (A); gel electrolyte (B); assembly of the device and electrical connection (C and D).

The obtained devices were tested with CD analyses with a current density of 5.0 mA cm^{-2}, EIS analyses and stability tests were performed for 1000 cycles (Fig. 14). The areal capacities values obtained from CD analyses are equal to 360.0 mC cm^{-2} (100.0 mAh cm^{-2}) for PANI-Au/Fe_3O_4 and 265.0 mC cm^{-2} (73.6 mAh cm^{-2}) for PANI-Au/Fe_3O_4@Yne. Additionally, for the devices made of PANI-Au/Fe_3O_4 @Yne an higher IRdrop was found in line with the results obtained for the single electrodes. The EIS results show a CPE2 value of 0.196 Ω^{-1} s^n for PANI-Au/Fe_3O_4 and 0.137 Ω^{-1} s^n for PANI-Au/Fe_3O_4@Yne (Fig. 15). The highest areal capacity and stability obtained for the device based on PANI-Au/ Fe_3O_4@Yne electrodes were probably due to the good adhesion between gel-state electrolyte and electrodes surface. The presence of Yne induces an open microstructure on electrode surface (see SEM analyses Fig. 5D) that improves the gel-electrolyte penetration and finally enhances the charge storage mechanism.

Stability tests showed a drastic drop in the performances of both devices within 200 cycles that we mainly ascribed to the assembling method chosen for their fabrication that leads to a variation in the physicochemical properties of the gel electrolyte. Nevertheless, the device based on PANI-Au/Fe_3O_4@Yne was able to retain a 30% of the initial capacitance after 1000 cycles.

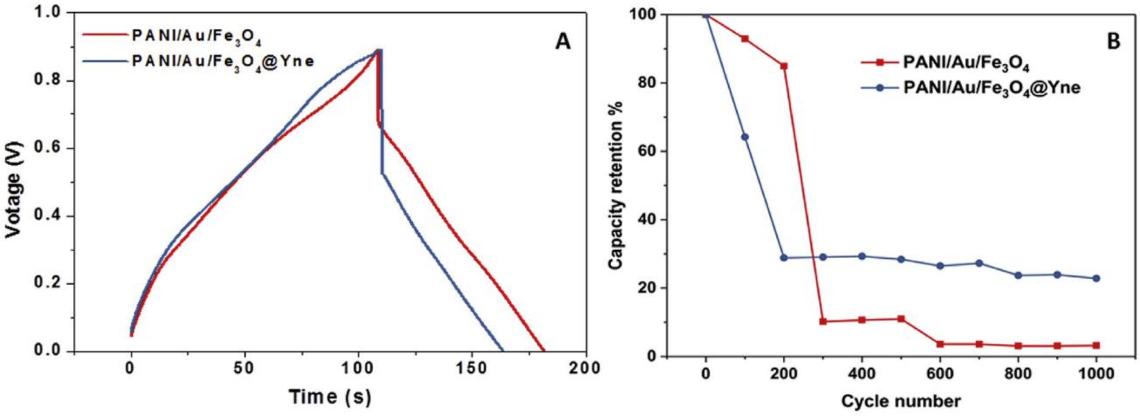

Fig. 14: CD curves at 5.0 mA cm^{-2} (A) and capacity retention behavior of the different devices at a current density of 5.0 mA cm^{-2} (B).

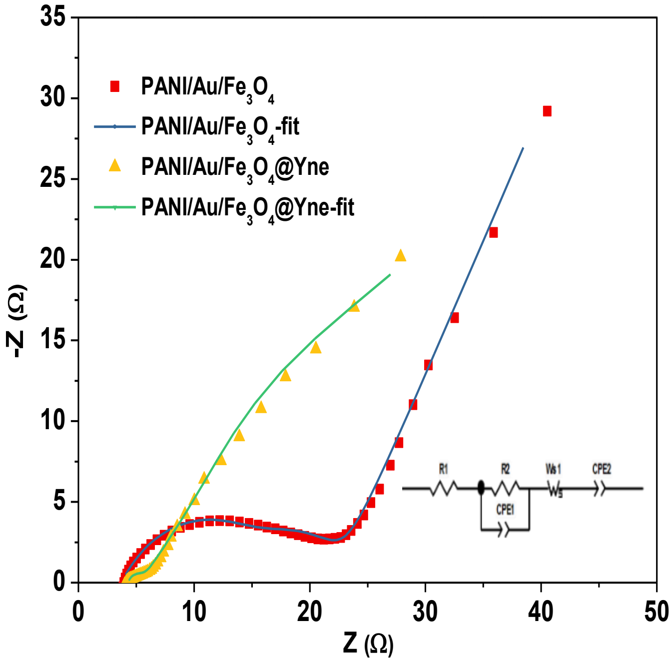

Fig. 15: Nyquist Plot of different devices in 0.5 M H_2SO_4 + 0.1 M $LiClO_4$ solutions and equivalent circuit[47]

Lastly, energy density (*E*) and power density (*P*) values were calculated for the gel-state symmetric devices from CD analyses: E equal to 9538 and 4533 mWh cm^{-3} (124 and 68 mWh cm^{-2}) and P equal to 131 and 85 mW cm^{-3} (1.70 and 1.28 mW cm^{-2}) were found for PANI/Au/Fe_3O_4 and PANI/Au/Fe_3O_4@Yne, respectively.

3.4 Conclusions

In summary flexible PANI nanocomposite-based electrodes and gel-state symmetric supercapacitors were fabricated. The electrochemical properties of the electrodes have been investigated. The PANI gold/magnetite nanocomposites were believed to possess a synergistic effect for improving the electrochemical performance; an areal capacitance around 340 mF cm^{-2}, resulting 3 times higher than the PANI value has been calculated. Moreover, the PANi/Au/Fe_3O_4 and PANi/Au/Fe_3O_4@Yne nanocomposite present favorable properties for assembling a gel-state symmetric supercapacitor.

3.5 Experimental section

3.5.1 Materials

Flexible graphite foil, GrF, (GRAFOIL GTJ, GRAFTECH International), used as current collector, was generously donated by VED company (https://www.ved.it). Electrodes of 4.0 x 2.0 cm dimension was obtained by cutting with scissors; a side of the graphite foil was treated with sandpaper (2000-2500) and then washed in ultrasonic bath for 3 min in water and then in methanol. Then a free conductive surface of 1.0 cm^2 was obtained by Teflon tape mask. Ultra-pure UPP water used during all synthesis was obtained with a Milli-Q plus system (Millipore Co., resistivity 18 MΩ·cm). Aniline (analytical grade) was purchased from Aldrich and used as received. The materials: Fe_3O_4 (d_{TEM} = 12±1 nm), Fe_3O_4@Yne (d_{TEM} = 12±2 nm), Au/Fe_3O_4 (Au d_{TEM} = 74±20 nm; Fe_3O_4 (d_{TEM} = 13±3 nm) and Au/Fe_3O_4@Yne (Au d_{TEM} = 15±3 nm; Fe_3O_4 d_{TEM} = 12±3 nm) were prepared following a recently reported protocol[28] summarized in Table 6.

Table 6: Parameters for the nanoparticles employed.

	Fe_3O_4 d_{TEM} (nm)	AuNPs d_{TEM} (nm)	Yne (wt%)	Au (wt%)
Fe_3O_4	12±1	---	---	---
Fe_3O_4@Yne	12±2	---	5	---
Au/Fe_3O_4	13±3	74±20	---	4.4±0.4
Au/Fe_3O_4@Yne	12±3	15±3	5	4.6±0.4

3.5.2 Preparation of PANI electrode

In a typical procedure, 0.5 M H_2SO_4 solution containing 0.1 M aniline and 0.1 M $LiClO_4$ was first degassed with N_2 for 10 min and then stirred for 20 min in an ultrasonic bath. The electrochemical synthesis of PANI on GrF was performed by potential cycling from -0.20 V to +0.89V *vs* SCE at potential sweep rate of 50 mV s^{-1} for 40 or 60 cycles[17-19].

3.5.3 Preparation of PANI-nanocomposite electrodes

The preparation of magnetic nanoparticles has been described in Chapter 2[31,48,49]. Electrosynthesis of nanocomposite electrodes were performed in the same conditions previously described. Briefly, depending on nanocomposite electrode prepared, 0.05 g of Fe_3O_4 or Au/Fe_3O_4 or Au/Fe_3O_4@Yne (in all the cases the concentration was equal to 2.0 g L^{-1}) were weighed and brought to volume with 25 mL of a previously prepared 0.1 M of aniline in 0.5 M H_2SO_4 + 0.1 M $LiClO_4$ solution. The suspension was placed in an ultrasonic bath for ca. 15 min to increase the oxide dispersion. The electrodeposition on GrF was carried out stirring the suspension with a glass-coated magnetic bar (0.5 cm) and cycling the potential from -0.20 V to +0.89 V *vs* SCE for 40 or 60 scans at v 50 mV s^{-1} [19]. The final electrodes were rinsed thoroughly with Milli-Q water and dried in air atmosphere.

3.5.4 Gel-state supercapacitor device fabrication

The final device was obtained with introduction of the gel electrolyte between the two electrodes and closed them with a metal clamp[33]. The gel-state electrolyte based on 0.5 M H_2SO_4 + 0.1 M $LiClO_4$ electrolyte and PMMA was prepared following a procedure previously reported[49,50]. In brief, a mixture of poly(methyl methacrylate) (PMMA, average MW 120000 g mol^{-1}, Sigma Aldrich) polyethylene glycol (PEG200, Merck) as plasticizers, propylene carbonate (PC 98 %, Sigma Aldrich) as ionic conductor was created using acetone as a solvent in order to simplify and accelerate the gelation process. The final composition of the dry gel was PMMA 25 wt %, PEG200 35 % and PC 40 wt %. After a complete components dissolution, the solvent was evaporated overnight and the obtained gel-electrolyte was applied for the preparation of the symmetrical supercapacitors.

3.5.5 Instruments and methods

TGA characterization was carried out using a Perkin Elmer TGA-7 instrument. In each analysis, 5–10 mg of the target sample was heated in a platinum crucible from room temperature to 900 °C, at a rate of 10 °C/min.

For the determination of the amount of Fe and Au in the electrode deposition, an Agilent Technologies 4210 Molecular Plasma – Atomic Emission Spectroscopy (MP-AES) instrument is used. For the best signal/noise ratio, two wavelengths for Au are chosen (242.795 nm, 267.595 nm) and three for Fe (373.486 nm, 385.991 nm and 371.993 nm). The samples for the analysis are prepared as follows: the 1.0 x 1.0 cm^{-2} deposited electrode section has been cut, weighted, and put into a 5 mL flask with 2 mL of HNO_3/HCl 1:3 and heated at 200 °C for 5 min. After cooling, the suspension was filtered and diluted to 5 mL. For the calibration curves, five standard solutions were prepared diluting a stock solution containing 100 ppm Fe and 4 ppm Au.

ATR-FTIR analysis was performed using a Perkin Elmer Spectrum Two spectrophotometer, equipped with a Universal ATR accessory, in the range 4000-400 cm^{-1}, with a resolution of 0.5 cm^{-1}. The electrodes were directly analyzed performing 40 scans for each analysis.

Scanning electron microscopy (SEM) observations were performed by a Zeiss Supra 40 field-emission SEM, equipped with a Bruker Z200 energy dispersive microanalysis (EDS) system for semi-quantitative chemical analysis. SEM observations have been carried out by secondary electrons (SE) to obtain topographic information and backscattered electrons (BSE) for compositional imaging. Furthermore, SEM cross sectional observations have been carried out to measure thickness of the deposited layer.

All electrochemical experiments were carried out on a potentiostat/galvanostat Autolab PGSTAT128 N (Metrohm-Autolab) controlled by NOVA 2.10 software. Electrochemical characterizations (cyclic voltammetry, galvanostatic charge/discharge curves end Electrochemical Impedance Spectroscopy) on single electrode were done in a three electrodes system where a bare or composite film modified graphite foil was used as the working electrode, a platinum wire as the auxiliary electrode and a saturated calomel electrode (SCE) as the reference electrode. The analyses were performed in a quiescent or stirring solution at room temperature, after nitrogen purging for 10 minutes. Aqueous 0.5 M H_2SO_4 + 0.1 M $LiClO_4$ were used as the electrolyte, whereas, in the case of the gel- state device, the PMMA-H_2SO_4 + $LiClO_4$ gel electrolyte was used.

Regarding the single electrodes, Cyclic voltammetry (CV) was conducted at sweep rates of 5, 10, 25, 50 and 100 mV s^{-1} to track the redox reactions of the deposited films and galvanostatic charge/discharge curves (CD) were carried out at 0.5 and 5.0 mA cm^{-2} between 0.00 and 0.89 V vs SCE to measure the capacitance of the deposited films. The specific capacity, C (C cm^{-2}, or if divided by 3.6, in mAh cm^{-2} units) can be calculated from the discharge curve of CD measurements:

$$\text{Specific capacity} = \frac{I\,\Delta t}{A}$$

where I is constant current (mA); Δt is discharge time (s); A is the effective area of the active materials (cm^{-2})[51,34,35].

The energy efficiency, η, can be calculated from the galvanostatic CD experiments as:

$$\eta = \frac{Qd}{Qc}\,100 = \frac{\Delta td}{\Delta tc}\,100$$

where Q_d and Q_c are the electric charges for discharging and charging (Coulomb), respectively. Δt_c and Δt_d are the times of charging and discharging (s), respectively.

The capacitances of the electrode materials were obtained from CD measurements, the volumetric capacitance (C_v, F m^{-3}) is expressed as[52-55]:

$$C_v = \frac{I\Delta t}{v\Delta V}$$

where I is the charge/discharge current (Ampere), Δt is the discharge time (s), m is the weight of the electrode material in the electrode layer (g), v is the volume of the deposited materials (cm^{-3}), ΔV (V) is the discharge branch of the voltage profiles avoiding the ohmic drop (IR_{drop})[59,60]. Alternatively an areal capacitance (C_{areal}, mF cm^{-2}) can be used[56]:

$$C_{areal} = \frac{I\Delta t}{A\Delta V}$$

where A is the areal of the electrode in cm^2.

Energy density (E in Wh cm^{-2} or Wh cm^{-3}, and power density (P in W cm^{-2} or W cm^{-3}) were calculated from equations[56]:

$$E = \frac{1}{2}\Delta V^2 C_{areal}$$

$$P = \frac{E}{\Delta t}$$

About symmetrical gel-state supercapacitors, CD analyses were done in the same conditions described before and pseudocapacitor cycle life was tested by measuring capacitance change over the course of 1000 charge–discharge cycles. Electrochemical impedance spectroscopy (EIS) studies were performed on both single electrodes and symmetrical devices in the frequency range of 100 kHz to 0.01 Hz with signal amplitude of 0.01 V.

References

1. B. Ballarin, E. Boanini, L. Montalto, P. Mengucci, D. Nanni, C. Parise, I. Ragazzini, D. Rinaldi, N. Sangiorgi, A. Sanson, M. C. Cassani, *Electrochim. Acta*, **2019**, 322, 134707.
2. G. Wang, L. Zhang, J. Zhang, *Chem. Soc. Rev.*, **2012**, 41, 797-828.
3. M. Zhi, C. Xiang, J. Li, M. Li, N. Wu, *Nanoscale*, **2013**, 5, 72-88.
4. C. Liu, F. Li, L.-P. Ma, H.-M. Cheng, *Adv. Mater.*, **2010**, 22, 28-62.
5. H. Wei, H. Gu, J. Guo, S. Wei, J. Liu, Z. Guo, *J. Phys. Chem. C*, **2013**, 117, 13000-13010.
6. A. Gonzalez, E. Goikolea, J. Andoni, R. Mysyk, *Technol. Mater.*, **2016**, 58, 1189-1206.
7. H. Wei, H. Gu, J. Guo, D. Cui, X. Yan, J. Liu, D. Cao, X. Wang, S. Wei, Z. Guo, *Adv. Compos. Hybrid Mater.*, **2017**, 10, 14-17.
8. R. Ramya, R. Sivasubramanian, M.V. Sangaranarayanan, *Electrochim. Acta*, **2013**, 101, 109-129.
9. M.V. Srivastava, S. K (Eds.), *Hybrid Nanomaterials: Advances in Energy, Environment, and Polymer Nanocomposites*, Wiley, **2017**.
10. V. D. Nithya, N. Sabari Arul, *J. Mater. Chem. A.*, **2016**, 4, 10767-10778.
11. S. Liu, S. Guo, S. Sun, X.-Z. You, *Nanoscale,* **2015**, 7, 4890-4893.
12. A. Mirmohseni, M.S.S. Dorraji, M.G. Hosseini, *Electrochim. Acta*, **2012**, 70, 182-192.
13. T. Prasankumar, B.R. Wiston, C.R. Gautam, R. Ilangovan, S.P. Jose, *J. Alloy. Comp.*, **2018**, 757, 466-475.

14. H. Fan, R. Niu, J. Duan, W. Liu, W. Shen, *ACS Appl. Mater. Interfaces*, **2016**, 8 19475-19483.

15. Q. Wang, L. Jiao, H. Du, Y. Wang, H. Yuan, *J. Power Sources*, **2014**, 245, 101-106.

16. L. Li, E. Liu, J. Li, Y. Yang, H. Shen, Z. Huang, X. Xiang, W. Li, *J. Power Sources*, **2010**, 195, 1516-1521.

17. M. Yang, B. Cheng, H. Song, X. Chen, *Electrochim. Acta*, **2010**, 55, 7021-7027.

18. H.H. Hsu, A. Khosrozadeh, B. Li, G. Luo, M. Xing, W. Zhong, A. Khosrozadeh, B. Li, G. Luo, M. Xing, W. Zhong, *ACS Sustain. Chem. Eng.*, **2019**, 7, 4766-477.

19. J. Arjomandi, J.Y. Lee, R. Movafagh, H. Moghanni-Bavil-Olyaei, M.H. Parvin, *J. Electroanal. Chem.*, **2018**, 810, 100-108.

20. A. Eftekhari, L. Li, Y. Yang, *J. Power Sources*, **2017**, 347, 86-107.

21. S. Mondal, U. Rana, S. Malik, *J. Phys. Chem. C*, **2017**, 121, 7573-7583.

22. T. Sen, S. Mishra, N.G. Shimpi, *RSC Adv.*, **2016**, 6, 42196-42222.

23. J. Arjomandi, N.K.I. Mossa, B. Jaleh, *J. Appl. Polym. Sci.*, **2015**, 132, 1-11.

24. H. Wang, J. Lin, Z.X. Shen, *J. Sci. Adv. Mater. Devices*., **2016**, 1, 225-255.

25. P. Khiew, M. Ho, D. Isa, T. Tan, W. Chiu, C. Chia, M. Hamid, R. Shamsudin, *Sains Malays.*, **2014**, 43, 885-894.

26. C. Janaky, A. Korm anyos, C. Visy, *J. Solid State Electrochem.*, **2011**, 15, 2351-2359.

27. M.M. Mezgebe, Z. Yan, G. Wei, S. Gong, F. Zhang, S. Guang, H. Xu, *Mater. Today Energy*, **2017**, 5, 164-172.

28. S.-Y. Wang, K.-C. Ho, S.-L. Kuo, N.-L. Wu, *J. Electrochem. Soc.*, **2006**, 153, 49-75.

29. A. Leon, M. Epifani, T. Chavez, J. Palma, R. Díaz, *Int. J. Electrochem. Sci*., **2014**, 9, 3837-3845.

30. H. Sayahi, M.A. Kiani, S.H. Kazemi, *J. Solid State Electrochem*., **2014**, 18, 535-543.

31. B. Ballarin, M.C. Cassani, D. Nanni, C. Parise, D. Barreca, G. Carraro, A. Riminucci, I. Bergenti, V. Morandi, A. Migliori, E. Boanini, *Ceram. Int.*, **2019**, 45, 449-456.

32. A.Q. Zhang, C.Q. Cui, J.Y. Lee, *Synth. Met*., **1995**, 72, 217-223.

33. Cheng, J. Pan, Y. Zhao, M. Liao, H. Peng, *Adv. Energy Mater*., **2018**, 8, 1702184.

34. T. Brousse, B. Daniel, J.W. Long, *J. Electrochem. Soc*., **2015**, 162, 5185-5189.

35. Y. Gogotsi, R.M. Penner, *ACS Nano*, **2018**, 12, 2081-2083.

36. B.E. Conway, *Electrochemical Supercapacitors: Scientific Fundamentals and Technology Applications,* Kluwer Accademy/Plenum Publishers, New-York, **1999**.

37. Y. Shao, M.F. El-kady, J. Sun, Y. Li, Q. Zhang, M. Zhu, H. Wang, B. Dunn, R.B. Kaner, *Chem. Rev*., **2018**, 118 9233-9280.

38. S. Rolda, D. Barreda, M. Granda, R. Mene, R. Santamarı, C. Blanco, *Phys. Chem. Chem. Phys*., **2015**, 17, 1084-1092.

39. M. Gvozdenovic, B. Jugovic, J. Stevanovic, B. Grgur, *Hem. Ind*., **2014**, 68, 673-684.

40. M. Khoobi, T. M. Delshad, M. Vosooghi, M. Alipour, H. Hamadi, E. Alipour, M.P. Hamedani, S.E. Sadat Ebrahimi, Z. Safaei, A. Foroumadi, A. Shafiee, *J. Magn. Magn. Mater*., **2015**, 375, 217–226.

41. A. M. Awwad, N.M. Salem, *J. Nanosci. Nanotechnol*., **2012**, 2, 208–213. doi:10.

42. X. Zeng, T. Ko, *Polymer*, **1998**, 39 1187–1195.

43. H. Gu, Y. Huang, X. Zhang, Q. Wang, J. Zhu, L. Shao, N. Haldolaarachchige, D.P. Young, S. Wei, Z. Guo, *Polymer,* **2012**, 53, 801–809.

44. T. K. Mahto, S. Chandra, C. Haldar, S. K. Sahu, *RSC Adv*., **2015**, 5, 47909–47919.

45. A. Mirmohseni, M. S. S. Dorraji, M. G. Hosseini, *Electrochim. Acta*., **2012**, 70, 182–192.

46. G. Wu, P. Tan, D. Wang, Z. Li, L. Peng, Y. Hu, C. Wang, *Nat. Publ. Gr*., **2017**, 1–8.

47. J. Ni, W.-J. Yu, L. He, H. Sun, Y. Cao, H.-Y. He, K.-N. Fan, *Green Chem*., **2009**, 11, 756–759.

48. X. Zhao, Y. Cai, T. Wang, Y. Shi, G. Jiang, *Anal. Chem*., **2008**, 80 9091–9096.

49. X. Cheng, J. Pan, Y. Zhao, M. Liao, H. Peng, *Adv. Energy Mater*., **2018**, 1702184, 1–16.

50. R. Bendoni, A. Barthélémy, N. Sangiorgi, A. Sangiorgi, A. Sanson, *J. Photoch. Photobio. A,* **2016**, 330, 8–14.

51. B. E. Conway, *Electrochemical supercapacitors*, Kluwer Academic /Plenum publisher NY, **1999**.

52. S. Mondal, U. Rana, S. Malik, *J. Phys. Chem. C,* **2017**, 121, 7573–7583.

53. K. Sharma, K. Pareek, *J. Energy Res*., **2019**, 43 604–611.

54. Y. Shao, M. F. El-kady, J. Sun, Y. Li, Q. Zhang, M. Zhu, H. Wang, B. Dunn, R. B. Kaner, *Chem. Rev*., **2018**, 118 9233–9280.

55. S. Rolda, D. Barreda, M. Granda, R. Mene, R. Santamarı, C. Blanco, *Phys. Chem.*

Chem. Phys., 2015, 17, 1084–1092.

56. Y. Horng, Y. Lu, Y. Hsu, C. Chen, L. Chen, K. Chen, *J. Power Sources*, **2010**, 195, 4418–4422.

4 Polyaniline-modified cellulose as electroactive material for a touch sensor

4.1 Aim of the chapter

A simple, inexpensive, and easily scalable industrial paper process to prepare sheets of conductive cellulose fibers coated with polyanilines is presented. First, bare fibers were coated by in situ oxidative polymerization of polyaniline then, the resulting composite fibers were used to fabricate electroactive sheets. The material was characterized from the chemical-physical and electrical point of view thanks to the use of different techniques such as ATR-FTIR, TGA, SEM, EDX and four probe tester.

The electronic properties of this composite material were investigated by assembling touch sensor devices with various geometries and in two different versions: the capacitive or resistive one. The tests carried out allowed us to choose the best shape and configuration in terms of response time and behaviour towards a pressure-stimuli. Moreover, a study about the performances of the material as sensor for monitoring the fermentation process of bread was conducted during a week stay ad ZHAW Zurich University of applied sciences.

Part of this work was published on Carbohydrate Polymers[1].

4.2 Introduction

In the current world, several daily life actions are eased by the presence of electrical devices but only 20 % of these appliances is correctly recycled. Many landfills continue to be stuffed with unwanted electronics and workers are exposed to hazardous and carcinogenic substances during informally recycling processes in developing countries. As new products are consumed by hungry customers wanting the latest and greatest technology, the sheer volume of these daily produced discarded materials makes this task apparently insurmountable (EU Report, 2020).

Research efforts are focused on the development of an alternative to traditional electronics that should be low-cost, degradable, compostable, and made from environmentally nontoxic substances. As a candidate, cellulose is one of the most investigated raw materials, mainly because of high abundance on Earth, biocompatibility, porosity, high flexibility and light-weight[2,3]. In addition, its low price (about 0.1 cent dm^{-2})[4] and its recyclability make cellulose an economically very viable option[5-7]. Despite its high surface resistivity at relative humidity of 20–40 % (typically 1011-1015 Ω sq^{-1})[4], it can be used as support to produce conductive paper that can be exploited in a wide range of applications, including supercapacitors, microfluidic systems, diagnostic devices, actuators and sensors[6,8,9].

Two different approaches to prepare conductive paper are described in literature. In the first one, organic or inorganic conductive, semiconductive and dielectric printable materials is deposited on paper employing screen, inkjet printing or flexographic techniques[3]. The second approach consists in embedding conductive materials such as functionalized multi-walled carbon nanotubes, inorganic nanoparticles and conducting polymers (CPs) in cellulose fibers making them conductive[10-19, 5, 2]. Conducting cellulosic fibers produced by coating with CPs (i.e. polyaniline (PANI), polypirrole (PPY), poly(3,4-ethylenedioxythiophene) (PEDOT) etc.) are being explored for various applications including supercapacitors, batteries, transistors, conductive wires, actuators and touch sensors[20,21,4].

In this scenario PANI is particularly interesting because of its low cost, easy preparation, good environmental stability and tuneable electrical properties by varying its oxidation state[4,22-24]. In situ polymerization is the most popular way of depositing PANI on cellulosic fibers. Different methods can be employed depending on the types of fiber, oxidants, medium, dopants, monomers, concentration used, processing steps and parameters [4,25, 21, 23].

The preparation of cellulose/PANI fibers (Cell/ PANI-F) is reported in which PANI, in the form of protonated conductive emeraldine salt, was obtained by a simple in situ oxidative polymerization of aniline on bare cellulose fibers in acidic media[21,25,26]. Successively, the fibers were assembled to give electroactive sheets (Cell/PANI-S) with different thickness and resistivity: 1.25 mm with a resistivity of 14 ± 1 Ω sq^{-1} (0.5 S cm^{-1}) or 0.4 mm with a resistivity of 237 ± 9 Ω sq^{-1} (0.1 S cm^{-1}). Finally, differently from those reported in the literature which are normally of resistive type[27,28], capacitive touch sensors (Cell/PANI-TS) with an optimized geometry were assembled. Both electroactive sheets and touch sensors were prepared using an industrially and easily scalable paper process provided by the industrial group Cromatos s.r.l.[29]. The capacitive touch sensors were finally interfaced with Arduino UNO developed board to investigate their dynamic response. All measurements have been conducted at room temperature and in natural environment humidity after that the Cell/PANI-S or the Cell/PANI-TS were kept in air at room temperature for 24 h.

4.2.1 Capacitive or resistive sensors

Despite mechanical devices, touch sensors do not contain moving parts, that allow them to be more durable, robust, and less subject to tear generated by dust[30]. Touch sensors could be divided into two categories: capacitive and resistive.

Capacitive touch sensors are widely used in most of the portable devices such as mobile phones, but they are present even in home appliances, automotive and industrial applications[31]. In this kind of devices, the electrode represents one of the plates of the capacitor. The second plate is represented by two elements: one is the environment of the sensor electrode which forms parasitic capacitor C1 and the other is a conductive object like a human finger which forms touch capacitor C2. A schematic representation of a capacitive touch sensor is shown in Fig. 1.

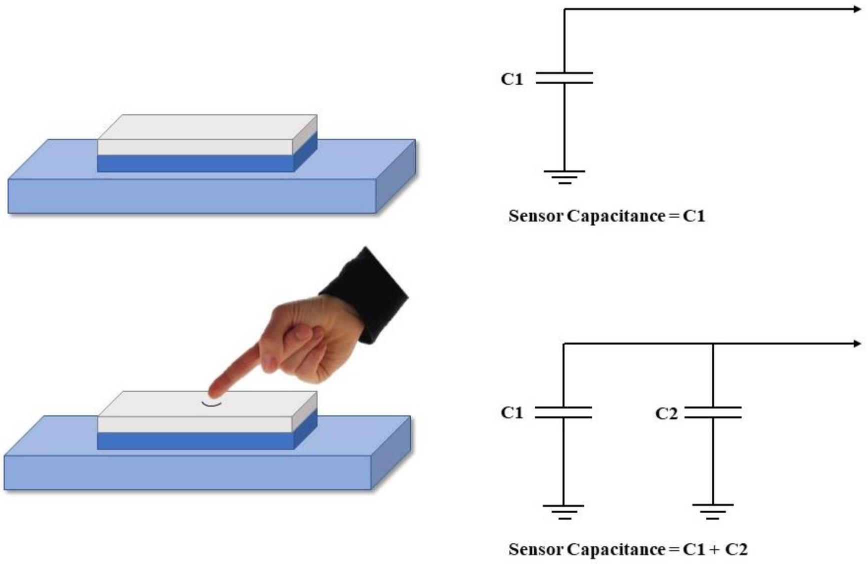

Fig. 1: schematic representation of a capacitive touch sensor

The sensor is connected to a measurement circuit and the capacitance is measured periodically. The output capacitance will increase if a conductive object touches or approaches the sensor electrode. The measurement circuit will detect the change in the capacitance and converts it into a trigger signal. The size of the sensors but also the covering material or the geometry will influence the sensitivity of the sensor.

Resistive touch sensors require an easier technology, because they are not dependent by the properties of capacitance. Thus, conductive materials (*i.e.* fingers) are not required to make the sensor works[32]. Simply, a conductive material is interposed between two connections and the variation of resistance between touched and untouched material is detected. The resistance of the material decreases if the distance between the connections is lower. A representation of a resistive touch sensor is given in Fig.2.

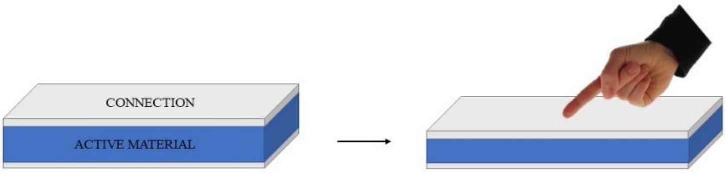

Fig. 2: a schematic representation of a resistive touch sensor

In summary, the main characteristics of the sensors are reported in Table1.

Table 1: advantages and disadvantages of capacitive and resistive sensors

	Advantages	**Disadvantages**
Capacitive	Excellent sensitivity	The size limits the accuracy
	Multi-touch capability	The price is higher
	Durable with glass front designs	Can’t be used with gloved hands or not sophisticated drivers
Resistive	Lower price	No availability for multi-touch
	Can be used with gloved hand or stylus	Not very sensitive
	Better for rugged environments	

4.3 Results and discussion

4.3.1 Characterization of PANI-modified cellulose fibers and sheets

The modification of bare cellulosic fibers with PANI was obtained via a simple in situ oxidative polymerization of aniline in acid media, as described in the experimental section. Firstly, fibers were characterized by SEM images. Pure Cell-F (Fig. 3A) displayed a very clean and smooth morphology, whereas the Cell/PANI-F displayed a relatively rough surface (Fig. 3B) due to the presence of PANI. The PANI layer showed a relative compact morphology and is homogeneously wrapped around the cellulose fibers with a thickness around 4.4 μm, as observable in Fig. 3C.

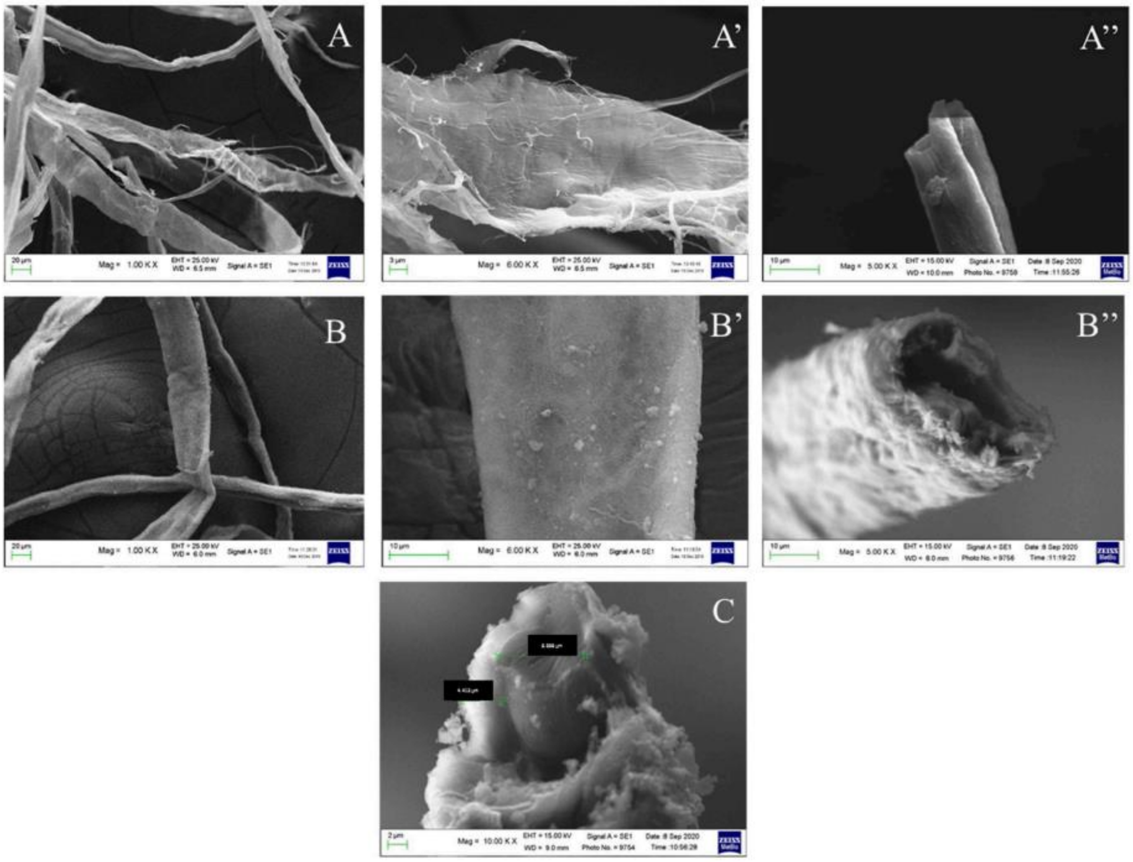

Fig. 3: SEM images of bare Cell-F (A, A’, A’’) and Cell/PANI-F (B, B’, B’’) at 1000X, 6000X and 5000X magnification, respectively; C) Cross-section of Cell/PANI-F at 10000X magnification.

SEM image and EDS element mappings of Cell/PANI-F sample are presented in Fig. 4. Within the elemental maps, the C signal originates from the cellulose fiber and PANI; O signal comes from cellulose fiber and the N signal, homogeneously distributed on the cellulose fibers, uniquely indicate the PANI regions.

The PANI average amount on cellulose fibers was measured using the Kjeldahl method after digestion of the Cell/PANI-F sample and resulted 22.3 wt%.

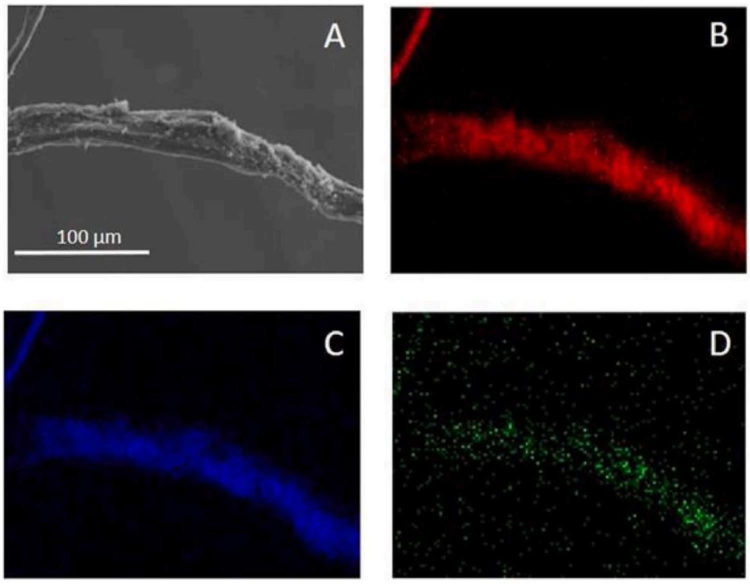

Fig. 4: SEM image (A) and EDS elemental map of CELL/PANI-F for Carbon (B), Oxygen (C) and Nitrogen (D).

The conductive sheets Cell/PANI-S were prepared from the Cell/ PANI-F, using a protocol commonly employed for colouring paper with acid dyes[33]. Briefly, a dispersion of 1:100 w/w in water (pH *ca.* 3.0 to maintain the polyaniline in the oxidized state, emeraldine salt) was drained on a flat sieve to obtain a sheet. With the help of a press, the half content of water was removed. Lastly, the sheets passed through a series of rollers at 100 °C to reach the complete dryness.

Depending on the quantity of fibres dried in the sieve, the thickness of the sheets could be varied. Sheets of 200 g for square meter (200 gsm) and a thickness of 0.40 mm were obtained. Alternatively, thicker sheets (1.25 mm; 630 gsm) were prepared in a similar fashion.

The ATR-FTIR spectrum of Cell/PANI-S (Fig. 5) shows all the characteristic peaks attributed to PANI: the stretching vibrations of benzoid N–B–N and quinoid N=Q=N structures show up at 1443 and 1564 cm^{-1}, separately. The absorption band at 1290 is ascribed to protonation of PANI. Bare cellulose shows the characteristic absorption peaks at ca. 3300 cm^{-1} attributed to the stretching of hydroxyl groups (− OH) and 2900 cm^{-1} attributed to the stretching of C–H groups; moreover, in the region of 1300 cm^{-1} the − OH bending and the C–O antisymmetric bridge stretching are present and the strong bands around 1000 cm^{-1} due to the C–O–C pyranose ring skeletal vibration are observed[34-36].

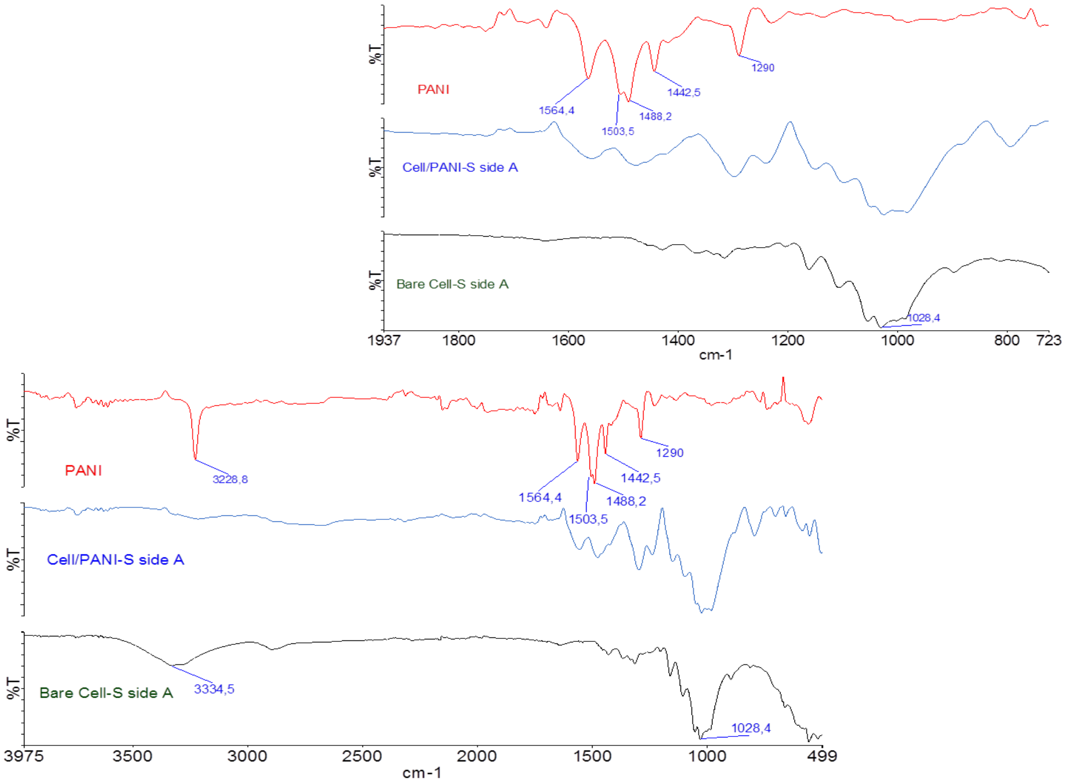

Fig. 5: ATR-FTIR spectra of bare Cellulose (black), PANI (red) and Cell/PANI-S (blue); inset: enlargement in the range 1900– 700 cm^{-1}.

4.3.2 Cell/PANI sheets electrical features

The Cell/PANI-S conductivity was evaluated by 4-line-probe measurements to avoid the contribution due to contact resistances. To evaluate the reproducibility of the influence of the environmental conditions during the real use, the electrical characterization was performed, for each thickness, at different times, on three different paper sheets at room temperature and balanced with the surrounding atmosphere. As expected, it was found that the conductivity of Cell/PANI-S depends on the sheet thickness being 0.105 ± 0.004 S cm^{-1} for a thickness of 0.40 mm and 0.56 ± 0.06 S cm^{-1} for a thickness of 1.25 mm; in the latter the value is only one order of magnitude lower than the highest values reported for pristine PANI. It is important to underline that the preparation method allows to obtain single cellulose fiber well covered with PANI which led to higher conductivity values (or similar, depending on the thickness) than those achievable by all the conductive papers presented in literature, as evident from the data reported in Table 2.

To clearly demonstrate the excellent conductivity of Cell/ PANI-S, two 1.25 mm thick paper sheets were successfully used as wires to transport the current necessary to power a LED with an applied voltage of 2.0 V (Fig. 6).

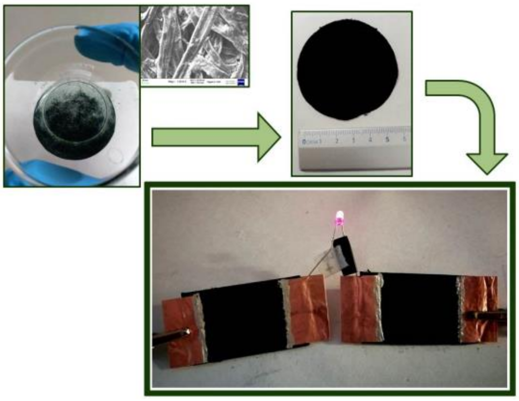

Fig. 6: Experimental setup with Cell/PANI-S (1.25 mm): preparation of sheets and connection with a LED.

Table 2: comparison of the conductivity of different samples based on PANI.

Material	Synthesis	Conductivity (S cm^{-1})
Cell/PANI-S[1]	In situ synthesis on the cellulose pulp (1.25 mm thickness)	$5.6 \pm 0.6\ 10^{-1}$
Cell/PANI-S[1]	In situ synthesis on the cellulose pulp (0.4 mm thickness)	$1.05 \pm 0.04\ 10^{-1}$
Rice pulp/PANI[37]	In situ synthesis on the cellulose pulp	$2.5\ 10^{-5}$
Pineapple fibers/PANI[38]	In situ synthesis on the cellulose pulp	$3.0\ 10^{-4}$
Cellulose pulp/PANI[39]	In situ synthesis on the cellulose pulp. Chemiometric optimization	$1.5\ 10^{-2}$
CA electrospun/PANI[40]	In situ polymerization onto electrospun cellulose membrane	$1.0\ 10^{-1}$
Cellulose/PANI[4]	Dispersed Cellulose + PANI	$4.7\ 10^{-8}$
Ink-jet printed PANI[41]	Ink composed by PANI nanoparticles	$4.0\ 10^{-4}$
Thin PANI film on filter paper[42]	In situ polymerizzation on masked paper sheet	$1.0\ 10^{-3}$
PANI bulk[43]		1-5

4.3.3 Capacitive Cell/PANI-TS assembling

Cell/PANI-TS was prepared by an industrial assembling method coupling a Cell/PANI-S (0.4 mm, 200 gsm) suitably cut with scissors in the required shape and a cellulose sheet (0.4 mm, 200 gsm), as described in the experimental section. By maintaining the composite under a 50 bars pressure for 10 s, a device with a thickness of 0.80 mm has been obtained as reported in Fig. 7. Dimensions and shape of the built circuit can be easily varied as reported in Fig. 8.

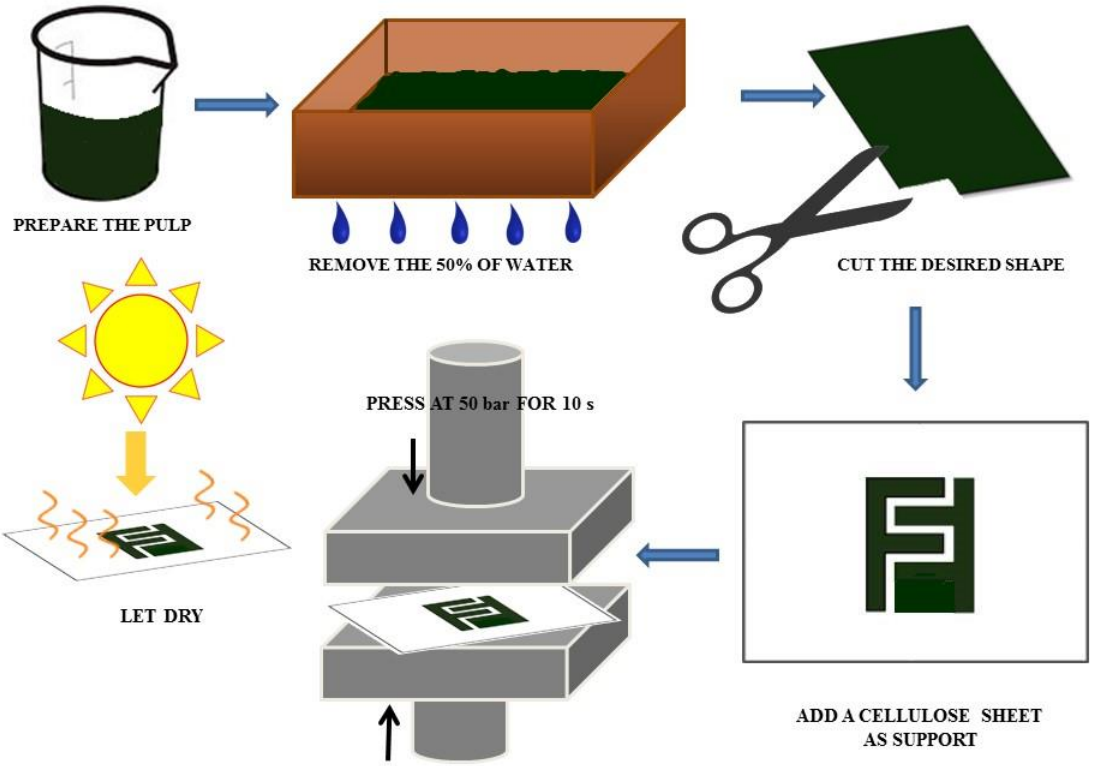

Fig. 7: sketch of fabrication process

Fig. 8: Different shapes for Cell/PANI-TS

The tensile strength of the Cell/PANI-TS has been measured and the resulting data compared with those obtained for Cell/PANI-S and bare Cell-S. The average value, obtained with three different samples, are: 11.5 ± 0.4 MPa, 1.2 ± 0.4 MPa and 5.0 ± 0.3 MPa, respectively.

4.3.4 Home-made setup for electrical measurements of the sensors and their performances

Home-made equipment for electric measurement of the capacitive sensors is reported in Fig. 9. It consists of three parts that are interconnected, controlled and managed by a program developed on the Arduino open-source platform:

1. a *Capacitance Meter* (*CM*), an electronic circuit capable of measuring the sensor capacity at each pressure increase;
2. a *Weight Force Generator* (*WFG*), a mechanical force-weight actuator capable of exerting a gradual and constant pressure on the sensor surface;
3. a *Weight Force Meter* (*WFM*), a force-weight meter necessary to measure in real time the pressure exerted on the sensor.

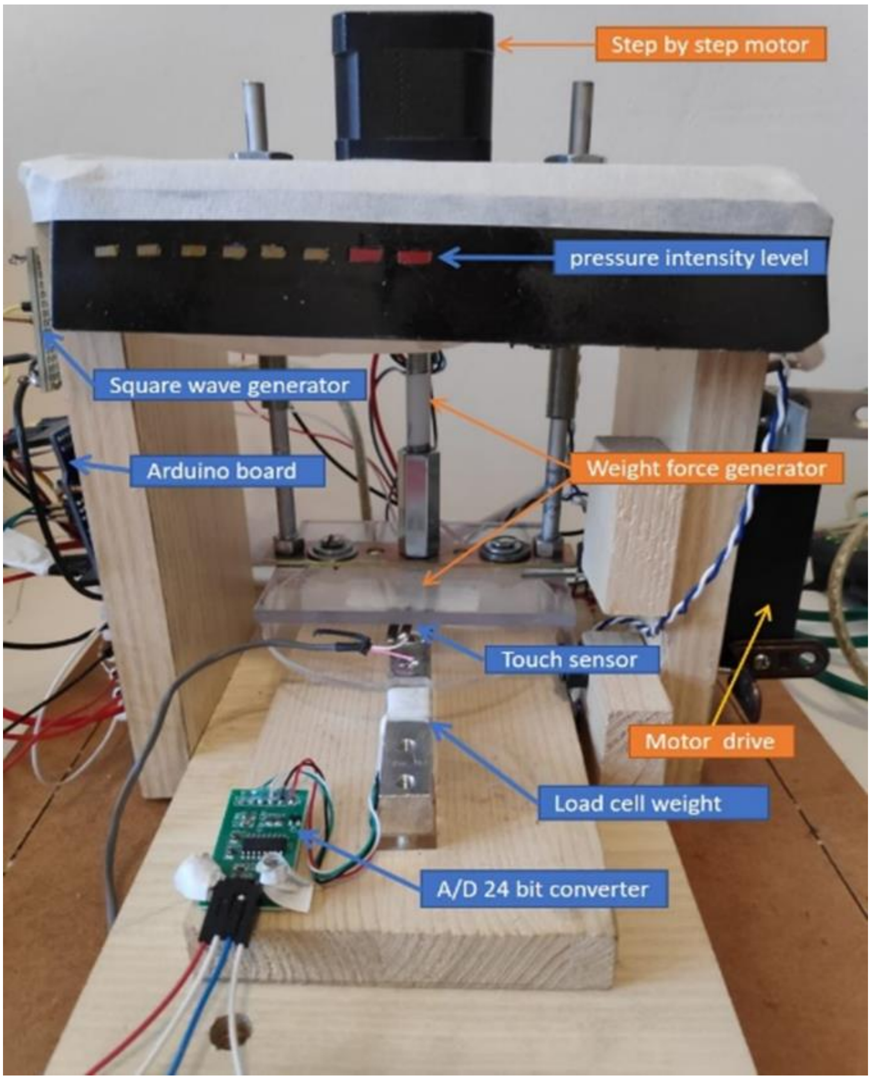

Fig. 9: home-made equipment for the sensor's electrical measurements

This home-made equipment allows to exercise and control the pressure given on the touch sensor with a step-by-step motor. The pressure was applied by keeping the position unchanged, and the whole area of the touch sensor was stimulated. Then the force-weight at each single advance step of the motor was measured and the capacity was recorded at the same time with Arduino UNO board.

Three Cell/PANI-TS samples with different geometries were tested (Fig. 8). For each, the capacitive component was measured without any touch interaction and during the dynamically induced increasing pressure up to a maximum value of 22 kPa (saturation level). The Cell/PANI-TS was excited by a square wave through the Weight Force Generator (WFG) while the out-put signal was observed with the oscilloscope and acquired with Arduino UNO development board. All three touch sensors have a starting capacity of about 93− 94 pF and different saturation capacity depending on the geometry employed, however an increase of 3–4 % of the initial value after pressure exertion is always obtained.

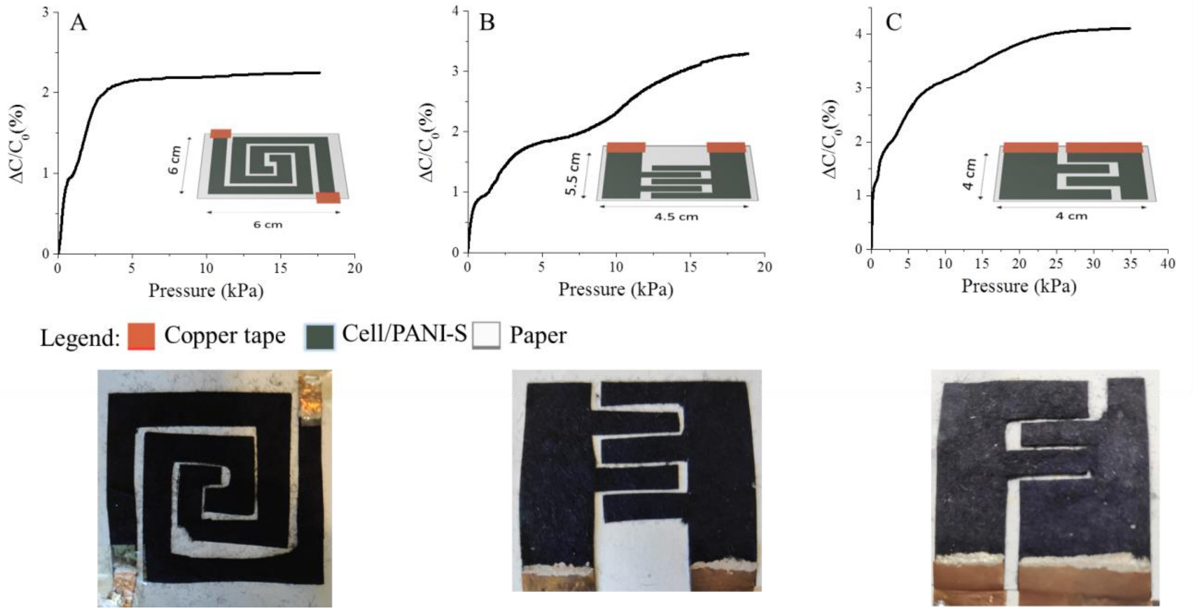

Fig. 10: Cell/PANI-TS with different geometries and related change of capacity with pressure curves. Shapes were chosen considering the highest surface area to be touched by the dielectric material.

Fig. 10 shows the results of the tests reporting $\Delta C/C_0$ % vs pressure, where ΔC is (C_P-C_0), C_P and C_0 correspond to the capacity with and without pressure[44]. From the data comparison, it can be observed that the geometry heavily affects the response.

A-type sensor shows two different linear trends with a sensitivity, defined by (C_P-C_0)/C_0/P where P is the used pressure[29, 17, 45], of 0.66 kPa^{-1} in a small pressure range (0–2 kPa) and 0.012 kPa^{-1} in a large pressure range (2–20 kPa) (Fig. 11).

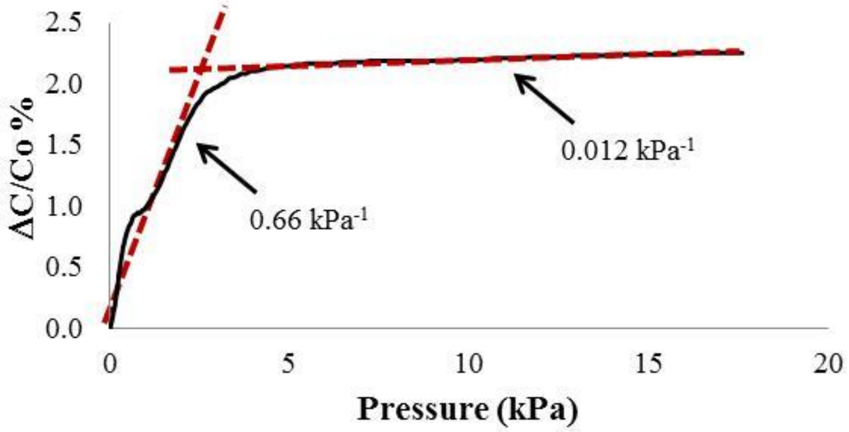

Fig. 11: Pressure response curve for A-type touch sensor.

On the contrary, the C-type sensor curve follows a logarithmic trend (Fig. 12) and shows sensitivities of 2.34 (0.45 σ%), 1.37 (0.44 σ%) and 0.19 (0.44 σ%) kPa^{-1} at pressures of 0.5, 2 and 20 kPa, respectively (average of five different measurements). Under each pressure both sensors display a good and stable response.

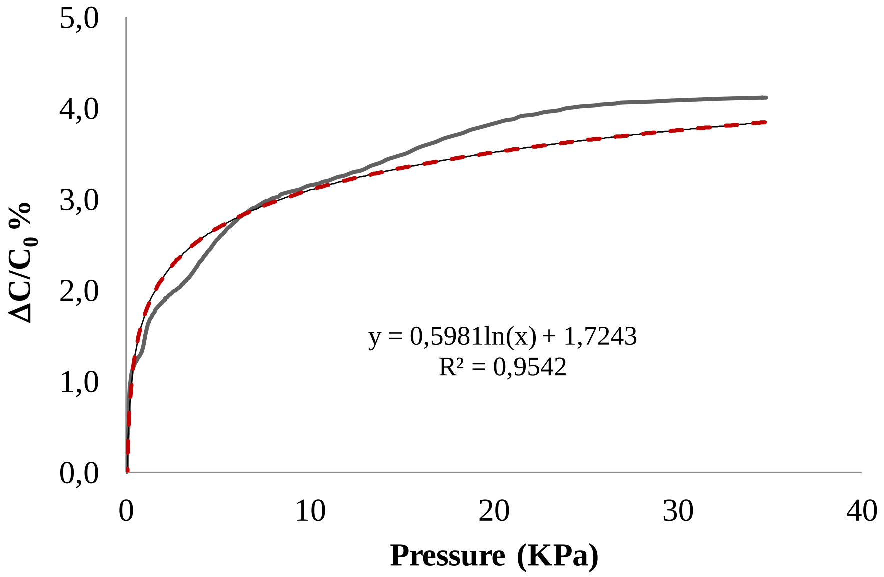

Fig. 12: Pressure response curve for C-type touch sensor.

Finally, B-type sensor present a different behaviour which cannot be traced back to a simple mathematical expression. Due to its logarithmic behaviour, we have chosen to carry out the repeatability and stability tests only on C-type sensors, recording, for each device, six independent $\Delta C/C_0$% vs pressure curves, at different periods. The results shown in Fig. 13, indicate a good reproducibility under all pressure range without a noticeable degradation of the performances. Finally, a pressure around 6 kPa was used to examine the sensors time response revealing a response time of 52 ± 1 ms.

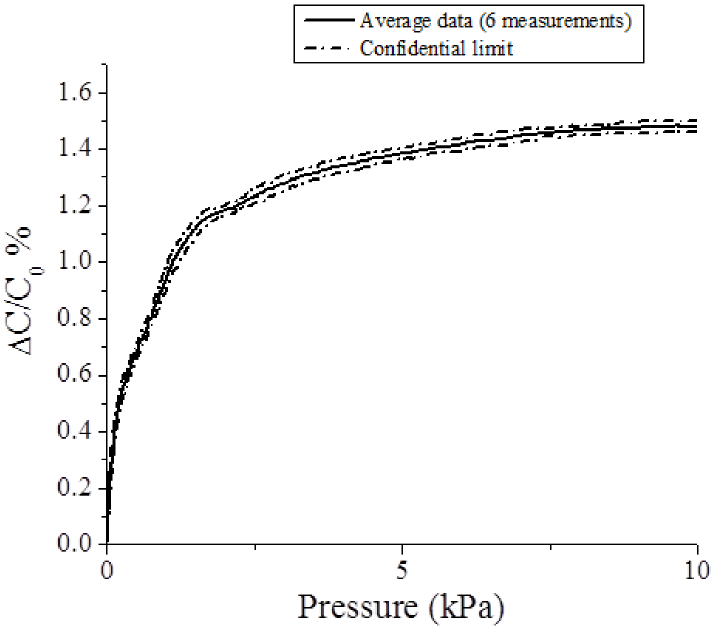

Fig. 13: Pressure response curve for C-type touch sensor obtained as average of six different measurements.

For what concerns resistive sensors, a simple test was performed connecting a sensor with the dimension of 1 cm^2 with an Arduino Uno board and putting and removing a weight of 50g on it. The setup of the system is shown in Fig. 14.

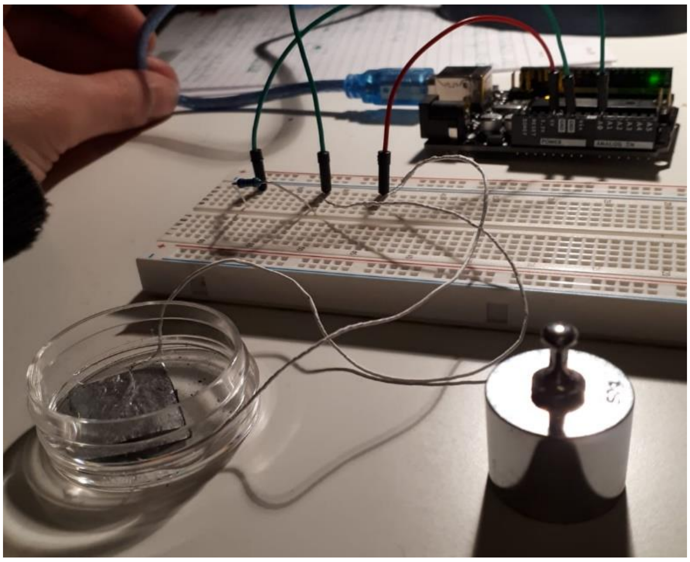

Fig. 14: setup for the resistive measurement

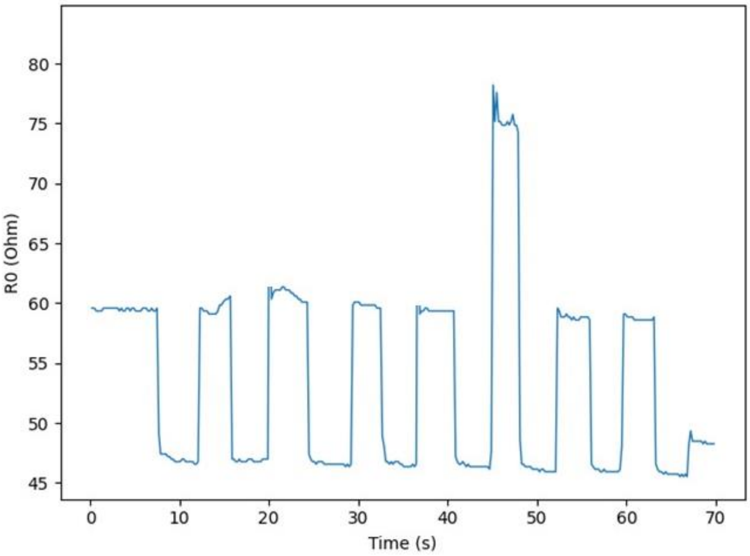

Fig. 15: response curve of the resistive sensor

As shown in Fig. 15, the sensor exhibited a good response time (50 ± 2 ms) and the repeatability, considering the home-made equipment used, is considerable.

4.4 Conclusions

An easily scalable industrial paper process was proposed to produce conductive paper sheets with excellent electrical performances as demonstrated by the success of their use in the fabrication of capacitive and resistive touch sensors. This method can provide an enormous improvement in the field of low-cost electronic technology. The electroactive sheets exhibit a conductivity around five times higher than those reported in literature for similar systems and can be employed to light a LED with an applied potential of 2.0 V, highlighting the outstanding electrical performances of these composite materials. The capacitive touch sensors show a very quick response time (52 ms), and a sensibility that can be easily modulated by changing the geometry of the device. Just few tests were performed on a resistive sensor made of the same material, but the response time is comparable with the capacitive one and the repeatability is promising.

4.5 Experimental section

4.5.1 Materials

All chemicals and solvents are ACS reagent grade, were purchased from commercial vendors and used directly unless otherwise stated. Sulfuric acid (H_2SO_4, 95.0–98.0 %), ammonium persulfate [$(NH_4)_2S_2O_8$), ≥ 98 %] and aniline (≥ 99 %), were purchased from Sigma-Aldrich (now Merck KGaA, Darmstadt, Germany); aniline was distilled under nitrogen prior to use. Citric acid (≥ 99.5 %) was purchased from VWR Chemicals (Vienna, Austria); a solution of ca. 25 wt% of $Al_2(SO_4)_3$ in water (commercial name FLOCLINE S8C) was purchased from Bio-Line s.r.l. (Milano, Italy). Bare cellulose fibers (pine tree long fiber with sulfate treatment) were kindly provided by Cromatos s.r.l. (Forlì, Italy).

4.5.2 Preparation of Cell/PANI-F

In a 1 L round bottom flask, 2.5 g of bare cellulose fibers were dispersed in demineralized water (250 mL) for 30 min; successively a solution made of 2.5 mL of aniline in 150 mL of 1.0 M citric acid ($C_6H_8O_7$) was added to the fiber suspension and stirred for 3 h at room temperature. In turn, the oxidative polymerization was carried out adding dropwise to the stirred suspension, previously cooled to 0 ◦C in an ice bath, a solution of 7 g of $(NH_4)_2S_2O_8$), dissolved in 200 mL of 1.0 M citric acid. After 24 h the coated fibers were filtered in a Buchner funnel and washed several times with 1.0 M citric acid solution. The conductive fibers were dried in air atmosphere for 24 h.

4.5.3 Preparation of Cell/PANI-S

In a typical procedure, 10 g of Cell/PANI-F were added to 1.0 L of an acid solution (ca. pH 3.0, 25 wt% $Al_2(SO_4)_3$ in demineralized water) and stirred for 5 min. The fibers were partially dried in a square sieve (21.0 cm x 14.8 cm size). The sheet was pressed at 50 bar pressure (P50 AXA manual hydraulic press) for 10 s to obtain the Cell/PANI-S (200 gsm, 0.40 mm thickness). Similarly, a 1.25 mm thick sheet was prepared by using 30 g of fibers.

4.5.4 Preparation of capacitive Cell/PANI-TS

The wet coupling method employed in the paper industry to produce sheets of paper with variable thicknesses or with greater resistance was used to prepare the Cell/PANI-TS samples. A Cell/PANI-S of 0.40 mm thickness was cut in the desired shape and coupled with a cellulose sheet (thickness 0.40 mm) moistened with water. The two sheets were then pressed (50 bar, 10 s) and dried at 80 ◦C for 10 min. The electrical connections were made afterwards with copper adhesive tape and silver glue.

4.5.5 Preparation of resistive Cell/PANI-TS

A Cell/PANI-S of 0.40 mm thickness was cut in a square shape of 1 cm^2. Upper and lower connections were made covering the surface of the active material with aluminium foil sticked with commercial glue for paper. Two copper wires were fixed on the aluminium foil using silver glue to form the connections for the Arduino board.

4.5.6 Instruments and methods

ATR-FTIR analyses were performed using a Perkin Elmer Spectrum Two spectrophotometer, equipped with a Universal ATR accessory, with a resolution of 0.5 cm^{-1} in the range 4000-400 cm^{-1}. The samples were directly analyzed performing 40 scans for any analysis.

The determination of PANI amount in Cell/PANI-F was performed with an automatic Kjeldahl Nitrogen Analyzer (Gerhardt Bonn). The Kjeldahl analysis was carried out on four Cell/PANI-F samples and a blank sample (cellulose bare fibre treated exactly as the Cell/PANI-F) using the following protocol: 1.0 g of each sample was put in a glass weighing flask and placed in a Kjeldahl test tube. A catalyst tablet (1 tablet contains 3.5 g of K_2SO_4 and 3.5 mg of Se) (Kjeldahl tablets, 1.18649 Supelco, Merck), 20 mL of concentrated H_2SO_4 (sulfuric acid 95–98 %, ACS reagent, 258105 Sigma-Aldrich) and 4 glass spheres were then added. The test tubes were heated to 350 °C for 5 h. The final solution must be clear and colourless. Finally, the test tubes were inserted in the Kjeldahl titration instrument and the potentiometric titration automatically start with 0.100 M HCl in presence of an acid basic indicator (a mixture of methyl red and bromocresol green).

SEM images were recorded at 25 kV with a Sem Zeiss EVO 50 EP equipped with Oxford INCA 350; EDS Spectrometer equipped with a Bruker Z200 energy dispersive microanalysis (EDX) system was used for semi-quantitative chemical analysis and mapping.

Tensile strength measurements have been carried out on a LBG UDI24Pro Instrument with a traction speed of 1 mm min^{-1}. The samples have been prepared following the TAPPI method reported in the literature[45] (Muchorski, 2006) by cutting the different sheets (cellulose, Cell/PANI-S and Cell/PANI-TS) into rectangles with a central size of 2 × 15 cm and 2.5 cm for each side for the crimping points.

Cell/PANI-S resistance was measured with a keysight B2902A source meter units in a 4-line-probe configuration by exploiting a home-made holder that is composed by 4 parallel copper electrodes on a glass slide (Fig. 16). The sample was prepared with a rectangular shape and was held down with an insulating material by exerting a uniform pressure on the whole surface. The inner electrodes measure the difference of potential while a constant current flow was forced between the two outer electrodes. The measurements were performed at different current values (100, 200, 300 µA) and a line passing from the origin was always obtained.

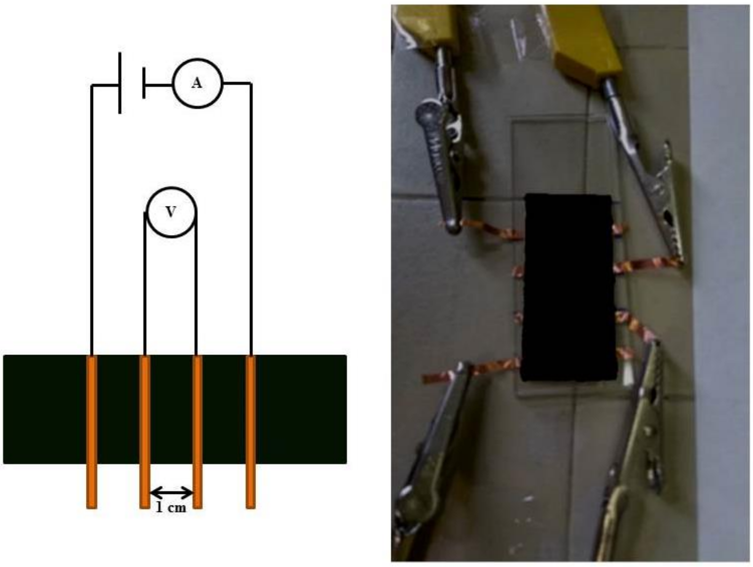

Fig. 16: Sample holder for Cell/PANI-S resistance measurements.

The resistance (R) was calculated with the Ohm's law and the sheet resistance ($R_{\blacksquare}$) is equal to:

$$R_{\blacksquare} = R\,\frac{W}{L}$$

Where W and L are the width and the length, respectively.

The specific resistance (ρ) can be calculated by:

$$\rho = R_{\blacksquare}\, t$$

Where t is the thickness. The specific conductance (κ) is calculated by:

$$\kappa = \frac{1}{\rho}$$

To standardize the measurements, a nitrile rubber (Buna-N, Perbunan - NBR) was chosen as dielectric material and was interposed between the pressure generator and the sensor. The sensor was housed in the appropriate seat apparatus and a force-weight was exerted with an increase step of 1.0 g (subsequently converted into Pascal) on the whole sensor surface and the capacity was recorded at the same time.

The *Capacitance Meter* (*CM*) (Fig. 17) was designed using a square wave generator (SQG)[47] connected to Arduino Digital Input board. SQG is an astable multivibrator designed using an Op-amplifier[48-50] (Scheme 1A).

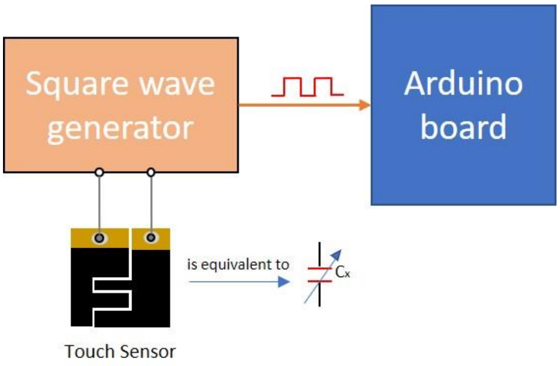

Fig. 17: Capacitance meter design.

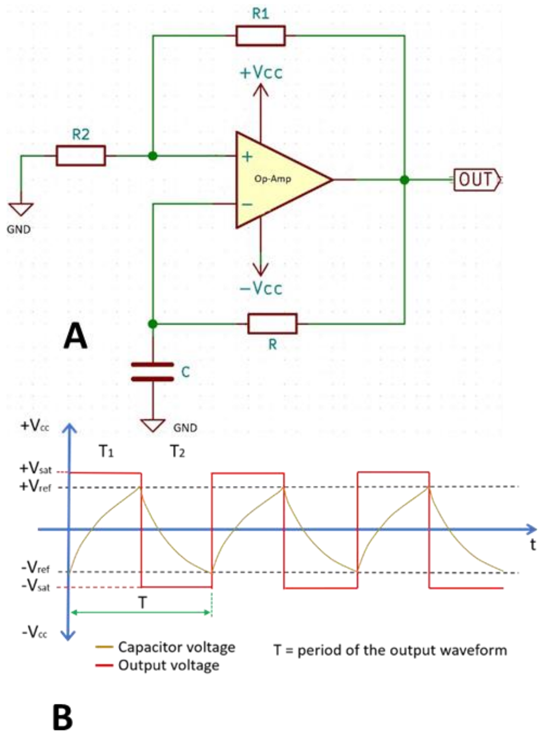

Scheme 1: A) Square Wave Generator: C = Capacitor (Farad); f = frequency (Hertz); R = Resistor (Ohm); R_1 and R_2 = determine the reference voltage (Ohm); +Vcc = positive supply voltage (V); **-**Vcc = negative voltage (V); GND = grounding. B) Theoretical value of RC charge, discharge and SWG signal.

The astable multivibrator circuit (Scheme 1A) works as an analogue comparator (Texas Instruments, 2003) that compares the voltages measured in the two inputs points with a reference value (V_{ref}) and gives a positive or negative output depending on the measured value is greater or lower than the reference one. The multivibrator output waveform period is determined by RC time constant of the two-timing components (T_1 and T_2 Figure S5B) and the feedback ratio established by R_1 and R_2 reference voltage[51]. The multivibrator output frequency (inverse of the period T) is inversely proportional of the charge and discharge time of the capacity C through the resistance R according to the equation:

$$f = \frac{1}{2RC \cdot l_n(1 + \frac{2R_1}{R_2})}$$

where C = Capacitor (Farad); f = frequency (Hertz); R = Resistor (Ohm); R_1 and R_2 determine the reference voltage (Ohm).

Finally, the SWG output is read by Arduino UNO which measures the frequency and calculates the corresponding sensor capacitance value by inverse of equation 1. Figure S6 shows as example the RC charge and discharge and SWG output measured by an oscilloscope.

The *weight force generator (WFG)* allows us to exercise and control the pressure given on the touch sensor and is shown in Scheme 2. It consists of a step by stepper motor, a power driver and a mechanical rotary-linear conversion system which, connected to a screw with step M8, allows for each revolution an advance of 1.25 mm. Since the motor performs 200 steps per revolution, each single step generates a linear feed of 6.25 µm. The WFG is controlled by Arduino board.

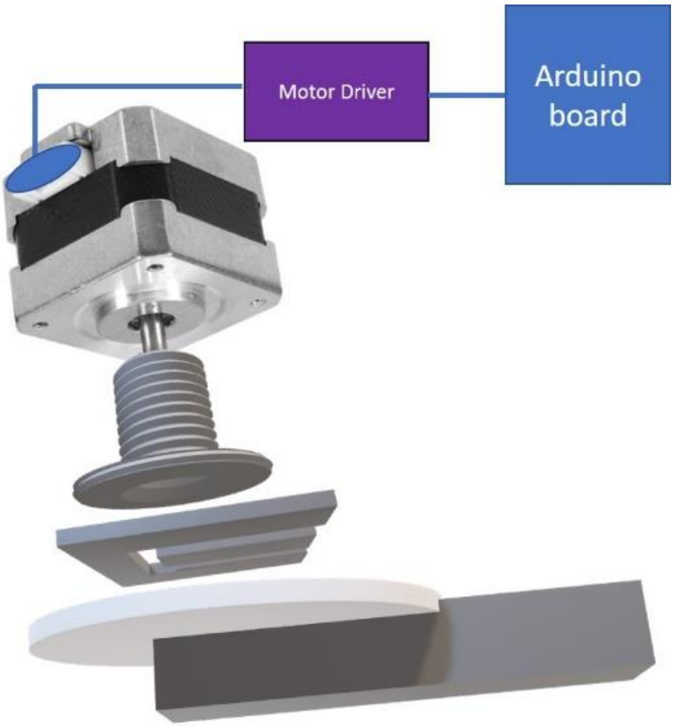

Scheme 7: Weight force generator

The *weight force meter (WFM)* (**Scheme 3**) consists of a Wheatstone bridge load cell connected to a 24-bit Analog/Digital converter via Arduino which measures the force-weight at each single advance step of the motor[52].

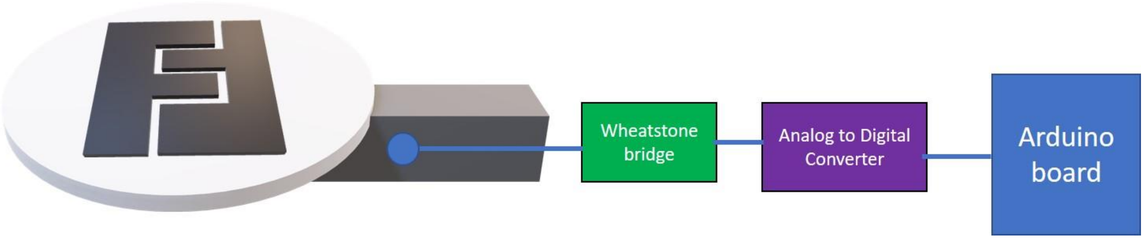

Scheme 8: Weight force meter.

The SEMMELI project: PANI, bread and breadboards

The work presented in this section represents the beginning of a project carried out in collaboration with prof. Marco Loschi, ZHAW (Zucher Hochsch fur Angewandte Wissenschaften) and and prof. Marco Mazza HEIA-FR (Haute Ecole d'Ingenierie et d'Architecture de Fribourg).

The aim of this collaboration is the monitoring of the fermentation process of Semmelies, characteristic Swiss little breads of a particular round shape. Nowadays, no monitoring is performed during the production, the amount of yeast and the temperature monitored during the fermentation process is enough to guarantee a bread with the desired characteristics. Sometimes perhaps, variation of environmental conditions causes mistakes in production and a huge quantity of bread must be discarded.

More generically, a dough of bread is a particular multiphase system composed by proteins, lipids, carbohydrates, water and air. Its ingredients and the processing conditions determine the macroscopic structure of baked products which, in turn, is responsible for their appearance, texture, taste and stability. To build up this structure, the ingredients are mixed and kneaded, the dough leavened and baked. Great structural changes take place during the bread making operations[53].

When ingredients are mixed, a three-dimensional network is formed giving the material viscoelastic properties. Afterwards, the metabolism of yeasts transforms carbohydrates into carbon dioxide and ethyl alcohol, that influence the interfacial tension within the dough. In addition, carbon dioxide, which partly dissolves in the aqueous phase of the dough, causes their growth.

It is important to distinguish between gas production and gas retention in fermented doughs[54]. The first factor is controlled by the yeast performance and the last one depends on the bubble characteristics. The desirable loaf volume of yeast-fermented products is achieved only if the dough provides a favourable environment for yeast growth and gas generation and, at the same time, possesses a gluten matrix capable of maximum gas retention[55].

Gas retention is most conveniently determined by measuring the volume increase of fermenting dough, whereas gas production can be estimated by any of the several available procedures such as the oven rise recorder[56], alveograph method and pressure meter methods[57]. Yeast-fermented doughs are difficult to study because they are very complex, and the dimensions and physical properties of the dough change with time[58]. Furthermore invasive, continuous measurements on dough are generally not adequate as they may provoke dough collapse. The choice of the most appropriate analytical procedure is thus crucial for the full comprehension of the underlying mechanisms of leavening.

As just underlined, he most apparent physical change related to the development of fermentation in the dough is the increase in its volume[59]. Although, an extensive the literature exists dealing with the control of the leavening process[60] and mathematical models and equations for expression of microbial growth in food[61].

However, a simple, inexpensive, and easy to be appliable in a large-scale production device to monitor the fermentation of Semmeli could simplify the optimization of the bread-making process. With this mind, a PANI modified cellulose sensor could be a valid candidate.

The industrial Semmeli’s preparation process consists in different steps outlined in detail in Scheme 4. Briefly, the flour is mixed with water and rest and left for 12 min. then, the dough is portioned into two bulk of 2 kg and a first fermentation is performed for about 20 minutes. Finally, the dough is portioned into the typical Semmeli shape of 70 g each and left to ferment in controlled atmosphere for 30 minutes. After this step, the breads are baked but this will not be subject of the study.

Scheme 4: principal steps of an industrial Semmeli’s preparation process

This first screening has also included the study about two different recipes with a different protein content as seen in Table 3. In fact, it is shown that varying the protein content of a dough, the rheological properties of the finished material will be different in terms of texture, elasticity, gas retention and roasting during the baking phase[62,63].

Bread with formula A was prepared as standard Semmeli recipe without addition of wheat gluten. In bread formula B, two percent of the wheat flour were substituted with wheat gluten, therefore increasing the overall protein content.

Table 3: description oft he two different recipes used

	Bread Formula A		**Bread Formula B**	
	[g]	**[bakers %]**	**[g]**	**[bakers %]**
Wheat flour, Typ 550 (Grüninger Mühlen, Flums, Switzerland, Lot: 7689)	2690	100	1614	80
Wheat gluten, 80 % protein (Pistor AG, Rothenburg, Switzerland)	-	-	1076	20

Water	1749	65	1749	65
Salt	54	2	54	2
Yeast, compressed (Hefe Schweiz AG, Stettfurt, Switzerland, Lot: L224)	108	4	108	4
Total	4600	171	4600	171

Investigating the sensor response also regarding the type of flour used could be interesting to add an in-line, easy and inexpensive characterization of the dough during the process. The measurements on the doughs were performed during three different steps of fermentation:

1. After the first portioning (called step BF, duration 20 minutes);
2. After the Semmeli's shape portioning (called step P, duration 30 minutes);
3. After the last fermentation until baking (called step AF, duration 5 minutes).

For each measurement, a dough of 70 g was taken and put on the sensor, one made of PANI-modified cellulose and another mad of Cu tape as reference.

In addition, a continuous measurement was performed taking 70 g of dough after the first portioning and leaving on sensors for all the time until baking (estimated time 55 minutes). Every batch measurement was repeated 7 times for reproducibility.

For what concerns the sensors, a 4-wire electrical impedance measurement was performed. The choice of the shape of the sensors was influenced by the kind of measurement to be conducted. As shown in Fig. 1, they were obtained simply cutting with scissors the sheets of PANI-modified cellulose. Stripes of the dimension of 5 mm x 100 mm were sticked with vinyl glue on an acetate sheet to have a non-conductive support. Sensors made of copper tape of the same dimensions and shape were formed as reference electrodes.

The 4-wires electrical impedance measurement was performed on dough samples of 70g *via* the EVAL-AD5940BIOZ Evaluation Board (Analog Devices Inc., Product Nbr.: EVAL-AD5940BIOZ). The evaluation board was connected to the Cu electrode and the PANI electrode following the schema on Fig. 18 (the signals name from the Eval board are F+, F-, S+, S-). For the measurements, four boards were used, two of them connected to the PANI electrodes, and two to the reference electrodes in Cu.

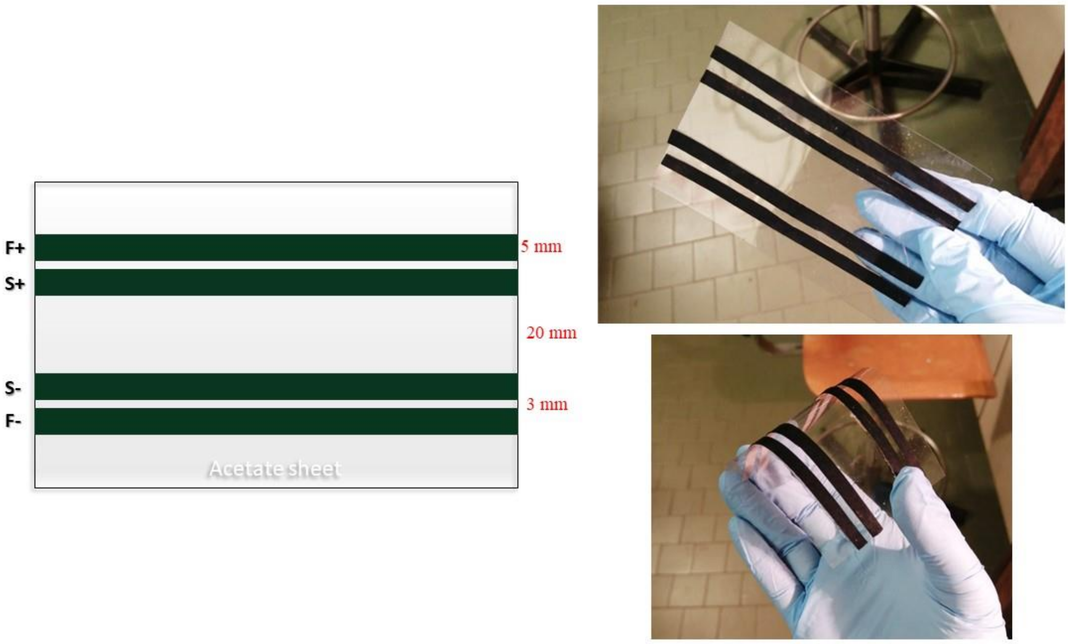

Fig. 18: the PANI-modified cellulose sensors on acetate support. On the right their foldability is showed.

During the setup of the system, it was noticed, that the magnitude of the impedance [Ohm] was too low for our system (the system we are using is set up to use an internal resistance R_{TIA} of 200 Ohm, that's the lowest R for the system without modification) as the value measured was lower than our R_{TIA} and therefore the system is not able to measure the impedance correctly. To solve this issue, a 1.5 kOhm resistor was added in series to raise the measured impedance magnitude as shown in Fig. 19. This added resistor will be then taken out in the data analysis part, to recuperate the real dough impedance value. The AD5940 will measure the current [A] and the voltage [V] on the dough and the software on the evaluation board will calculate the impedance magnitude [Ohm] based on the read values and the internal component of the chip itself (R_{TIA} resistor).

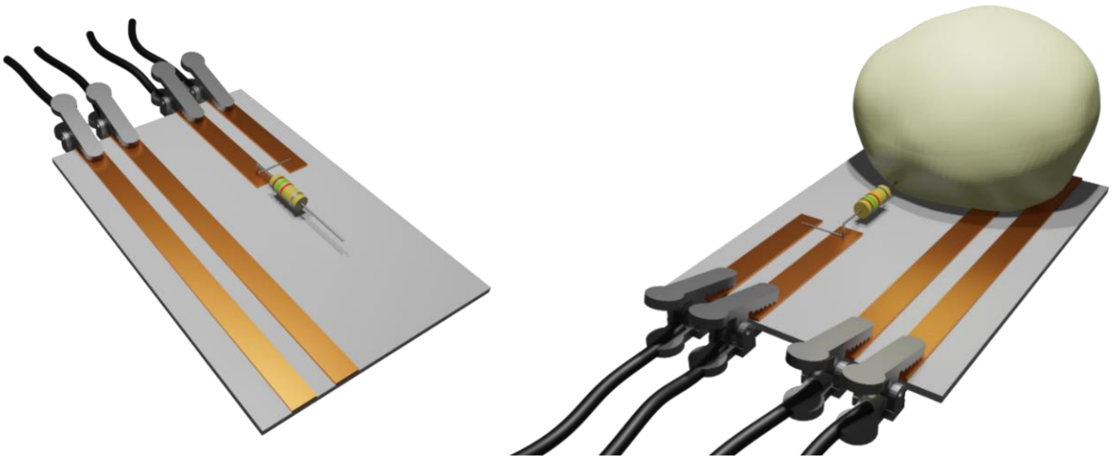

Fig. 19: schematic representation of a reference electrode with the additional resistance of 1.5 KΩ

The code was modified to allow to set how much time needed to pass between each measurement (in our case 10 s) and the frequency at which the measurement is made was changed from the default 50 kHz to 1 kHz. Moreover, to allow an easier recording of the data generated by the evaluation Board, a Python code (using Python 3.7) was created that read the serial signal sent by each card and saved it in a CSV file to be easily used later for the data analysis. Lastly, a computer with 4 USB ports (one for each evaluation board) or a USB-Hub with 4 ports it's needed to connect the four systems to the PC on which the python code for the recording of the data will run, visible in Fig. 20.

Fig. 20: setup of the breadboards and the pc connected

A typical response curve obtained changing the dough at every step of fermentation is given in Fig. 21. Spikes were obtained when the dough was removed and replaced with the new one to be measured. Each step was fitted whith an exponential curve (EXP.dec) and two main values were extrapolated:

1. The average of the impedance values in the linear part of the curve, when the signal was stable. This value of impedance could be related to the fermentation step;
2. The response time τ, that is the speed of decreasing of the exponential curve. It is an indication of what the sensor is measuring.

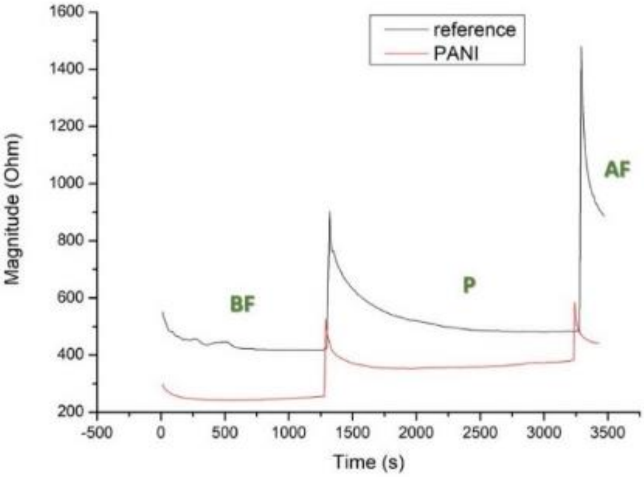

Fig. 21: a typical response curve of a discontinuous measurement

On the other hand, an example of continuous measurement is given in Fig. 22.

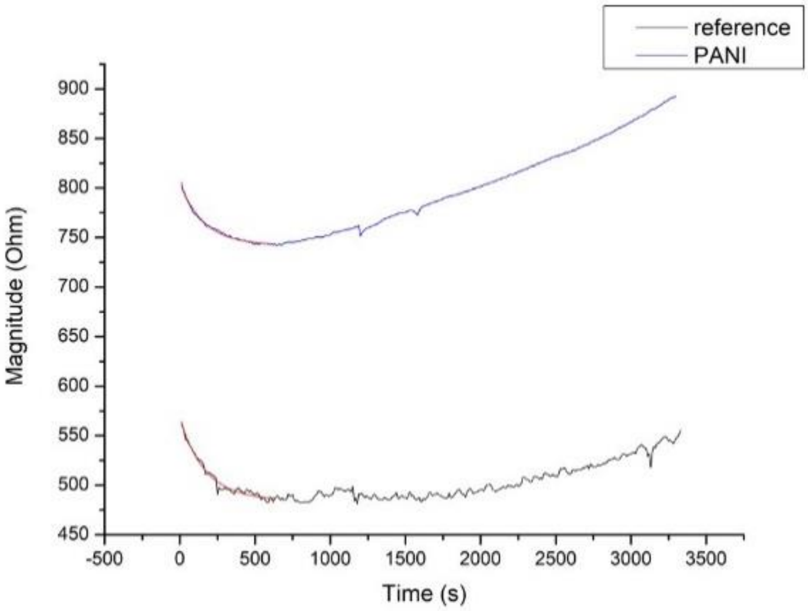

Fig. 22: a response curve of a continuous measurement

In this case, no spikes were observed because the dough was not changed. In addition, a drift in current was noticed both for the PANI-modified cellulose and the Cu-reference, suggesting that the sensors measured principally the change in humidity of the dough. Polyaniline could act not only as a conductive material, but it could be active for example as carbon dioxide sensor due to its simple cycle response through doping-dedoping[63-67]. In dough fermentation, CO_2 is produced by the metabolism of yeasts, so it is possible that the drift, accentuated for the PANI-modified cellulose sensor, is caused also by CO_2 sensing. More tests are intended to be performed about that topic.

The magnitude trend obtained for discontinuous measurements for recipe A (gluten free) is shown in Fig. 23.

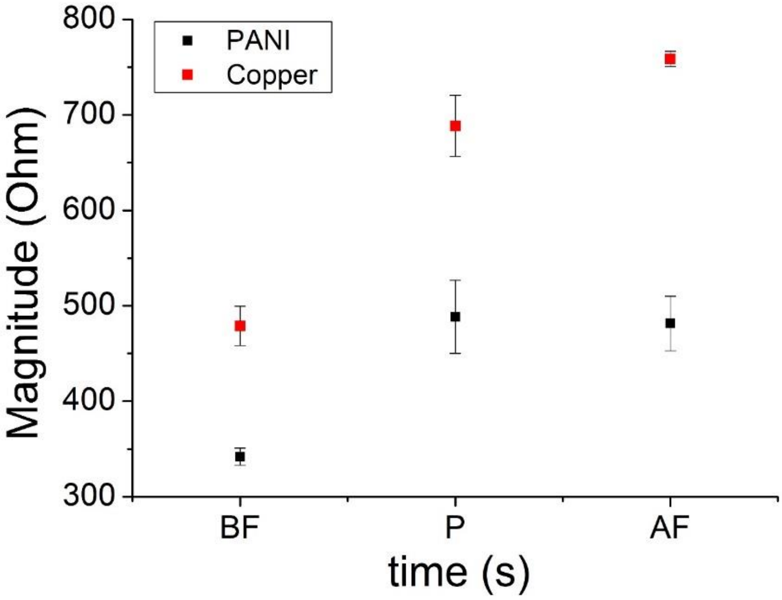

Fig. 23: magnitude trend for discontinuous measurements (recipe A)

For the first two steps, the response of the PANI-modified cellulose is comparable with the Cu-reference, while the third step was different. It is to be considered that the last steps lasts less than the others because measurements time are dictated by industrial procedures of making bread and not by the stabilization time of the sensors, this may cause more errors in the data treatment. Magnitude trends registered for recipe B (with gluten), result more comparable for PANI and Cu sensors, as observable in Fig. 24, but no substantial differences were observed between the two recipes.

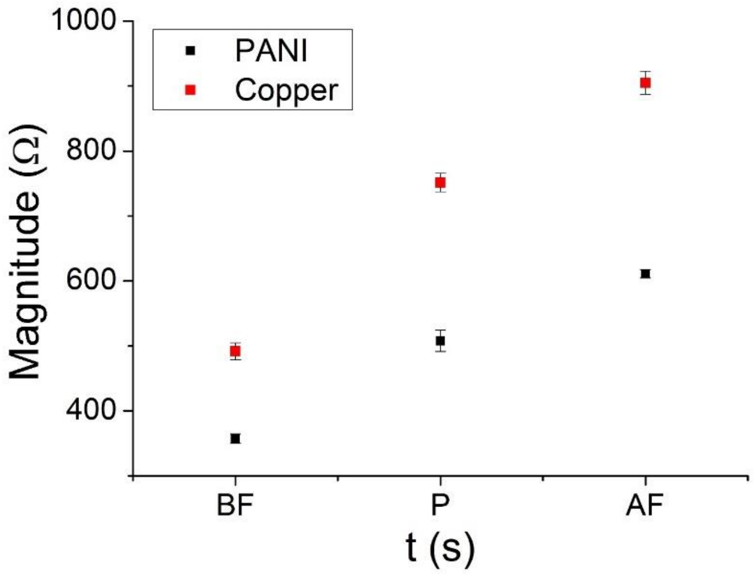

Fig. 24: magnitude trend for discontinuous measurements (recipe B)

Considering the response time τ for the discontinuous measurements, the results obtained are summarized in Table. 4.

Table 4: time responses for the discontinuous measurement

Recipe A	**reference**	**PANI**
τ_1	468 ± 305	148 ± 114
τ_2	425 ± 265	68 ± 25
τ_3	66 ± 49	41 ± 9
Recipe B		
τ_1	403 ± 116	216 ± 143
τ_2	333 ± 145	106 ± 77
τ_3	57 ± 23	45 ± 19

Preliminary results show a correlation between the fermentation step and the impedance value was present; nevertheless, the variation of the data registered was too high and a better setup of the system was certainly needed. Moreover, the results obtained with continuous measurements (not reported) shown a high variability suggesting the need of more investigation on a topic that remains still very interesting for a possible application.

References

1. I. Ragazzini, I. Gualandi, S. Selli, C. Polizzi, M. C. Cassani, D. Nanni, F. Gambassi, F. Tarterini, D. Tonelli, E. Scavetta, B. Ballarin, *Carbohydr. Polym*., **2021**, 254 117304.
2. A. Khan, Z. Abas, H. S. Kim, J. Kim, *Sensors*, **2016**, 16, 1-30.
3. Y. Luo, J. Huang, *Sci. China Chem*., **2014**, 57, 1672–1682.
4. D. Tobjork, R. Osterbacka, *Adv. Mat*., **2011**, 23, 1935–1961.
5. A. John, S. K. Mahadeva, J. Kim, *Smart Mater. Struct*., **2010**, 19.
6. S. Kanaparthi, S. Badhulika, *Sens. Actuators B Chem*., **2017**, 242, 857–864.
7. Y. Tian, K. Qu, X. Zeng, *Sens. Actuators B Chem*., **2017**, 249, 423–430.
8. N. D. Sanandiya, Y. Vijay, M. Dimopoulou, S. Dritsas, J. G. Fernandez, *Sci. Rep*., **2018**, 8, 1–8.
9. Q. Wang, J. Sun, Q. Yao, C. Ji, J. Liu, Q. Zhu, *Cellulose*, **2018**, 25, 4275–4301.
10. P. Das, V. C. Mai, H. Duan, *ACS Appl. Polym. Mater*., **2019**, 1, 1505–1513.
11. Y. Gu, J. Huang, *Colloids Surf. A Physicochem. Eng. Asp*., **2013**, 433, 166–172.
12. Z. Pang, Z. Yang, Y. Chen, J. Zhang, Q. Wang, F. Huang, Q. Wei, *Colloids Surf. A Physicochem. Eng. Asp*., **2016**, 494, 248–255.
13. E. Rafatmah, B. Hemmateenejad, *Sens. Actuators B Chem*., **2020**, 304, 127335.
14. L. E. Silva, P. I. Cunha Claro, R. C. Sanfelice, M. Guimaraes, J. E. de Oliveira, J. C. Ugucioni, G. H. Denzin Tonoli, *Cellul. Chem. Technol*., **2019**, 53, 775–786.

15. K. Sharma, K. Pareek, R. Rohan, P. Kumar, *Int. J. Energy Res.*, **2019**, 43, 604–611.

16. H. Yan, Y. Guo, S. Lai, X. Sun, Z. Niu, P. Wan, *ChemistrySelect*, **2016**, 1, 2816–2820.

17. X. Zang, Y. Jiang, X. Wang, J. Ji, M. Xue, *Sens. Actuators B Chem.*, **2018**, 273, 1195–1201.

18. W. Zhang, Z. Wu, J. Hu, Y. Cao, J. Guo, M. Long, D. Jia, *Sens. Actuators B Chem.*, **2019**, 127233.

19. Y. Zhang, Z. Yang, Y. Yu, B. Wen, Y. Liu, M. Qiu, *ACS Appl. Polym. Mat.*, **2019**, 1, 737–745.

20. R. Aguado, D. Murtinho, A. J. M. Valente, *Nord. Pulp Paper Res. J.*, **2019**, 34, 395–416.

21. Z. Ma, W. Wang, D. Yu, *J. Mater. Sci.*, **2020**, 55, 796–805.

22. N. Shoaie, M. Daneshpour, M. Azimzadeh, S. Mahshid, S. M. Khoshfetrat, F. Jahanpeyma, M. Foruzandeh, *Mikrochim. Acta*, **2019**, 186.

23. P. Singh, S. K. Shukla, *J. Mater. Sci.*, **2020**, 55, 1331–1365.

24. Y. Wang, A. Liu, Y. Han, T. Li, T. *Polym. Intern.*, **2019**, 5907.

25. S. Ke, T. Ouyang, K. Zhang, Y. Nong, Y. Mo, Q. Mo, F. Cheng, *Macromol. Mater. Eng.*, **2019**, 304, 1–10.

26. A. Masood, Z. Shoukat, Z. Yousaf, M. Sana, M. Faisal Iqbal, A. R. Rehman, A. Razaq, *J. Appl. Polym. Sci.*, **2019**, 136, 1–6.

27. Q. Shao, Z. Niu, M. Hirtz, L. Jiang, Y. Liu, Z. Wang, X. Chen, *Small*, **2014**, 10, 1466–1472.

28. L. Q. Tao, K. N. Zhang, H. Tian, Y. Liu, D. Y. Wang, Y. Q. Chen, T. L. Ren, *ACS Nano*, **2017**, 11, 8790–8795.

29. Cromatos s.r.l. is an industrial group operating worldwide dedicated to the production, formulation and marketing of dyes, pigments and chemical products for industry. https://www.cromatos.com.

30. F. M. L. Van der Goes, C. M. Gerard, *Analog. Integr. Circuits Signal Process.*, **1997**, 14, 249-260.

31. G. C. Meijer, J. Drecht, P. C. Jong, H. Neuteboom, *Sens. Actuators A*, **1992**, 35, 23-30.

32. G. C. M. Mejer, *Sens, Actuators A*, **1992**, 42, 183-191.

33. Mengucci, *Corso di Tecnologie per Tecnici Cartari*, Cartari, **2003**.

34. F. Cases, F. Huerta, P. Garces, E. Morallon, J. L. Vazquez, *J. Electroanal. Chem.*, **2001**, 501, 186–192.

35. U. M. Chougale, J. V. Thombare, V. J. Fulari, A. B. Kadam, *International conference on energy efficient technologies for sustainability*, **2013**,1078–1083.

36. S. Dhibar, C. K. Das, *Ind. Eng. Chem. Res.*, **2014**, 53, 3495–3508.

37. A. M. Youssef, M. A. El-Samahy, M. H. Abdel Rehim, *Carbohydr. Polym.*, **2012**, 89, 1027–1032.

38. S. I. A. Razak, N. H. M. N. Sharif, *Fibers Polym.*, **2014**, 15, 1107.

39. H. Sharifi, M. Zabihzadeh, M. Ghorbani, *Carbohydr. Polym.*, **2018**, 194, 384–394.

40. A: C. Baptista, I. Ropio, B. Romba, J. P. Nobre, C. Henriques, J. C. Silva, I. Ferreira, *J. Mat. Chem. A*, **2018**, 6, 256–265.

41. O. Ngamna, A. Morrin, A. J. Killard, S. E. Moulton, M. R. Smyth, M. R., G. G. Wallace, *Langmuir*, **2007**, 23, 8569–8574.

42. W. Gao, H. Ota, D. Kiriya, K. Takei, A. Javey, *Acc. Chem. Res*., **2019**, 52, 523–533.

43. M. Y. Teo, L. Stuart, H. Devaraj, C. Y. Liu, K. C. Aw, J. Stringer, *J. Mater. Chem. C*, **2019**, 7, 2219–2224.

44. P. Cataldi, S. Dussoni, L. Ceseracciu, M. Maggiali, L. Natale, G. Metta, I. S. Bayer, *Adv. Sci.*, **2018**, 5, 1700587–1700597.

45. Z. Yu, Y. Tang, G. Cai, R. Ren, D. Tang, *Anal. Chem*., **2019**, 91, 1222–1226.

46. D. Muchorski, *Tensile properties of paper and paperboard (using constant rate of elongation apparatus)*. TAPPI, **2015**.

47. Crecraft, D. Gorham, *Electronics*, 2nd ed., ISBN CRC Press, **2002**.

48. https://www.arduino.cc/reference/en/language/functions/digital-io/digitalread/.

49. *R. P. Jain, M. Anand, Using Integrated Circuits. McGraw-Hill Education, **1983***.

50. G. B. Clayton, *Operational Amplifiers*, 2nd Ed. Elsevier., **2013**.

51. U. A. Bakshi, A. P. Godse, *Analog Digital Electronics*, **2009**, 6-19.

52. H. Taub, D. Schilling, *Digital integrated electronics McGraw-Hill electrical and electronic engineering series*, McGraw-Hill, **1977**.

53. K. Autio, T. Laurikainen, *Trends Food Sci. Technol*., **1997**, 8, 181–185.

54. S. P. Cauvain, *Breadmaking. Cereals processing technology*. Cambridge England CRC Press, **2001**.

55. S. Sahlstro, W. Park, D. R. Shelton, *Cereal Chem*., **2004**, 43, 250-255.

56. C. Marek, W. Bushuk, *Cereal Chem*., **1967**, 44, 300–307.

57. C. H. Bailey, *Cereal Chem*., **1937**, 16, 665–670.

58. A. H. Bloksma, *Cereal Food World*, **1990**, 35, 237–244.

59. E. J. Pyler, *Dough fermentation*, 3rd edition. Sosland Publishing Company, **1988**.

60. B. De Cindio, S. Correra, *J. Food Eng*., 2005, 24, 379–403.

61. Y. Fan, W. Yingying, P. Qian, J. Gu, *Int. Biodeterior. Biodegrad*., **2004**, 53, 57–63.

62. B. S. Khatkar, A. E. Bell, J. D. Schofield, *J. Cereal Sci*., **2007**, 22,29-44.

63. A. M. Janssen, T. Vliet, J. M. Vereijken, J. Cereal Sci., **1966**, 23, 43-54.

64. K. Ogura, H. Shiigi, T. Oho, T. Tonosaki, *J. Electrochem. Soc.*, 2000, 147, 4351–4355.

65. T. Tonosaki, T. Oho, H. Shiigi, K. Isomura, K. Ogura, *Anal. Sci.*, **2001**, 17, 249–252.

66. S. Neethirajan, M.S. Freund, D.S. Jayas, C. Shafai, D.J. Thomson, N.D.G. White, *Biosyst. Eng.*, **2010**, 106 395–404.

67. M. Irimia-Vladu, J.W. Fergus, *Synth. Met*., **2006**, 156, 1401–1407.

5 Poly(2-acrylamido-2-methyl-1-propanesulfonic acid) (PAAMPSA) and Polyaniline modified cellulose as new material for humidity sensing and ECG monitoring.

5.1 Aim of the chapter

A new material based on cellulose coated with polyaniline and poly(2-acrylamido-2-methyl-1-propanesulfonic acid) (Cell/PANI-PAAMPSA) is synthesized in a simple way and shown in this chapter. The morphology, structure and electrical properties were investigated by means of several complementary techniques. Moreover, the material was studied for different possible applications:

1) As humidity sensor with particular attention towards the humidity conditions within museums and buildings holding collections of cultural heritage. The performances of this new material were compared with the ones of an already discussed material in this thesis: cellulose covered with polyaniline (Cell/PANI).

2) as electrode for electrocardiogram monitoring (ECG monitoring).

5.2 Introduction

In recent decades, cellulose has been used in various highly value-added applications due to its insolubility in water and in most organic solvents, such as in the food packaging industry, in the development of innovative batteries, supercapacitors, electrochromic materials and biosensors[1-3]. Indeed, cellulose has greatly captured the interest of scientists because of its large availability, biodegradability, low density, sustainability, good mechanical properties, and non-toxicity[4]. Moreover, the mechanical properties and processability of cellulose composites are significantly improved by the incorporation of different polymeric materials, which can self-assemble into 2-D or 3-D super strong architectures through hydrogen bonding. Between these, cellulose-based materials show great potential in applications of polyaniline (PANI) composites[5].

Compared to other conducting polymers, polyaniline has a unique doping-dedoping mechanism and redox chemical structure. PANI remains one of the most investigated conjugated polymers because of its high electrical, its multiple electronic states, electrical tuneability, nontoxicity, low manufacturing costs and relative environmental stability[6-8]. The dopants normally used for doping PANI are small molecule organic or inorganic acids that can evaporate at room or higher temperature, causing a depression of the conductivity of the acid-doped polymers. This drawback can be overcome by using polymeric acid dopants[9,10]. In addition, polymeric acid with a glass transition temperature (Tg) lower than that of PANI can be expected to enhance the flexibility of the polymeric film[9-12]. Consequently, the microstructure of the polymeric acid doped PANI and therefore its properties are expected to be different from that of small size protonic acid-doped one. Among the polymeric acids that can be used, the poly(2-acrylamido-2-methyl-1-propanesulfonic acid) (PAAMPSA) confers several advantages on the materials. Firstly, as shown in Scheme 1, PAAMPSA contains amide groups in its repeating units that can provide additional hydrogen bonding swich should enhance water dispersibility of the material. In addition, both the monomer and the polymer are strong acids in aqueous solution, so the pH of aniline polymerization medium could be maintained around 2 which is crucial for the synthesis of the conductive form of PANI, preserve the electrical conductivity and improves the flexibility of the final material[9-13].

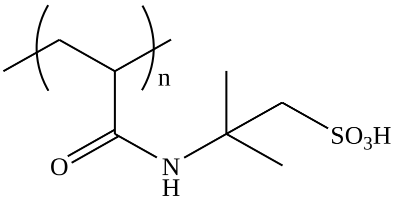

Scheme 1: chemical structure of PAAMPSA

Finally, it is known that the conductivity of PANI-PAAMPSA depends on the molecular weight of the PAAMPSA template. More specifically, the conductivity increases monotonically with the decreasing of PAAMPSA molecular weight ranging from 0,4 to 1,1 S cm^{-1} for a PAAMPSA that is lower than 800 Kg mol^{-1} [14,15].

Among the applications that a conductive material based on cellulose could have, humidity sensing is interesting due to its crucial role in the maintenance of drug storage areas, hospitals, food storage and packaging, electronic device fabrication and air conditioning systems[17,18]. Moreover, the preservation of artefacts in museum collections is profoundly affected by fluctuations in temperature and relative humidity (RH)[19-22]. To ascertain seasonal, architectural and visitor's impact on the local microclimate inside the buildings often it is necessary to obtain information on the dynamics of the environmental fluctuations in a comprehensive way throughout long periods of time. The humidity is usually recorded in the atmosphere surrounding the objects, without an evaluation of water interaction with the artefacts or the materials to be preserved.

The commercially available humidity sensors based on conventional inorganic semiconductor have high fabrication and maintenance costs, significant power consumption and require high temperature fabrication process[23,24]. Therefore, they can hardly be exploited to monitor the real exposure of objects (artefacts, drug, food packaging etc..) to humidity and estimate its effect on their conservation. Moreover, materials used to produce commercial sensors exhibit mechanical features (stiffness, flexibility, porosity) that hinder the embedding of the transducer inside real-life objects. Hence, considerable efforts have been directed towards the development of humidity-sensitive organic materials (phthalocyanine along with doped conductive polymers like polypyrrole, polythiophene), organic-inorganic composites (*i.e.* Nickel phthalocynine, copper oxide, poly-N-epoxypropylcarbazole), etc. that answer these demands[25-27].

Recently we have investigated on a composite material based on conductive cellulose fibers coated with polyaniline (Cell/PANI)[16], herein a new material, the Cell/PANI-PAAMPSA, synthesized in a simple way, starting from cellulose fibers and PANI using PAAMPSA as dopant is presented. The morphological features, mechanical properties, thermal stability and electrical conductivity of the Cell/PANI-PAAMPSA composite were investigated. The applications of this new composite materials as humidity sensor were examined and compared with those of Cell/PANI. Moreover, a possible application as ECG electrode has been tested.

5.3 Results and discussion

5.3.1 Characterization of PANI-PAAMPSA modified cellulose compared with PANI modified cellulose

The morphological properties of the synthesized PANI-PAAMPSA modified cellulose were evaluated by SEM microscopy. Fig. 1 presents the SEM micrographs of Cell/PANI-PAAMPSA (Fig. 1 B) compared with pristine cellulose and Cell/PANI (Fig. 1 A and C respectively). It was observed that PANI and PANI-PAAMPSA coatings were uniformly deposited on cellulose fiber substrates, but no significant differences between PANI and PANI-PAAMPSA coatings were observed.

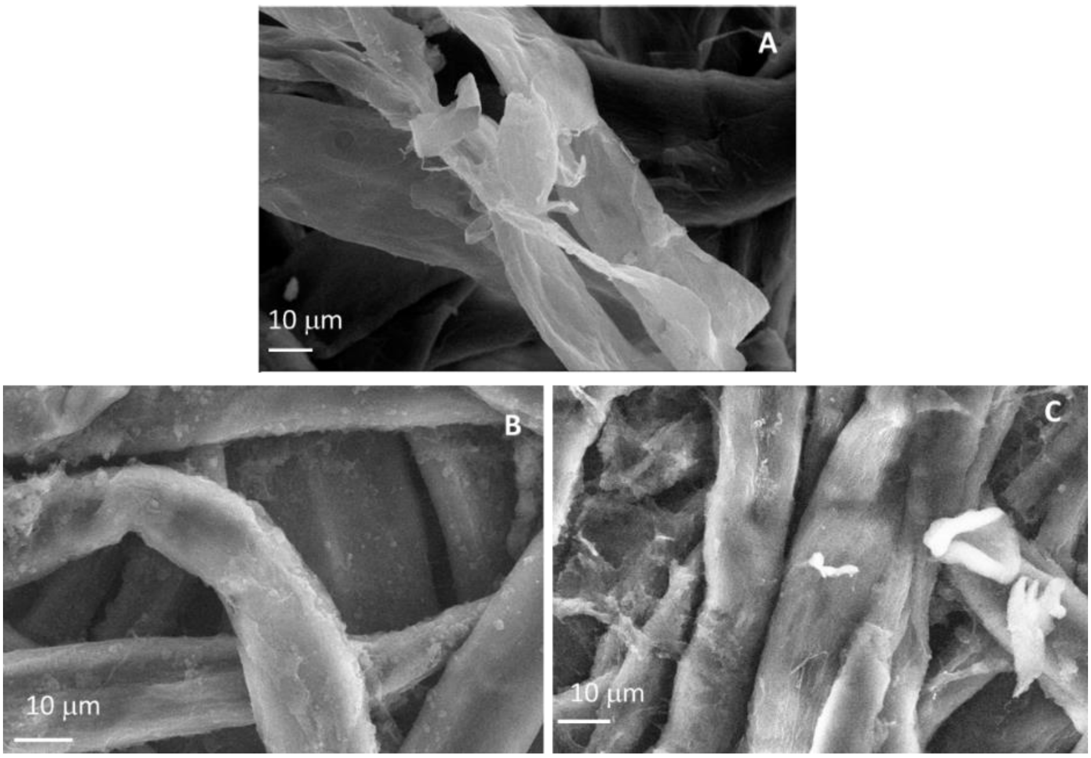

Fig. 1: SEM micrographs of pristine cellulose (A), Cell/PANI-PAAMPSA (B) and Cell/PANI (C).

In addition, ATR-FTR spectra of cellulose, Cell/PANI and Cell/PANI-PAAMPSA were studied (Fig. 2). All of them show the characteristic tapes of PANI emeraldine salts at the wave numbers of 1560-1570 cm^{-1}, 1480-1490 cm^{-1} (attributed to the C=C stretching vibration bands to the quinonoid and benzenoid units appeared respectively), 1302-1304 cm^{-1}, 1243-1245 cm^{-1}, 1108-1119 cm^{-1} [28-30]. The characteristic absorption peaks for PAAMPSA are visible in the Cell/PANI-PAAMPSA spectrum as shown in Fig. 2: 1654 cm^{-1} (−S=O vibration), 1188 cm^{-1} (asymmetric $S(=O)_2$ stretching, =C−H in-plane deformation, and twisting and rocking of the methylene groups), 1042 cm^{-1} (symmetric $S(=O)_2$ stretching), 923 cm^{-1} (S−O stretching), and 795 cm^{-1} (C−S stretching and C−H out-of plane bending)[31].

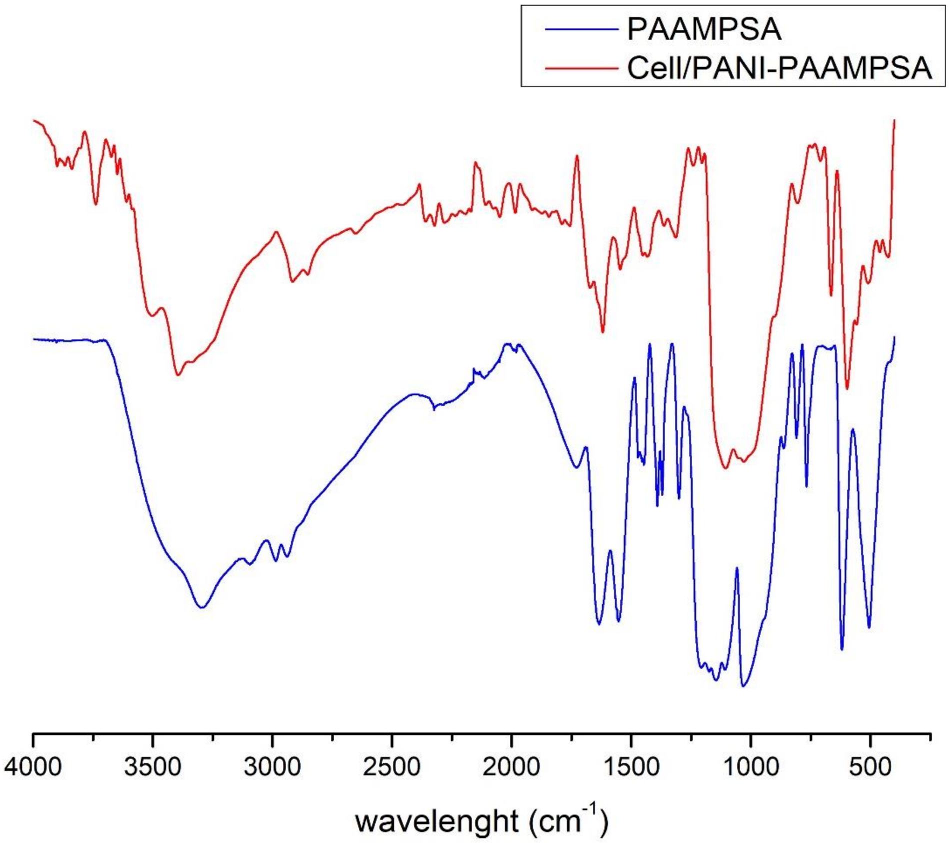

Fig. 2: IR-ATR spectra of Cell-PANI/PAAMPSA (red) and PAAMPSA (blue)

The TGA curves of the Cell/PANI-PAAMPSA and Cell/PANI are reported in Fig. 3. Due to the highly hygroscopic nature of cellulose and polyaniline, a first stage of mass loss (about 5%) from room temperature to 160-180 °C can be attributed to the loss of volatiles, such as water. The second stage that starts at around 160 °C (lower in the case of PAAMPSA: 57.6 vs 65.2 % for PANI) is due to loss of dopant and low molar mass oligomers, cross-linked fragments of chains and the initiation of polymer degradation. The last stage of mass loss that occurs at around 500 °C corresponds to the total rupture of polymer bonds (polyaniline and cellulose), as well as heavier fragments in even smaller fractions and gaseous by-products. The residues remaining at 900 °C for Cell/PANI-PAAMPSA (24.3 %) are inert materials, such as fragments of carbonized polymer chains[29].

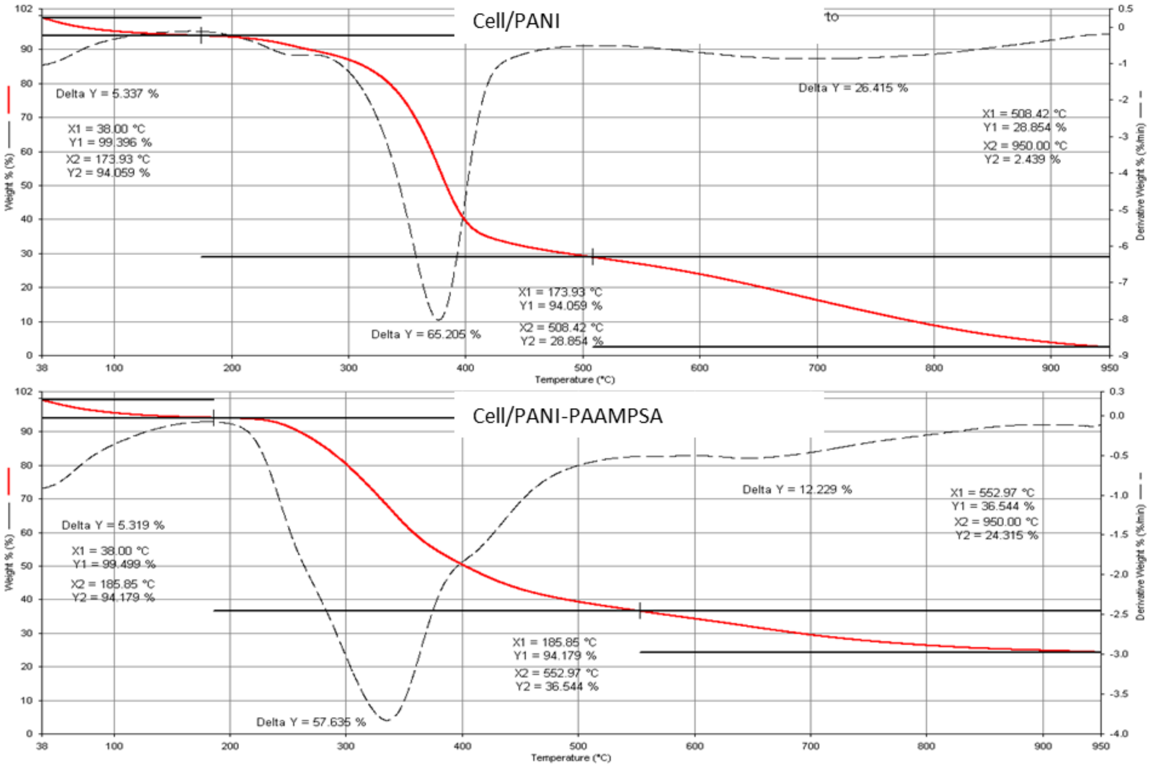

Fig. 3: TGA curves of Cell/PANI and Cell/PANI-PAAMPSA

Cell/PANI and Cell/PANI-PAAMPSA electrical resistance were measured with a Keysight B2902A source meter units in a 4-line-probe configuration by exploiting a home-made holder that is composed by 4 parallel copper electrodes on a glass slide. The data are reported in Table 1 and represent averages from five measurements each with the transmission.

Table 1: Conductivity values for Cell/PANI and Cell/PANI-PAAMPSA

Samples	**S cm^{-1}**
Cell/PANI	$3.45\pm0.01\ 10^{-1}$
Cell/PANI-PAAMPSA	$0.537\pm0.001\ 10^{-1}$

As expected, the conductivity of Cell/PANI-PAAMPSA is lower than the Cell/PANI because PAAMPSA is inherently insulating. The results obtained are still suitable to obtain a sensor that is reasonable to study.

To better investigate the mechanical properties of the materials, the tensile strength of the Cell/PANI-PAAMPSA samples has been measured and compared with Cell/PANI and pristine Cellulose. The results reported in Table 2 and shown in Fig. 4, are the average of the measures made for three different samples for each type of material.

Table 2: Tensile strength values obtained after mechanical tests for Cell, Cell/PANI and Cell/PANI-PAAMPSA

Sample	**Tensile strength (MPa)**
cellulose	9,38 ± 1,08
Cellulose/PANI	3,95 ± 0,82
Cellulose/PANI-PAAMPSA	15,7 ± 1,2

It is clearly visible that PAAMPSA imparts an improvement in mechanical properties of the modified cellulose, resulting in a tensile strength that is more than three times higher compared to the one of cell-PANI. Reasonably, the hydrogen bonds and electrostatic interactions between PAAMPSA and PANI construct a homogeneous dynamic network, which contribute to the elasticity and soft compliant nature of the as-prepared electronic polymer material with high omni-directional stretchability[32-35].

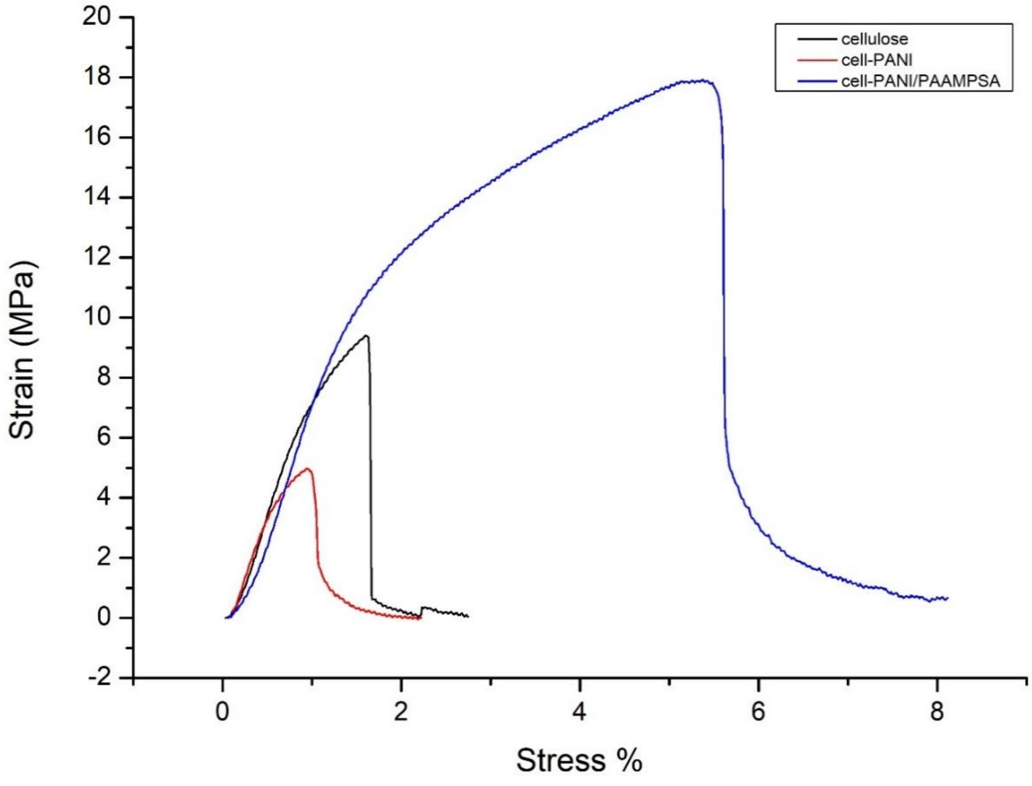

Fig. 4: stress-strain curves obtained for Cell (black), Cell/PANI (red) and Cell/PANI-PAAMPSA (blue)

The bending properties of a material appliable in different conditions and substrates are very important. To study the behaviour of Cell-PANI/PAAMPSA in comparison with Cell-PANI, a homemade 3d-printed support is built to fold pieces of paper in a reproducible way (Fig. 5). The behaviour of materials was studied in terms of conductivity (measured with a 4-probe tester) before and after a certain number of foldings.

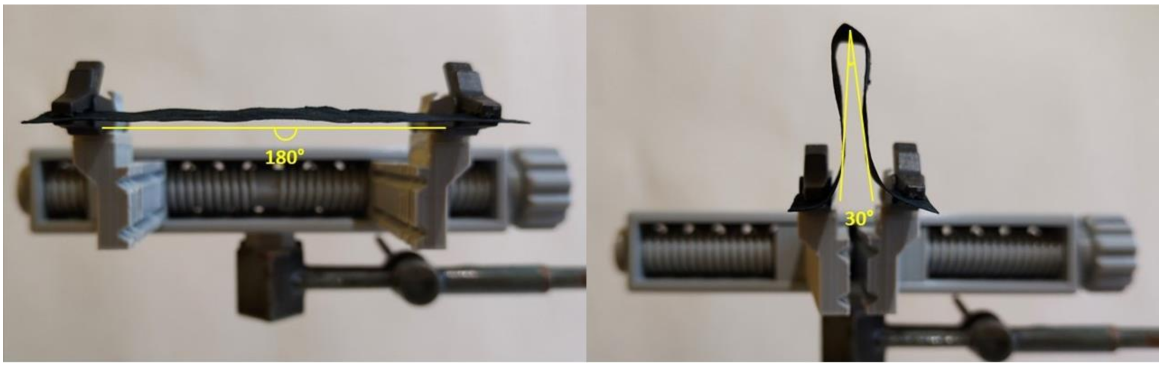

Fig. 5: bending angles for mechanical tests

As shown in Fig. 6, the conductivity of PANI-modified cellulose decreased progressively during the foldings, and the material broke in the middle after 200 foldings. On the coutrary, the cell-PANI/PAAMPSA remained practically unchanged, demonstrating better properties in terms of possible applications.

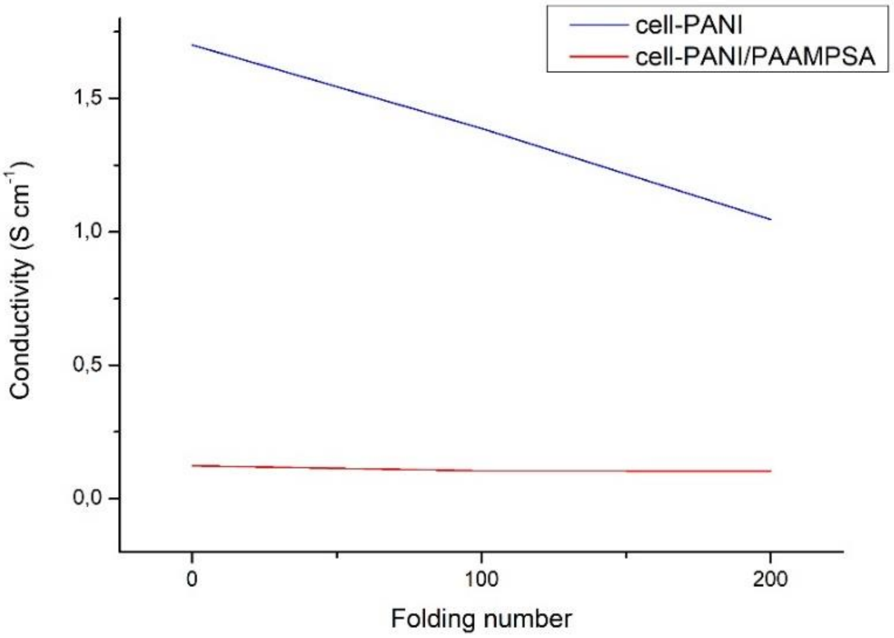

Fig. 6: conductivity graphs for Cell/PANI (blue) and Cell/PANI-PAAMPSA (red) before and after bending tests.

The conducting behaviour of emeraldine form of PANI exists when the polymer is doped with counter anions[28,2]. Unlike of the use of PAAMPSA, when the counter anion is a small molecule acid, such as hydrochloric acid, this could be released during the aging time. To investigate the stability of the materials we tested Cell/PANI and Cell/PANI-PAAMPSA in a close chamber in the presence of a pH tester paper for 72 h.

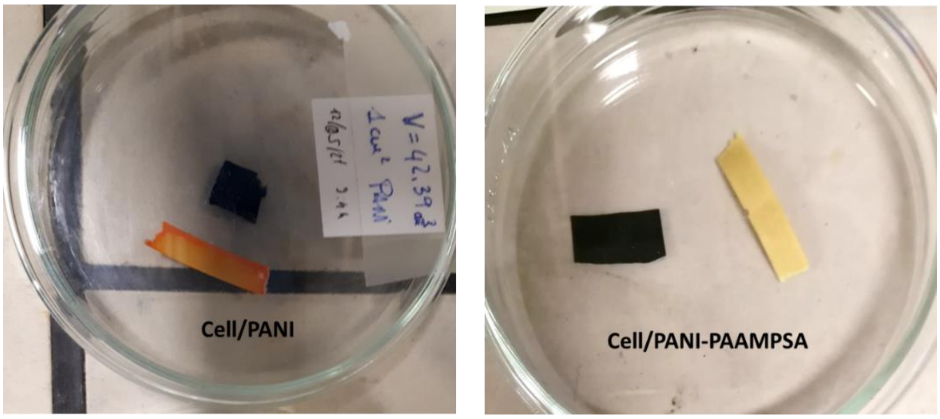

Fig. 7: close chamber tests for Cell/PANI and Cell/PANI-PAAMPSA

As observable in Fig. 7 when exposed in proximity to Cell/PANI the pH tester paper turns in red colour in about 48 h indicating an acid release. No change in colour occurs with Cell/PANI-PAAMPSA exposure. The experiment repeated on Cell/PANI after it had been equilibrated for 67 h under vacuum exhibited no more acid release. This behaviour was confirmed even measuring the drift of the current with time registered at room temperature and 60 %RH before and after the vacuum treatment, as observed in Fig. 8 a stable signal was obtained after 67 h. So, we decided to deal Cell/PANI samples under vacuum for 67 h before their use. Similar treatment, even if not need, was applied at Cell/PANI-PAAMPSA with the aim of being able to compare the two samples for later tests.

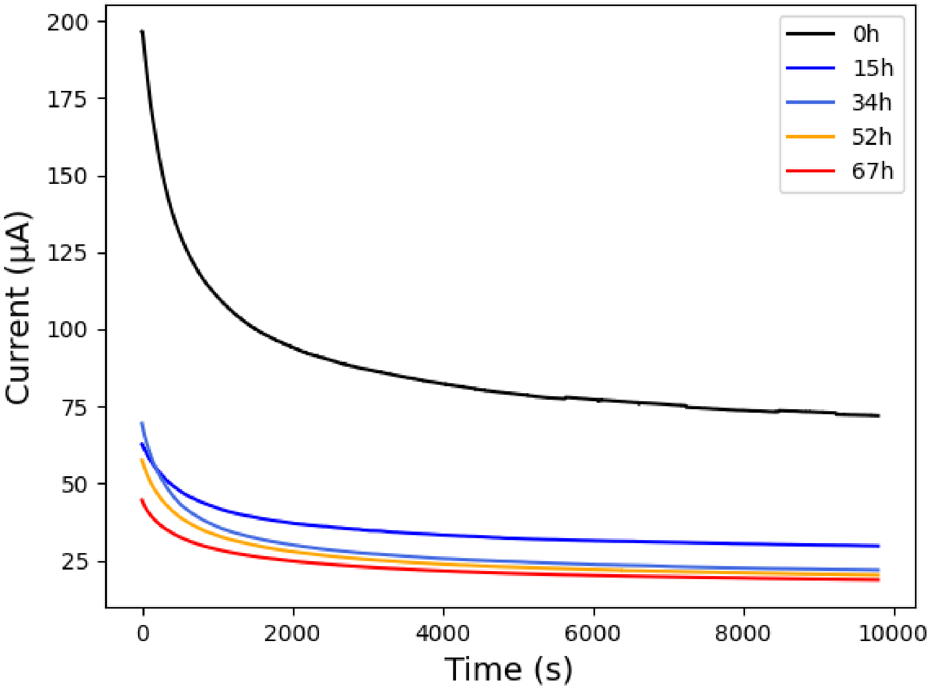

Fig. 8: drift of current at different hours under vacuum for Cell/PANI

5.3.2 Humidity Sensing Studies

The pulse-stimuli characteristics of the sensors were analysed based on a series of current responses on dynamic switches between two different % RH range:

i) dry and wet nitrogen (N_2) flow (2-44 % RH);

ii) two different wet N_2 flow (22 and 44 % RH)

employing the homemade controlled set-up and a flow rate of 3 ml s^{-1} with long and short cycling time (see Scheme 2). During the tests a commercial digital-output relative humidity and temperature sensor (DHT22) was employed, in parallel, for comparison.

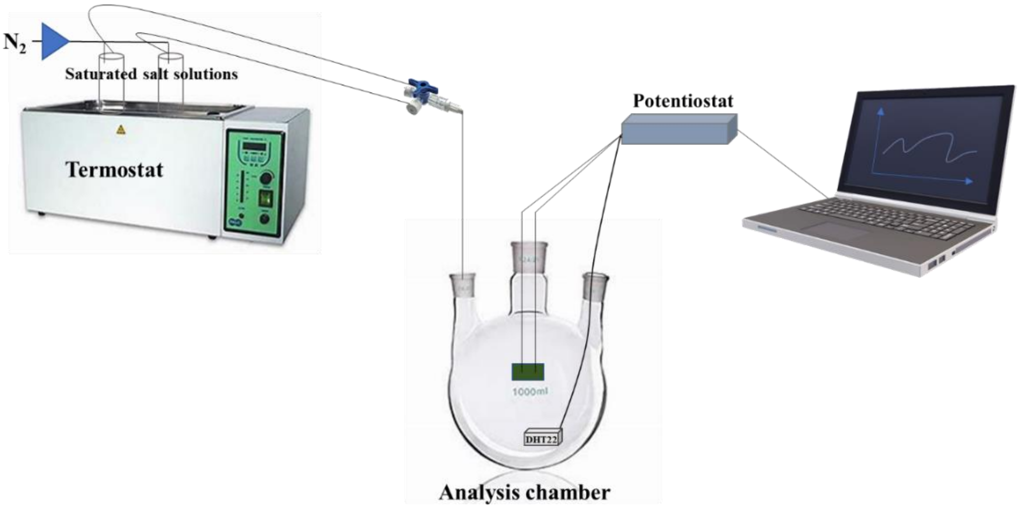

Scheme 2: Set-up of the homemade controlled-humidity enclosures used.

As shown in Fig. 9 for the 2 - 44 % RH stimuli, as the Cell/PANI and Cell/PANI-PAAMPSA were exposed to the wet flow, the current of the sensor promptly jumped (4 - 5 s) since reached a relative stable equilibrium value. Once the moist flow was switched to dry nitrogen, the current rapidly (4- 5 s) returned to the initial value. Similar behaviour was observed for the 22- 44 % RH range (see Fig. 10).

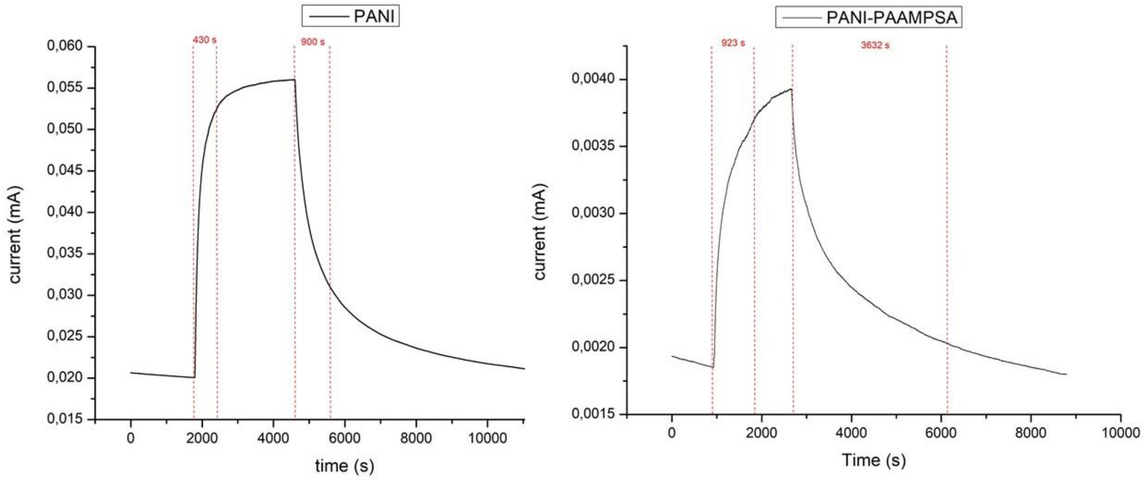

Fig. 10: Response and recovery times of the Cell/PANI and Cell/PANI-PAAMPSA under pulse stimuli obtained by switching between dry (2 % RH) and wet (44 % RH) N_2 flow. All test were conducted under bias voltage of 0.1 V at stable 25°C temperature.

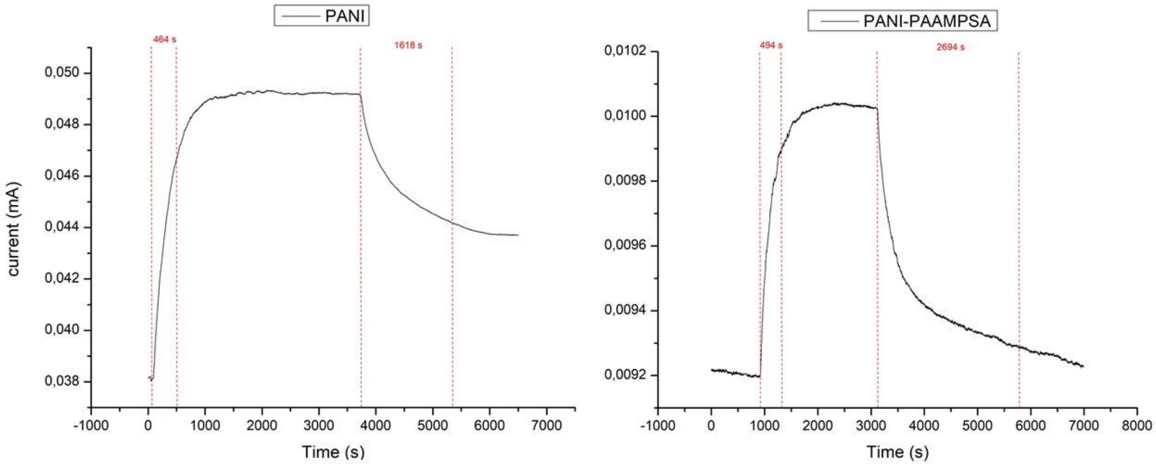

Fig. 11: Response and recovery times of the Cell/PANI and Cell/PANI-PAAMPSA under pulse stimuli obtained by switching between dry (22 % RH) and wet (44 % RH) N_2 flow. All tests were conducted under bias voltage of 0.1 V at stable 25°C temperature.

The recovery times defined as the time required to reach the 90% of the final equilibrium value[36] as well as the orders of magnitude in the current change registered before and after the stimuli, were reported in Table 3.

Table 11: Recovery time and magnitude current change for Cell/PANI and Cell/PANI-PAAMPSA in the two different humidity range.

2 - 44 %RH	**Recovery time up (s)**	**Recovery time down (s)**	**Order of magnitude of current change**
Cell-PANI	430	900	2.8
Cell-PANI/PAAMPSA	932	3932	2.1
22 - 44 %RH	**Recovery time up (s)**	**Recovery time down (s)**	**Order of magnitude of current change**
Cell-PANI	464	1618	1.3
Cell-PANI/PAAMPSA	494	2694	1.1

It is noteworthy that the humidity sensor based on PANI-PAAMPSA showed slightly response and recovery times. The negative effect of the acid doping agents on the sensor's response and recovery times would be ascribed to the enhanced hydrophilicity of the interfacial PANI surface by the doping because the sensor requires the prolonged time to absorb higher amount of water until establishing a new equilibrium state[36]. In any case both the sensor's responses result effective in both wide and narrow humidity ranges.

The humidity sensors displayed good dynamic reproducible responses on pulse moisture stimuli (obtained switching N_2 flow between 2, 22 and 44 % RH), as observable in Fig. 11 for Cell/PANI.

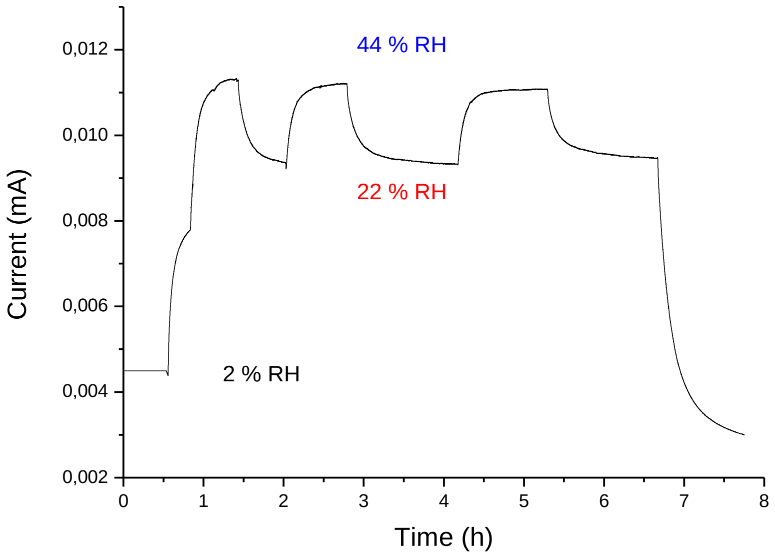

Fig. 11: The cycling behaviour of Cell/PANI sensor under switching between 2, 22 and 44 % RH. The test was conducted under an applied voltage of 0.1 V at 25 °C.

Sensors were tested also at short cycling time, switching the relative humidity from 2% to 44% using dry and wet nitrogen flow. Switches were made every two minutes. Also in this case the response time (t 90) were good both for cell-PANI and cell-PANI/PAAMPSA that were about 100s every time. The detailed results are reported in Table 4 and represent an average of 10 different switches in the same conditions (0.1V applied at 25°C), shown in Fig. 12.

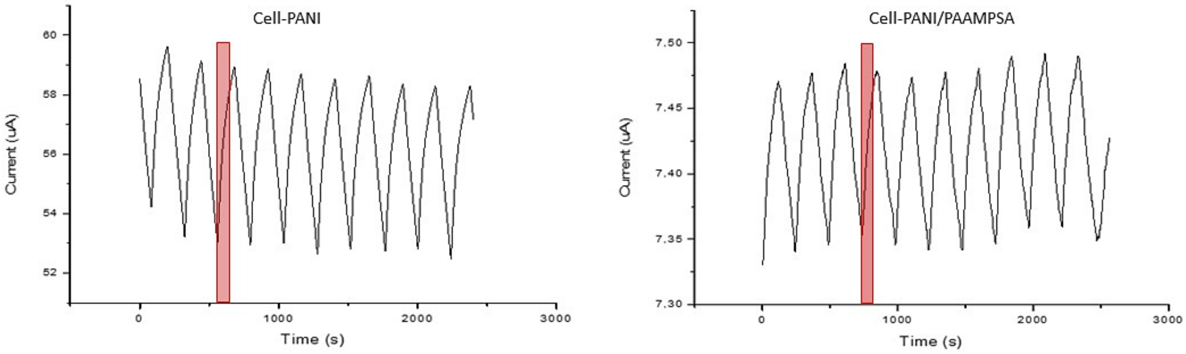

Fig. 12: switches for Cell/PANI and Cell/PANI-PAAMPSA performed at 0.1 V

Table 4: Recovery time and magnitude current change for Cell/PANI and Cell/PANI-PAAMPSA in the 2-44 % humidity range with short cycling time.

2 - 44 %RH	**Recovery time up (s)**	**Recovery time down (s)**	**Order of magnitude of current change**
Cell-PANI	96,8	101	1,10
Cell-PANI/PAAMPSA	97,5	111	1,02

Finally, to investigate a possible real application, the Cell/PANI and cell-PANI/PAAMPSA have been tested in a climatic chamber at a fixed temperature of 21°C following the current response of the humidity sensor at an applied potential of 0.100 V, under a set step uphill (5 %) from 30 up to 50% RH; each step was maintained for 1 h and 15 min that is time needed to stabilize the chamber and followed with the climatic chamber internal sensor.

The RH range and temperature were chosen in accordance with the restrictions in which museums and buildings holding collections of cultural heritage objects are often maintained (50 ± 5 %RH and 20 or 21 ± 2°C) to provide safe and stable conditions for hygroscopic artifact[37,38]. As previously reported, during the tests a commercial digital-output relative humidity and temperature sensor (DHT22) was employed in parallel with those internal of climatic chamber and with our systems, for comparison; in this case the measurements were directly in % RH. A schematic representation of the used setup is shown in Fig. 13.

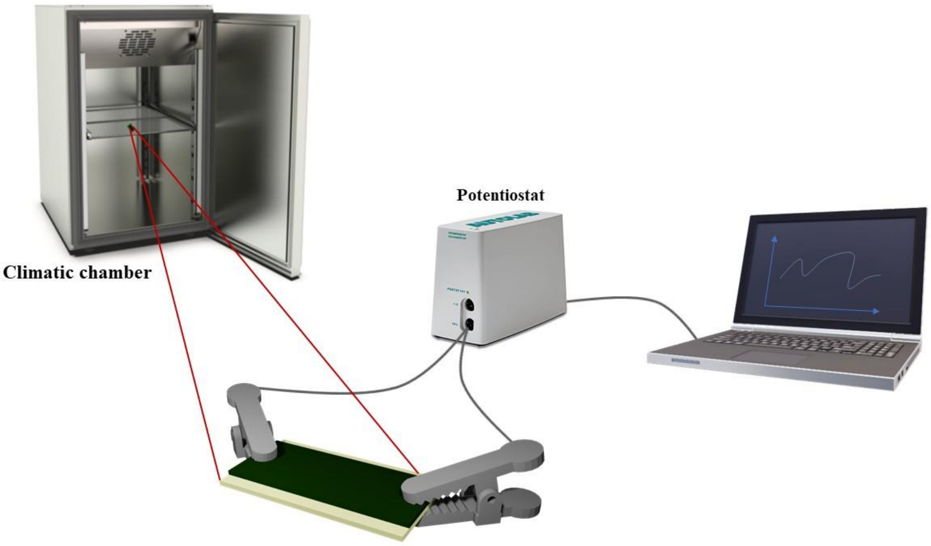

Fig. 13: set-up for climatic chamber

The current *vs* time curves for Cell-PANI and cell-PANI/PAAMPSA sensors and % RH *vs* time curves registered with DHT22 are shown in Fig. 14; the oscillation in the signal, observed with all the sensors employed are due to the fluctuations present in the chamber for each % RH variation (in order to remain as close as possible to the programmed % RH ramp, inside the climatic chamber occurs a variation of the temperature and a nebulization of water, to adjusts the climatic conditions).

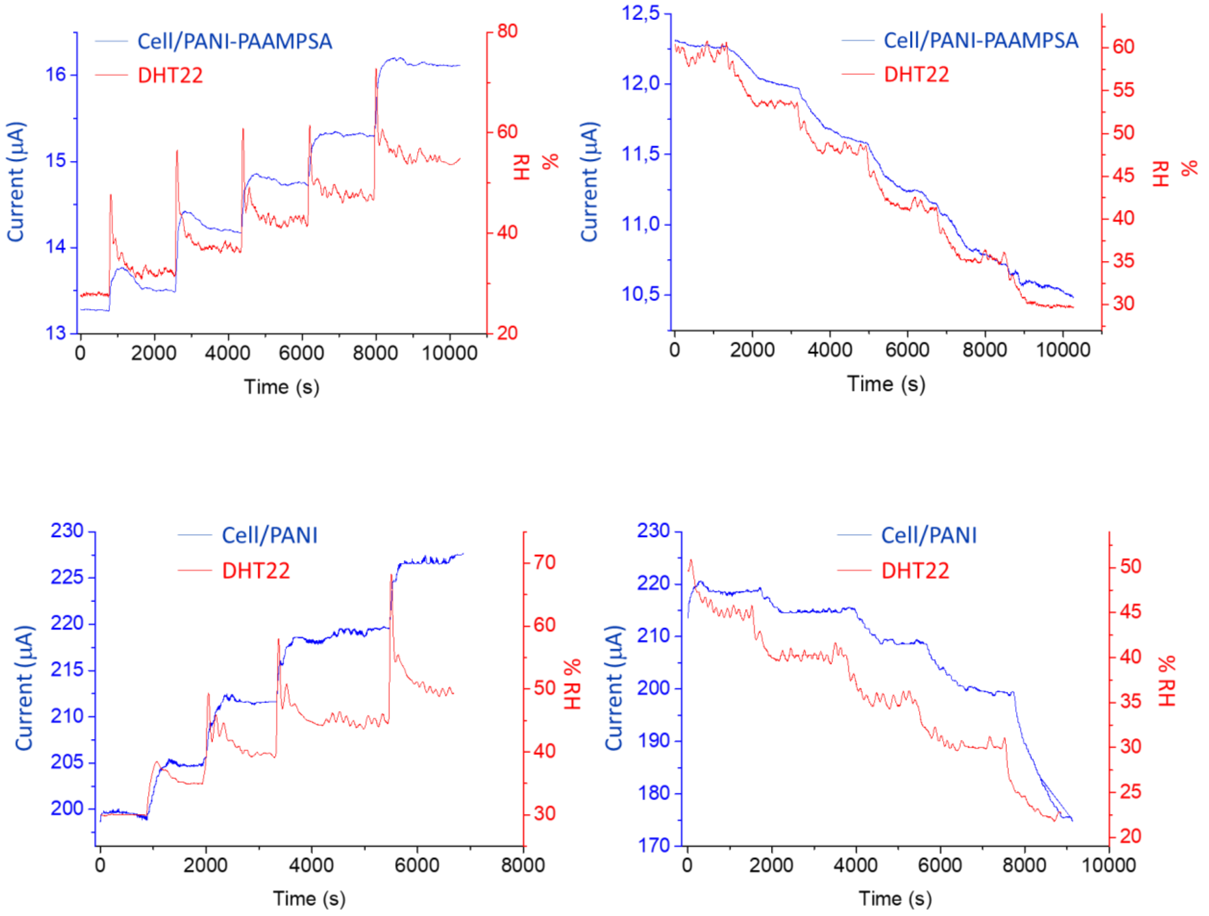

Fig. 14: current vs time curves and %RH vs time curves registered uphill and downhill for Cell/PANI-PAAMPSA and Cell/PANI.

As shown in Fig. 14., Cell/PANI and cell-PANI/PAAMPSA have been tested even going down in the same conditions, that means at a fixed temperature of 21°C following the current response of the humidity sensor at an applied potential of 0.100 V, under a set step downhill (5 %) from 50 up to 30% RH. In particular for cell-PANI/PAAMPSA, even if the trend is clear and comparable to the DHT22, it was difficult to observe a plateau and make a calibration curve accordingly. The study is ongoing in my research group, so only the uphill study will be treated further on in that section.

From the response values obtained (considering the values in the middle of the plateau registered for each step, the current vs % RH curves have been calculated, as shown in Fig. 15.

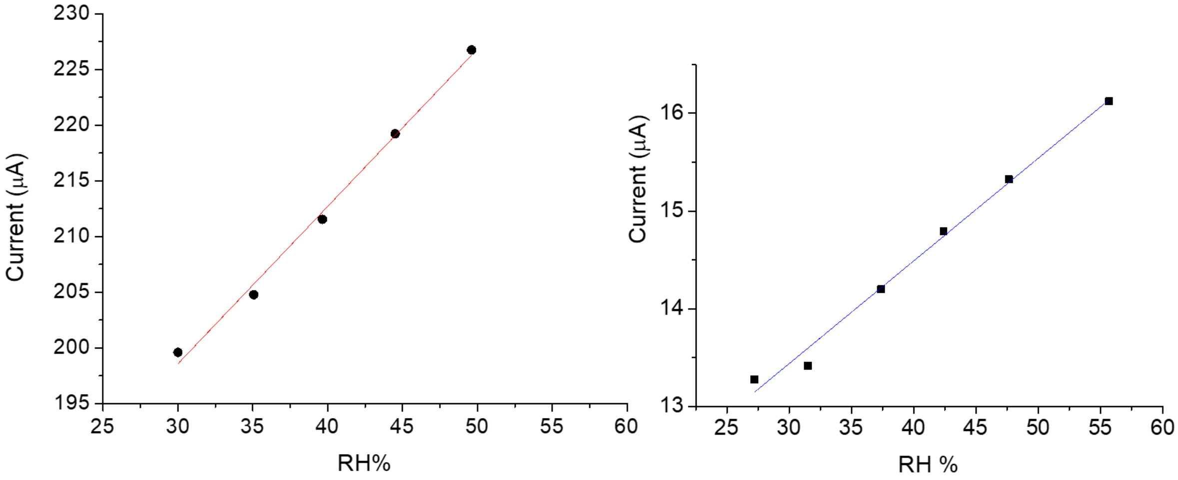

Fig. 15: Current versus % RH response curves characteristic for Cell/PANI and Cell/PANI PAAMPSA. Equations: $y = 1.41x + 156.18$ ($R^2 = 0{,}999$) and $y = 0.11x + 10.28$ ($R^2 = 0.996$).

A linear trend was observed in both the case; the slope of response for Cell/PANI results about one order of magnitude higher than that of Cell/PANI-PAAMPSA, which was 1.41 and 0.11 (µA/%RH), respectively. Overlapping the data with a simple elaboration shown in "Materials and Methods" of this chapter, a very similar response is observed between the DHT22 signal and our sensors, as shown in Fig. 16.

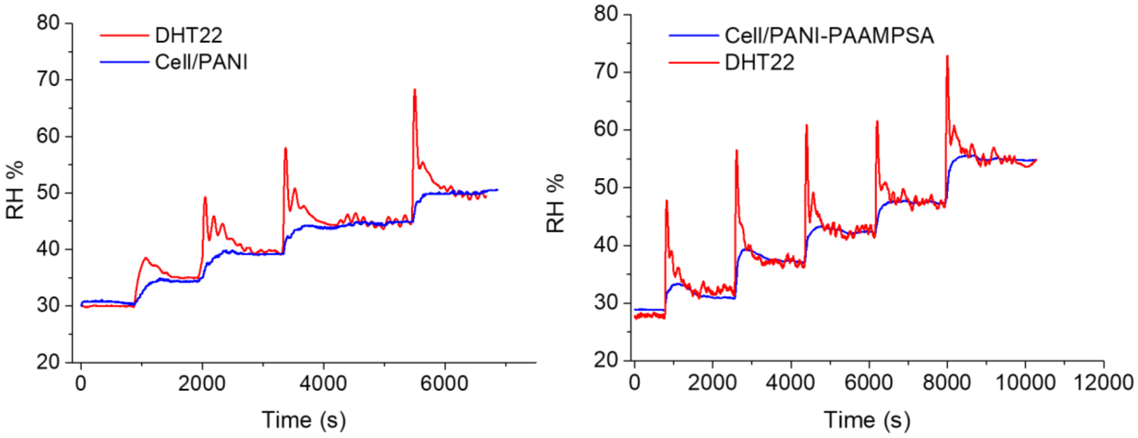

Fig. 16: Comparison between the response of the Cell/PANI and Cell/PANI-PAAMPSA and DHT22 under pulse stimuli obtained by switching between 30- 55 % RH in a climate chamber. The test was conducted under an applied voltage of 0.100 V at 21±1 °C.

The response vs RH relationship of the Cell/PANI and DHT22 sensors are reported in Fig. 17, also Cell/PANI-PAAMPSA present a good linearity (R^2 = 0.9979) in the RH% range investigated. The comparison of the slope of the curves for Cell/PANI-PAAMPSA (0.30± 0.12) with Cell/PANI and DHT22 (3.34 ± 0.11 and 3.44 ± 0.03 respectively) show that the rate of change response of the three sensors is clearly statistically equal. The distinction of the slope of the curves for Cell/PANI and Cell/PANI-PAAMPSA (0.70 ± 0.02 and 0.87 ± 0.05 respectively) shows that the rate of change response of Cell/PANI-PAAMPSA sensor results higher than that of Cell/PANI.

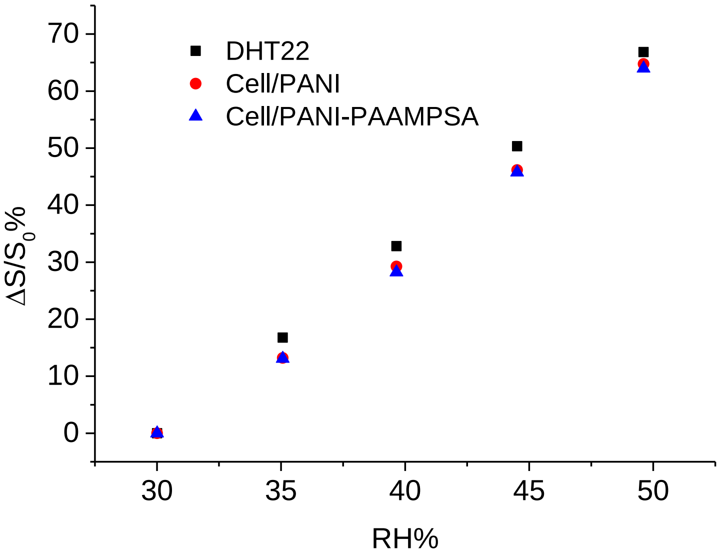

Fig. 17: Response vs RH relationship of Cell/PANI-PAAMPSA (calibration function = y= 3.30 x -101.09 (Cell/PANI and DHT22 sensors calibration functions: y= 3.34 x -102.10 and y = 3.44 x -103.31 respectively).

5.4 Conclusions

The humidity sensing performance of conductive cellulose fibers coated with polyaniline and PANI-PAAMPSA were explored. The current which flows in the material due to an applied potential is recorded while sensors are placed in a climate chamber (30 – 50 % RH, 21±1 °C), used to vary humidity and simulate a real application. The sensors showed a linear and rapid response and a stability in the signal for short and long-time humidity cycling. Moreover, the rate of change response of devices results perfectly comparable with that of a commercial digital-output of a relative humidity and temperature sensor highlighting the promising performance in low-cost humidity monitoring. Finally, the use of paper as substrate could give the way to new applications in packaging with a potential improvement of the storage conditions of preserved goods.

5.5 Experimental section

5.5.1 Materials

All chemicals and solvents are ACS reagent grade, were purchased from commercial vendors and used directly unless otherwise stated. Sulfuric acid (H_2SO_4, 95.0-98.0%), ammonium persulfate [$(NH_4)_2S_2O_8$), ≥ 98%, APS] and aniline (≥ 99%), were purchased from Sigma-Aldrich (now Merck KGaA, Darmstadt, Germany); aniline was distilled under nitrogen prior to use. Chloridric acid (≥ 37%) was purchased from VWR Chemicals (Vienna, Austria); a solution of ca. 25 wt% of $Al_2(SO_4)_3$ in water (commercial name FLOCLINE S8C) was purchased from Bio-Line s.r.l. (Milano, Italy). Bare cellulose fibers (pine tree long fiber with sulfate treatment) were kindly provided by Cromatos s.r.l. (Forlì, Italy). Poly(2-acrylamido-2-methyl-1-propanesulphonic acid) (PAAMPSA), M.W. ~800,000, 10% (w/w), was purchased from Acros Organics. Universal pH paper test (Jovitec).

5.5.2 In Situ Syntheses of the PANI-Paper Composites

Firstly, the cellulose-PANI composites were fabricated. In a 1 L round bottom flask, 2.5 g of bare cellulose fibers were dispersed in demineralized water (250 mL) for 30 min; successively a solution made of 2.5 mL of aniline in 150 mL of 1.0 M hydrochloric acid (HCl) was added to the fiber suspension and stirred for 3 h at room temperature. In turn, the oxidative polymerization was carried out adding dropwise to the stirred suspension, previously cooled to 0 °C in an ice bath, a solution of 7 g of $(NH_4)_2S_2O_8$ dissolved in 200 mL of 1.0 M hydrochloric acid. After 24 h the coated fibers were filtered in a Buchner funnel and washed several times with 1.0 M citric acid solution. The conductive fibers were dried in air atmosphere for 24 h.

To obtain a 0.25 mm thickness sheet, 10 g of Cell/PANI fibers were added to 1.0 L of an acid solution (ca. pH 3.0, 25 wt% $Al_2(SO_4)_3$ in demineralized water) and stirred for 5 min, then the fibers were partially dried in a square sieve (21.0 cm x 14.8 cm size). Finally, the sheet was pressed at 50 bar pressures (P50 AXA manual hydraulic press) for 10 s. The coating of the fibers was determined by Kjieldahl analysis and resulted in 22,3% of PANI.

The fabrication of PANI-PAAMPSA modified cellulose was similar. Briefly, in a 1 L round bottom flask, 2.5 g of bare cellulose fibres were dispersed in demineralized water (300 mL) for 30 min, then 2.54 mL of aniline and 58.0 g of PAAMPSA were added to the fibre suspension and stirred for 1 h at room temperature. Successively, 5.8 g of APS in 25 mL of distilled water was slowly adding dropwise to the stirred suspension, the flask was cooled to 0 °C in an ice bath for 6 hrs. After 24 h the coated fibres were filtered in a Buchner funnel and washed several times with 1.0 M citric acid solution. The conductive fibres were dried in air atmosphere for 24 h. To obtain a 0.25 mm thickness sheet, 5 g of Cell/PANI-PAAMPSA fibres were added to 1.0 L of demineralized water and stirred for 5 min, then the fibres were partially dried in a square sieve (21.0 cm x 14.8 cm size). Finally, the sheet was pressed at 50 bar pressures (P50 AXA manual hydraulic press) for 10 s

5.5.3 Fabrication of the Humidity Sensors

To increase the mechanical resistance of the conductive sheets we employed the industrially wet coupling method: a Cell/PANI sheet of 0.25 mm thickness was coupled with a bare cellulose sheet (thickness 0.40 mm), previously prepared, moistened with water. The two sheets were then pressed (50 bar, 10 s) and dried at 80 °C for 10 min. A similar procedure was used for Cell/PANI-PAAMPSA sheets. Finally, sensors of 2.2 x 0.9 cm dimension were obtained from the conductive sheets.

5.5.4 Humidity Sensing set up

A simple controlled-humidity enclosures constructed using a sealed container, connected with a different saturated salt solution in which it will be fluxed nitrogen (N_2) at a fixed flow and temperature (25 °C) to obtain different % RHs (*i.e.* 44% and 22%) was used to make preliminary stability tests of our humidity sensors. A commercial Digital-output relative humidity & temperature sensor/module DHT22 (DHT22 also named as AM2302, Guangzhou Aosong Electronics Co.,Ltd, China) was used to monitor the % RH and temperature inside the sealed chamber. A potentiostat/galvanostat was used to monitor the chronoamperometric response of the humidity sensor at an applied potential of 0.1 V. The used salt saturated solution (SS) were potassium acetate (CH_3COOK, 22 % RH) and potassium carbonate (K_2CO_3, 44 % RH) [20]; the 2 % RH was obtained with dry N_2. Alternatively, a climate chamber has been used. In this case the tests have been conducted at a fixed temperature of 21 ± 1 °C following the chronoamperometric respond of the humidity sensor at an applied potential of 0.1 V. For the tests with 0.4 mm thick Cell/PANI and Cell/PANI-PAAMPSA sensors we set steps uphill from 5% up to 55% RH, each step maintained for 1 h and 15 min (total time for each measure: 7.5 h).

5.5.5 Instruments and methods

SEM images were recorded at 25 kV with a Sem Zeiss EVO 50 EP equipped with Oxford INCA 350; EDS Spectrometer equipped with a Bruker Z200 energy dispersive microanalysis (EDX) system was used for semi-quantitative chemical analysis and mapping. TGA characterization was carried out using a Perkin Elmer TGA-7 instrument. In each analysis, a piece of weight ca. 4.0 mg of the target electrode was heated in a platinum crucible from room temperature from 38 °C to 950 °C (or 800 °C for cellulose), at a rate of 10 °C min^{-1}, under N_2 atmosphere. ATR-FTIR analyses were performed using a Perkin Elmer Spectrum Two spectrophotometer, equipped with a Universal ATR accessory, with a resolution of 0.5 cm^{-1} in the range 4000-400 cm^{-1}. The samples were directly analyzed performing 40 scans for any analysis.

The determination of PANI amount in Cell/PANI-F was performed with an automatic Kjeldahl Nitrogen Analyzer (Gerhardt Bonn). The Kjeldahl analysis was carried out on four Cell/PANI-F samples and a blank sample (cellulose bare fibre treated exactly as the Cell/PANI-F) using the following protocol. 1.0 g of each sample was put in a glass weighing flask and placed in a Kjeldahl test tube. A catalyst tablet (1 tablet contains 3.5 g of K_2SO_4 and 3.5 mg of Se) (Kjeldahl tablets, 1.18649 Supelco, Merck), 20 mL of concentrated H_2SO_4 (sulfuric acid 95-98%, ACS reagent, 258105 Sigma-Aldrich) and 4 glass spheres were then added. The test tubes were heated to 350 ° C for 5 h. The final solution must be clear and colourless. Finally, the test tubes were inserted in the Kjeldahl titration instrument, and the potentiometric titration automatically start with 0.100 M HCl in presence of an acid basic indicator (a mixture of methyl red and bromocresol green).

The chronoamperometric measurements were performed using a potentiostat/galvanostat Autolab PGSTAT128N (Metrohm-Autolab) controlled by NOVA 2.10 software.

A cooling incubator with controlled humidity (climatic chamber, ClimaCell 111 comfort, MMM Group) was used for the humidity tests at a fixed temperature of 21±1 °C following the chronoamperometric response of the humidity sensor at an applied potential of 0.100 V. For the tests with 0.40 mm thick Cell/PANI-PAAMPSA sensors we set steps uphill (5 %) from 30 % up to 50 %RH, each step maintained for 1 h and 15 min (total time for each measure: 7.5 h).

A commercial digital-output relative humidity & temperature sensor/module DHT22 (also named as AM2302, Guangzhou Aosong Electronics Co.,Ltd, China) was used to monitor the % RH and temperature inside the climatic chamber at each measurement, for comparison.

Tensile strength measurements have been carried out on a LBG UDI24Pro Instrument with a traction speed of 1 mm min^{-1}. The samples have been prepared following the TAPPI method reported in the literature by cutting the different sheets (cellulose, Cell/PANI-S and Cell/PANI-TS) into rectangles with a central size of 2 × 10 cm and 1.5 cm for each side for the crimping points[39].

Using the equations 1 and the parameters of the linear curves of both the sensors, it is possible to transform the current signal into an RH% signal, so that it became possible directly compare the DHT22 response with those of our sensors.

$$RH\%\ signal = \frac{i(\mu A) - intercept(\mu A)}{slope\left(\frac{\mu A}{RH\%}\right)} \qquad (1)$$

In order to contract the humidity sensitivity between Cell/PANI and Cell/PANI-PAAMPSA, the current signal was treated as the normalized response, which is defined as eq. 2 [28][29]:

$$\frac{\Delta S}{S_0}\,\% = \frac{S - S_0}{S_0}\,100 \qquad (2)$$

where S_0 is the signal of the sensor at 30 % RH and S stands for the signal at targeted RH environment.

Cell-PANI/PAAMPSA: an electrode for monitoring heart rate

Bioelectric signals coming from the human body could give important information about physiological functions and have been widely studied in medicine and other scientific fields[40,41]. One of the most investigated technologies in this field is Electrocardiogram (ECG) that, collecting bioelectrical signals with electrodes on the surface of the body, could give not only a clinical diagnosis of various heart diseases, but also a simple but effective tool to explain arrhythmia and conduction disorders[42-44].

The mechanism of these electrodes is based on the polarization and depolarization of myocardial cells that generates electric current[45,46]. An important criterion for suitable electrodes is low impedance to limit the noise generated during signal recording. The stratum corneum (SC), which is the top layer of the skin has a high impedance[47], that is why a wet gel is often used: the gel hydrates the SC creating an ionic path between the metal part of the electrode and the skin below the SC layer, which makes the transduction of ionic current into electric current easier. Therefore, the gel lowers the skin-electrode impedance. Furthermore, the flexible gel stays in good contact with the skin during movement, hence the impedance also remains low when the subject is moving[48].

Sometimes, the conductive gel will cause allergic symptoms on the skin and dry in a short time causing noise in the electrical signals obtained[49]. To avoid this problem, also dry electrodes have been commercialized, but they need to be fixed on the skin with medical tape, that incur in uncomfortable feeling of the patients[50,51].

Among the possible candidates, cellulose modified with PANI- PAAMPSA could be a valid option, dude its high sensitivity, biocompatibility and low cost[52]. In addition, the gel needed in that case could be simply water, because PANI remains in the conductive form thanks to the presence of PAAMPSA template. Finally, its excellent flexibility and mechanical stability confers to that material the potential to be regarded as structural support for wearable devices[53].

Just a few measurements were performed in my laboratory about this application because the study is at the very beginning stage. Briefly, while the subject was sitting on a chair and not moving, two electrodes made of cell-PANI/PAAMPSA with the dimensions of 3 cm were positioned as shown in Fig. 18 and connected to a CHI660C potentiostat. The electrodes were wet with water before recording signals. The results obtained are reported in Fig. 19.

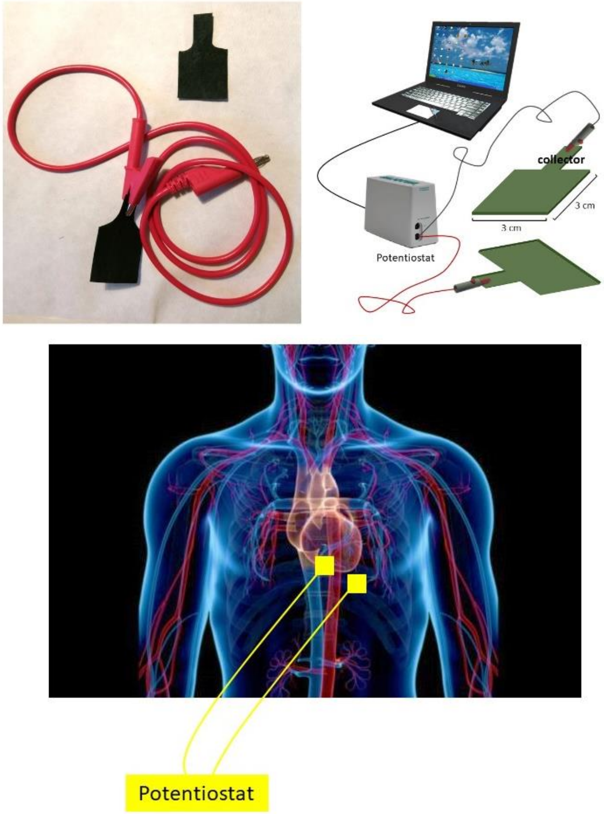

Fig. 18: positioning of electrodes oh human subject

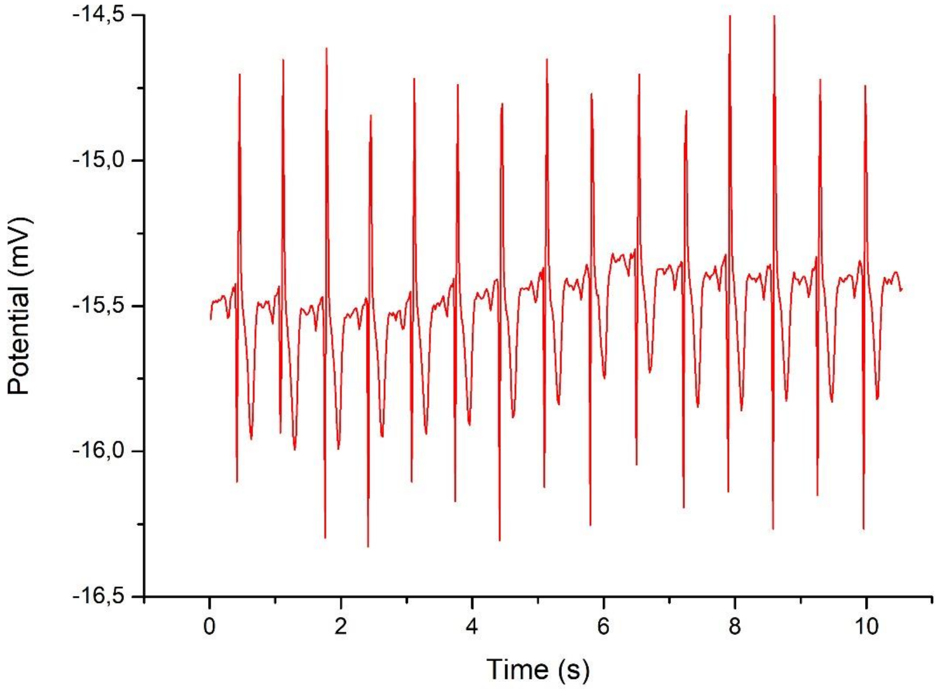

Fig. 19: output ECG obtained with that homemade setup.

Even if the baseline was not linear due to the approximate setup of the system (it was the very first measurement), the heart rate was clearly visible, allowing us to calculate a rate of about 86 beats per minute, that is aligned with a healthy subject[53]. A lot of other measurements and studies must be conducted about this topic, but these results were very promising to obtain ECG electrodes of new generation that could be low cost, of light weight, and disposable to preserve hygiene during monitoring.

References

1. G. Barandun, M. Soprani, S. Naficy, M. Grell, M. Kasimatis, K.L. Chiu, A. Ponzoni, F. Güder, *ACS Sensors.*, **2019**, 4, 1662–1669.
2. J. Fan, S. Zhang, F. Li, Y. Yang, M. Du, *Cellulose*, **2020**, 27 9157–9179.
3. H. Seddiqi, E. Oliaei, H. Honarkar, J. Jin, L.C. Geonzon, R.G. Bacabac, J. Klein-Nulend, *Cellulose,* **2021**, 28, 1893-1931.
4. L. N. V. K. Devabaktuni Lavanya, P. K. Kulkarni, M. Dixit, P. K. Raavi, *Int. J. Drug Formul. Res.*, 2015, 2, 19–38.
5. W. He, J. Tian, J. Li, H. Jin, Y. Li, *BioResources*, **2016**, 11, 8535–8547.
6. F. V. A. Dutra, B. C. Pires, T. A. Nascimento, V. Mano, K. B. Borges, *RSC Adv.*, 2017, 12639–12649.
7. S. Ke, T. Ouyang, K. Zhang, Y. Nong, Y. Mo, Q. Mo, Y. Wei, F. Cheng, *Macromol. Mater. Eng.*, 2019, 304, 1–10.
8. O. Hajlaoui, R. Khiari, L. Ajili, N. Batis, L. Bergaoui, *Chem. Africa.*, 2020, 3, 783–792.
9. J. E. Yoo, J. Bae, *Bull. Korean Chem. Soc.*, 2013, 34, 3825–3828.
10. J. E. Yoo, J. L. Cross, T. L. Bucholz, K. S. Lee, M. P. Espe, Y. L. Loo, *J. Mater. Chem.*, 2007, 17, 1268–1275.
11. M. J. R. Cardoso, M. F. S. Lima, D. M. Lenz, *Mater. Res.*, **2007**, 10, 425–429.
12. J. W. Jeon, J. O’Neal, L. Shao, J. L. Lutkenhaus, *ACS Appl. Mater. Interfaces.*, **2013**, 10127–10136.

13. E. M. Kutorglo, F. Hassouna, D. Kopecký, L. Fišer, I. Sedlářová, A. Zadražil, M. Šoóš, *Colloids Surfaces A Physicochem. Eng. Asp.*, **2018**, 557 137–145. https://doi.org/10.1016/j.colsurfa.2017.10.082.

14. T. Bucholz, Y. Sun, Y. L. Loo, *J. Mater. Chem.*, **2008**, 18, 5835-5842.

15. X. Zhang, J. Zhu, N. Haldolaarachchige, J. Ryu, D. P. Young, S. Wei, Z. Guo, *Polymer (Guildf).*, **2012**, 53, 2109–2120.

16. I. Ragazzini, I. Gualandi, S. Selli, C. Polizzi, M.C. Cassani, D. Nanni, F. Gambassi, F. Tarterini, D. Tonelli, E. Scavetta, B. Ballarin, *Carbohydr. Polym.*, **2021**, 254, 117304.

17. T. A. Blank, L. P. Eksperiandova, K. N. Belikov, *Sens. Actuators B Chem.*, **2016**, 228, 416–442.

18. W. Ahmad, *Materials (Basel).*, **2021**, 14, 1–19.

19. S. Xia, D. Zhang, Z. Liu, and H. Zhang, *Int. Conf. Meas. Technol. Mechatronics Autom.*, **2019**, 322–326.

20. J. K. Atkinson, *Stud. Conserv.*, **2014**, 59, 205–212.

21. L. J. Klein, *Sensors (Switzerland)*, **2017**, 17, 1–21.

22. M. Maksimović, M. Cosović, *Int. Symp. Infoteh-jahorina*, **2019**, 20–22.

23. M. A. Najeeb, Z. Ahmad, R. A. Shakoor, *Adv. Mater. Interfaces*, 2018, 21,1–19.

24. D. G. Yarkin, *Sens. Actuators A Phys.*, **2003**, 107, 1–6.

25. Y. Sakai, M. Matsuguchi, N. Yonesato, *Electrochim. Acta*, **2001**, 46, 1509–1514.

26. S. S. Sandhu, *IEEE Sens. J.*, **2020**, 20, 12574–12581.

27. Z. Ahmad, Q. Zafar, K. Sulaiman, R. Akram, K. S. Karimov, *Sensors*, **2013**, 13, 3615–

3624.

28. Z. Pang, Z. Yang, Y. Chen, J. Zhang, Q. Wang, F. Huang, Q. Wei, *Colloids Surfaces A Physicochem. Eng. Asp.*, **2016**, 494, 248–255.
29. I. Rahayu, D. R. Eddy, A. R. Novianty, R. Rukiah, A. Anggreni, H. Bahti, S. Hidayat, *IOP Conf. Ser. Mater. Sci. Eng*., **2019**, 509, 12051.
30. N. C. Nepomuceno, A. A. Seixas, E. S. Medeiros, T. J. A. Mélo, *J. Solid State Chem.*, **2021**, 302, 122372.
31. A. Murthy, A. Manthiram, *Chem Commun (Camb).*, 2011, 47, 68824.
32. K. K. Kim, *Nano Lett*, **2015**, 15, 52407.
33. M. Z. Seyedin, J. M. Razal, P. C. Innis, and G. G. Wallace, *Adv. Funct. Mater*., **2014**, 24, 2957-2966.
34. M. Wu, Y. Li, N. An, J. Sun, *Adv. Funct. Mater*., **2016**, 26, 6777- 6784.
35. C. S. Boland, *ACS Nano*, 2014, 8, 8819-30.
36. M. J. R. Cardoso, M. F. S. Lima, D. M. Lenz, Mater. Res., 2007, 10, 425–429.
37. M. I. S. Veríssimo, J. A. B. P. Oliveira, D. V. Evtuguin, M. T. S. R. Gomes, *ACS Sens.* 2019, 4, 2915-2921.
38. M. Sinha, P. Verma S. Panda, *Flex. Print. Electron.*, **2020**, 5, 14014.
39. Muchorski, D., *Tensile properties of paper and paperboard*, TAPPI, **2006**.
40. G. Acar, O. Ozturk A. J. Golparvar, T. A. Elboshra, K. Böhringer, M. K. Yapici, *Electronics*, **2019**, 8, 479.
41. A. Ankhili, X. Tao, C. Cochrane D. Coulon V. Koncar, *Materials*, **2018**, 11.

42. A. M. Shathi, C. Minzhi, N. A. Khoso, H. Deb, A. Ahmed, W. Sai Sai, *Synth. Met.*, **2020**, 263, 116329.

43. Y. Yamamoto, D. Yamamoto, M. Takada, H. Naito, T. Arie, S. Akita, K. Takei, *Adv. Healthcare Mat.*, **2017**, 6, 1700495

44. M. K. Yapici, T. E. Alkhidir, *Sensors*, **2017**, 17, 17040875.

45. S. Kaplan Berkaya, A. K. Uysal, E. S. Gunal, S. Ergin, M. B. Gulmezoglu, *Biomed. Sign. Process Control.*, **2018**, 43, 216-235.

46. G. Acar, O. Ozturk, A. J. Golparvar, T. A. Elboshra, K. Böhringer, M. K. Yapici, *Electronics*, **2019**, 10, 8050479.

47. J. G. Webster, J. W. Clark, *Medical Instrumentation: Application and Design*, Wiley, **2008**.

48. A. Amale, T. Xuyuan, C. Cédric, K. Vladan, C. David, T. Jean-Michel, *Sensors*, **2018**, 12, 3890.

49. R. Castrillón, J. J. Pérez, H. Andrade-Caicedo, *Biomed. Eng. Online.*, **2018**, 17, 38.

50. M. M. Puurtinen, S. M. Komulainen, P. K. Kauppinen, A. V. Malmivuo, *Int. Conf. IEEE Eng. Med. Soc.*, **2006**, 6012-6015.

51. S. Tsukada, H. Nakashima, K. Torimitsu, *Plose*, **2012**, 7, 33689.

52. K. Zhang, P. Tao, Y. Zhang, X. Liao, X. Nie, *Carb. Polym.*, **2019**, 213, 228-235.

53. G. Ruffini, S. Dunne, L. Fuentemilla, C. Grau, E. Farres, J. Marco-Pallares, P. C. Watts, *Sens. Actuators A Phys.*, **2008**, 144, 275–279.

6 An investigation on different catalysts for Oxygen Evolution Reaction to be applied in a dual circuit Redox Flow Battery

6.1 Aim of the chapter

The work described in the present chapter is part of a project carried out during a six-month stay at EPFL (Ecolé Polytechnique Fédérale de Lausanne) Sion under the supervision of prof. Hubert Girault.

At first, the possibility of synthesizing IrO_x by using a novel technique called photonic curing was investigated by varying the pH of Iridium salt precursor and parameters of the Xe flashing lamp. Then, the synthesis of Mn-doped RuO_2 and Zn-doped RuO_2 was carried out with the same technique and performances towards oxygen evolution were evaluated electrochemically. Chosen the best synthesized catalyst, it was applied in a dual circuit Redox Flow Battery where the electrolyte was used as mediator together with the catalyst to produce oxygen *via* water splitting reaction.

6.2 Introduction

6.2.1 A new concept of Redox Flow Battery

One of the biggest challenges all over the world regards the transition from fossil fuels to a hydrogen driven energy economy. Today, most of the hydrogen is produced by steam reforming of CH_4 [1-4]. A green alternative consists of producing hydrogen by water electrolysis as shown in equation (1). As an advantage, also oxygen could be produced in the meantime.

$$(1) \qquad 2H_2O \rightarrow 2H_2 + O_2$$

Amstutz and co-workers proposed in 2014 the idea to couple a system for water electrolysis to a Redox Flow Battery (RFB). In this dual circuit, as schematized in Scheme 1 the species present in the battery could also act as redox mediators (electron donors or acceptors) to make the water splitting [5]. The main advantage of this system is the possibility to carry on HER and OER separately in two outer reservoirs on the negative and positive side of the battery, avoiding the recombination of water molecules [6]. Moreover, every reaction can be conducted independently from the other in terms of speed of the reaction and choice of catalyst.

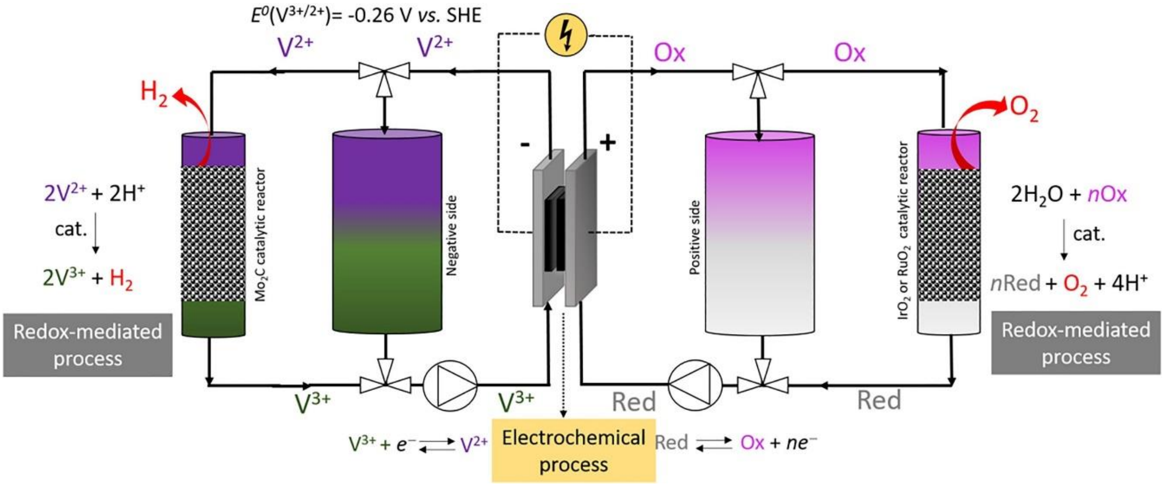

Scheme 1: dual circuit redox flow battery based on Vanadium and Manganese for water splitting.

Focusing on the positive side, the redox couple Mn^{III}/Mn^{II} represents a valid candidate as a mediator for the OER, with a potential of 1.51 *vs* SHE. This couple is of great interest also in the battery because of the higher energy density compared to the well-known all Vanadium RFB[7]. The main disadvantage of having manganese in the system is its instability in solution and its disproportionation reaction as shown in equation (2):

(2) $$2\mathrm{Mn}^{3+} + 2\mathrm{H_2O} \rightarrow \mathrm{Mn}^{2+} + \mathrm{MnO_2} + 4\mathrm{H}^+$$

To avoid this side reaction, one solution is to use high acid concentrations for displacing the equilibrium to the left and stabilising the Mn^{3+} species. For this reason, an acid-resistant electrocatalyst is needed for the redox mediated OER. Many studies were conducted in the past decades on this topic. Earlier in 1966 for example, Damjanov *et al.* studied the catalytic behaviour of different metals, showing activities in the following order: $Ir \approx Ru > Pd > Rh > Pt > Au > Nb$. Moreover, oxides of each catalyst exhibit oxygen overpotentials much lower than their respective metallic elements[8].

In the water splitting, oxygen evolution reaction (OER) mechanism has been extensively studied and numerous pathways have been proposed, but it is still an enigma in the field of electrocatalysis due to the possible presence of non-insulatable intermediates. Moreover, it is kinetically limited due to its four electrons transfer redox reaction that requires a higher overpotential than HER. Thus, the need of an active electrocatalyst for this reaction is of great interest among researchers[3,4]. A representation of OER is given in Scheme 2.

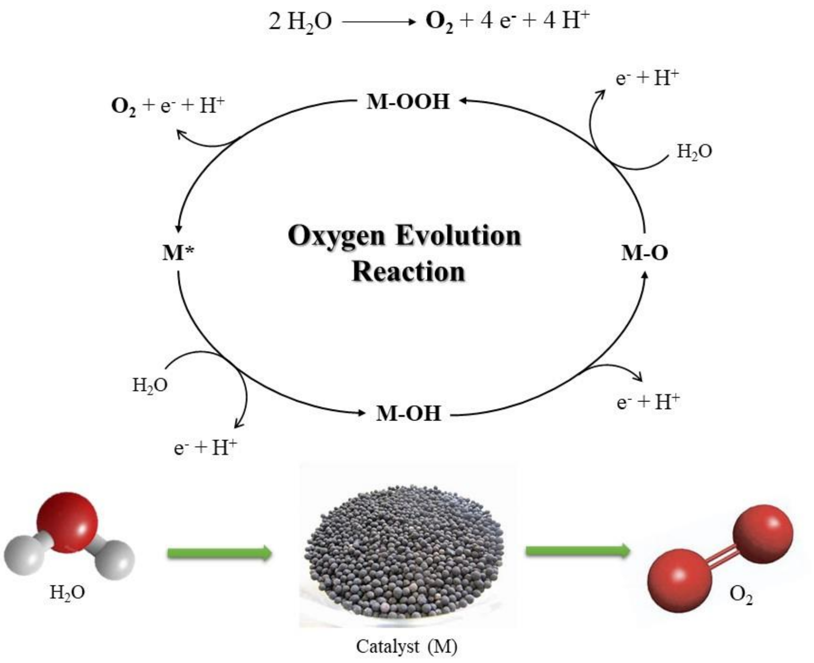

Scheme 2: representation of OER mechanism

Considering their higher activities, Ir and Ru oxides are the most widely used catalysts for OER. In particular, RuO_2 is often more active than IrO_2, but the problems related to instability (corrosion) limit its use in acidic media[9].

6.2.2 Iridium oxides for OER

Iridium chemistry deals with a wide range of species in which the metal is present in oxidation states that vary from 0 to +6, although only the +1, +3 and +4 compounds are commonly formed and studied. The +3 and +4 states form complex ions in aqueous solutions with a coordination number equal to 6. Different suggestions have been presented about the chemical nature of iridium(IV) oxides, because it's easy to form different species during the synthesis, varying from IrO_2 [9-11] to $Ir(OH)_4$ [12] to mixture of the two [13]. This is the reason why in literature the label IrO_x is often reported[14]. Moreover, as shown in Fig.1, Iridium amorphous oxides were demonstrated to have a higher catalytic activity towards OER compared to the rutile IrO_2[15]; the enhanced activity was found to be related to the presence of electronic defects in the near-surface region of the catalyst[16].

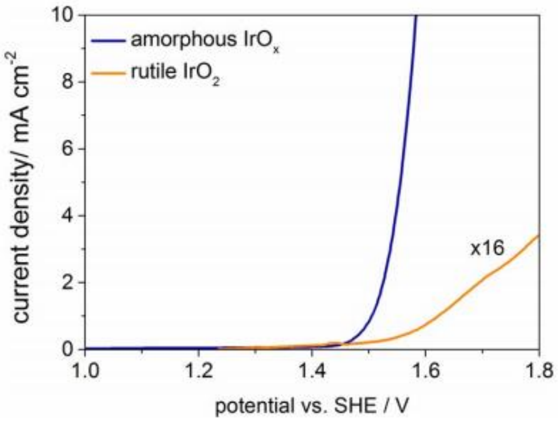

Fig. 1: LSV curves of amorphous IrO_x and rutile IrO_2

Hence, as well-known, the availability of certain edge atoms is improved decreasing the particle size of the catalyst[17]. The most reported method in literature for the synthesis of nanoparticles of IrO_x is that of Mallouk and co-workers. Briefly, K_2IrCl_6 is firstly converted into hexahydroxoiridate(III) ($Ir(OH)_6^{3-}$) by a ligand exchange reaction, and finally oxidized into iridium oxide[18,19]. Starting from the same potassium salt, some others pathways are reported using for example microwave[3] or plasma[20] assisted techniques. Briefly, the reaction is presented in Scheme 3 below.

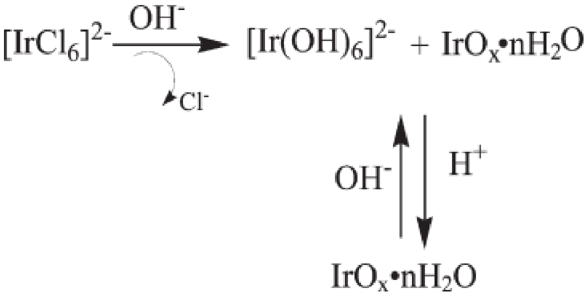

Scheme 3: reaction pathway for the hydrolysis and condensation of IrO_x

After the hydrolysis in alkaline conditions, $[Ir(OH)_6]^{2-}$ partially polymerizes to form IrO_x * nH_2O, stabilized by OH^- groups. These became anionic clusters that get protonated and they made a condensation with $[Ir(OH)_6]^{2-}$, protonated too. This condensation reaction is very slow, only 30% yield in alkaline media. If H^+ is added, the yield is completed to 100%. If the pH is increased, the reaction is pushed towards the hydroxyde form of Ir^{IV}, and the yield decreases again[21]. The large-scale production of IrO_x, and possibly low-cost, is of great interest, but not many researches are conducted on a particular technique called photonic curing, which can provide also fastness and low temperature heating of the samples.

6.2.3 Ruthenium oxides for OER

In the acidic conditions, it is well known that RuO_2 can exhibit much higher catalytic activity than iridium oxides, while it is unstable because of the formation of soluble RuO_4 at anodic potential. Therefore, tremendous endeavours have been made to the design and development of highly efficient RuO_2 catalysts with great success, and many effective strategies have thus been well developed, such as morphology design, electronic structure engineering, defect engineering, enhancing conductivity, and heterostructure engineering[22-28].

Metal doping is considered as an effective strategy to improve the electrocatalytic activity of RuO_2, since the incorporation of suitable foreign metal atoms can effectively enhance the conductivity and alter the electronic structures[29-31]. Furthermore, the defects/vacancies in ultrasmall nanoparticles are expected to enhance the intrinsic activity. Hence, engineering ultrasmall and defective RuO_2 nanoparticles is a promising strategy to achieve excellent OER activity in acidic media.

Replacing Ru ions with divalent Zn ions for example, can induce some oxygen vacancies and reduce the crystallinity of RuO_2. Correspondingly, is reported that the size of Zn doped RuO_2 nanoparticle can be reduced. Lastly, the Zn species can be readily removed by means of acid treatment so some defects would be created and the particle sizes are further reduced. A representation is given in Fig. 2.

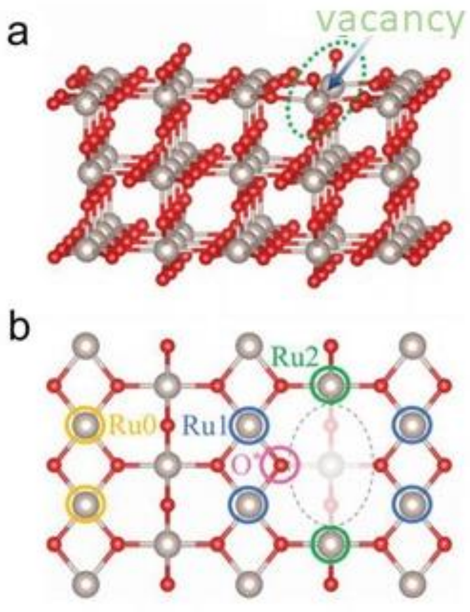

Fig. 2: a) side view and b) top view of defective RuO_2 structure[32]

Doping RuO_2 with different atoms gave interesting results not only with Zn. For example, is reported that partial charges of Ru atoms in Cu-doped RuO_2 become less positive, resulting in a more moderate binding strength toward oxygen intermediates and thus substantially improved OER activity[33].

The doping of Mn ions in RuO_2 can effectively increase the performance of OER through impairing oxygen binding and heightening hydroxyl binding toward electrocatalysts. According to the density functional theory (DFT) calculation, the p-band center of O and d-band center of Ru increase the gap between the Fermi level, hence, improving the performance of oxygen evolution because of the optimized energy level. In comparison with RuO_2 nanocrystals, Mn-doped RuO_2 nanocrystals exhibit larger current density at the same overpotential with an unprecedented electrocatalytic activity and excellent durability in the process of OER as shown in Fig. 3.

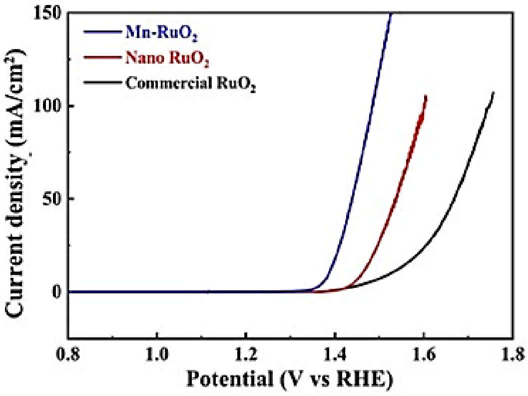

Fig. 3: LSVs of doped RuO$_2$[34]

6.2.4 Photonic curing

The photonic curing (also known as flash light annealing or intense pulsed light sintering) is a technique of heating and sintering thin films by using an intense light pulse generated by a Xenon flash lamp. The first and still most common application of this technique is the sintering of Ag and Cu nanoparticles to fabricate conductive paths on thermally sensitive substrates for printed electronics[35]. In addition, it is employed also in synthesis of thin-film transistors[36], solar cells[37] and RFID components[38].

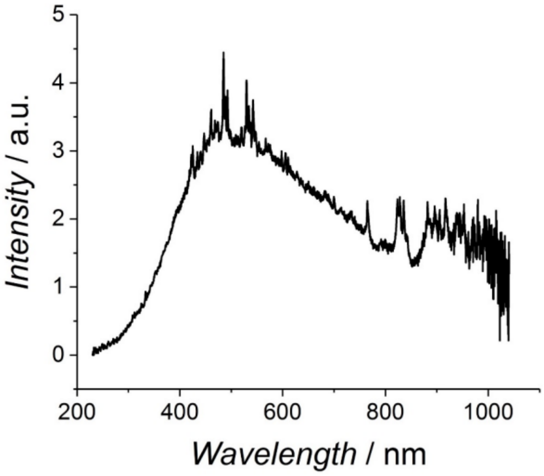

Fig. 4: emission spectrum of a Xenon flash lamp with 750 V of blank voltage and 220 µs pulse length

The lamp emits a broad spectrum of wavelengths (*i.e.* 190 – 1100 nm, spectrum shown in Fig. 4) as micro to milliseconds pulses that the materials receive in comparison with their specific absorption of energy and result in a contactless heating of the samples. Meanwhile, the energy density varies as a function of the applied voltage (reaching up to 30 J cm^{-2} per light pulse). Facilities for printed light synthesis is shown in Fig. 5[38].

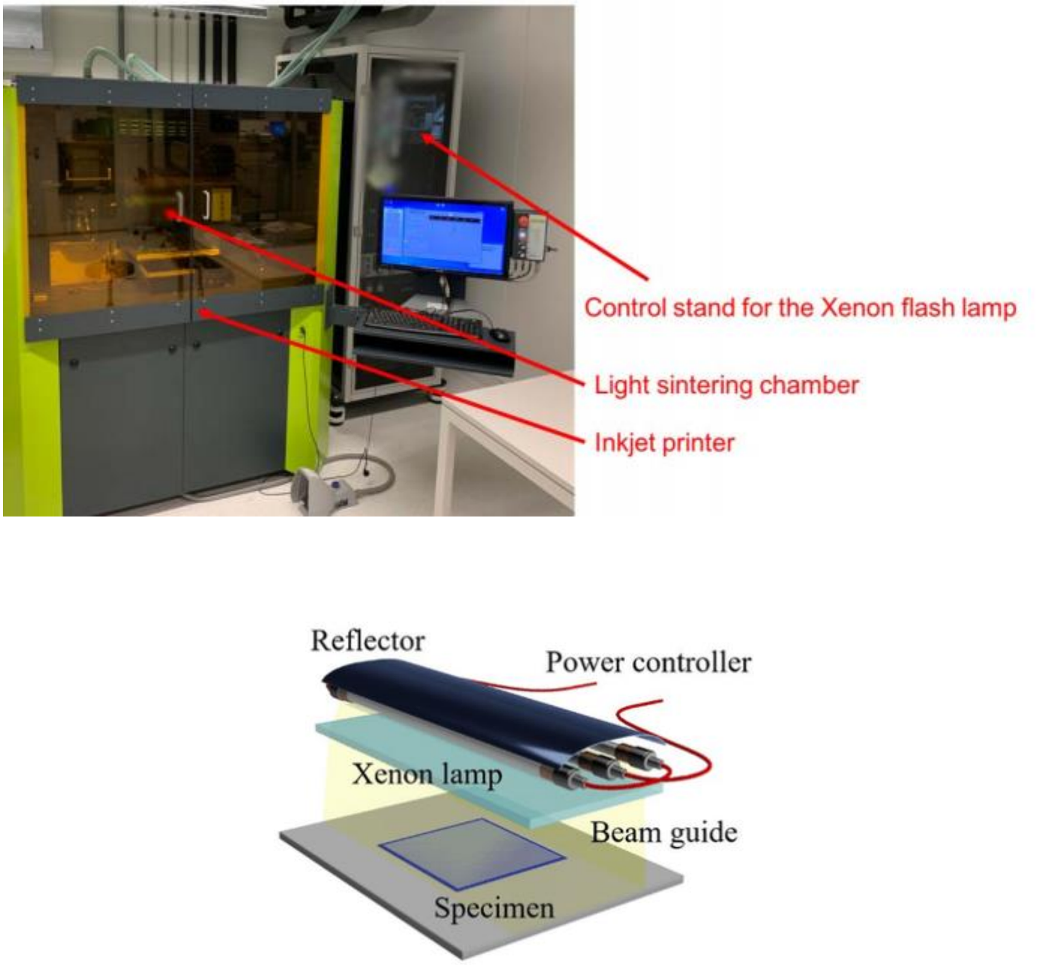

Fig. 5: printed light synthesis facilities.

Depending on the optical properties of the samples cured, many various reactions (such as sintering, thermal decomposition or redox reactions) could take place during the very short period of time of a flash and hundred degrees of temperature could be reached.

Substrates that are poorly absorbing light or non-absorbing at all, are not directly affected by this technique, but can play a role in the reaction in any case because of the heat transfer of the absorbing species eventually present [39].

More specifically, the fundamental principle of photonic curing is the light absorption by metal-based thin films, promoting electrons from the valence to the conduction band. If electrons have more than the required energy from the conduction band, the excess is released as phonons leading to localized heating of the material[23]. Hence, the thermal energy generated is a consequence of the light absorbed and it is attributable both to the absorptivity of the film and to the thickness.

Irradiating materials with high energetic photons as, in our case, with a Xenon flash lamp, the so called *hot-electrons* are generated. Hot electrons are essentially electrons that are not in thermal equilibrium with their immediate environment (generally, the atoms comprising a material). They have a very high effective temperature (as high as several thousand Kelvin) compared to room temperature, due to their kinetic energy. This excess can be dissipated within free electrons via an electron-electron scattering mechanism. This process is known as *thermalization* as it leads to the formation of a hot electron gas with a well-defined electronic temperature. In case of a system composed of the metal nanoparticle or nanoparticle/adsorbate, the electron-molecular vibration scattering is transferred into adsorbates. Hence, immediately after the absorption of the energy pulse a nonequilibrium distribution of nascent nonthermal electrons is created. The non-equilibrium electron is temporarily transferred into an empty electronic level, in the adsorbate with an energy, leading to the creation of an intermediate negative ion state. The electron then could scatter back with an energy into the metal conduction band or induce chemical transformations in the adsorbate molecule (*i.e.* reduction).

The role of the substrate is very important in the degradation of the adsorbates, besides the convection of heat because of light absorption. The chosen substrates promote initial generation of the hot-electrons. This effect has been described in literature by Clavero[24]. If the substrates would be uncoated the hot-electrons would decay in the material and only a local temperature heat would be generated. If the substrates are coated with precursor salts, during the excitation hot-electrons enter the LUMO of the adsorbate molecule and decay inside the adsorbate energy level before returning to the initial state in the substrate. Such can lead to the generation of heat in the precursor molecule and initiate the thermal degradation step of the precursor. The initial degradation will lead to a cascade of events, where, after the first cluster of metallic nanoparticles is generated, the reaction will expand. Such mechanism can explain the initial degradation of the precursor salts[25].

6.3 Results and discussion

6.3.1 Influence of pH on the flashed synthesis of IrO_x

Firstly, nanoparticles of IrO_x to be used as reference were synthesized following a chemical method reported by Zhao and co-workers [21]. The formation of IrO_x was confirmed by a change in colour of the reaction mixture from brown to dark blue, which occurred after few minutes from the beginning (Fig. 6). Afterwards, the reaction mixture was aged for 24 hours in static conditions (without stirring) before proceeding with the characterization of the product.

Fig. 6: reaction steps of the chemical synthesis of IrO_x

The same precursor salt K_2IrCl_6 was dissolved in solutions at different pH and flashed varying the reaction conditions. To follow the reaction, UV-Vis was used as first characterization. Three absorbtion peaks are important in the spectrum of the iridium salt before and after the reaction[21]:

$\lambda = 313$ nm: $[Ir(OH)_6]^{2-}$ strong, in the UV region. It increases with temperature with a maximum at 90°C. After the hydrolisis step, it decreases due to the formation of IrO_x but it is still present due to the low yield of the reaction. It disappears when nitric acid is added due to the complete yield of the reaction and appears again increasing the pH. (nitric acid is an interference in this region)

$\lambda \approx 580$ nm: $IrO_x * nH_2O$, in the visible region, due to the formation of Ir-O-Ir bonds, both of the colloidal and of the bulk material. It is present after the hydrolysis step but low. It increases after the condensation step. It decreases increasing the pH after the condensation, because the reaction reverses.

$\lambda = 420$ nm, not well described. Probably an intermediate step in the formation of the oxide. Probably due to the protonation of $[Ir(OH)_6]^{2-}$. It becomes larger and decreases with time and conversion. It is probably a slower condensation step.

For the characterization of the flashed materials, only the absorbance peak at 580 nm is considered and it is compared with the one obtained following the reaction used as reference. The maximum absorbance peak for IrO_x is found to be precisely at 578,298 nm in the reported spectra. The absorbance values are referred to that.

First, a qualitative screen is performed in the liquid state to see if some reactions occur varying the pH of the iridium salt solution to be cured. Under alkaline conditions, the presence of OH^- groups is necessary to perform the hydrolysis of the Ir-Cl bonds and the consequent formation of the $[Ir(OH)_6]^{2-}$ complex. The condensation of that complex lead to the formation of Ir^{IV}-O-Ir^{IV} bonds.

As a demonstration that the reaction occurs following the path described, no changes are observed in the UV-Vis spectra until pH 7 was reached. The analysis was repeated 4 times and the samples were cured with 20 pulses at 575 V. As shown in Table 1, the absorbance at 580 nm is not negligible at pH 7, but it has the same value of the starting material, so it is not attributable to IrO_x.

Table 1: UV-vis analyses of sample at pH7. PC: photonic curing.

Sample	Absorbance at 580 nm	
	Before PC	After PC
1	0,22	0,23
2	0,20	0,19
3	0,21	0,21
4	0.19	0,21

Successively, solutions of K_2IrCl_6 from pH 7 to 13 were prepared and studied. As shown in Fig. large variations in the colour of the solution were observed without flashing, from light yellow to pink. The colours also changed with time but the solution at pH 7 was still the same even after 48 hours. The spectra reported were recorded after 48 hours. The peaks around 400 - 450 nm suggest that the first step of the reaction described in Scheme 3 occurs rapidly, leading to the formation of protonated $[Ir(OH)_6]^{2-}$ even whitout any change in the environment. Only time is not enough for the formation of IrO_x with a high yield, in fact no significant absorbance was observed at 580 nm not even after 48 hours (Fig. 7).

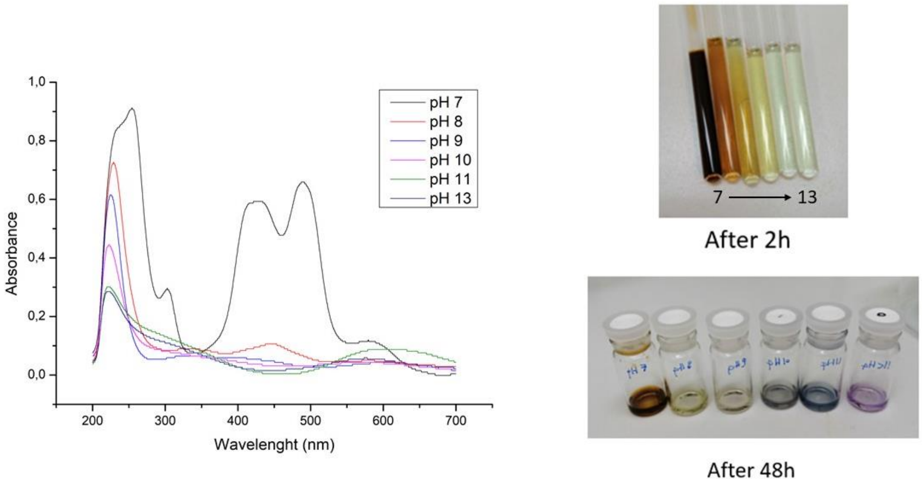

Fig. 7: Uv-vis spectra and colour changes of Iridium salt precursor at different aging time.

The hydrolysis step is necessary for the formation of nanoparticles of IrO_x because no reaction occurred if the pH is less than 10. The maximum of absorbance at 580 nm was obtained with the starting solution at pH 13. Considering the absorbance of the reference IrO_x chemically prepared as 100% (in addition, the value is comparable with the method followed) , a yield of 80% was obtained with photonic curing technique.

The effect of the photonic curing conditions was investigated on the sample at pH 13. The charging voltage of the capacitors in the instrument and the quantity of pulses given to every sample were changed. The yield of the formation of IrO_x nanoparticles was determined by Uv-Vis absorbance at 580 nm also in this case. The results are shown in Fig. 8. Five pulses were not enough to suggest any change in the samples even if the voltage was increased. It is reasonable to think that the temperature raised in the samples during the pulses was insufficient to lead to the formation of the complex $[Ir(OH)_6]^{2-}$ in high yields and the consequent condensation step. The absorbance obtained was directly dependent by the number of pulses and the voltage applied and the highest absorbance was obtained at 575 V with 20 pulses.

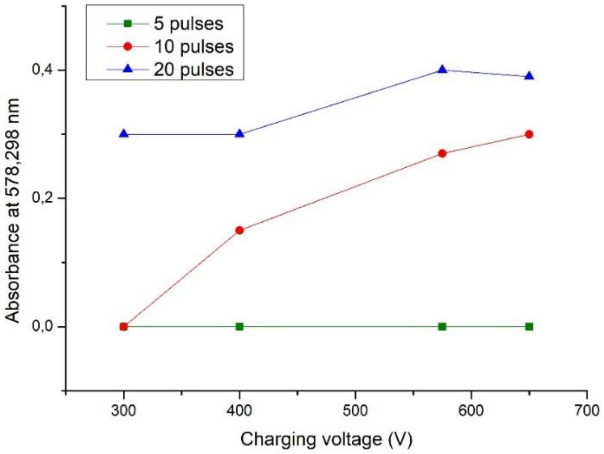

Fig. 8: Flashing condition study about the synthesis of IrO_x

6.3.2 Physical and electrochemical characterization of IrO_x

The SEM analysis of the chemically synthesized IrO_x as reference, revealed the presence of white clusters with an inhomogeneous pattern of dimensions ranging from flakes of 80 – 100 nm to larger agglomerates of more than 2 µm as visible in Fig. 9.

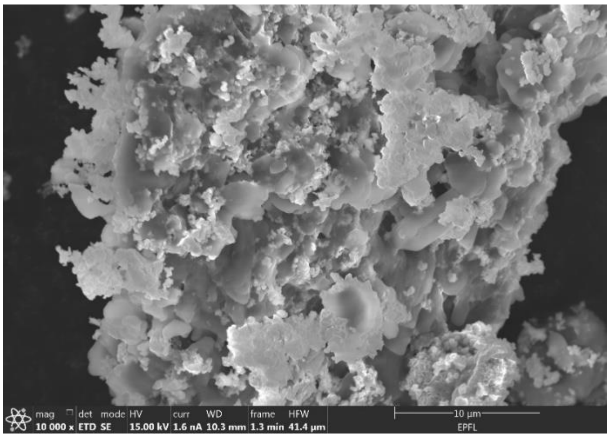

Fig. 9: SEM analysis of IrO_x chemically synthesized.

Besides, the SEM images of the flashed IrO_x revealed the presence of two population of particles. In particular, the average size of the bigger population with a sea-urkin like shape is around 2,0 – 2,5 µm, while for the smaller particles an average size of 0,20 – 0,25 µm was observed (Fig. 10)

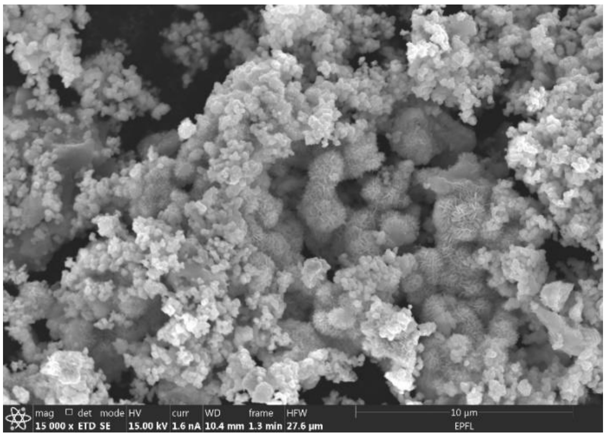

Fig. 10: SEM image of flashed IrO_x

Both the dimensions declared for the chemically synthesized and the flashed IrO_x was confirmed by DLS analyses, suggesting that the dimensions obtained were not in nanometric scale as expected and described in the reference article[21].

Given the ambiguous results obtained with SEM analyses revealing different morphologies and the XRD patterns that were not satisfactory, more analyses were suggested and the physical characterization of IrO_x is currently under examination. On the contrary, electrochemical performances towards OER of both IrO_x obtained *via* chemical route and by photonic curing gave good and comparable results. Particles solution obtained were firstly sonicated for 15 minutes and used in a three electrodes cell setup with a glassy carbon as working electrode. 1.4 V *vs* Ag/AgCl were applied for 60 minutes to deposit IrO_x on the electrode and then tested by LSV technique.

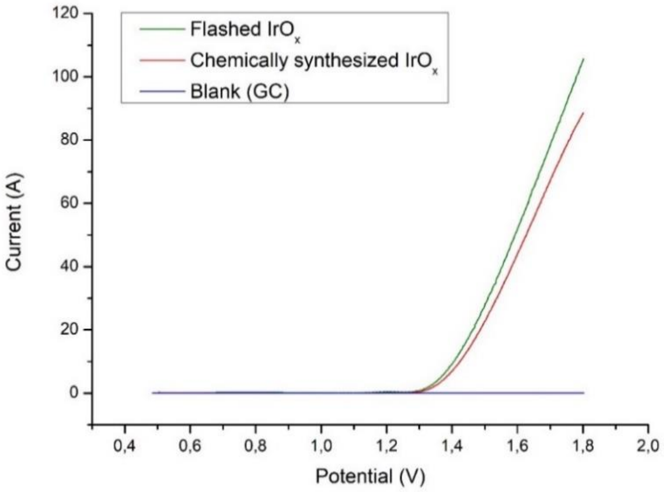

Fig. 11: LSVs comparison between flashed and chemically synthesized IrO_x

Both the materials show an onset potential around 1.3 V *vs* Ag/AgCl as seen in Fig. 11, suggesting that the material synthetized by the new route is the same of the reference. The tests were repeated three times using materials synthesized in different times and they gave the same results aiming that the synthesis of the material is reproducible.

6.3.3 Zn and Mn doping of RuO_2

Considering the previously described state of the art, a step towards the evolution of the here described electrocatalyst was taken by depositing Zn-doped and Mn-doped RuO_2 on carbon cloth by photonic curing technique instead of annealing, were the substrate dark colour helps to increase the amount of the electromagnetic radiation absorbed. In addition, a supported catalyst is much more versatile in terms of application and removal when used in an RFB.

The photonic curing conditions were previously optimized for the synthesis of IrO_x and have been kept unchanged for RuO_2. Briefly, every sample received 20 flashes at 575V, 13 µs pulses. The obtained catalysts were studied and compared with the annealed ones synthesized following a previous reported procedure[32].

Firstly, CC/RuO_2 and Zn-doped RuO_2 were analyzed by means of SEM images (Fig. 12 and 13). It is clear that the addition of Zn and subsequent etching resulted in an increased material porosity, which equals to a greater surface area.

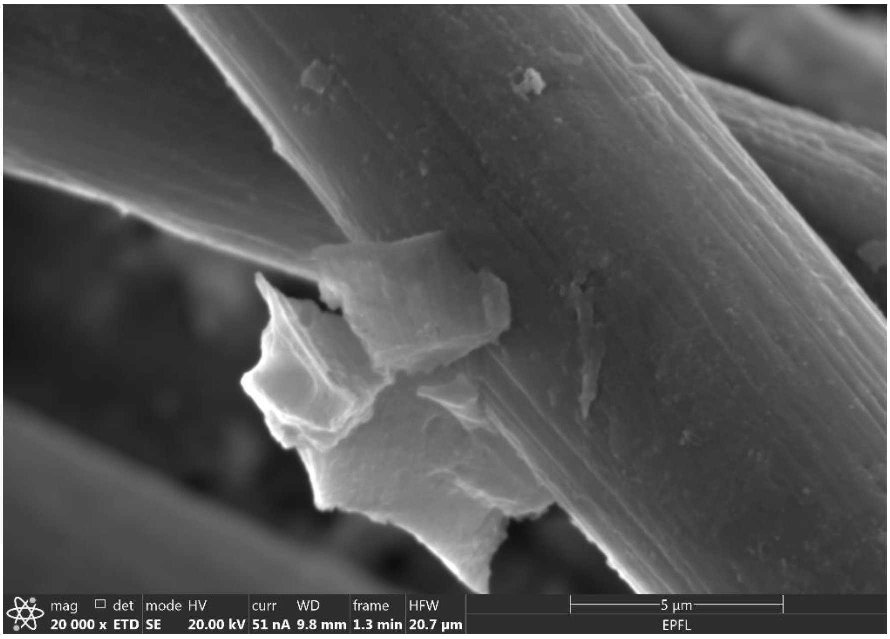

Fig. 12: RuO_2 obtained by photonic curing

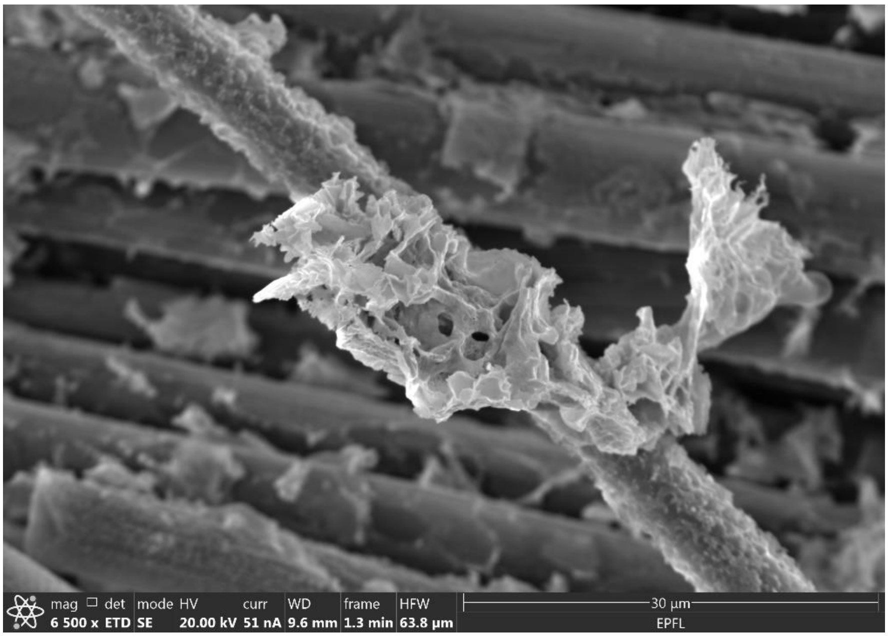

Fig. 13: Zn-doped RuO_2 obtained by photonic curing

Moreover, EDX analyses on Zn-doped RuO_2 before and after etching were performed to confirm that treating samples in 1M H_2SO_4 for 18 hours after flashing was necessary to remove all Zn species present in samples. As shown in Fig. 14, the peak attributable to Zn atoms was not present after etching.

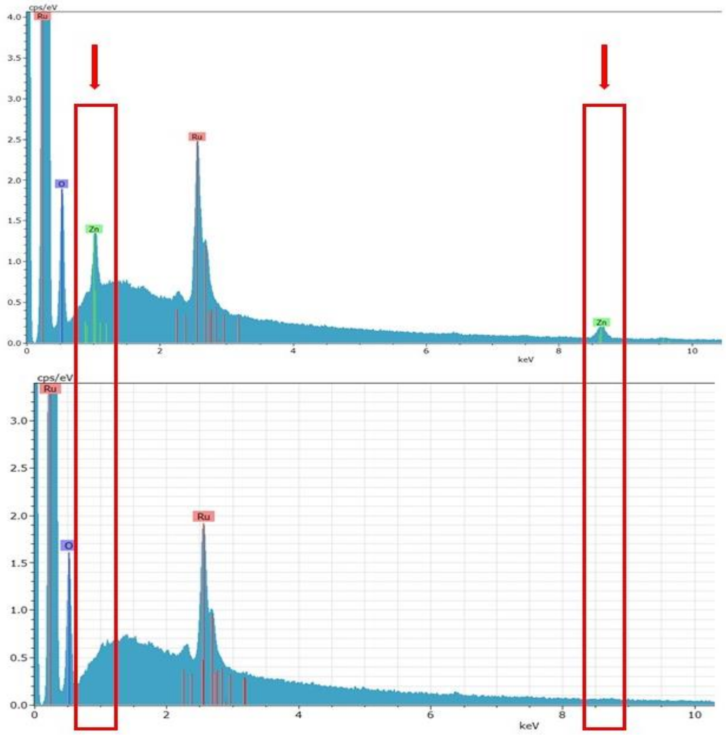

Fig. 14: EDX analyses of Zn-doped RuO_2 before and after etching

Electrochemical performances towards OER were studied for both annealed and flashed Zn-doped catalysts through LSV. As shown in Fig. the performances obtained were very similar, both annealed and flashed catalysts shown an onset potential of 1,25 V *vs* Ag/AgCl and the slope is even better for the flashed sample.

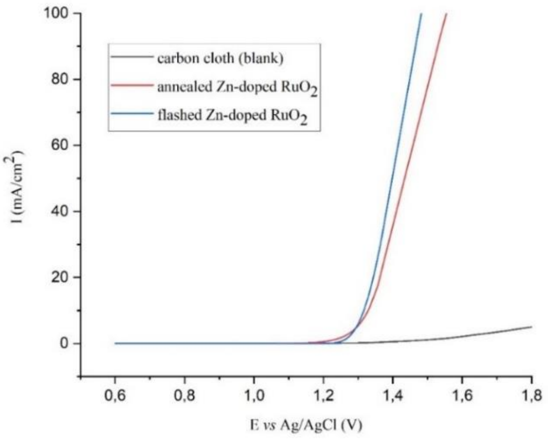

Fig. 15: LSVs comparison between annealed and flashed Zn-doped RuO_2

Electrochemically Active Surface Area (ECSA) is a determintaion of mass activity of a given catalyst. A detailed description of the calculations is reported in “Materials and Methods” section of this chapter, but the obtained results are shown in Fig. 16 and Table 2. Also Mn results are included in this section.

Table 2: ECSA calculations of different samples. C_{dl}: double layer capacitance, RF: roughness factor

Sample	C_{dl} (mF)	ECSA (cm^2)	RF
Carbon Cloth (CC)	3,28	93,770	478,2
CC/RuO_2	6,74	192,82	983,8
CC/Mn-doped RuO_2	8,69	240,24	1266
CC/Zn-doped RuO_2	10,5	301,44	1538

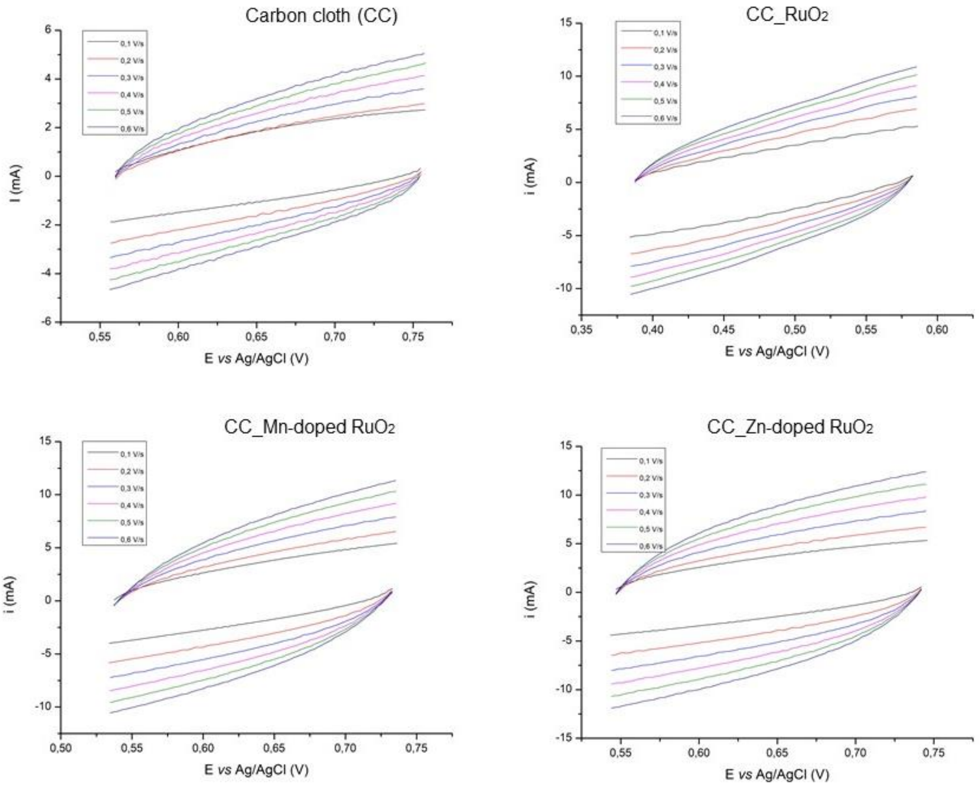

Fig. 16: CVs of different catalysts for ECSA calculations.

As reported in Table. Zn-doped RuO_2 shown an higher ECSA compared to the simple RuO_2, confirming what already declared with SEM images. Contrary to what was expected from the images, the ECSA of Zn-doped material is only 1,5 times higher of RuO_2, suggesting that the activity is probably emphasized more on the surface of the catalyst than in the bulk of the material.

Considering Mn-doped RuO_2, calculations revealed also in this case an increase in the active surface area, confirmed also by SEM analysis as shown in Fig. 17.

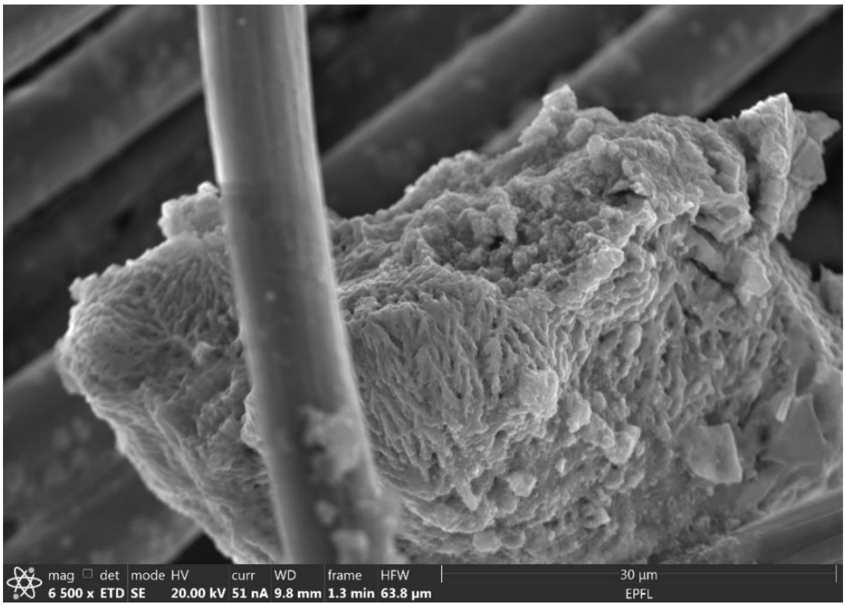

Fig. 17: SEM analysis of Mn-doped RuO_2

In this case, the surface of the catalyst presented cavity and grooves even if not accentuated like the Zn-doped material. An explanation was probably found in the presence of Mn atoms inside the cristallyne structure of RuO_2. Nevertheless, phisical properties of those catalysts are still ongoing.

In addition, LSVs of flashed and annealed CC/Mn-doped RuO_2 were compared. Performances towards OER were found to be comparable also in this case, and a lower onset potential was found for the flashed sample (Fig. 18).

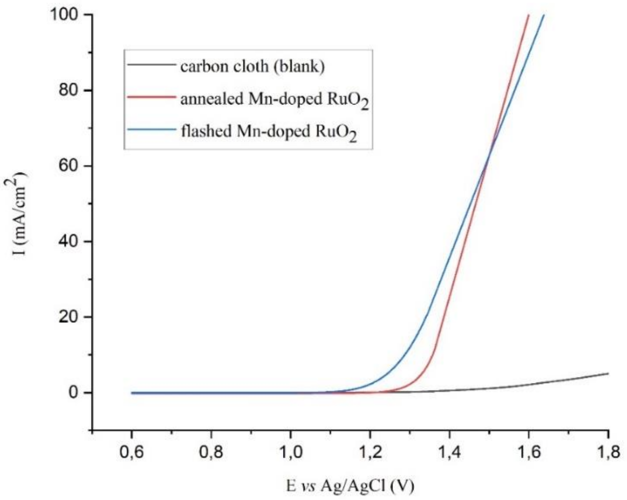

Fig. 18: LSVs comparison between annealed and flashed Mn-doped RuO_2

All the flashed catalysts were compared *via* LSV technique in order to choose the best one. Of course, in this case as for ECSA calculations, the molar amount of $RuCl_3{\cdot}xH_2O$ was equal to the total amount of $RuCl_3{\cdot}xH_2O$ and $MnSO_4{\cdot}xH_2O$in the Mn-doped catalyst because Mn was not etched after being cured. It was not the same in the case of Zn-doped catalyst because Zn was used only to produce porosity in the RuO_2 structure and then removed. In Fig. 19 all the LSVs were summarized and reported. Although it possessed a lower onset potential, CC/Mn-doped RuO_2 had worse performances in terms of production of oxygen than CC/Zn-doped RuO_2, as evidenced by the lower slope of the curve, even if they were very similar.

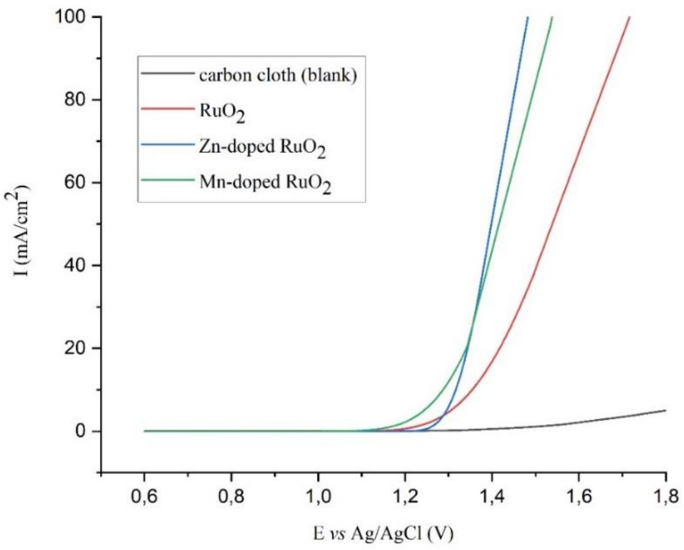

Fig. 19: LSVs of different catalysts

Finally, chosen CC/Zn-doped RuO_2 as the best catalyst of the present study, a test in the RFB was performed. Considering the dimension of the battery available, a catalyst of the dimension of 10 cm^2 was prepared and a mass load of 12.5 mg cm^{-2} was determined using a high precision microbalance. The electrolyte in the RFB was composed of V^{5+} and Mn^{3+} both in 1M concentration and H_2SO_4 3M was used as solvent. It was studied that V^{5+} act as stabilizer despite disproportionation reaction of Mn species. The discharge of the electrolyte solution was followed by Uv-vis where Mn^{3+} had a maximum absorbance peak at 475 nm. As shown in Fig. 20, starting from 40 mL of electrolyte solution at 75% of state of charge, after 150 min of reaction Mn^{3+} could be considered mostly reduced.

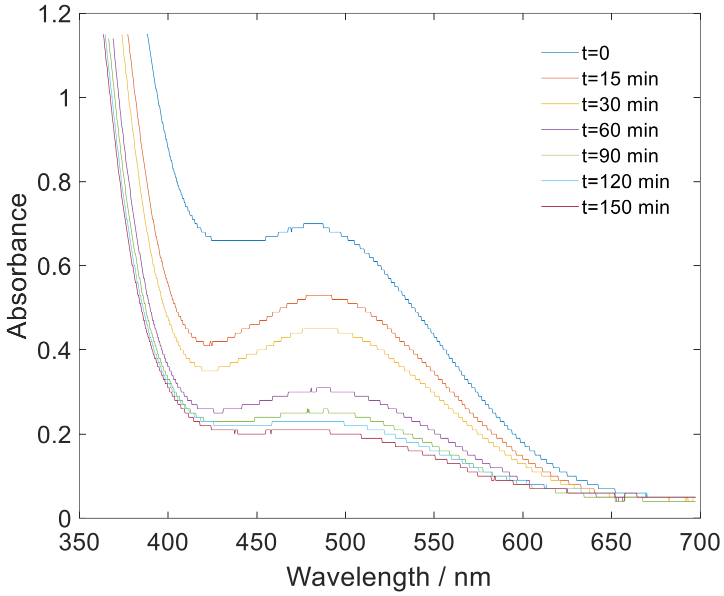

Fig. 20: UV-vis spectra of Mn-containing electrolyte at different times of reaction

Accordingly, discharging the electrolyte, oxygen was produced because Mn^{3+} acted as mediator for OER on the catalyst synthesized. As a demonstration, the amount of oxygen produced was detected with a flowmeter and reported in Fig. 21, (about 14 mL in 150 minutes of reaction).

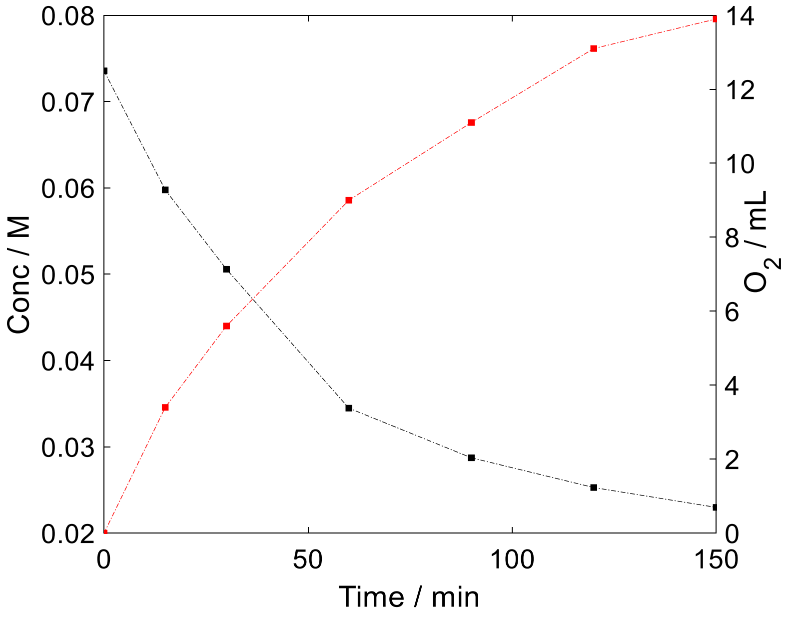

Fig. 21: oxygen produced during OER and decreasing of Mn^{3+} concentration

6.4 Conclusions

The synthesis of IrO_x was carried out *via* photonic curing and the flashing conditions were investigated. Firstly, the pH of the precursor salt solution was studied and monitored by Uv-vis analyses. It was found that the best condition to synthesize IrO_x in a yield of about 80% was to operate at pH 13. The reaction was studied also in terms of power, duration and number of pulses of the Xe flash lamp used and the most promising results were obtained with 20 pulses at 575V, 13µs length.

Furthermore, an investigation on another good catalyst for OER, that is RuO_2, was conducted. In particular an investigation on doping RuO_2 with different metals by annealing was found in literature and used to synthesize Zn-doped and Mn-doped RuO_2 on carbon cloth. These catalysts were used as reference to the newly synthesized ones using photonic curing technique. The best result was obtained with the Zn-doped RuO_2 that exhibited a higher porosity in comparison with non-doped RuO_2.

In conclusion, the best catalyst obtained was tested in the RFB and studied in terms of discharging of the electrolyte and production of oxygen demonstrating that a catalyst of the dimension of 10 cm^2 and a mass load of 12.5 mg cm^{-2} was able to product 14 mL of O_2 in 150 min.

6.5 Experimental section

6.5.1 Materials

All chemicals and solvents are ACS reagent grade, were purchased from commercial vendors and used directly unless otherwise stated. Potassium hexachloroiridate (K_2IrCl_6, 99.99%), Ruthenium(III) chloride hydrate($RuCl_3 \cdot xH2O$), Manganese(II) sulphate monohydrate ($MnSO_4 \cdot xH_2O$), Zinc chloride ($ZnCl_2$), Hydrochloric acid (HCl 36% wt), Nitric acid (HNO_3 68% wt), Sodium Hydroxyde (NaOH pellets) and Sulfuric acid (H_2SO_4, 95.0–98.0 %) were purchased from Sigma-Aldrich (now Merck KGaA, Darmstadt, Germany). The CC substrate is commercially available and was treated at 120 °C for 4 h to enhance the hydrophilicity. Deionized water was used throughout all experiments.

6.5.2 Synthesis of IrO_x

Briefly, 50 mL of 2 mM K_2IrCl_6 was adjusted at pH 13 by adding NaOH 10%. The solution was heated at 90 °C for 90 minutes. After cooling down, the solution was put in ice bath with vigorous stirring for 20 minutes. 1 mL of HNO_3 3M was added rapidly and the solution stirred for 80 minutes. The solution was left overnight to perform the complete condensation of IrO_x. For the photonic curing, samples were prepared adjusting 2 mM K_2IrCl_6 at desired pH by adding NaOH 10%. NMR tubes were used for flashing samples.

6.5.3 Synthesis of doped RuO_2

Generally, 1.20 g $RuCl_3 \cdot xH_2O$, and 0.40 g of $ZnCl_2$ or 0,5 g of $MnSO_4 \cdot xH_2O$, and 0.5 mL of hydrochloric acid (36% wt) were dissolved into 10 mL of deionized water under magnetic stirring. The resulting precursor solutions were stored under dark for further use. A piece of CC (1 cm × 2 cm) was dipped into the precursor solution for ≈5 s and was subsequently taken out. After drying under 60 °C, the obtained carbon cloth was annealed at 350 °C for 3 h (ramping rate: 10 °C min^{-1}) in air. Zn-doped RuO_2 samples were then immersed in 1.0 M H_2SO_4 for 18 h. The final products were obtained after washing and drying. 1,20 g of $RuCl_3 \cdot xH_2O$ and 0.5 mL of hydrochloric acid (36% wt) were dissolved into 10 mL of deionized water under magnetic stirring and used to prepare CC-RuO_2. The typical loading masses of defective RuO_2/CC and RuO_2/CC were determined to be 0.94 and 1.25 mg cm^{-2}, respectively, using a high precision microbalance.

6.5.4 Photonic curing

Four repetitions of K_2IrCl_6 solutions 9,40 mM are cured adjusting the pH from 7 to 13 with NaOH 0.5 M. A PulseForge 1300 system (Novacentrix, USA) integrated in a X-Serie CeraPrinter (Ceradrop, France) was used for the study. The energy of the flashes was adjusted by controlling the lamp driver charging voltage, which were 575 V long pulse profile, 13 µp of length, 20 pulses every sample excluding the photonic curing conditions study. The solutions were neutralized with H_2SO_4 after the process.

6.5.5 UV-Vis characterization

The photonic curing reaction was monitored by UV-Vis. The characteristic peak of iridium oxides is set at 580 nm according to literature[28]. The absorbance value of the reference was considered as 100% yield and the other values were related to that. All the images and the spectra reported below are referred to the neutralized samples and obtained after a baseline correction.

6.5.6 Electrochemical characterization

Electrochemical characterizations of the samples were performed in a three-electrode cell. To be characterized, IrO_x was deposited on GC applying 1.4 V *vs* Ag/AgCl for 60 minutes using acidic colloidal solution previously prepared. Rotating disk with the diameter of 5 mm tested in H_2SO_4 1 M *via* Linear SweepVoltammetry (LSV), rotation rate 900 rpm.

6.5.7 Instruments and methods

The photonic curing of the samples was performed with a PulseForge 1300 system (Novacentrix, USA) integrated in a X-Serie CeraPrinter (Ceradrop, France). The energy of the flashes was adjusted by controlling the lamp driver charging voltage, which were 575 V long pulse profile, 13 µp of length, 20 pulses every sample. UV-Vis analyses were performed with an Ocean Optics FLAME-S spectrometer with a 1 mL disposable methacrylate cuvette. Electrochemical characterizations of the samples were performed with a PGSTAT 204 Autolab potentiostat (Metrohm, Nederlands) in a three-electrode cell using a GC-RD electrode modified as working electrode (WE), an Ag/AgCl (3M KCl) as reference electrode (RE, CHI111, CH Instruments) and a carbon felt as counter elecrode (CE). The dimension of the particles synthesized were determined using a Zetasize Dynamic Light Scattering (Malvern Panalytical, United Kingdom), in a disposable 1 mL methacrylate cuvette. Electrochemically active surface area (ECSA) is calculated from measurements of double layer capacitance (C_{DL}) with cyclic voltammetries (CVs) at diffenrent scan rates. This procedure is particularly convenient because it involves the use of an easily accessible equipment and a small number of analyses, facilitating the screen of a large number of catalysts in a reduced period of time. GC was chosen as the electrode support due to its relative inactivity for Oxygen Evolution Reaction (OER) at moderate overpotentials[40]. 3 M H_2SO_4 is chosen as acidic electrolyte. Also carbon cloth was investigated as background. CV measurements were conducted in static solution by sweeping the potential across the non faradaic region from the more positive to the negative potential and back at six different scan rates: 0.1, 0.2, 0.3, 0.4, 0.5 and 0.6 V s^{-1}. The working electrode was held at each potential vertex for 5 s before beginning the next sweep[41]. The electrochemical capacitance was determined by measuring the non-Faradaic capacitive current associated with the double layer charging from the scan rate dependence of cyclic voltammograms. All measured currents in this non-Faradaic potential region is assumed to be due to the double layer charging. The charging current i_c is measured taking the Cvs at different scan rates. The double layer charging current i_c is equal to the product of the scan rate υ and the electrochemical double layer capacitance C_{dl} as shown in equation below[42].

$$i_c = \upsilon C_{dl}$$

Thus, a plot of i_c as function of υ yields a straight line with a slope equal to C_{dl}. The cathodic (red open circle) and anodic (blue open square) charging currents measured at −0.05 V vs SCE plotted as a function of scan rate. The determined double-layer capacitance of the system is taken as the average of the absolute value of the slope of the linear fits to the data. The ECSA of a catalyst was calculated according to the equation:

$$ECSA = \frac{C_{dl}}{C_s}$$

where Cs is the specific capacitance of the sample or the capacitance of an atomically smooth planar surface of the material per unit area under identical electrolyte conditions (C_s = 0.035 mF cm^{-2} for those calculations). While ideally one would synthesize smooth, planar surfaces of each catalyst to measure Cs and estimate ECSA, this is not practical for most electrodeposited systems. The roughness factor (RF) is calculated by taking the estimated ECSA and dividing by the geometric area of the electrode, 0.195 cm^2. Moreover, in estimating the ECSA from C_{dl}, we do not take into account other possible contributions to the measured capacitance including pseudocapacitance due to ion adsorption and intercalation or chemical capacitance due to the population of electron trap states. The double-layer capacitance measurements assume that the metal oxide catalysts are equally conductive, which is another potential source of error in these measurements.

References

1. D. W. Oxtoby, H. Norman, H. Nachtrieb, H. P. Gillis, H. Norman, H. Helal, *Principles of Modern Chemistry*, Grove, **2002**.
2. C. N. R. Rao, S. Dey, *PNAS*, **2017**, 114, 13385–13393.
3. J. R. Esquius, D. J. Morgan, I. Spanos, D. G. Hewes, S. J. Freakley, G. J. Hutchings, *ACS Appl Energy Mater.*, **2020**, *3*, 800–809.
4. T. Nishimoto, T. Shinagawa, T. Naito, K. Takanabe, *J. Catalysis*, **2020**, 391, 435–445.
5. V. Amstutz, K. E. Toghill, F. Powlesland, H. Vrubel, C. Comninellis, X. Hu, H. H. Girault, H. H., *Energy Environ.*, **2014**, 7, 2350-2358.
6. C. Acar, I. Dincer, G. F. Naterer, *Int. J. Energy Res.*, **2016**, 40,1449–1473.
7. D. Reynard, S. Maye, P. Peljo, V. Chanda, H. H. Girault, S. Gentil, *Chem. Eur. J.*, **2018**, *26*, 7250–7257.
8. S. Chalupczok, P. Kurzweil, H. Hartmann, C. Schell, *Int. J. Electrochem.*, **2018**, 1–15.
9. M. Carmo, D. L. Fritz, J. Mergel, D. Stolten, *Int. J. Hydrog. Energy*, **2013**, 38, 4901–4934.
10. M. Yagi, E. Tomita, T. Kuwabara, *J. Electroanal.l Chem.*, **2005**, 579, 83–88.
11. C. U. Pinnow, I. Kasko, N. Nagel, T. Mikolajick, C. Dehm, F. Jahnel, M. Seibt, U. Geyer, K. Samwer, *J. Appl. Phys.*, **2002**, 91, 1707–1709.

12. G. Lodi, A. De Battisti, G. Bordin, C. D. Asmundis, A. Benedetti, *J. Electroanal. Chem. Interfacial Electrochem.*, **1990**, 277, 139–150.

13. R. Kötz, S. Stucki, S., *Electrochim. Acta*, **1986**, 31, 1311–1316.

14. S. Serrano Lopez, V. Reyes Cruz, J. A. Cobos-Murcia, M. A. Veloz Rodríguez, J. Hernandez Avila, *Int. J. Electrochem. Sci.*, **2015**, 10, 9933–9942.

15. H. Guan, Q. Ke, C. Lv, N. Zeng, C. Hu, S. Wang, X. Ge, J. Cai., *Chem. Lett.*, **2020**, 49(6), 705–708.

16. V. Pfeifer, T. E. Jones, J. J. Velasco Vélez, C. Massué, M. T. Greiner, R. Arrigo, D. Teschner, F. Girgsdies, M. Scherzer, J. Allan, M. Hashagen, G. Weinberg, S. Piccinin, M. Hävecker, A. Knop-Gericke, R. Schlögl, *Phys. Chem. Chem. Phys.*, **2016**, 18, 2292–2296.

17. T. Reier, M. Oezaslan, P. Strasser, *ACS Catalysis*, **2012**, *2*, 1765–1772.

18. J. Ruiz Esquius, D. J. Morgan, I. Spanos, D. G. Hewes, S. J. Freakley, G. J. Hutchings, *ACS Appl. Energy Mater.*, **2020,** *3*, 800–809.

19. M. Jović, J. C. Hidalgo-Acosta, A. Lesch, V. Costa Bassetto, E. Smirnov, F. Cortés-Salazar, H. H. Girault, *J. Electroanal. Chem.*, **2017**, 819, 384–390.

20. H. Guan, Q. Ke, C. Lv, N. Zeng, C. Hu, S. Wang, X. Ge, J. Cai, J. *Chem. Lett.*, **2019**, 49, 705–708.

21. Y. Zhao, E. A. Hernandez-Pagan, N. M. Vargas-Barbosa, J. L. Dysart, T. E. Mallouk, *J. Phys. Chem. Lett.*, **2011**, 2, 402–406.

22. Z. Wang, B. Xiao, Z. Lin, et al., *J. Energy Chem.*, **2021** 54, 510–518.

23. C. Hegde, X. Sun, K.N. Dinh, et al., *ACS Appl. Mater. Interfaces*, **2020**, 12, 2380–2389.

24. J. Chen, H. Li, C. Fan, et al., *Adv. Mater.*, **2020**, 32, 2003134.

25. S. M. Galani, A. Mondal, D. N. Srivastava, *Int. J. Hydrogen Energy*, **2020**, 45, 18635–18644.

26. Y. Wen, T. Yang, C. Cheng, *Chin. J. Catal.*, **2020**, 41, 1161–1167.

27. Y. Li, Y. Wang, J. Lu, et al., *Nano Energy*, **2020**, 78, 105185.

28. Y. Tian, S. Wang, E. Velasco, *iScience*, **2020**, 23, 100756.

29. R. G. González-Huerta, G. Ramos-Sánchez, P. B. Balbuena, *J. Power Sources*, **2014**, 268, 69.

30. J. S. Kim, B. Kim, H. Kim, K. Kang, *Adv. Energy Mater.*, **2018**, 8, 1702774.

31. G. Wu, W. Chen, X. Zheng, D. He, Y. Luo, X. Wang, J. Yang, Y. Wu, W. Yan, Z. Zhuang, X. Hong, Y. Li, *Nano Energy*, **2017**, 38, 167.

32. R. Ge, L. Li, J. Su, Y. Lin, Z. Tian, and L. Chen, *Adv. Energy Mater.*, **2019**, 9, 1901313.

33. J. Su, R. Ge, K. Jiang, Y. Dong, F. Hao, Z. Tian, G. Chen, L. Chen, *Adv. Mater.*, **2018**, 30, 1801351.

34. J. Rossmeisl, Z. Qu, H. Zhu, G. Kroes, J. K. Nørskov, *J. Electroanal. Chem.*, **2007**, 607, 83−89.

35. R. F. Pierret, G. W. Neudeck, Advanced Semiconductor Fundamentals, Cambridge, **1987**.

36. C. Clavero, *Nat. Photonics.*, **2014**, 8, 95-103.

37. H. J. Hwang, K. H. Oh, S. Kim, *Sci. Rep.* **2016**, 6.

38. M. Jovic, H. J. Costa, A. Lesch, V. C. Bassetto, E. Smirnov, F. Cortés-Salazar, H. H. Girault, *Electroanal. Chem*., **2018**, 819, 384 – 390.

39. A. Lesch, *Adv. Mater. Technol.*, **2018**, *3*, 1–10.

40. M. Noel, P. N. Anantharaman, *Surf. Coat. Technol.*, **1986**, 28, 161−179.

41. J. D. Benck, Z. Chen, L. Y. Kuritzky, A. J. Forman, T. F. Jaramillo, *ACS Catalysis*, **2012**, 2, 1916−1923.

42. R. Boggio, A. Carugati, S. J. Trasatti, *Appl. Electrochem*. **1987**, 17, 828−840.